

A Quantum Chemical Exploration of Main Group Complexes



A thesis submitted to Maynooth University in fulfilment of the
requirements for the degree of

Doctor of Philosophy

by

Keelan Byrne, B.Sc.

Department of Chemistry,

Maynooth University,

Maynooth,

Co. Kildare,

Ireland

October 2024

Research Supervisor: Dr. Tobias Krämer

Head of Department: Prof. A. Denise Rooney

Table of Contents

Acknowledgements	i
Abstract.....	iii
1 Introduction	1
1.1 Main Group Chemistry	1
1.2 Aluminium(I) Chemistry	9
1.3 Catalytic Hydrogenation – Alkali metal mediation	30
1.4 Outline and Scope.....	35
2 Theoretical Background.....	37
2.1 Introduction	37
2.2 The Time-Independent Schrödinger Equation	37
2.3 Many-electron wavefunctions	41
2.4 The Hartree-Fock method	43
2.5 Wavefunction Theory Methods	45
2.6 Density Functional Theory	57
2.7 Basis Sets	73
3 The Diradicaloid Electronic Structure of Dialumenes: a Benchmark Study at the Full CI Limit	80
3.1 Introduction	80
3.2 Methods	82
3.3 Results & Discussion.....	84
3.4 Conclusions	116
4 Characterisation of a Base-stabilised Dialumene.....	119
4.1 Introduction	119

4.2	Methods.....	122
4.3	Results & Discussion	123
4.4	Conclusions.....	147
5	Reactivity of a Base-stabilised Dialumene	148
5.1	Introduction.....	148
5.2	Methods.....	155
5.3	Results & Discussion	156
5.4	Conclusions.....	199
6	FLP-type cooperativity in an alkali metal aluminyl complex: proposal of a hydride rebound mechanism	200
6.1	Introduction.....	200
6.2	Methods.....	206
6.3	Results & Discussion	208
6.4	Conclusions.....	246
7	Mechanistic Insight into Alkali-Metal Mediation of Styrene Transfer Hydrogenation	247
7.1	Introduction.....	247
7.2	Methods.....	249
7.3	Results & Discussion	251
7.4	Conclusions.....	272
8	Conclusion.....	274
9	Bibliography.....	277

Acknowledgements

I would like to sincerely thank my supervisor, Dr. Tobias Krämer. Your attention to detail and strong beliefs in scientific rigor has pushed me to hold myself to a high standard, in any work that I have carried out throughout my PhD. You have provided me with many collaborative opportunities, which has allowed me to get to know many interesting people. I am grateful for this, as well as the supervision and support that you have given me throughout the entire process. I wish you the best going forward, and I hope to stay in contact with you.

I would like to thank to Dr. Ragnar Björnsson, for being a fantastic mentor during my research trip to Grenoble in France. I was provided with significant training that has enabled me to explore a whole other side of computational chemistry. Furthermore, I greatly appreciated Ragnar's encouragement to improve my coding skills, with small side projects. Finally, I am grateful to Ragnar and Lindsey for including me on their weekend excursions, that allowed me to explore the beautiful French mountains, caves and countryside.

I would like to acknowledge the Irish Research Council for awarding the funding that allowed me to carry out my research and attend many national and international conferences. I would also like to thank Maynooth University for the studentship that funded me for the first two years of my PhD.

Thank you to all the postgraduate students in the Department of Chemistry, both past and present, in making the day to day of my PhD so much easier. Doing a PhD is a

lonely experience in many respects, but having people to chat to, complain to and joke around with makes that so much easier. I know that we all will be going our separate ways, to live our own lives, so I wish everyone the best, and hope to see you at some point in the future.

I am forever grateful to my mam and dad, for providing me with a world of opportunities throughout my life. Being given the chance to pursue an education, all the way to the highest level is a great privilege, and I could not have done it without your love and support, the whole way. A big thank you also to my sister Ella for always knocking sense into me when I inevitably start to over think my actions and decisions. You have always been a great source of laughs, and as I have always said, would make a great stand-up comedian.

Finally, I could not have gotten through the PhD without the immense love and support of my partner, Megan. You have been a steady and supporting presence during the entire process. From the number of times you have had to listen to my presentations, you basically know my research as well as I do! Thank you so much for reading the thesis in its entirety multiple times and giving me feedback and encouragement on my writing. I do not think I have met anyone who can read as fast as you! Now that we are both finished with our studies, I look forward to whatever comes next for us. The important thing is that whatever it is, we will be together.

Abstract

This thesis aims to address fundamental questions regarding the electronic structure and reactivity of main group complexes, across Group 1, 2 and 13 of the periodic table, using quantum chemical calculations. Chapter 1 provides a literature review and outline of the thesis. Chapter 2 outlines the theoretical background, starting from the time-independent Schrödinger equation. Chapter 3 details the high-level *ab initio* study carried out, to provide insight into the electronic structure of dialumenes, beginning with a model complex, and building to real synthetic examples. Questions regarding the suitability of various quantum chemical methodologies in describing the exotic electronic structure are addressed. Chapter 4 outlines the computational characterization of the third exemplar of a base-stabilised dialumene, work that was published collaboratively with the Cowley group. Building upon this previous chapter, Chapter 5 outlines the mechanistic work carried out to ascertain the mode of reactivity in the activation of dihydrogen and ethene. This work is expanded to other prototypical low-oxidation state aluminium complexes and challenges the currently accepted mechanistic paradigm. Chapter 6 details how a frustrated Lewis pair (FLP) type mechanism, previously postulated, was located for the cooperative activation of dihydrogen by an alkali metal anionic aluminyll complex. This chapter demonstrates how this FLP-type mechanism contradicts previous computational work from Schaefer, with extensive electronic structure analysis carried out. Finally, adhering to the theme of alkali metal mediation, Chapter 7 outlines the mechanistic work, investigating the transfer hydrogenation of styrene, catalysed by an alkali metal magnesiate bimetallic species. It is demonstrated that the monometallic components in isolation are not competent catalysts, while the bimetallic complex efficiently catalyses the transfer hydrogenation, exploiting the individual strengths of the monometallic components.

1 Introduction

1.1 Main Group Chemistry

Since the beginning of the 1970s, the area of main group chemistry has flourished, with the isolation and characterisation of new compounds featuring interesting electronic structures that challenged chemists' understanding of chemical bonding. This chapter will first outline significant historical developments that put main group chemistry on the map, in the context of notable syntheses and reactivity. This discussion will be kept brief, with a focus on key developments in the field, so as to leave space for a more in depth discussion of topics specific to the work carried out in this thesis. For expanded reviews on the topics touched upon in this brief introduction to main group chemistry, the reader is directed towards several reviews.^{1–}

⁴ The topics that will be reviewed in more detail are as follows: neutral Al(I) species, formally anionic Al(I) species and then finishing with a short discussion of alkali metal mediation in the context of s-block catalysis. Finally, the content of the subsequent chapters will be briefly outlined.

1.1.1 Historical developments

It has been known for a long time that the electronic properties of heavier main group elements were fundamentally different to that of their lighter congeners.^{5,6} However, up until the final quarter of the 20th century, certain generalisations or presumptions were made about heavier main group complexes e.g. a lack of open coordination sites, large energy gaps between frontier orbitals and perhaps most importantly, the presumed inability of heavier main group elements to form double bonds between themselves.¹ This latter presumption was known as the “double bond rule”.^{5,7} It was

eventually recognised that in order to isolate double bonded compounds using heavier main group elements, bulky substituents would be required. This was due to the larger radii of these elements, relative to the lighter main group elements of the second period.⁵ This larger size permits higher coordination numbers e.g. $[\text{Al}(\text{OH}_2)_6]^{3+}$ and PCl_5 . The first breakthrough in this regard came in the 1970s, when Lappert successfully isolated tin and germanium analogues of alkenes, R_2MMR_2 ($\text{M} = \text{Sn}, \text{Ge}$), by utilising the bulky $-\text{CH}(\text{SiMe}_3)_2$ alkyl group. The intent was to synthesise the first stable monomeric Group 14 dialkyls. However, in the solid state, the structures were determined to be dimeric (monomeric in solution), and exhibited a trans-bent structure (Figure 1.1).^{8,9}

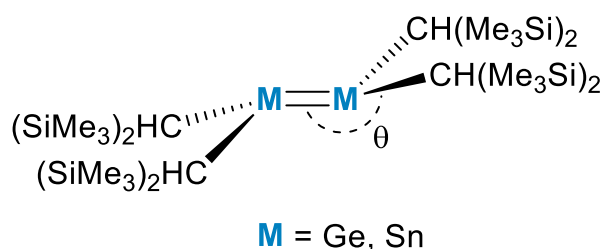


Figure 1.1: The trans-bent structure of Lappert's germanium and tin alkene analogues, R_2MMR_2 ($\text{M} = \text{Ge}, \text{Sn}$; $\text{R} = \text{CH}(\text{SiMe}_3)_2$). The trans-bending angle is given by θ .

Following this, a landmark publication from West in 1981 reported the first disilene, $\text{Mes}_2\text{Si}=\text{SiMes}_2$ ($\text{Mes} = 2,4,6\text{-trimethylphenyl}$). This disilene featured a planar core structure, akin to a classical double bond such as in ethene, and a $\text{Si}=\text{Si}$ bond length of $\sim 2.16 \text{ \AA}$, shorter than the single bond length of $\sim 2.34 \text{ \AA}$.^{1,10} In the same year, the first stable $\text{P}=\text{P}$ double bond from Yoshifuji, as well as the first silaethene ($\text{Si}=\text{C}$) were also reported (Figure 1.2).^{11,12} These three compounds, along with Lappert's distannylene, broke the double bond rule once and for all. Analogously, heavier Group 14 alkyne analogues have also been reported, down to the heaviest element, lead.^{13–}

1 - Introduction

¹⁶ These compounds exhibit the same trend observed for their double bonded counterparts i.e. upon descending the group, the degree of trans-bending of the structure increases.

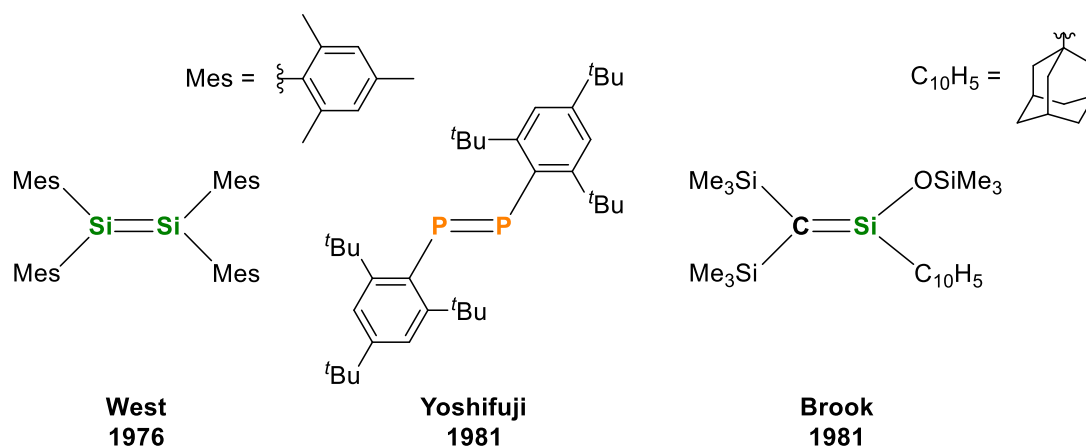


Figure 1.2: The double bonded Group 14 and 15 complexes that collectively broke the “double bond” rule.

The geometrical distortions observed for these heavier main group multiple bonded species have been explained by several different bonding models, summarised in Figure 1.3. Lappert and co-workers proposed a simple donor-acceptor bonding model⁹ (Figure 1.3a), which demonstrates how the trans-bending distortion permits the favourable double donation of the lone pair of electrons of one main group centre (in the singlet ground state) into the empty p-orbital of the opposing main group centre. In the absence of the trans-bending distortion, the lone pairs of each main group centre would experience a steric repulsion, preventing bond formation. Valence bond theory has also been used to rationalise non-classical multiple bonds, using a resonating lone pair model (Figure 1.3b).¹⁷ Trinquier and Malrieu have also utilised valence bond arguments to derive a relationship between the singlet-triplet gap of the monomeric fragments, and the degree of trans-bending present in the dimer.¹⁸ Finally,

the bonding has been rationalised by a second order Jahn-Teller effect, arising from the symmetry-allowed mixing of bonding and anti-/non-bonding orbitals.¹⁹ The weakened, more distorted bonding observed for the heavier elements results in a closer approach of the frontier orbital energy levels, leading to a greater degree of mixing i.e. there is an inverse relationship. The explanation of this model will be expanded upon in Chapter 4.

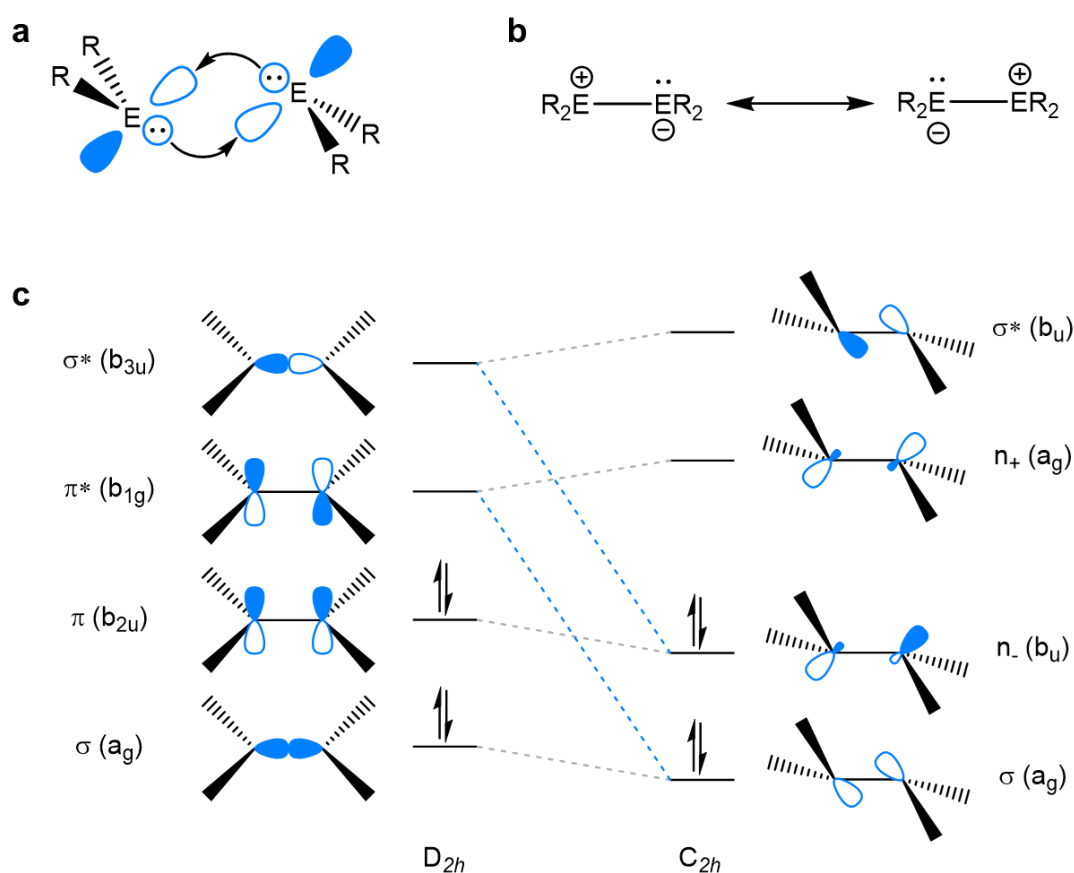


Figure 1.3: Bonding models for heavier main group dimetallene species. (a) The double-donor acceptor model proposed by Lappert and co-workers (b) The resonating lone pair model, in the context of valence bond theory (c) Second-order Jahn-Teller distortion model.

There have also been significant breakthroughs in accessing multiple bonded Group 13 compounds. With regards to triple-bonded species, there was the first report of a

1 - Introduction

Ga—Ga triple-bonded complex, $\text{Na}_2\text{ArGaGaAr}$ ($\text{Ar} = \text{C}_6\text{H}_3\text{-2,6}(\text{C}_6\text{H}_2\text{-2,4,6-}i\text{-Pr}_3)_2$), somewhat controversially due to the presence of the bridging alkali metals and the extreme trans-bending angles of $128.5(4)^\circ$ and $133.5(4)^\circ$ that were present (Figure 1.4).²⁰ The first diboryne was reported in 2012, containing a defined B—B triple bond ($1.449(3) \text{ \AA}$).²¹ Double bonded species for all Group 13 members have been reported, with the isolation of the first base-stabilised dialumene species in 2017 from Inoue completing the series (see more detailed review of dialumenes in section 1.2.2).^{22–26}

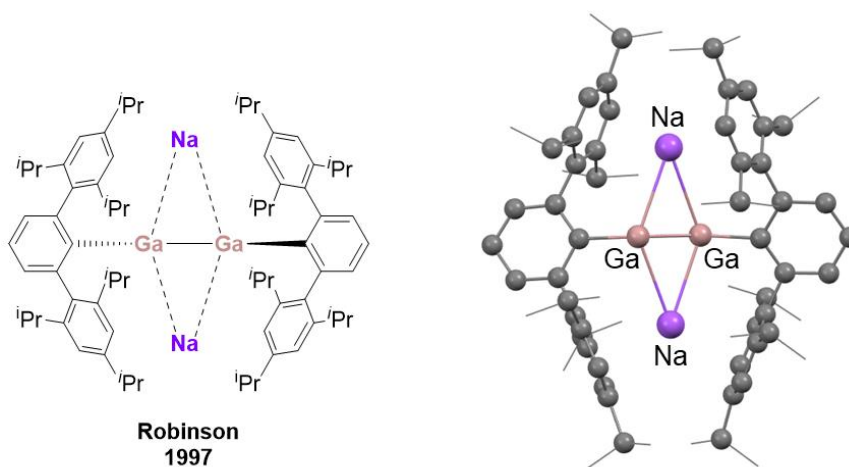
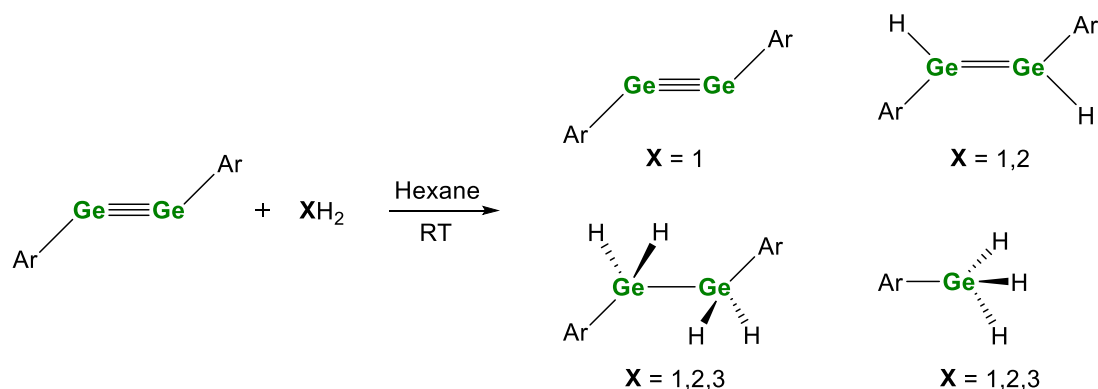


Figure 1.4: The Ga—Ga triple bonded species, $\text{Na}_2\text{ArGaGaAr}$ ($\text{Ar} = \text{C}_6\text{H}_3\text{-2,6}(\text{C}_6\text{H}_2\text{-2,4,6-}i\text{-Pr}_3)_2$). The X-ray crystal structure is shown on the right (H atoms omitted for clarity).

1.1.2 Significant reactivity

Traditional transition metal (redox) catalytic cycles can be broken down into elementary reactions, including oxidative additions, reductive eliminations and insertion reactions. These reactions usually occur with small molecules such as dihydrogen, olefins, alkyl halides or carbon monoxide. Of these reactions, the oxidative addition of dihydrogen is perhaps the most fundamental, having relevance across both industry and academia. In 2005, Power demonstrated the first H—H bond

activation by a main group molecule, where a germanium alkyne analogue, ArGeGeAr , ($\text{Ar} = \text{C}_6\text{H}_3\text{-2,6}(\text{C}_6\text{H}_3\text{-2,6-}^i\text{Pr}_2)_2$) was shown to activate one, two or three equivalents of dihydrogen under mild conditions (Scheme 1.1).²⁷



Scheme 1.1: Reaction of the germanium alkyne analogue, ArGeGeAr ($\text{Ar} = \text{C}_6\text{H}_3\text{-2,6}(\text{C}_6\text{H}_3\text{-2,6-}^i\text{Pr}_2)_2$) with one, two or three equivalents of dihydrogen.

This reactivity was extended to the tin analogue, with subsequent calculations identifying synergistic frontier orbital interactions, drawing a parallel to transition metal reactivity (Figure 1.5).^{28,29} These interactions include a donation from the σ orbital of dihydrogen into the non-bonding LUMO of ArEEAr ($\text{E} = \text{Ge}, \text{Sn}$). Accompanying this is a donation from the π orbital (HOMO) of ArEEAr into the σ^* orbital of dihydrogen. Demonstrating the generality of this frontier orbital comparison, the activation of dihydrogen and ammonia by a two-coordinate germylene species³⁰, as well as the analogous tin complex was demonstrated.³¹

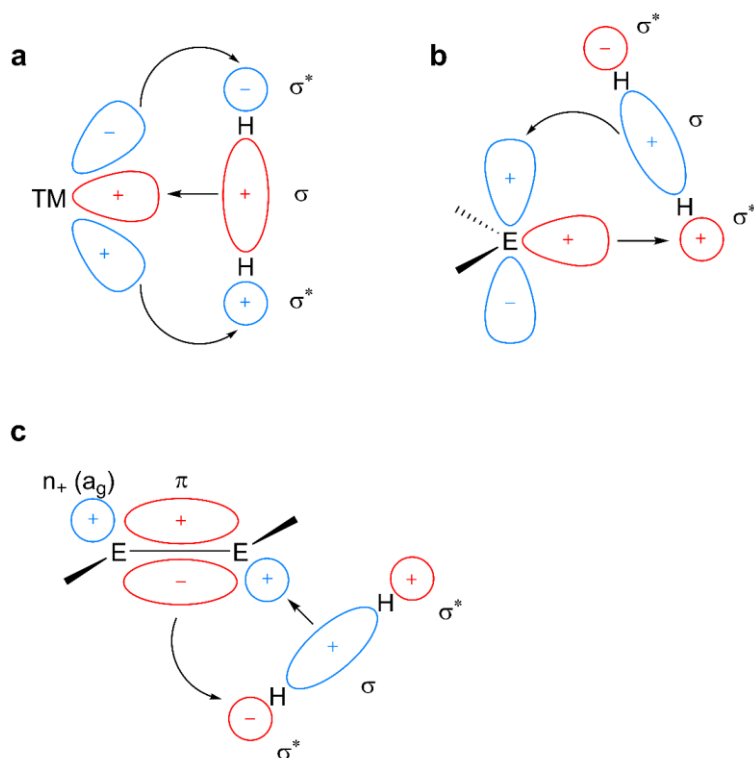
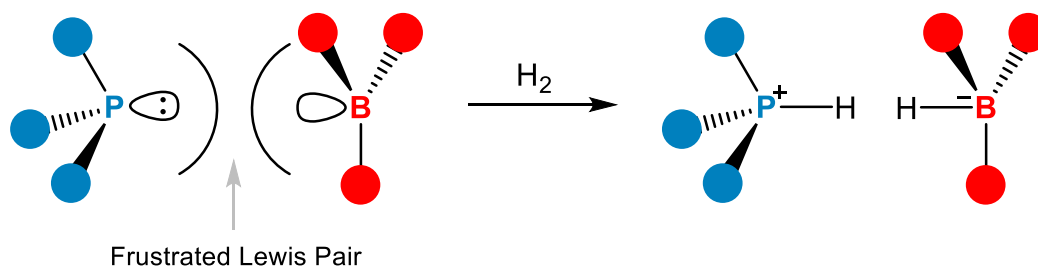


Figure 1.5: a) The interaction of H_2 with the frontier d-orbitals of a transition metal (TM) complex b) The interaction of H_2 with the p-orbital and lone pair of a monomeric main group carbenoid species c) The interaction of H_2 with the π and n_+ frontier orbitals of a main group multiple bonded species (E = main group element).

Another major advance came when it was shown that dihydrogen could be reversibly activated through the use of a “frustrated Lewis pair” (FLP) strategy, using a phosphine borane acid-base pair.³² This strategy was developed by Stephan independently and in parallel to the work from Power. Metal-free activations of dihydrogen were relatively scarce³³, and thus it represented a paradigm shift in the approach taken by chemists to activate and cleave the H—H bond. By utilising the steric bulk of the phosphine ligand, the formation of the acid-base adduct was prevented, thereby preserving the electron pair donating and accepting capabilities of the phosphine and borane, respectively (Scheme 1.2). This permitted a synergistic interaction of the empty borane 2p orbital and phosphine lone pair with the dihydrogen

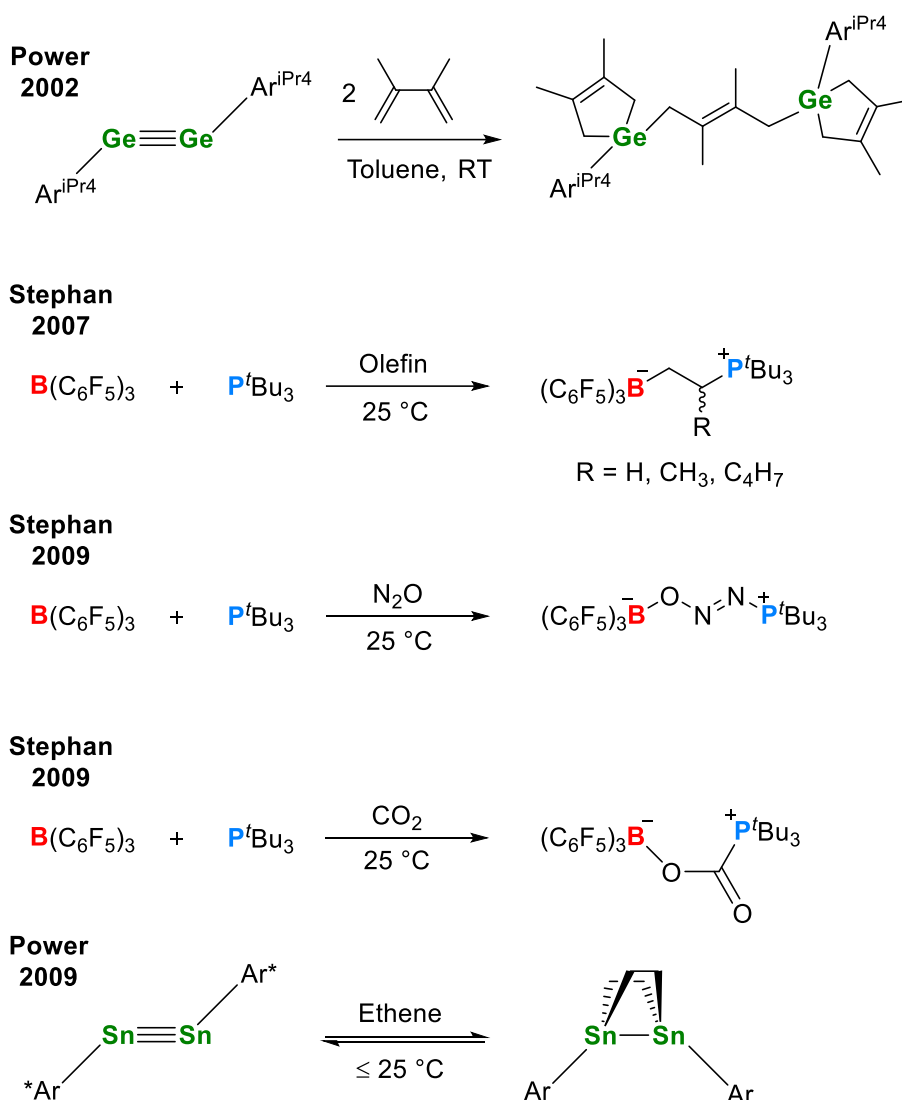
molecule. Since this initial discovery, many more donor/acceptor combinations of main-group elements that utilise this FLP strategy have been developed, with several recent reviews covering significant developments.^{34,35}



Scheme 1.2: The activation of dihydrogen by a frustrated Lewis pair (FLP).

In addition to the activation of saturated small molecules such as hydrogen and ammonia, there has also been progress made in the activation of unsaturated small molecules. Several multiple bonded Group 14 species react with alkenes and alkynes (Scheme 1.3).³⁶ For example, Power has reported the reaction of a bulky digermene with two equivalents of 2,3-dimethyl-1,3-butadiene.³⁶ Furthermore, Stephan has demonstrated the FLP activation of olefins, N_2O and CO_2 .^{37–39} The reversible activation of alkenes or alkynes using main group compounds is much rarer. One notable example is the reversible activation of ethene by a distannylene species, to yield a double cycloadduct at ambient conditions (Scheme 1.3).⁴⁰ A more thorough review of cycloaddition reactions, with a focus on low-valent aluminium(I) compounds will be given in the next section.

1 - Introduction



Scheme 1.3: Notable examples of activations of unsaturated molecules by main group complexes ($\text{Ar}^* = \text{Ar}^{\text{iPr}_4}$ ($\text{C}_6\text{H}_3\text{-2,6-(C}_6\text{H}_3\text{-2,6-}^i\text{Pr}_3)_2$) or $\text{Ar}^{\text{iPr}_8} = \text{C}_6\text{H}_2\text{-2,6-(C}_6\text{H}_2\text{-2,4,6-}^i\text{Pr}_3)_2\text{-3,5-}^i\text{Pr}_2$)).

1.2 Aluminium(I) Chemistry

1.2.1 Initial Developments

For a long time, it was believed that stable complexes of aluminium could only exist in the +3 oxidative state, due to the thermodynamic instability of the +1 and +2 oxidation states. However, in the 80s and 90s, there were significant developments in the isolation of stable molecular low oxidation state aluminium species. A key strategy

in this regard was the use of sterically demanding and strongly σ - and π -donating ligands. The first examples in this area were of a dialane species, containing an unsupported Al—Al single bond (R_2AlAlR_2 , $R = CH(SiMe_3)_2$), and a low oxidation state cluster ($K_2[Al_{12}Bu_{12}]$), reported by Uhl in 1988 and 1991, respectively (Figure 1.6).^{41,42} Aluminium in these complexes exists in the +2 oxidation state.

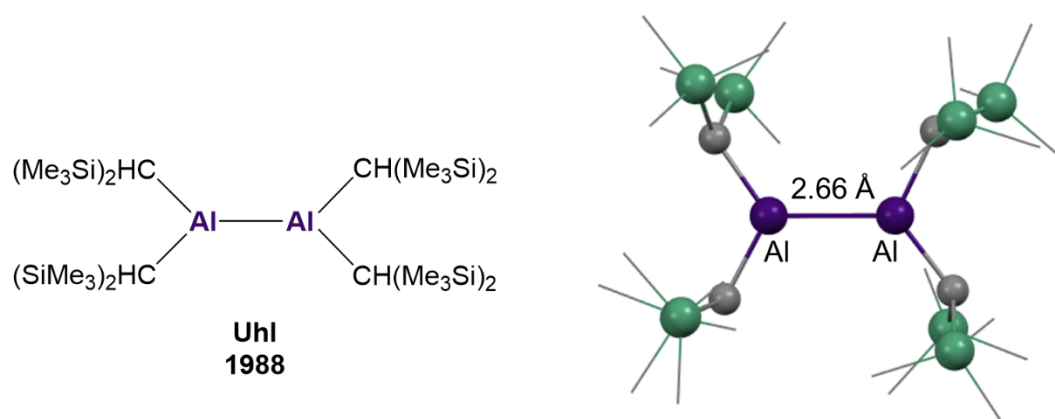


Figure 1.6: Uhl's dialane species, the first report of an unsupported Al—Al single bond. The X-ray crystal structure is shown on the right (H atoms omitted for clarity).

In 1991, the first stable molecular aluminium(I) complex, $[(Cp^*Al)_4]$ (Cp^* = pentamethylcyclopentadienyl), isolated at room temperature, was reported by Schnöckel (Figure 1.7).^{43,44} The initial synthesis was achieved by exploiting the steric bulk of the Cp^* ligand in $[Mg(Cp^*)_2]$, where treatment of a metastable solution of AlCl₃ afforded the desired complex. More recently, an alternative synthesis, that proceeds via the reduction of $[Cp^*AlCl_2]$ and a redox reaction of $[Cp^*_2AlH]$ has been reported.⁴⁵ At room temperature, this complex maintains a tetrameric structure in solution, but has been shown to react with small molecules such as azides and oxygen, and deliver $Cp^*Al(I)$ as a ligand to transition metal centres.⁴⁶

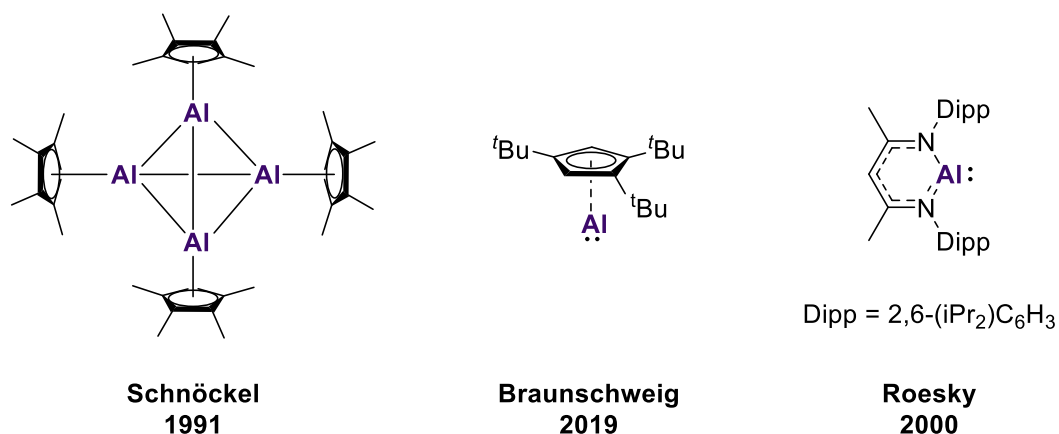
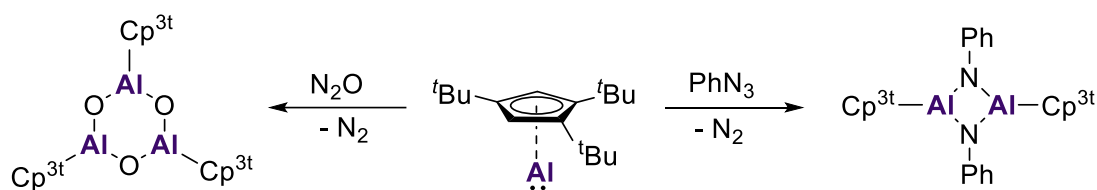


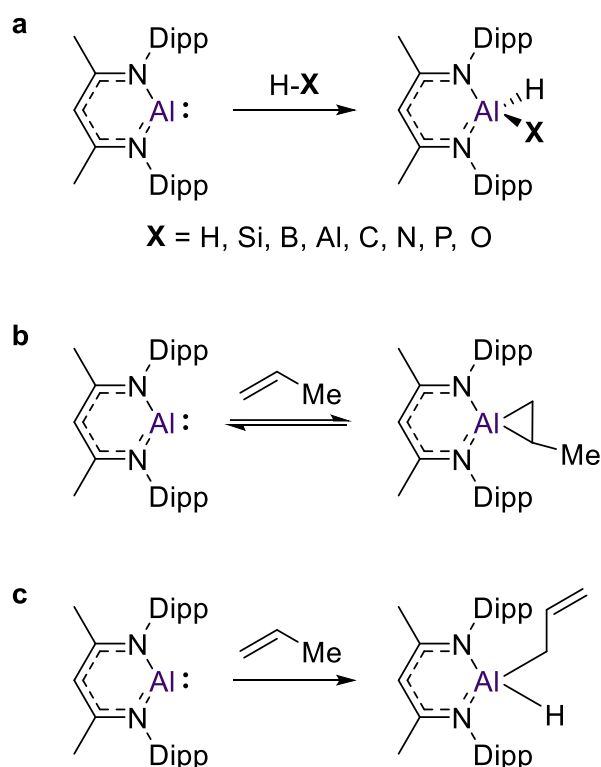
Figure 1.7: Key examples of stable molecular Al(I) species.

By varying the substituents of the Cp ring, perturbation of the equilibrium between different aggregation states can be achieved, due to the dependence on sterics and temperature.^{47,48} In 2019, Braunschweig and co-workers successfully observed in solution the first monomeric variant (Figure 1.7), where the sterically demanding 1,3,5-tri-tertbutylcyclopentadienyl (Cp^{3t}) ligand was utilised.⁴⁹ The monomeric structure promoted more rapid and selective reactivity than that of the tetrameric variant (Scheme 1.4).

Scheme 1.4: Key examples of the reactivity of Braunschweig's monomeric Cp^{3t}Al complex (Cp^{3t} = 1,3,5-tri-tertbutylcyclopentadienyl).

In a further development, Roesky synthesized the first monomeric Al(I) complex in the solid state, NacNacAl(I) (Figure 1.7, $\text{NacNac} = [\text{DippNC(Me)CHC(Me)NDipp}]^-$; Dipp

= 2,6- $\text{Pr}_2\text{C}_6\text{H}_3$).⁵⁰ This complex utilised the bulky 2,6-diisopropylphenyl (Dipp) β -diketiminate ligand, and is structurally analogous to a carbene. Since the synthesis of NacNacAl(I) , there have been extensive investigations into the reactivity of this complex. The oxidative addition of a range of H-X bonds across the Al(I) centre have been reported (Scheme 1.5a), as well as the reversible addition of alkenes (Scheme 1.5b) and allylic C-H activation (Scheme 1.5c).⁵¹⁻⁵³ These are just some key examples of the reactive capability of this complex. Several more in depth reviews have been published.^{46,54} The electronic structure and reactivity of this complex will be further investigated in Chapter 5.



Scheme 1.5: Key examples of reactivity exhibited by NacNacAl(I) .

1.2.2 Group 13 Multiple Bonds

Historically, it was believed that multiple bonds between elements of Group 13 were not possible. This was due to these elements possessing only three valence electrons available to partake in bonding, weak bonding energies, as well as a strong tendency to decompose. This belief was put to rest with the use of strong Lewis bases, which provided significant stabilisation through their electron donating ability. In particular, N-heterocyclic carbenes (NHC) have demonstrated significant success in this area.⁵⁵ For example, NHCs have enabled the isolation of the first diborene and diboryne, by Robinson and Braunschweig, respectively (Figure 1.8).^{21,22} As Group 13 is descended, the stability of the lone pair increases, due to the inert pair effect, which refers to the fact that the highest oxidation state becomes increasingly unfavourable when moving down a given p-block main group, thus promoting the stability of the +1 oxidation state, in the case of Group 13. The stabilisation provided by Lewis bases such as NHCs is then no longer required, with bulky aryl ligands (e.g. Dipp = 2,6-*i*-Pr₂C₆H₃) permitting the isolation of trans-bent double bonded complexes of the heavier members of the group (Ga-Tl), namely the digallene, diindene and dithallene (Figure 1.8).^{24–26}

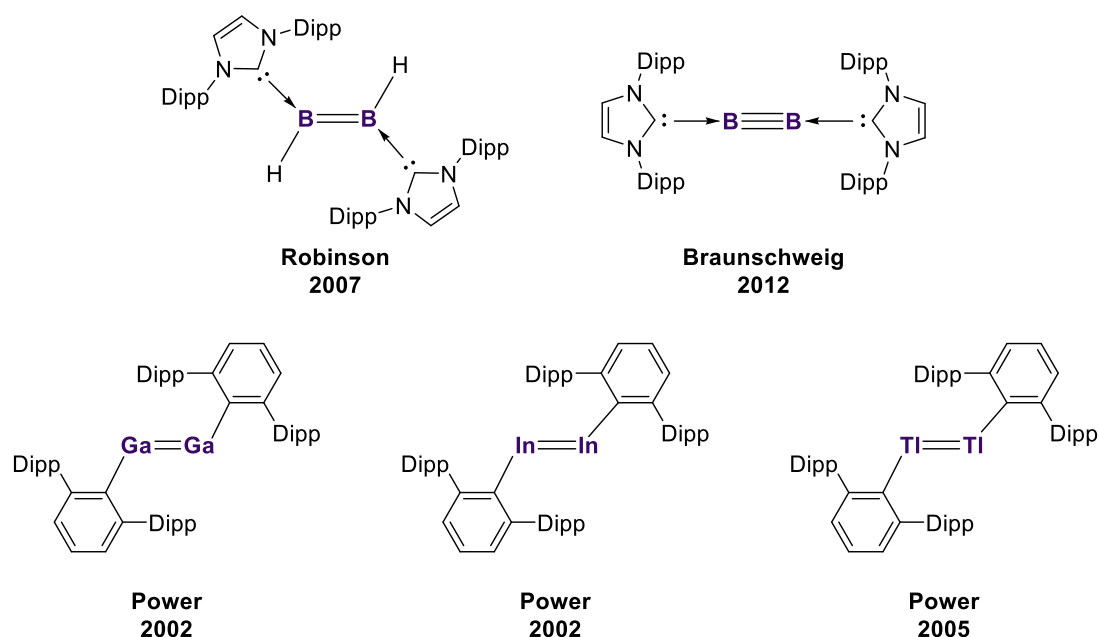


Figure 1.8: Selected examples of Group 13 multiple bonded complexes, excluding aluminium (Dipp = 2,6-*i*-Pr₂C₆H₃).

Up until recently, there were no known isolated examples of Al—Al multiple bonds in the solution or solid phase. In the gas phase however, there has been progress in accessing ligand-free Al=Al double and Al≡Al triple bonds, using pulsed arc discharge techniques.^{56,57} Base-stabilised dialumenes were first isolated in 2017, with Inoue reporting the first stable and neutral example, **1**, containing an Al=Al double bond (Figure 1.9a).²³ This was achieved through the use of a sterically bulky and strongly σ -donating di-*tert*-butyl(methyl)silyl substituent, in conjunction with the strong coordinating ability of an NHC. Single crystal X-ray diffraction revealed a trans-planar geometry, with an Al=Al bond length of 2.3943(16) Å. This is significantly shorter than previous structurally characterised Al—Al single bonds, such as in Uhl's dialane.⁴¹ Density functional theory calculations at the B3LYP/6-311G(d) level of theory revealed that the HOMO was the out-of-plane π bond, while the HOMO-1 was the Al—Al σ bond. Natural bond orbital (NBO) analysis predicted electron occupancies of the Al—Al σ and π bond of 1.91 and 1.78 electrons, respectively. Furthermore, a Wiberg bond

index (WBI) of 1.67 was calculated. Recent calculations from Krossing on dicationic digallene and diindene complexes of the form $[E(dcpe)]_2^{2+}$ ($E = Ga, In$) have predicted WBIs of 1.31 and 0.81 for the digallene and diindene, respectively.⁵⁸ By comparing the WBI of **I** to those calculated by Krossing, it can be concluded that **I** possesses significant multiple bond character.

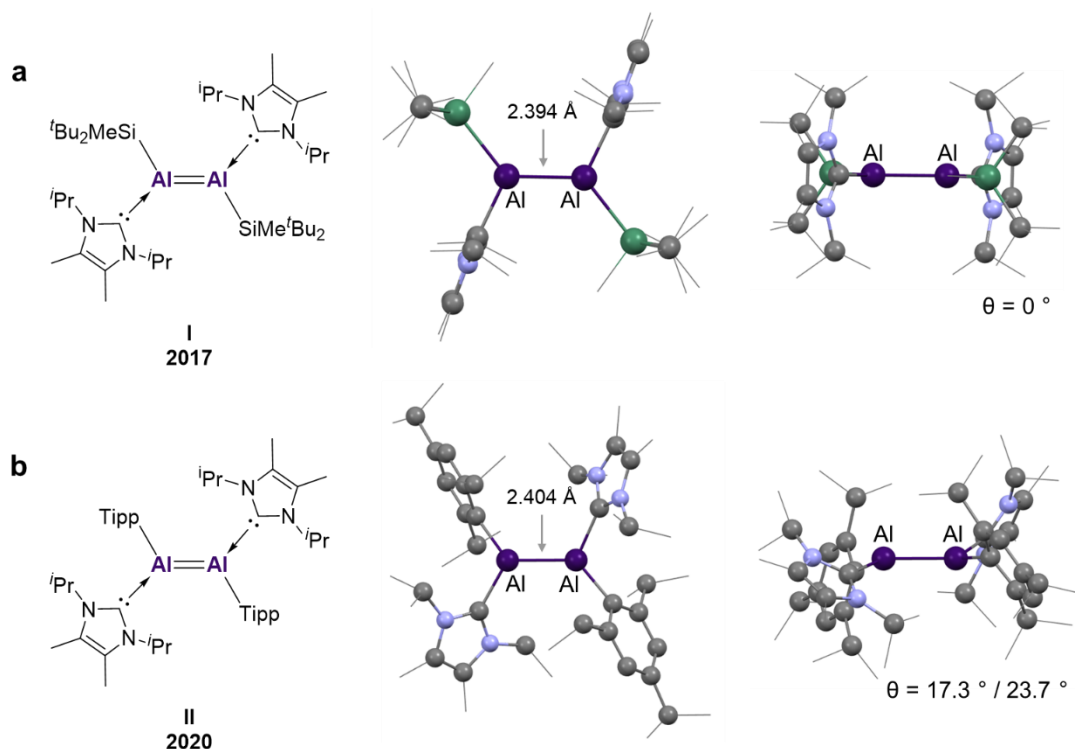
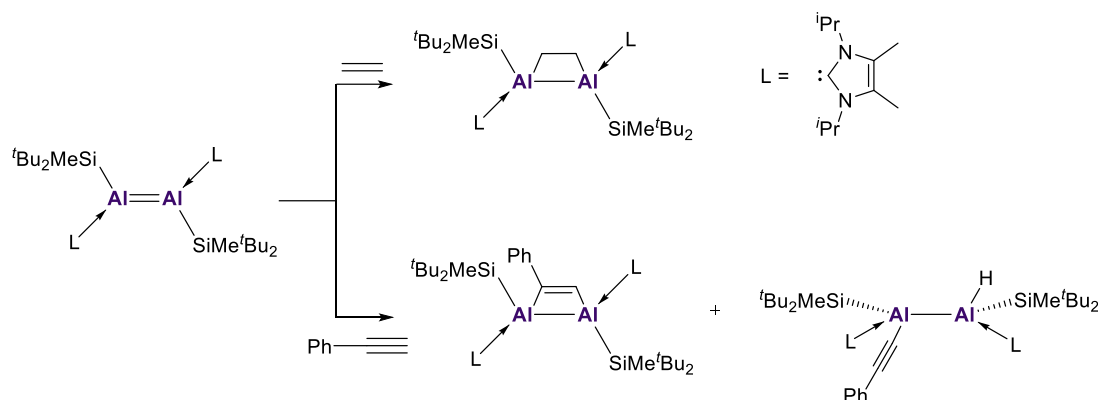


Figure 1.9: a) Silyl ($-\text{SiMe}^t\text{Bu}_2$) substituted NHC stabilised dialumene, **I** b) Tipp ($-\text{2,4,6-}^i\text{Pr}_2\text{C}_6\text{H}_3$) substituted NHC stabilised dialumene, **II**. X-ray crystal structures of both dialumenes are shown from the front-on view (middle panel) and side-on view (right panel). H atom omitted for clarity. Trans-bending angle given by θ .

In order to further prove the formation of the double bond in **I**, the reactivity was explored. Upon exposure to ethene gas at room temperature, a dialuminacyclobutane product was formed, resulting from a formal $[2+2]$ cycloaddition (Scheme 1.6). When

reacted with phenylacetylene, the corresponding [2+2] cycloaddition product was formed, but in addition, a C—H insertion product was also observed.



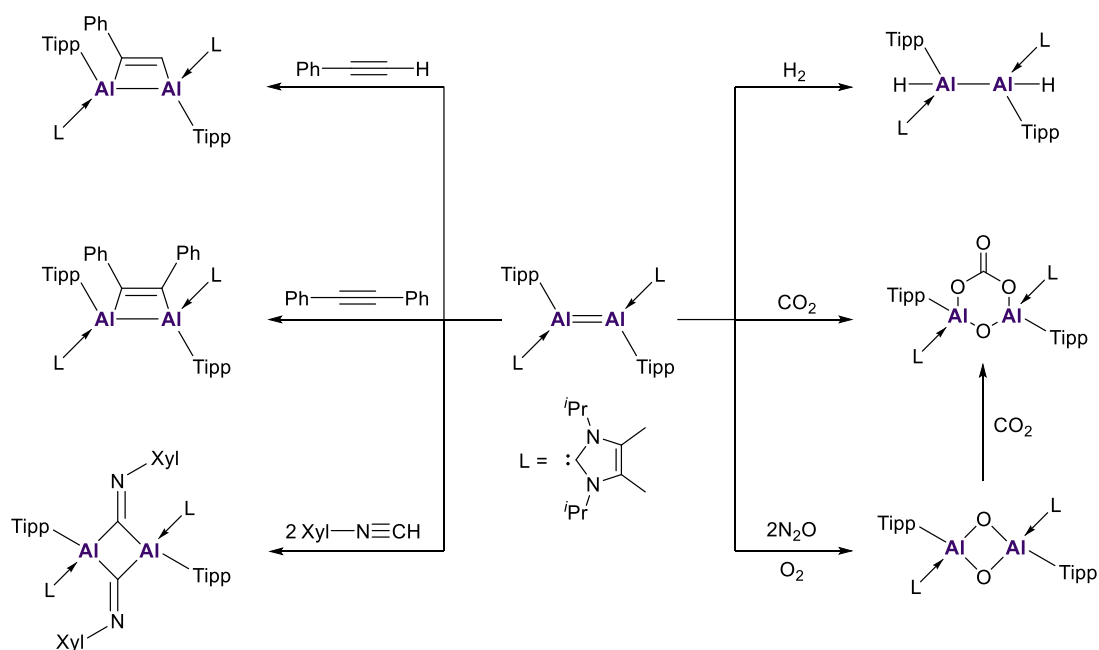
Scheme 1.6: Reactivity of the first base-stabilised dialumene with ethene and phenylacetylene.

To further explore the effects of different substituents on the geometry and reactivity, a second NHC-stabilised dialumene, **II**, was successfully synthesised, substituted by the bulky Tipp (2,4,6-*i*Pr₂C₆H₃) ligand (Figure 1.9b).⁵⁹ X-ray crystallographic analysis revealed a trans-bent (~20 °) and twisted (~12 °) geometry, with an Al=Al bond length of 2.4039(8) Å. Density functional theory calculations revealed a smaller HOMO-LUMO gap (1.86 eV) than **I** (2.24 eV), with the differing electronic structures attributed to the change in substituent from a more electron donating (silyl) to a more electron withdrawing one (Tipp).⁶⁰ NBO analysis revealed a decrease in the WBI from 1.67 (**I**) to 1.53 (**II**), in line with reduced but still notable multiple bonding character.

When reacted with ethene, the analogous dialuminacyclobutane product, as observed for **I**, was formed. However, when reacted with phenylacetylene, formation of *only* the [2+2] cycloaddition product was observed, with no C—H insertion occurring (Scheme 1.7). **II** was further shown to react with diphenylacetylene, forming the [2+2]

1 - Introduction

cycloaddition product, which contrasts with that of **I**, where no reactivity was observed, even at elevated temperatures. This enhanced reactivity was attributed to the increased flexibility of the Tipp ligand, allowing for greater access of bulky substrates. It was also found that 2,6-dimethylphenylisocyanide reacted with **II**, to form a bridging XylC=N product. The same reaction, when attempted with **I** was found to yield an intractable mixture of products.



Scheme 1.7: Reactivity of the second base-stabilised dialumene, **II**.

Finally, **II** was found to react with CO_2 to form a carbonate complex (Scheme 1.7), via initial CO_2 fixation (analogous to **I**, although fixation product not isolated), however the increased reactivity of **II** made the characterisation of this product difficult (only confirmed via ^{13}C NMR). A dioxo product could be formed through reaction with O_2 or two equivalents of N_2O . When the dioxo product was further reacted with CO_2 , the carbonate product could be accessed.

More recently, the third exemplar of a base-stabilised dialumene, **1**, was reported by Cowley (Figure 1.10).⁶¹ Previously, a chiral amidophosphine ligand framework was used as a stereochemical reporter by the Cowley group, in order to probe hidden reversible reductive elimination processes.⁶² In this previous study, a transient alumanyl monomer was implicated in the reductive elimination of an Al(II) dihydrodialane. Given these results, an isolable dialumene of the same ligand framework was successfully synthesised by reducing the Al(III) diiodo precursor complex using a Na/K alloy. This was reported in a joint experimental (Cowley) and computational (Krämer) study.⁶¹ As well as being the third exemplar, it was also the first example of a dialumene that could reversibly dissociate in solution to its monomeric form. It was revealed that this dialumene has an extremely long (2.5190(14) Å) and heavily trans-bent (48.8 °) Al=Al double bond, with a low bond dissociation energy and order. The detailed quantum chemical characterisation of the electronic structure of this dialumene will be discussed in detail in Chapter 4, with Chapter 5 investigating the reactivity that this dialumene undergoes.

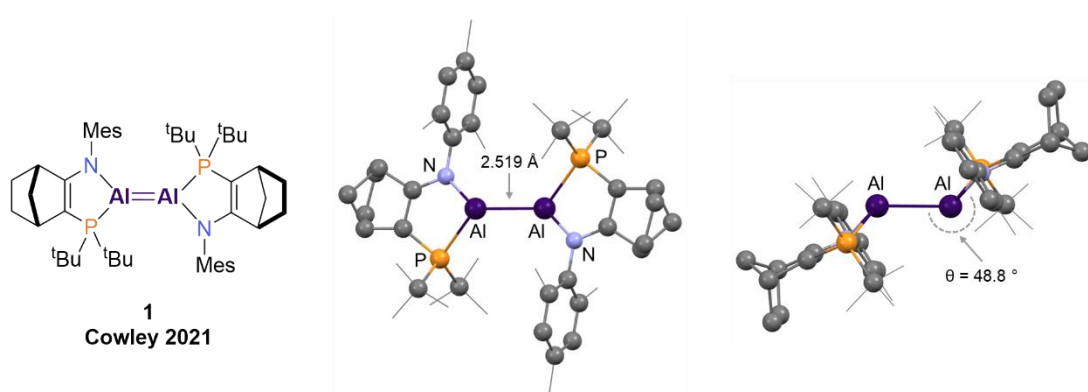
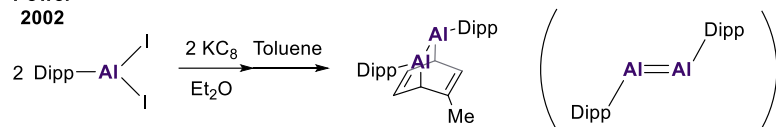


Figure 1.10: The amidophosphine stabilised dialumene from Cowley. X-ray crystal structure from a top (middle) and side-on view (right). H atoms omitted for clarity.

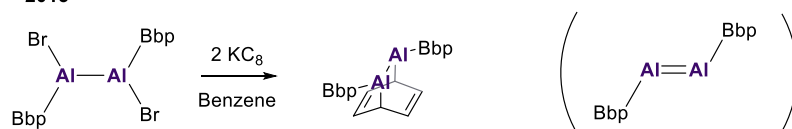
Although there have been three reported base-stabilised dialumenes, several attempts have been made prior to 2017 to isolate a complex containing an Al=Al double bond. For example, in 2003, a transient (non-base-coordinated) dialumene species was implicated in the reduction of a Dipp-substituted Al(III) diiodo precursor.⁶³ Rather than isolating the transient dialumene species, cycloaddition with the solvent, toluene, occurred (Scheme 1.8). A similar outcome occurred in 2013, when Tokitoh attempted to reduce a dialane precursor, substituted with a bulky Bbp (2,6-[CH(SiMe₃)₂]₂C₆H₃) ligand.⁶⁴ The benzene solvent was proposed to react with a transient dialumene to form the cycloaddition product. More recently, in 2022, Bakewell investigated the stoichiometric reduction of a series of Al(III) dihydrides, using Roesky's NacNacAl(I) monomeric species.⁶⁵ A range of new low oxidation state species were synthesised, including that of a masked dialumene, containing an amidinate ligand framework. These examples demonstrate the highly reactive nature of dialumenes, relative to the heavier members of Group 13, where unsupported double bonds have been successfully synthesised through the use of bulky ligand architectures (Figure 1.8).

1 - Introduction

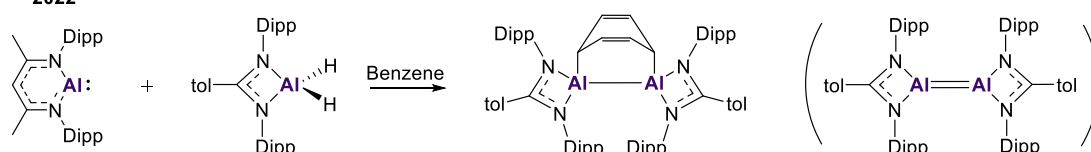
**Power
2002**



**Tokitoh
2013**



**Bakewell
2022**

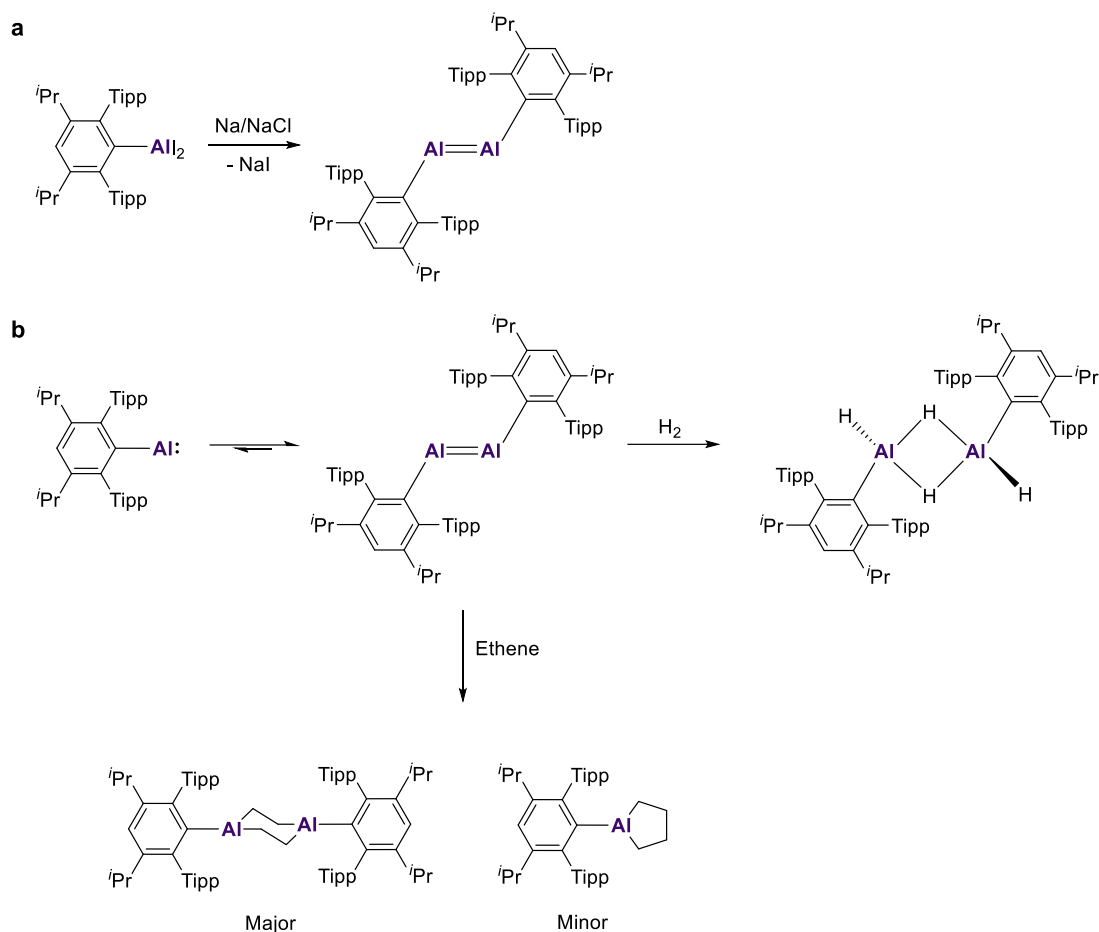


Scheme 1.8: Examples of masked dialumenes, postulated as intermediates in cycloaddition reactions with benzene and toluene (Dipp = 2,6- $\text{iPr}_2\text{C}_6\text{H}_3$, Tipp = 2,4,6- $\text{iPr}_2\text{C}_6\text{H}_3$, Bbp = 2,6- $[\text{CH}(\text{SiMe}_3)_2]_2\text{C}_6\text{H}_3$, tol = Toluene).

Despite this lack of success prior to 2017, the first “free” dialumene (with no base stabilisation) has been successfully isolated in the solid state only recently.⁶⁶ Through careful analysis of the crystals formed during the reduction of Ar^*AlI_2 ($\text{Ar}^* = \text{C}_6\text{H}-2,6-(\text{C}_6\text{H}_2-2,4,6-\text{iPr}_3)_2-3,5-\text{iPr}_2$), it has been shown that the dialumene $\text{Ar}^*\text{Al}=\text{AlAr}^*$ forms alongside the corresponding alanedyl (Scheme 1.9a). Analysis of the X-ray crystal structure revealed an Al=Al bond distance of 2.648 Å, which is by far the longest reported Al=Al double bond to date. The authors concluded that the bonding is best described as a double dative interaction, augmented with a small amount of diradical character. The diradical character was analysed via a broken symmetry approach at the UPBE0-D3BJ/def2-TZVP level of theory, where a minor RHF/UHF instability was located in the closed-shell Kohn Sham single determinant. Furthermore, the extreme bulkiness of the Ar^* ligand architecture provides stabilising dispersive interactions.⁶⁷ This was evidenced by decomposing the interaction energy, using energy decomposition analysis, between the two alanedyl fragments into its various

1 - Introduction

components (electrostatic attraction, Pauli repulsion, orbital stabilisation and dispersion).



Scheme 1.9: a) Synthesis of the free dialumene $\text{ArAl}=\text{AlAr}$ ($\text{Ar} = \text{C}_6\text{H}-2,6-(\text{C}_6\text{H}_2-2,4,6-\text{iPr}_3)_2-3,5-\text{iPr}_2$). b) Reactivity of $\text{ArAl}=\text{AlAr}$, assumed to proceed via association to the dimer in solution.

The alanedyl was found to react rapidly with dihydrogen (Scheme 1.9b), at room temperature, yielding the bridged $\text{Ar}^*\text{Al}(\text{H})(\mu\text{-H})_2\text{Al}(\text{H})\text{Ar}^*$ species (the dialumene decomposed to the alanedyl in solution). Density functional theory calculations revealed that this reactivity proceeded preferentially via the dimer, with an activation barrier of $17.4 \text{ kcal mol}^{-1}$ calculated, while the barrier for monomeric activation was calculated to be $45.9 \text{ kcal mol}^{-1}$. The reaction of the alanedyl with ethene gave the

products 1,4-dialuminacyclohexane and the aluminacyclopentane, as major and minor products, respectively. Calculations revealed that these products form via initial activation of one equivalent of ethene by the alanediy, contrasting the dimeric activation demonstrated in the case of dihydrogen. In a previous study from the same authors⁶⁸, preliminary calculations for the addition of propene to a free dialumene (only known theoretically at that point) was postulated to proceed via a stepwise mechanism involving a diradicaloid intermediate. Despite this, a corresponding mechanism was not explored for the activation of ethene.

It is clear from the discussion thus far that a common feature among heavier Group 13 dimetallenes species are the more strained or trans-bent geometries, contrasting those observed for alkenes. These strongly trans-bent geometries weaken the E=E bond and cause an accumulation of electron density on the E centres, thus increasing the non-bonding lone pair character (Figure 1.11). For the lighter dialumenes, this translates into a small to moderate level of singlet diradicaloid character⁶⁹, as already hinted at by the above discussion of the reactivity of the first free dialumene with ethene.⁶⁶ However, it is not fully apparent as to how well density functional theory describes the electronic structure of dialumenes, as well as their reactivity.⁶⁸ This is a topic that will be explored in great detail in Chapter 3.

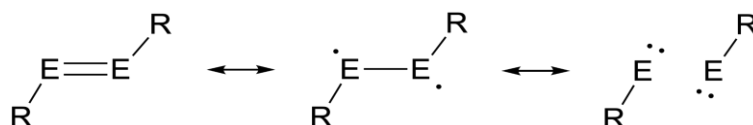


Figure 1.11: Canonical resonance structures representing contributions to the bonding in REER dimetallene species.

1.2.3 Anionic Al(I) – Aluminyls

Given the extensive chemistry of carbenes, of the general form X_2C (X_2 = dianionic ligand set, such as $[(^t\text{BuNCH})_2]^{2-}$), there has been significant interest in isolating stable isoelectronic Group 13 analogues. In order to achieve this isoelectronic relationship with carbenes i.e. an atom centred lone pair and an empty p-orbital, the Group 13 centre must be in the +1 oxidation state. The dianionic ligand set then gives the resulting complex an overall negative charge (Figure 1.12).

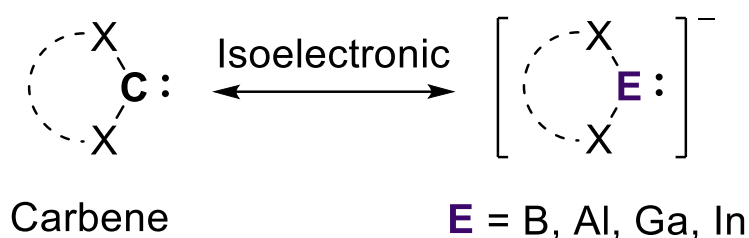


Figure 1.12: Relationship between neutral carbenes and the isoelectronic Group 13 carbene analogues (X = anionic ligand).

The first Group 13 carbene analogue to be successfully isolated was the gallyl anion, $[(^t\text{BuDAB})\text{Ga}]^-$ ($^t\text{BuDAB} = [(^t\text{BuNCH})_2]$, from Schmidbauer in 1999 (Figure 1.13).⁷⁰ This was isolated as a separated ion pair, with $[\text{K}(18\text{-c-}6)]^+$ (18-c-6 = 18-crown-6) acting as the countercation. This was followed by a diaryl substituted version in 2002⁷¹, and a dpp-bian (1,2-bis[(2,6-diisopropylphenyl)imino]acenaphthene) stabilised version from Fedushkin in 2008.⁷²

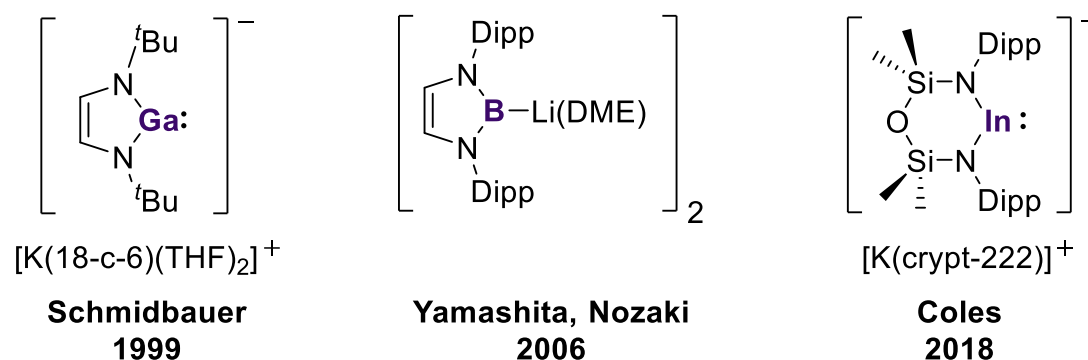


Figure 1.13: The first reported gallyl, boryl and indyl anions (18-c-6 = 18-crown-6, crypt-222= cryptand 222).

In 2006, Yamashita and Nozaki reported the first boryl lithium complex, $[(DippDAB)BLi(DME)]_2$ ($DippDAB = [(DippNCH)_2]$), the first example of a boryl anion (Figure 1.13).⁷³ The $B \cdots Li$ bond was found to be highly polarised, with a bond distance of 2.291 Å. ^{27}Li NMR indicated that there was likely an interaction present with the quadrupolar nucleus of boron. Furthermore, this complex was found to exist as a dimer in the solid state. A monomeric version has since been reported.⁷⁴ Since this initial synthesis, several more boryl anions have been reported, utilising an array of chelating ligands.⁷⁵ Of the heavier members of the group, it was not until 2018 that the first indyl anion was reported, by Coles and co-workers (Figure 1.13).^{76,77} This complex was reported as a separated ion pair (shown), as well as a more tightly bound lithium complex.

Most notably, the first report of an aluminyl anion came in 2018, from Aldridge and Goicoechea (Figure 1.14).⁷⁸ This complex was prepared by the two electron reduction of the neutral Al(I) precursor, $(NON)AlI$ ($NON^{2-} = 4,5$ -bis(2,6-diisopropylanilido)-2,7-di-tert-butyl-9,9-dimethylxanthene) using the reducing agent KC_8 . X-ray crystallographic analysis, as well as DOSY NMR, revealed that the resulting complex is dimeric in both

the solid and solution phases, respectively. The bulky xanthene-based diamido ligand (NON) provides significant stabilisation, with the dimer being held together by intermolecular interactions between the flanking Dipp (2,6-*i*-Pr₂C₆H₃) groups on the NON²⁻ ligand and the potassium centres. In the crystal structure, the distance between the two aluminium centres was measured to be greater than 6.6 Å, far larger than the sum of the covalent radii, strongly implying that there is no interaction between these centres. Finally, there is a relatively weak dative interaction between the oxygen centres in the NON backbone, and the Al centres (2.279(2) Å).

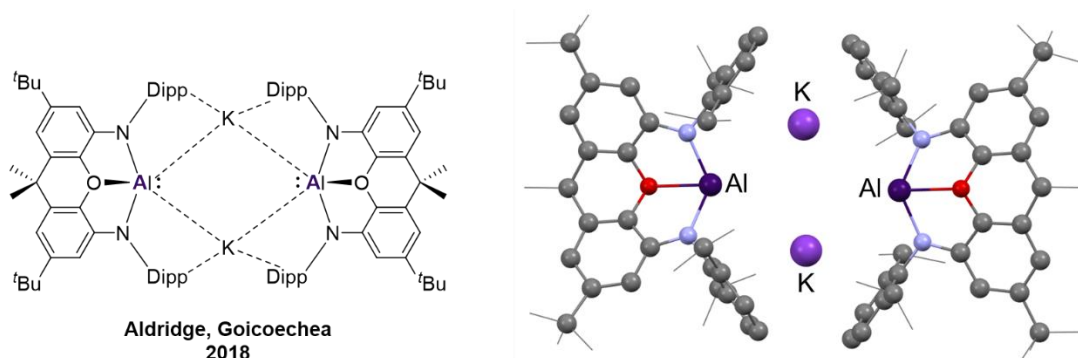
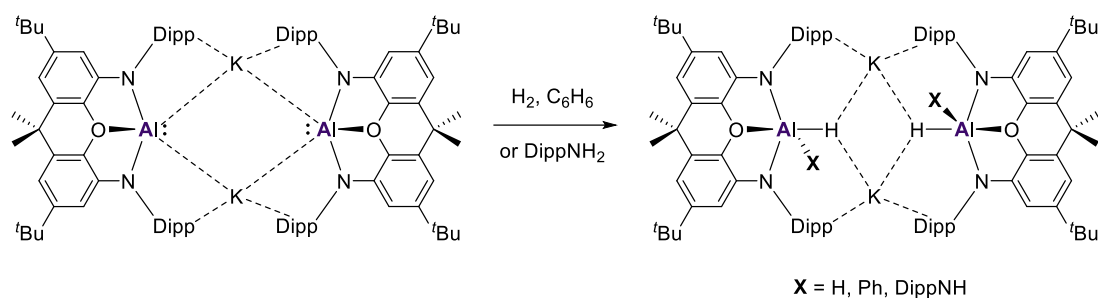


Figure 1.14: The first alumanyl anion, $[K\{Al(NON)\}]_2$ (NON = 4,5-bis(2,6-diisopropylanilido)-2,7-di-tert-butyl-9,9-dimethylxanthene). The X-ray crystal structure is shown on the right (H atoms omitted for clarity).

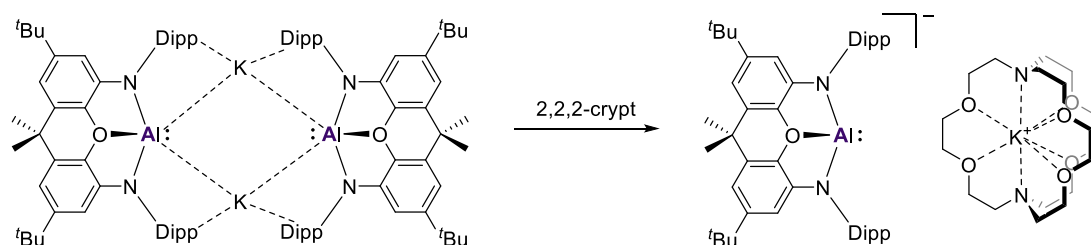
$[K\{Al(NON)\}]_2$ has been shown to exhibit a range of reactive capability. For example, the oxidative cleavage of the H—H bond of H₂ and a C—H bond of benzene could be carried out under mild reaction conditions (Scheme 1.10).⁷⁸ In both cases, the dimeric aggregation state was retained in the product. More recently, the activation of an NH bond of DippNH₂ was achieved, affording the corresponding oxidative addition product (Scheme 1.10).⁷⁹

1 - Introduction



Scheme 1.10: Examples of bond activations by $[\text{K}\{\text{Al}(\text{NON})\}]_2$.

In 2019, the charge separated complex $[\text{K}(2,2,2\text{-crypt})][\text{Al}(\text{NON})]$ was successfully isolated, with the potassium cations sequestered by a cryptand species (Scheme 1.11).⁸⁰ This marked the first report of a so called “naked” alumanyl anion complex. X-ray crystallography confirmed that in the solid state, the potassium cations are fully encapsulated within the cryptand, and that the $[\text{Al}(\text{NON})]^-$ engages in no significant interactions with the potassium cations (the $\text{K}\cdots\text{Al}$ distances are all greater than 7 Å).

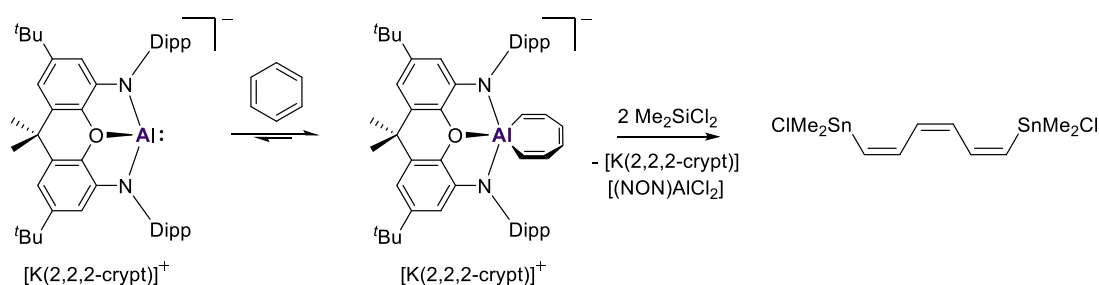


Scheme 1.11: Sequestration of the potassium cations from $[\text{K}\{\text{Al}(\text{NON})\}]_2$ to generate the monomeric “naked” alumanyl anion, $[\text{Al}(\text{NON})]^-$.

Contrary to the reactivity of the dimer, where only C—H activation was observed (Scheme 1.10), the “naked” alumanyl anion was shown to activate a C—C bond of benzene, at room temperature, to yield a 7-membered aluminium heterocycle (Scheme 1.12).⁸⁰ This reaction was found to be reversible when heated. Furthermore,

1 - Introduction

density functional theory calculations, at the PBE0-D3/def2-TZVP level of theory, were carried out to model the mechanism for the C—C and C—H bond cleavage of benzene.⁸⁰ The C—H bond cleavage pathway was predicted to be thermodynamically more favourable than the C—C bond cleavage pathway (-34.9 and -4.1 kcal mol⁻¹, respectively). However, the barrier to C—C bond cleavage was calculated to be greater than 5 kcal mol⁻¹ lower in energy. This is consistent with the observed formation of the 7-membered aluminium heterocycle.



Scheme 1.12: Reactive capability of the naked aluminyll anion [Al(NON)]⁻.

Building on the success of [K{Al(NON)}]₂, a series of 6- and 7-membered cyclic aluminyll anions have been reported since, primarily consisting of bidentate diamido based ligands (Figure 1.15).^{81–86} The first of these, [K₂{Al(SiNON)}]₂, was reported in 2019 by Coles and co-workers⁸¹, followed by the closely related [K₂{Al(NCCN)}]₂⁸², by Hill. The mesityl substituted variant of this latter example has since been reported.⁸⁴ In an attempt by Harder to boost the reactivity of the Al(I) β-diketiminato complex, NacNacAl(I)⁵⁰, through the addition of a potassium base, deprotonation of one of the methyl groups in the ligand backbone occurred, generating the diamido ligand, and thus the corresponding aluminyll anion.⁸³ An analogous Di pep (Di pep = 2,6-C(H)Et₂C₆H₃) substituted version has since been reported.⁸⁶ Another notable example is that from Yamashita in 2022, where an aluminyll anion, possessing a *N,N'*-bis(2,6-diisopropylphenyl)-1,3-propanediamine ligand was reported.⁸⁵ In addition to the

1 - Introduction

potassium alumanyl complexes reported, complexes utilising the whole of the Group 1 alkali metals have also been reported for the Harder (Ar = Dipp) and Coles complexes.^{87,88}

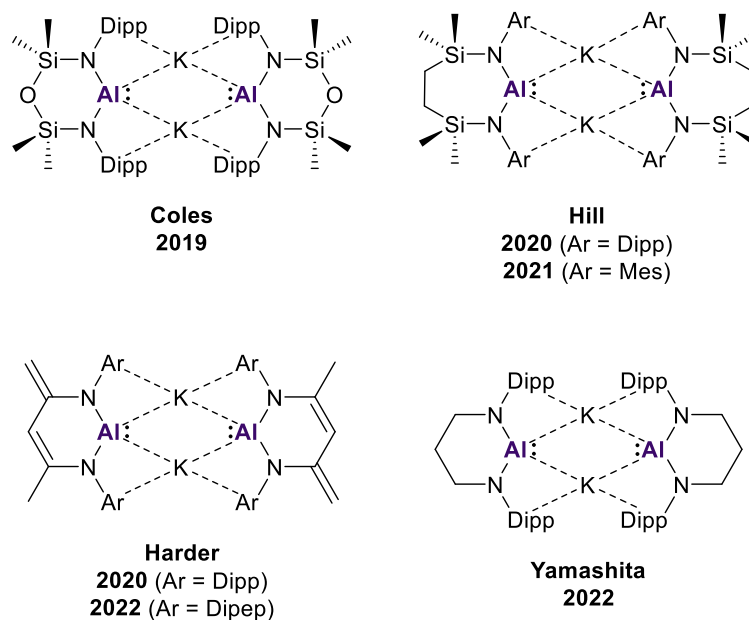


Figure 1.15: Examples of diamido disubstituted alumanyl complexes (Dipp = 2,6-*i*-Pr₂C₆H₃, Mes = 2,4,6-Me₃C₆H₃, Dipec = 2,6-C(H)Et₂C₆H₃).

In addition to the above reported complexes, 5-membered cyclic alumanyl anions have also been reported, containing a mixture of *C,N*- (alkyl-amido) and *C,C*- (alkyl) supporting ligands (Figure 1.16).^{89–91} Of the three examples shown, the two *C,N*- complexes reported by Kinjo in 2020 and 2022 are “naked” alumanyl anions, while the complex reported by Yamashita in 2020 possesses a significant interaction between the aluminium and potassium centres. Similar to that observed for the boryl lithium discussed above, the distance between the Al and K centres, at 3.4549(5) Å, is considerably longer than the sum of the covalent radii (3.28 Å), indicating an electrostatic interaction.⁷³

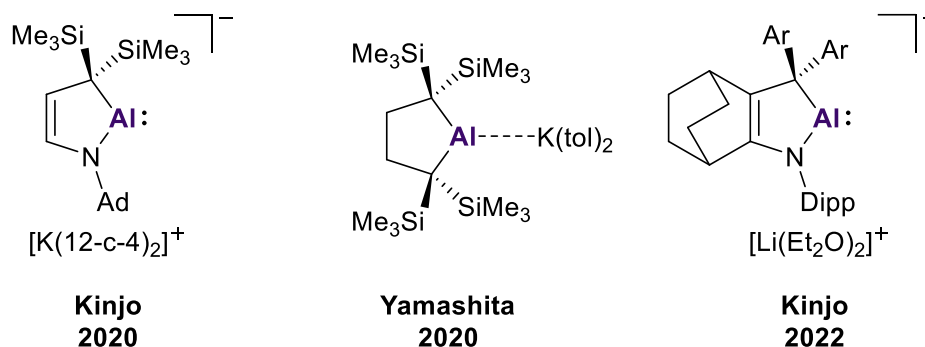


Figure 1.16: Potassium and lithium *C,N*-(Alkyl)(Amido) and *C,C'*-(Dialkyl) aluminyls (tol = toluene, Dipp = 2,6-*i*-Pr₂C₆H₃, Ar = 3,5-*i*Bu₂C₆H₃).

All the complexes discussed thus far have been cyclic. Recently though, there have been the first reports of acyclic aluminyl anions (Figure 1.17).^{92,93} In 2023, Liptrot reported the first example, [K₂{Al(N(Dipp)SiMe₃)₂}]₂, supported by an acyclic ligand framework, and isolated as the potassium bridged dimer.⁹² It was found that upon addition of sequestering agents or donor solvents, rapid decomposition of the aluminyl anion occurred. In addition to this example, the very first “naked” acyclic aluminyl anion has been reported by Aldridge.⁹³ By exploiting the large steric profile of a *N*-heterocyclic boryloxo ligand (-OB(NDippCH)₂) and its ability to stabilise the HOMO, the naked acyclic aluminyl anion [K(2,2,2-crypt)][Al{OB(NDippCH)₂}₂] was isolated. This recent example represents the very first O-ligated aluminyl anion.

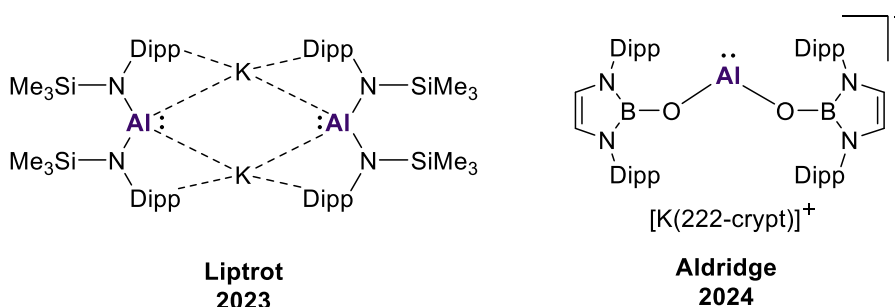


Figure 1.17: Reported acyclic aluminyl complexes (Dipp = 2,6-*i*-Pr₂C₆H₃).

1.3 Catalytic Hydrogenation – Alkali metal mediation

The catalytic hydrogenation of unsaturated bonds is a fundamental reaction across both industry and academia.⁹⁴ This area is dominated by late-transition metal catalysts, such as that from Wilkinson and Crabtree (Figure 1.18).^{95,96} Despite the excellent performance of these catalysts, regarding their selectivity and functional group tolerance, many of these late-transition metals are becoming increasingly scarce.⁹⁷ Therefore, there has been significant research efforts into identifying and developing alternative catalytic platforms based on more abundant elements.

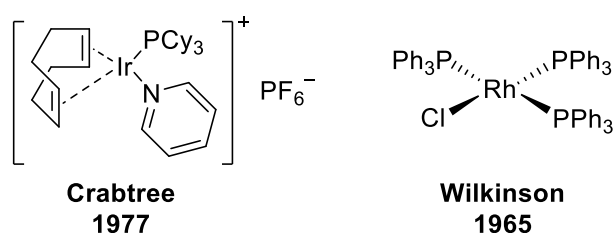


Figure 1.18: Examples of late-transition metal complexes that catalyse the hydrogenation of unsaturated bonds (PCy = tricyclohexylphosine, PPh₃ = triphenylphosphine).

In this regard, the Group 1 and 2 metals have become key targets, due to their relatively low toxicity and high abundance. It has been demonstrated that complexes of Group 1 and 2 can act as potential mediators in several different chemical transformations, including catalytic hydrogenation. Typically, the active catalyst is a highly reactive monometallic metal hydride complex (Figure 1.19).^{98–102} The electropositive s-block metal enhances the nucleophilic character of the hydride ligand, thus promoting the insertion into unsaturated bonds.

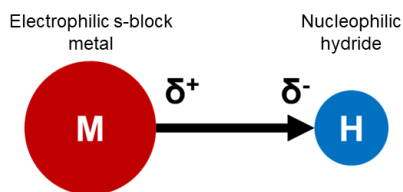
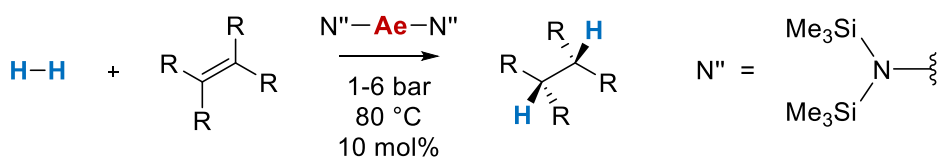


Figure 1.19: Generic representation of the typical highly reactive metal hydride catalyst that promotes insertion of the hydride into unsaturated bonds (M = Group 1 or 2 metal).

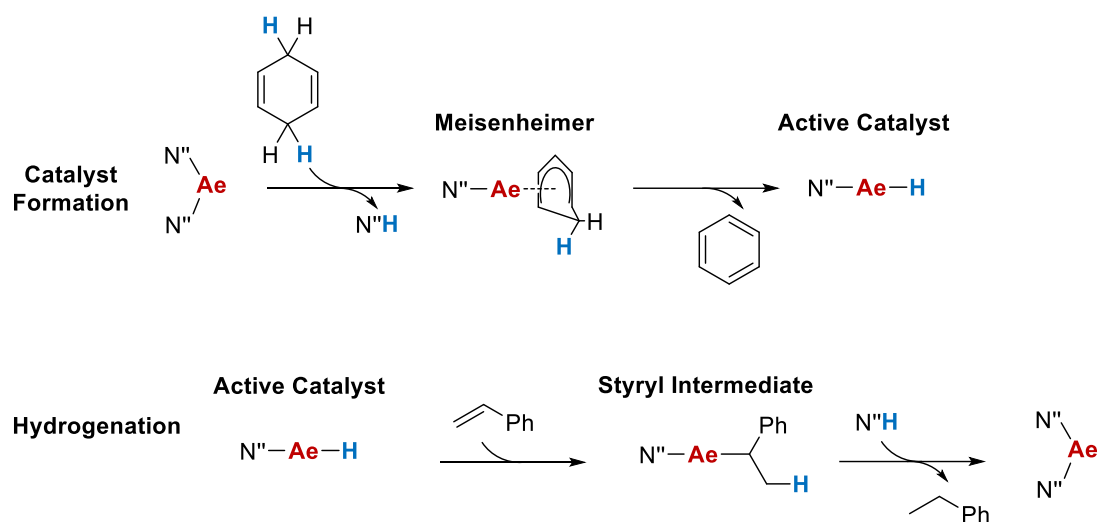
For example, Harder has demonstrated alkene and imine hydrogenation, using molecular hydrogen, catalysed by a series of alkaline earth metal complexes, of the form $\text{Ae}\{\text{N}(\text{SiMe}_3)_2\}_2$ [Ae = Mg, Ca, Sr, Ba; $\text{N}(\text{SiMe}_3)_2$ = 1,1,1,3,3,3-hexamethyldisilazide, HMDS (N'')]^{103,104} It was shown that under relatively low pressures (1-6 bar) and temperatures of 80-120 °C, these hydrogenations could be carried out efficiently (Scheme 1.13). A range of activated, semi-activated and non-activated alkenes could be successfully reduced. The smallest metal tested, magnesium, was shown to exhibit no catalytic activity, with activity increasing as the metal size increased from calcium to barium. A recent theoretical study from de Tobel has shown that the lack of reactivity for magnesium is likely due to the lack of *d*-orbital participation (resulting in a more linear $\text{N}''\text{—Mg—H}$ angle), and the relatively strong Mg—H bond (hindering insertion into the unsaturated bond).¹⁰⁵



Scheme 1.13: Alkene hydrogenation, catalysed by the series of alkaline earth metal amides, AeN''_2 [Ae = alkaline earth metal, $\text{N}'' = \text{N}(\text{SiMe}_3)_2$].

1 - Introduction

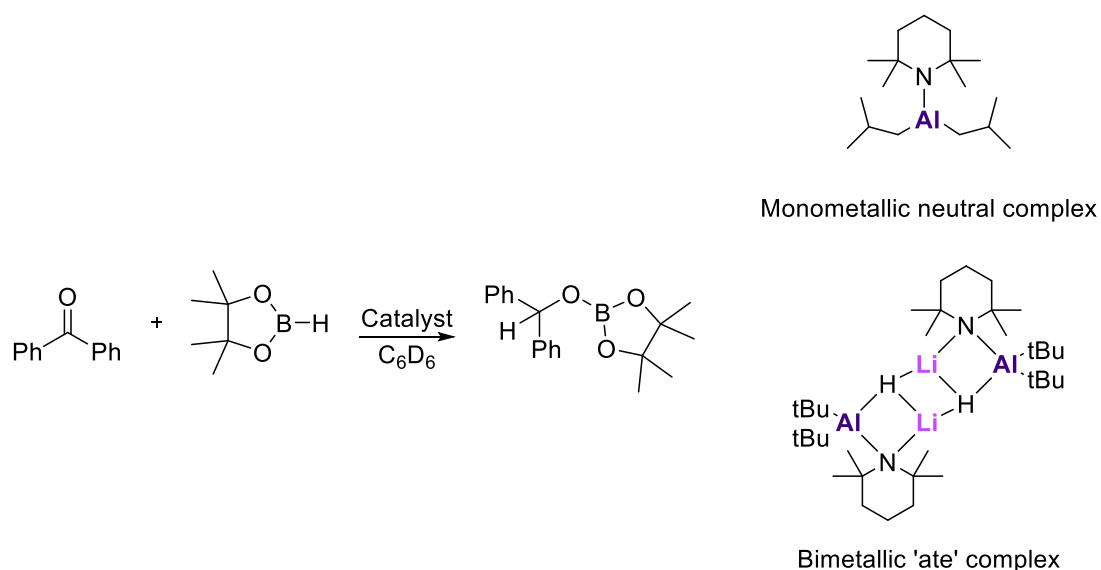
More recently, these same complexes have been shown to catalyse the transfer hydrogenation of various alkenes, using 1,4-cyclohexadiene (1,4-CHD) as the hydrogen source (Scheme 1.14).¹⁰⁶ The same trend in reactivity was observed, as the size of the alkaline earth metal increased. To form the active hydride catalyst, initial deprotonation of 1,4-CHD occurs, carried out by N'' . Subsequent release of the amine, $N''H$, yields an unstable Meisenheimer-type intermediate. Following a β -hydride elimination, the thermodynamically favourable release of benzene can occur, thus generating the active catalyst.



Scheme 1.14: Proposed reaction mechanism for transfer hydrogenation of styrene with 1,4-CHD catalysed by AeN''_2 (Ae = alkaline earth metal, $N'' = N(SiMe_3)_2$).

Having formed the active catalyst, reduction of styrene can occur, yielding a styryl intermediate, that is stabilised by a strong $Ae-C_\alpha$ bond. Finally, protonation by the previously liberated amine can occur, generating ethylbenzene and reforming the starting complex. The presence of the amine is crucial, as it prevents unwanted chain growth reactions from occurring, thereby promoting the formation of the desired product.

Given the variable performance of these species, with respect to the identity of the metal, there have been efforts to exploit bimetallic cooperativity, to enhance or fine tune the reactivity of these monometallic complexes. For example, in the lithium-aluminate catalysed hydroboration of benzophenones, a key hydrido intermediate was shown to be more polarised in the bimetallic compound, relative to its neutral monometallic counterpart, resulting in higher reactivity (Scheme 1.15:).¹⁰⁷



Scheme 1.15: The hydroboration of benzophenone, catalysed by the bimetallic "ate" complex, $[\text{tBu}_2\text{AlTMP}(\text{H})\text{Li}]_2$ and its monomeric neutral counterpart.

In another example, the hydroamination of diphenylacetylene could be efficiently catalysed by bimetallic alkali metal magnesiate species, of the form $[\text{AMMgR}_3]$ (AM = Alkali metal).¹⁰⁸ The alkali metal cation was seen to activate the substrate towards nucleophilic attack by the amide anion (Figure 1.20).

1 - Introduction

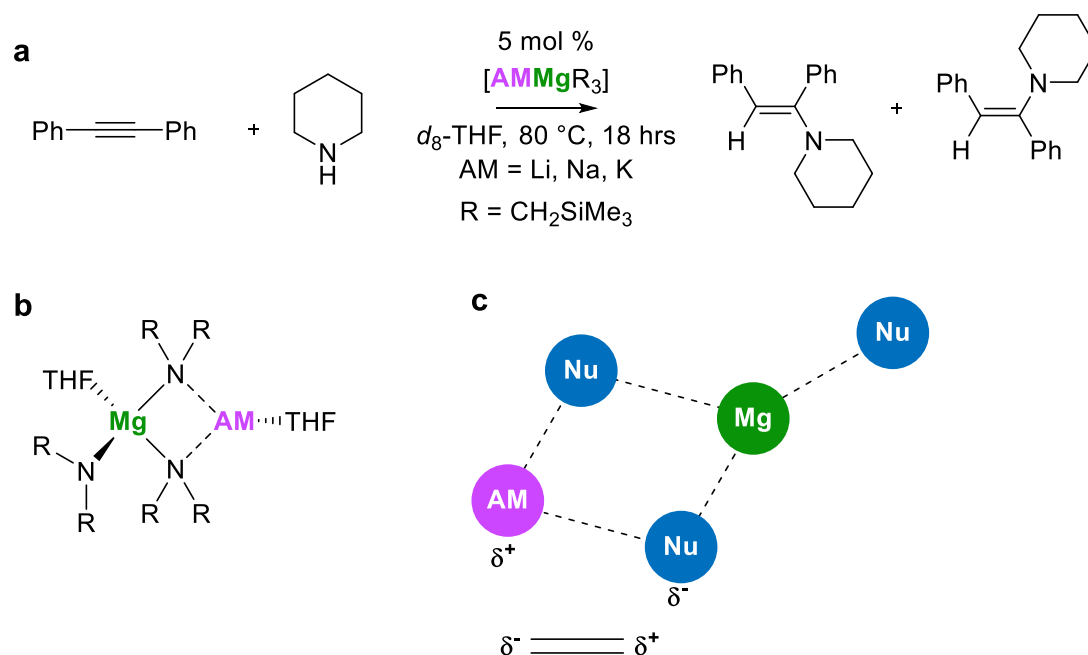
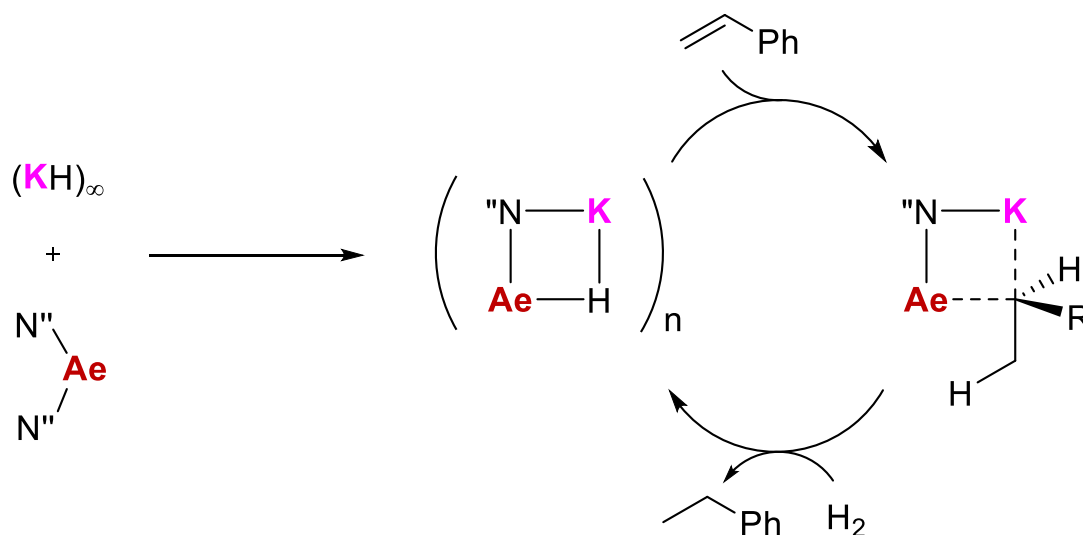


Figure 1.20: a) The hydroamination of diphenylacetylene, catalysed by alkali metal magnesiates. b) Depiction of a cooperative alkali metal magnesiate system. c) Representation of how the alkali metal ion in bimetallic alkali metal magnesiate systems can polarise an unsaturated substrate.

This synergy has been exploited by Guan, to catalyse the hydrogenation of styrene and other alkenes using heterobimetallic s-block metal hydrides (Scheme 1.16).¹⁰⁹ By combining KH and AeN⁺₂ (Ae = Mg, Ca), it was shown that the bimetallic catalyst exhibited superior activity, in comparison to the monometallic components in isolation. The active species in this case could not be structurally authenticated, but was believed to be the dimeric ate complex [KN⁺₂AeH]₂.



Scheme 1.16: Proposed mechanism by Guan for the hydrogenation of styrene, catalysed by combined KH / Ae metal amides (Ae = alkaline earth, N'' = N(SiMe₃)₂).

1.4 Outline and Scope

This thesis attempts to address fundamental questions regarding the electronic structure and reactivity of both theoretically and synthetically relevant main group complexes, across Group 1,2 and 13 of the periodic table. Much of the work described herein is collaborative and informed by experiment. However, independent theoretical work has also been carried out, to address underlying questions regarding the suitability of various quantum chemical methods in describing the electronic structure and reactivity of relevant main group species. This thesis will be structured as follows: In Chapter 2, the theoretical background of the computational methods employed throughout this thesis will be outlined, starting with a discussion of Hartree-Fock (HF) theory, and building to more advanced wavefunction and density functional based methods. Chapter 3 will outline the high-level *ab initio* study that was carried out, in order to gain fundamental insights into the electronic structure of dialumenes, from the simplest possible transient species to realistic synthetic base-stabilised examples. This work has been published in *Phys. Chem. Chem. Phys.*¹¹⁰ In Chapter 4, the work

carried out to computationally characterise the third example of a base-stabilised dialumene will be discussed. This work, as part of a collaborative computational-experimental study with the Cowley group, has been published in *Angew. Chem. Int. Ed.*⁶¹ Chapter 5 will outline the mechanistic investigations into the varied reactivity that this dialumene can undergo. This work is part of a follow-up collaborative study with the Cowley group, and a manuscript is in preparation, to be submitted for review to *J. Am. Chem. Soc.*. Moving away from dialumenes, the apparent cooperativity present in the activation of dihydrogen by alkali metal aluminyl complexes will be explored in Chapter 6. This chapter is part of a joint computational-experimental study with the Aldridge group, which has been published in *Chem. Eur. J.*¹¹¹ Finally, mechanistic work into transfer hydrogenation reactions, catalysed by the cooperative action present between alkali and alkaline earth metals will conclude this thesis. This work, based on previously published experimental results¹¹², has been published as a purely theoretical study in *ChemCatChem*.¹¹³

2 Theoretical Background

2.1 Introduction

This chapter provides an overview of the theoretical background that underlies the computational methods employed to carry out the work contained in this thesis. The time-independent Schrödinger equation will be discussed first. The Hamiltonian operator and the Born-Oppenheimer approximation will then be outlined. Hartree-Fock theory will then be introduced. More advanced methods that aim to improve upon the shortcomings of Hartree-Fock theory, primarily concerning the poor treatment of electron correlation, will then be discussed. Finally, Kohn-Sham Density Functional Theory (DFT) will be discussed in detail, with this chapter concluding with a description of basis sets.

2.2 The Time-Independent Schrödinger Equation

One of the fundamental postulates of quantum mechanics is that there exists a wavefunction for any chemical system, given by Ψ , that when acted upon by the appropriate operator, will return the observable properties of that system. The operator that returns the system energy, is called the Hamiltonian operator, \hat{H} , expressed as the eigenvalue equation

$$\hat{H}\Psi = E\Psi \quad (2.1)$$

which is the Schrödinger equation. The Hamiltonian operator has five major components which contribute to the total energy of the system, given by

$$\hat{H} = -\sum_i \frac{\hbar^2}{2m_e} \nabla_i^2 - \sum_k \frac{\hbar^2}{2m_k} \nabla_k^2 - \sum_i \sum_k \frac{e^2 Z_k}{r_{ik}} + \sum_{i<j} \frac{e^2}{r_{ij}} + \sum_{k<l} \frac{e^2 Z_k Z_l}{r_{kl}} \quad (2.2)$$

2 - Theoretical Background

The first two terms are the kinetic energies of the electrons and nuclei, respectively. The third term is the electrostatic attraction between the electrons and the nuclei. The final two terms are the interelectronic and internuclear repulsion terms, respectively. The indices i and j run over the electrons, k and l run over the nuclei, \hbar is Planck's constant divided by 2π , m_e is the mass of the electron, m_k is the mass of the nucleus k , ∇^2 is the Laplacian operator, e is the charge of the electron, Z is the atomic number and r_{ab} is the distance between any two particles a and b .

Equation 2.1 has infinitely many acceptable wavefunctions, Ψ_i , each associated with a particular energy, E_i . Multiplication of *Equation 2.1* on the left by Ψ_j and integrating gives

$$\int \Psi_j \hat{H} \Psi_i dr = \int \Psi_j E_i \Psi_i dr \quad (2.3)$$

Using the orthonormality of the set of acceptable wavefunctions, and the fact that E is a scalar quantity, the right-hand side of *Equation 2.3* can be simplified, and rewritten as

$$\int \Psi_j \hat{H} \Psi_i dr = E_i \delta_{ij} \quad (2.4)$$

where δ_{ij} is the Kronecker delta, equal to 1 if $i = j$, and equal to zero otherwise.

The bounded nature of quantum mechanics dictates that there must be an energetic state of a system that is lower than all others, given by E_0 . The quality of various wavefunctions can thus be determined by their associated energies. In other words, *the lower the energy, the better the wavefunction*. This is the variational principle, given by

$$\frac{\int \Phi \hat{H} \Phi dr}{\int \Phi^2 dr} \geq E_0 \quad (2.5)$$

where Φ is some linear combination of the set of complete wavefunctions, Ψ_i , and is normalized. This variational nature demonstrates that the guess wavefunction does not have to be constructed as a linear combination of unknown orthonormal wavefunctions. Instead, the guess wavefunction can be constructed in any manner, and the quality is determined by the calculated energy.

To simplify matters, the so-called Born-Oppenheimer approximation may be invoked. This approximation is based on the fact that the masses of the proton and the neutron are approximately 1800 times larger than that of the electron. Therefore, the motion of electrons is essentially instantaneous, relative to the motion of the nuclei. Therefore, by decoupling the motions of the nuclei and electrons, the electrons are treated as if they are moving in a field of fixed nuclei. This results in the electronic Schrödinger equation, given by

$$(\hat{H}_{el} + V_N)\Psi_{el}(q_i; q_k) = E_{el}\Psi_{el}(q_i; q_k) \quad (2.6)$$

\hat{H}_{el} is the electronic Hamiltonian, which excludes the nuclear kinetic energy and nuclear-nuclear repulsion term. The electronic coordinates, q_i , are independent variables, while the nuclear coordinates, q_k , are fixed parameters. The nuclear-nuclear repulsion term, V_N , is a constant since the positions of the nuclei are fixed. The constant V_N is added to the pure electronic energy to give the final electronic energy, E_{el} .

By considering a chemical system possessing only a single electron and a single nucleus, the need to account for electron-electron correlation is eliminated. The solutions of the corresponding electronic Schrödinger equation have the form of the

2 - Theoretical Background

hydrogenic atomic orbitals. These functions are used in the construction of more complicated molecular orbitals. Thus, a guess wavefunction Φ can be constructed from a linear combination of atomic wavefunctions, given by

$$\phi = \sum_{i=1}^N a_i \varphi_i \quad (2.7)$$

where N refers to the number of functions and φ_i refers to a specific atomic wavefunction, with coefficient a_i . This is the linear combination of atomic orbitals (LCAO) approach, where the set of N functions is called the basis set. By inserting *Equation 2.7* into the left-hand side of *Equation 2.5*, an expression is obtained for the energy corresponding to the guess wavefunction, given by

$$\begin{aligned} E &= \frac{\int (\sum_i a_i \varphi_i) \hat{H} (\sum_j a_j \varphi_j) dr}{\int (\sum_i a_i \varphi_i) (\sum_j a_j \varphi_j) dr} \\ &= \frac{\sum_{ij} a_i a_j \int \varphi_i \hat{H} \varphi_j dr}{\sum_{ij} a_i a_j \int \varphi_i \varphi_j dr} \\ &= \frac{\sum_{ij} a_i a_j H_{ij}}{\sum_{ij} a_i a_j S_{ij}} \end{aligned} \quad (2.8)$$

H_{ij} is known as the resonance integral and S_{ij} is known as the overlap integral. The overlap integral represents the degree to which two basis functions overlap in space. The generalized resonance integral does not have a clear-cut physical explanation. The goal is to minimize the electronic energy, with respect to the basis function coefficients a_i . This is given by

$$\frac{\partial E}{\partial a_k} = 0 \quad \forall k \quad (2.9)$$

where a_k runs over the coefficients. A set of N equations (running over k) is obtained, given by

2 - Theoretical Background

$$\sum_{i=1}^N a_i (H_{ki} - ES_{ki}) = 0 \quad \forall k \quad (2.10)$$

involving N unknowns (a_i). A set of equations such as this, where there are N equations in N unknowns has a non-trivial solution if and only if the determinant formed from the corresponding coefficients, $H_{ki} - ES_{ki}$, is equal to zero. This is the secular equation, and is given by

$$\begin{vmatrix} H_{11} - ES_{11} & H_{12} - ES_{12} & \cdots & H_{1N} - ES_{1N} \\ H_{21} - ES_{21} & H_{22} - ES_{22} & \cdots & H_{2N} - ES_{2N} \\ \vdots & \vdots & \ddots & \vdots \\ H_{N1} - ES_{N1} & H_{N2} - ES_{N2} & \cdots & H_{NN} - ES_{NN} \end{vmatrix} = 0 \quad (2.11)$$

By expanding the determinant in *Equation 2.11*, N energies E_j are obtained. The lowest energy corresponds to the ground state of the system of interest, and the higher energies correspond to excited states. Each energy E_j is inserted into *Equation 2.10* to yield a unique set of coefficients a_{ij} , which define an optimal wavefunction within the basis set, given by

$$\phi_j = \sum_{i=1}^N a_{ij} \phi_i \quad (2.12)$$

2.3 Many-electron wavefunctions

To begin a discussion of many-electron wavefunctions, a one-electron Hamiltonian is considered, so that for each electron in a system, only the kinetic energy of that electron and its attraction to all nuclei is accounted for. The one-electron Hamiltonian is given by the equation

$$\hat{H} = \sum_{i=1}^N \hat{h}_i \quad (2.13)$$

2 - Theoretical Background

where the summation is over the individual one-electron Hamiltonian operators \hat{h}_i , given by

$$\hat{h}_i = -\frac{1}{2}\nabla_i^2 - \sum_{k=1}^M \frac{Z_k}{r_{ik}} \quad (2.14)$$

There is a set of eigenfunctions that must satisfy the one-electron Schrödinger equation

$$\hat{h}_i\psi_i = \varepsilon_i\psi_i \quad (2.15)$$

Each orbital ψ_i is an eigenfunction of its own operator, given by

$$\hat{h}_i = -\frac{1}{2}\nabla_i^2 - \sum_{k=1}^M \frac{Z_k}{r_{ik}} + V_i\{j\} \quad (2.16)$$

The final term on the right-hand side of *Equation 2.16* is an interaction potential of an electron in orbital i with all other electrons in orbitals j , given by

$$V_i\{j\} = \sum_{j \neq i} \int \frac{\rho_j}{r_{ij}} dr \quad (2.17)$$

To form the one-electron Hamiltonians, a set of orbitals must be available, but it is these orbitals that must be obtained in the first place. A self-consistent field (SCF) approach must be utilised. This approach was first introduced by Hartree in 1928.¹¹⁴ A set of orbitals are provided as a guess, to form the individual one-electron Hamiltonian operators, which are then used to solve the individual one-electron Schrödinger equations (*Equation 2.15*). This results in an updated set of orbitals. This is repeated until an arbitrary convergence threshold has been reached between the current and previous set of orbitals.

All electrons are characterized by a set of quantum numbers, one of which is the spin quantum number, arising as a natural consequence of applying a relativistic treatment

to quantum mechanics. In the non-relativistic treatment, spin is introduced in an *ad hoc* manner. The spin eigenfunctions are orthonormal, only have two possible eigenvalues, $\pm\hbar/2$, and are denoted by α or β . The Pauli exclusion principle states that no two electrons can have the same set of quantum numbers. Therefore, a molecular orbital may only contain up to two electrons, differing at least by their spin quantum numbers. A more general statement of the Pauli exclusion principle is that wavefunctions must change sign upon interchanging the coordinates of any two electrons i.e. they must be anti-symmetric. If any two rows of a determinant are interchanged, the overall sign of the determinant changes. This made the representation of anti-symmetrized wavefunctions as determinants a convenient approach, and was first recognized by Slater in 1930.¹¹⁵ For a system containing N number of electrons a generalised Slater determinant (SD) is given by

$$\psi_{\text{SD}} = \frac{1}{\sqrt{N!}} \begin{vmatrix} \chi_1(1) & \chi_2(1) & \cdots & \chi_N(1) \\ \chi_1(2) & \chi_2(2) & \cdots & \chi_N(2) \\ \vdots & \vdots & \ddots & \vdots \\ \chi_1(N) & \chi_2(N) & \cdots & \chi_N(N) \end{vmatrix} \quad (2.18)$$

where χ_i is a spin-orbital, which is the product of a spatial orbital and an electron spin eigenfunction.

2.4 The Hartree-Fock method

It was proposed by Fock to extend Hartree's SCF procedure to use Slater determinantal wavefunctions. Roothan proposed a matrix algebraic formulation that allowed the HF equations to be solved within a basis set representation.¹¹⁶ Focussing on closed-shell systems, the HF equations can be presented in their restricted formalism. The one-electron Fock operator is given by

$$\hat{f}_i = -\frac{1}{2}\nabla_i^2 - \sum_k^{\text{nuclei}} \frac{Z_k}{r_{ik}} + V_i^{\text{HF}}\{J\} \quad (2.19)$$

2 - Theoretical Background

and is defined for each electron i . The final term on the right-hand side of *Equation 2.19* is the interaction potential of electron i with all other electrons, defined as

$$V_i^{\text{HF}}\{J\} = 2J_i - K_i \quad (2.20)$$

where J_i and K_i are the Coulomb and exchange integrals defined below. The secular equation, given by

$$\begin{vmatrix} F_{11} - ES_{11} & F_{12} - ES_{12} & \cdots & F_{1N} - ES_{1N} \\ F_{21} - ES_{21} & F_{22} - ES_{22} & \cdots & F_{2N} - ES_{2N} \\ \vdots & \vdots & \ddots & \vdots \\ F_{N1} - ES_{N1} & F_{N2} - ES_{N2} & \cdots & F_{NN} - ES_{NN} \end{vmatrix} = 0 \quad (2.21)$$

can then be solved. The S matrix elements are the overlap matrix elements, while the F matrix elements are specific to the HF procedure and are called the Fock elements. Each Fock element is defined by

$$\begin{aligned} F_{\mu\nu} = & \left\langle \mu \left| -\frac{1}{2} \nabla^2 \right| \nu \right\rangle - \sum_k^{\text{nuclei}} Z_k \left\langle \mu \left| \frac{1}{r_k} \right| \nu \right\rangle \\ & + \sum_{\lambda\sigma} P_{\lambda\sigma} \left[(\mu\nu | \lambda\sigma) - \frac{1}{2} (\mu\lambda | \nu\sigma) \right] \end{aligned} \quad (2.22)$$

where the lower-case Greek letters represent individual basis functions. The first and second terms on the right-hand side of *Equation 2.22* are one-electron integrals involving the Laplacian and distance operators (to a particular nucleus), respectively. The final term contains two two-electron integrals (inside the square brackets). The first of these, given by

$$(\mu\nu | \lambda\sigma) = \iint \phi_\mu(1)\phi_\nu(1) \frac{1}{r_{12}} \phi_\lambda(2)\phi_\sigma(2) dr(1)dr(2) \quad (2.23)$$

defines the Coulomb repulsion between the probability densities of different electrons, defined by ϕ_μ and ϕ_ν for electron 1, and ϕ_λ and ϕ_σ , for electron 2. Attenuating this is the exchange integral (the second term within the square brackets). This integral is

2 - Theoretical Background

preceded by a factor of one-half, due to the limitation of exchange integrals only being present for electrons of the same spin. The final summation term in *Equation 2.22* defines the density matrix, $P_{\lambda\sigma}$, which gives the relative weights of different basis functions to a particular molecular orbital. The density matrix is defined as

$$P_{\lambda\sigma} = 2 \sum_i^{\text{occupied}} a_{\lambda i} a_{\sigma i} \quad (2.24)$$

where the coefficients $a_{\zeta i}$ define the normalised contribution of basis function ζ to molecular orbital i and the factor of 2 preceding the summation sign accounts for closed-shell systems where each molecular orbital is doubly occupied. These orbital coefficients that are required to form the density matrix are unknown. They must therefore be guessed at the beginning of the calculation, in order to solve the HF equations, which then lead to new orbital coefficients. The equations are solved iteratively until a desired level of convergence is reached.

2.5 Wavefunction Theory Methods

Hartree-Fock theory provides a prescription for finding the lowest energy eigenvalue of a system within the limit of a basis set, when the wavefunction for this system is represented by a single Slater determinant. The major limitation of Hartree-Fock theory is that each electron is assumed to move in a mean field created by all other electrons. This results in instantaneous electron-electron correlation, known as dynamic correlation, not being accounted for. Therefore, the remaining correlation energy, given by

$$E_{\text{corr}} = E - E_{\text{HF}} \quad (2.25)$$

must be captured. Using the HF wavefunction as a leading term in the expansion, the total wavefunction can be written as

$$\Psi = c_0 \Psi_{\text{HF}} + c_1 \Psi_1 + c_2 \Psi_2 + \dots \quad (2.26)$$

where the set of coefficients c represents the relative weighting of each determinant to the total wavefunction. The HF wavefunction is the major contributor typically. The missing correlation energy may be large, but the individual contributions of the other determinants are usually small, unless there is significant multi-reference character present. This section will outline the approaches that are available to introduce the treatment of dynamic and static correlation. The limitations of these approaches will be discussed, as well as approaches that have been developed in recent years to reduce the cost of these high-accuracy methods.

2.5.1 Multiconfigurational Self-Consistent Field Theory

A single-determinantal approach fails to describe a system where there is equal likelihood of populating frontier orbitals, due to near or exact degeneracy. In HF theory, only the coefficients of occupied orbitals are optimized, and a single-determinantal approach defines only one possible occupancy of the degenerate frontier orbitals. This leads to these orbitals not being treated equivalently in the wavefunction. The so called multi-configurational self-consistent field (MCSCF) approach can be utilised to optimize the orbitals for a combination of configurations. A configuration or configuration state function (CSF) refers to the molecular spin state and occupation numbers of the orbitals. An MCSCF wavefunction thus provides the specification of what orbitals may be occupied in the configurations appearing in *Equation 2.26*, where the variational optimum of both the molecular orbital and the weight of each configuration in the total wavefunction are calculated.

2 - Theoretical Background

As a particular orbital can be populated by up to two electrons, there is not a unique energy eigenvalue associated with that orbital. Instead, using

$$(occ.no.)_{i,MCSCF} = \sum_n^{CSFs} (occ.no.)_{i,n} a_n^2 \quad (2.27)$$

the occupation number of an orbital is calculated by summing over all CSFs and weighting the occupation number of the orbital in that CSF by the square of its expansion coefficient, a_n . These orbitals that can be occupied are known as the active orbitals, and the set of these orbitals are referred to as the active space, represented by (n,m), specifying n electrons in m orbitals. Rather than choosing where to place the electrons within the set of active orbitals, every possible combination of the n electrons in m orbitals can be considered. This is referred to as a complete active space (CAS) or CASSCF calculation. The number of CSFs can quickly grow, and one way that CASSCF calculations can be made more efficient is to freeze the core and inactive orbitals at the HF level of theory, enforcing either double or zero occupancy (Figure 2.1). MCSCF methods such as CASSCF only improve upon HF theory by introducing a treatment of static correlation. A treatment of dynamic correlation has not been considered outside of the active space.

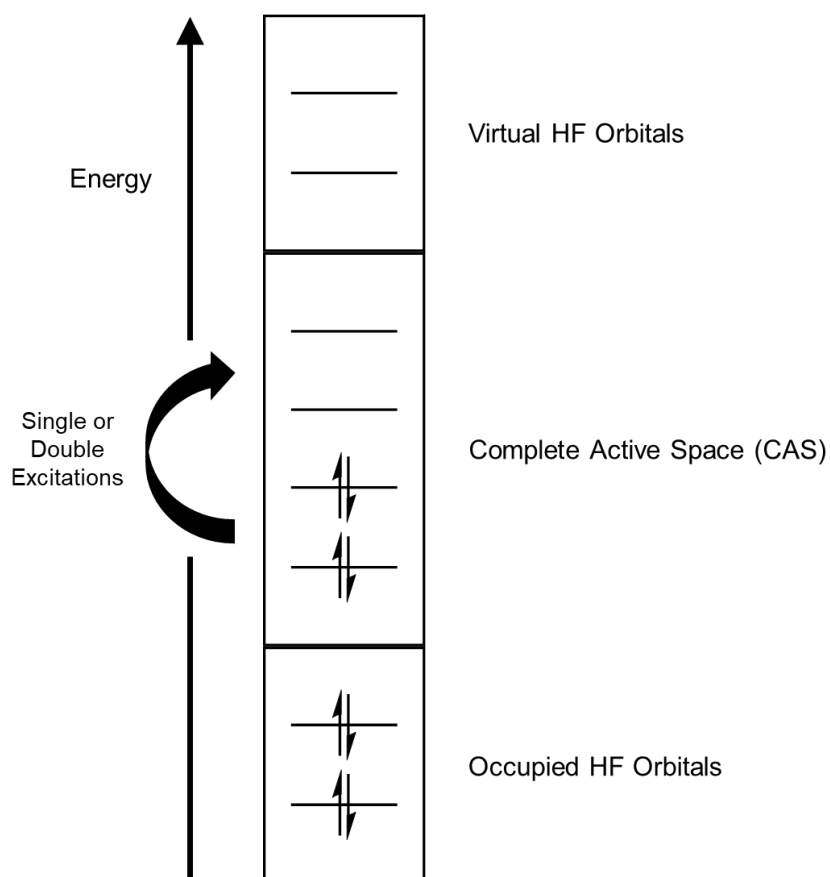


Figure 2.1: Example representation of the CASSCF formalism.

2.5.2 Configuration Interaction

For CASSCF, the choice of the active space was limited to all possible CSFs within that space, while keeping the orbitals outside of the active space frozen at the HF level. Therefore, there is no treatment of dynamic correlation between the electrons inside and outside of the active space. One strategy is to consider an active space where all electrons are permitted to occupy every orbital. This approach is known as full configuration interaction (FCI), and if carried out using an infinite basis set, returns the exact solution to the non-relativistic, time-independent, Born-Oppenheimer Schrödinger equation. No optimization of the HF input orbitals needs to be undertaken in this case as the set of CSFs is a complete set.

2 - Theoretical Background

To reduce the computational cost, limited excitations can be considered. Rewriting the generic *Equation 2.26* as

$$\Psi = a_0 \Psi_{HF} + \sum_i^{occ.} \sum_r^{vir.} a_i^r \Psi_i^r + \sum_{i < j}^{occ.} \sum_{r < s}^{vir.} a_{ij}^{rs} \Psi_{ij}^{rs} + \dots \quad (2.28)$$

reflects this, where i and j are occupied molecular orbitals in the HF wavefunction, while r and s are virtual or unoccupied orbitals in the HF wavefunction. The first summation on the right-hand side of *Equation 2.28* represents all possible single excitations, while the second represents all possible double excitations, and so on. The molecular orbital coefficients are not reoptimized in this case, with only the expansion coefficients being determined. This is one of the major distinctions between CI- and MCSSF-based methods. Variationally determining the expansion coefficients gives a matrix, whose elements are given by

$$H_{mn} = \langle \Psi_m | \hat{H} | \Psi_n \rangle \quad (2.29)$$

where $\Psi_1 = \Psi_{HF}$, with single excited determinants and higher excited determinants being referred to by higher values of m or n . A special case occurs when matrix elements between the HF determinant and a singly excited determinant must be evaluated. The Condon-Slater rules dictate that such a matrix element is evaluated as

$$\begin{aligned} H_{1n} &= \langle \Psi_{HF} | \hat{H} | \Psi_i^r \rangle \\ &= \langle \phi_r | \hat{F} | \phi_i \rangle \end{aligned} \quad (2.30)$$

where \hat{F} is the Fock operator. The orbitals indexed by i and r are eigenfunctions of the Fock operator, so the orbital energy eigenvalue ε_i can be obtained, given by

$$\begin{aligned} \langle \phi_r | \hat{F} | \phi_i \rangle &= \varepsilon_i \langle \phi_r | \phi_i \rangle \\ &= \varepsilon_i \delta_{ir} \end{aligned} \quad (2.31)$$

2 - Theoretical Background

The final line of *Equation 2.31* tells us that matrix elements between the HF determinant and any singly excited determinant will always be zero, as the orbital indices i and r can never be equal. This result is known as Brillouin's theorem.¹¹⁷

For ground states, due to Brillouin's theorem and the fact that the CI matrix in this context is block diagonal, the inclusion of only single excitations has no effect on the ground state energy. Only including double excitations (CID) leads to a result that is lower in energy than the HF energy. Triple excitations could also be employed, using the CIDT method. The inclusion of triples can interact with the ground state indirectly by mixing with the doubly excited configurations. In the same way that triples can mix with the HF wavefunction indirectly through the double excitations, so can the singly excited configurations. This is known as the CISD method, which is variational in nature, ensuring that the calculated energy is always an upper bound to the true ground state energy. The CI method is not size consistent, which can lead to errors in the calculation of energetic properties such as dissociation energies.

2.5.3 Perturbation Theory

By stripping away troublesome parts of an operator, a simplified version of that operator can be obtained, where the exact eigenfunctions and eigenvalues are known. The exact eigenfunctions and eigenvalues can then be estimated, through the use of a perturbative operator. This is the basis of the Rayleigh-Schrödinger method, given by

$$\hat{A} = \hat{A}^{(0)} + \lambda \hat{V} \quad (2.32)$$

where \hat{A} is some operator, the exact eigenfunctions and eigenvalues of which are unknown, $\hat{A}^{(0)}$ is the simplified operator of which exact solutions are known, and \hat{V} is

the perturbative operator. Finally, λ is a scalar quantity, that allows the mapping (by varying from a value of 0 through 1) of $\hat{A}^{(0)}$ on to \hat{A} . Møller and Plesset proposed the use of this scheme for approaching the exact solution of the Schrödinger equation, collectively referred to as the MP n methods ($n = 1, 2, 3, \dots$).¹¹⁸ The simplified operator is the non-interacting Hamiltonian, as defined by

$$\hat{H}^{(0)} = \sum_{i=1}^n \hat{f}_i \quad (2.33)$$

The corresponding wavefunction, $\Psi^{(0)}$, for this operator is a Slater determinant of the occupied orbitals i.e. the HF wavefunction. Operating with $\hat{H}^{(0)}$ on this wavefunction gives

$$\hat{H}^{(0)}\Psi^{(0)} = \sum_i^{\text{occ.}} \varepsilon_i \Psi^{(0)} \quad (2.34)$$

where individual orbital energies are the eigenvalues of the one-electron Fock operators, and the sum of these defines the total energy eigenvalue $a^{(0)}$. To retrieve the HF energy, a perturbative term must be included that corrects for the overcounting of electron-electron interactions. This is given by

$$\hat{V} = \sum_i^{\text{occ.}} \sum_{j>i}^{\text{occ.}} \frac{1}{r_{ij}} - \sum_i^{\text{occ.}} \sum_j^{\text{occ.}} \left(J_{ij} - \frac{1}{2} K_{ij} \right) \quad (2.35)$$

The energy eigenvalue corresponding to this perturbation is the first-order correction, given by $a^{(1)}$. Summing up $a^{(0)}$ and $a^{(1)}$ yields

$$\begin{aligned} a^{(0)} + a^{(1)} &= \langle \Psi^{(0)} | H^{(0)} | \Psi^{(0)} \rangle + \langle \Psi^{(0)} | V | \Psi^{(0)} \rangle \\ &= \langle \Psi^{(0)} | H^{(0)} + V | \Psi^{(0)} \rangle \\ &= \langle \Psi^{(0)} | H | \Psi^{(0)} \rangle \\ &= E_{\text{HF}} \end{aligned} \quad (2.36)$$

which establishes that the HF energy is the energy correct through first-order. The second-order correction term is given by

$$a^{(2)} = \sum_i^{\text{occ.}} \sum_{j>i}^{\text{occ.}} \sum_a^{\text{vir.}} \sum_{b>a}^{\text{vir.}} \frac{[(ij | ab) - (ia | jb)]^2}{\epsilon_i + \epsilon_j - \epsilon_a - \epsilon_b} \quad (2.37)$$

where the sum of $a^{(0)}$, $a^{(1)}$ and $a^{(2)}$ defines the MP2 energy. This method scales by approximately N^5 , where N is the number of basis functions. In an improvement over approximate CI-based methods, MP n theory is size-consistent. However, it is not variational, meaning that the correlation energy can be overestimated. Another disadvantage of perturbation theory is that it is most successful and quickly convergent when the perturbation is small. However, the perturbative term in MP theory corrects for the overcounting of electron-electron repulsion, which can be substantial. The MP methods therefore suffer from convergence issues. Finally, MP theory captures a considerable amount of dynamic correlation, but due to its inherent single-reference nature, can fail in the description of systems that benefit from a multi-reference treatment.

2.5.4 Coupled Cluster Theory

Coupled cluster theory was developed by Cizek¹¹⁹, where the central idea is that the exact full-CI wavefunction is represented as

$$\Psi = e^{\hat{T}} \Psi_{\text{HF}} \quad (2.38)$$

where the cluster operator \hat{T} , is given by

$$\hat{T} = \hat{T}_1 + \hat{T}_2 + \hat{T}_3 + \dots + \hat{T}_n \quad (2.39)$$

2 - Theoretical Background

where n goes from 1 to the total number of electrons. Each \hat{T}_i operator generates all possible determinants having at most i excitations from the reference determinant. For example,

$$\hat{T}_2 = \sum_{i < j}^{\text{occ.}} \sum_{a < b}^{\text{vir.}} t_{ij}^{ab} \psi_{ij}^{ab} \quad (2.40)$$

is the operator corresponding to all double excitations, with t being the cluster amplitudes. By considering only the \hat{T}_2 operator i.e. the double excitations, the coupled cluster doubles (CCD) method is defined, given by

$$\begin{aligned} \psi_{\text{CCD}} &= e^{\hat{T}} \psi_{\text{HF}} \\ &= \left(1 + \hat{T}_2 + \frac{\hat{T}_2^2}{2!} + \frac{\hat{T}_2^3}{3!} + \dots \right) \psi_{\text{HF}} \end{aligned} \quad (2.41)$$

The cluster operator is represented by a Taylor expansion, where the first two terms are equivalent to the CID method. The remaining terms involve increasing powers of the \hat{T}_2 operator. This ensures that the coupled cluster method is size-consistent.

By including the single and double excitation cluster operators, the resulting method is the CCSD method, which scales as N^6 , where N is the number of basis functions. If connected triples are included, using the \hat{T}_3 operator (not the disconnected triples resulting from products of \hat{T}_1 and \hat{T}_2), the CCSDT method is defined, scaling as N^8 . To account for triples approximately, a perturbative approach can be taken, defining the CCSD(T) method, which scales as N^7 . This method benefits from favourable error cancellation, as the error from not including quadruple excitations is offset by the overestimation of the connected triples contribution by the perturbative approach.¹²⁰ Therefore, high-accuracy is achieved, making this the “gold-standard” of electronic structure calculations. In the truncated form, coupled cluster is not variational.

2.5.5 Modern approximations

In practice, many of these methods discussed so far are feasible for systems containing only a few atoms. There have been a number of approaches developed that aim to expedite correlated wavefunction theory methods without a loss of accuracy. Two of these methods will be briefly outlined. The first is the domain local pair natural orbital (DLPNO) approximation. The second is the ICE-CI method, a so-called selected-CI method that allows one to calculate essentially exact FCI wavefunctions.

2.5.5.1 Domain local pair natural orbital (DLPNO) approximation

It was reported by Löwdin in 1955 that when natural orbitals were ordered with respect to their occupation number, CI calculations using these natural orbitals were more quickly convergent.¹²¹ Building on this idea, Edmiston and Krauss introduced the concept of pair natural orbitals (PNO), where a set of natural orbitals were used to correlate electron pairs.^{122,123} The introduction of this concept sparked significant development of correlated wavefunction based methods that used PNOs.^{124–133} The use of PNOs in correlated calculations drastically reduced the computational cost, while only coming with marginal errors in the correlation energy. Unfortunately, despite this flurry of advancement in the 1970s, the integral transformations and disk storage required for these calculations caused this approach to be abandoned, due to the lack of computational resources at the time.

With access to more computational resources, and by utilising density fitting approximations, Neese revived the use of PNOs in correlated wavefunction theory calculations, with the introduction of a modern LPNO implementation of the coupled

electron pair approximation (CEPA)¹³⁴ and CCSD method.¹³⁵ The LPNO-CCSD method was subsequently redesigned to reduce the formal N^5 scaling behaviour, giving rise to the DLPNO-CCSD method.¹³⁶ This method combines the use of PNOs with pair atomic orbitals (PAO), and provides near linear-scaling behaviour. As mentioned previously, the CCSD(T) method is considered to be the “gold standard” in electronic structure calculations, and a DLPNO-CCSD(T) implementation has also been developed.¹³⁷

These methods provide chemical accuracy, while coming at only a fraction of the cost of their canonical counterparts. By tightening the truncation parameters, convergence to the canonical results can be achieved. Furthermore, due to near linear scaling behaviour within the DLPNO framework, calculations on much larger molecules may be carried out. For example, it has been demonstrated that a DLPNO-CCSD(T) calculation could be carried out on an entire protein containing 644 atoms and more than 6000 basis functions.¹³⁷ A more in-depth discussion of the development and application of the LPNO methods, as well as the technical details of the computational steps involved can be found in a review from Neese.¹³⁸

2.5.5.2 Near-FCI wavefunctions with ICE-CI

Due to the factorial scaling of the FCI procedure, generating a FCI wavefunction for a system of interest is computationally intractable. For example, one may want to obtain highly accurate densities or energies for a small system, or perhaps carry out large-scale CASSCF calculations, past the typical active space limit of about 14 orbitals. Obtaining a near-exact FCI wavefunction is sufficient to gain the appropriate insight into chemical systems at a high level. With this in mind, the the Iterative-Configuration

Expanded Configuration Interaction (ICE-CI) method was developed.^{139,140} The primary goal of ICE-CI is to provide compact near-exact wavefunctions, at a fraction of the computational cost. While this method is highly accurate, it is designed to treat small systems, up to a few dozen electrons and orbitals. This is in contrast to the previously discussed DLPNO-CC methods, which are designed to be highly accurate methods for the efficient treatment of large systems.

The major steps carried out in the ICE-CI procedure are displayed in Figure 2.2. First, a many-particle state that has a sizeable contribution from a given configuration \mathbf{n}^0 is considered. Only configurations that differ by at most two orbital occupations will interact with \mathbf{n}^0 . By using perturbation theory, the single and double excitations that interact most strongly with \mathbf{n}^0 are selected. The variational problem is then solved. The CI vector is then analysed, and the configurations that make a dominant contribution to the ground state are chosen as the generator set, while the remainder are the variational set. The T_{gen} threshold determines what configurations make it into the generator set. In the next iteration, single and double excitations are performed relative to this generator set, and a new set is selected according to their interaction with the dominant part of the previous CI vector. This whole procedure is repeated until no new generator configurations are produced, and convergence of the energy is reached. ICE-CI has been shown to provide polynomial, rather than factorial scaling as is the case for regular FCI. As the user tightens the T_{gen} threshold, the resulting wavefunction becomes more accurate, but the computation time increases by a factor of 10 for each magnitude of tightening of this threshold.

2 - Theoretical Background

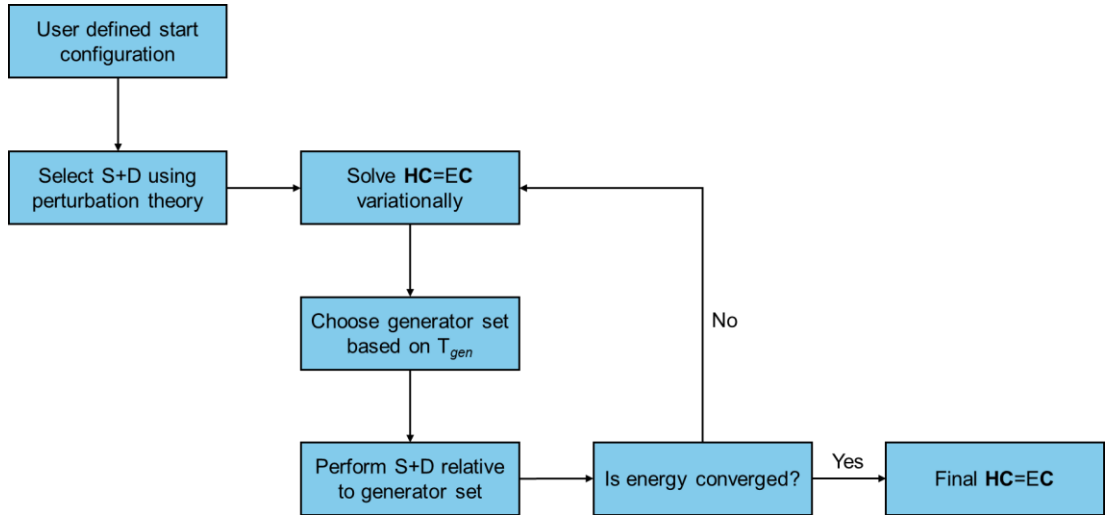


Figure 2.2: Flowchart describing the major steps involved in the ICE-CI procedure developed by ORCA. S+D refers to single and double excitations.

2.6 Density Functional Theory

The wavefunction is not physically observable, and only by casting it into a form such as the Slater determinant in HF theory, can a tractable form be obtained. The Hamiltonian operator only requires three pieces of information: the nuclear positions, the atomic numbers of the nuclei and finally, the number of electrons. This latter quantity, the number of electrons, implies that the electron density may be a useful observable, as when integrated over all space, the density returns the number of total electrons. This is expressed as

$$N = \int \rho(r) dr \quad (2.42)$$

where N is the total number of electrons. Assuming fixed nuclear positions, the atomic numbers of the nuclei can be obtained using

$$\left. \frac{\partial \bar{\rho}(r_A)}{\partial r_A} \right|_{r_A=0} = -2Z_A \rho(r_A) \quad (2.43)$$

2 - Theoretical Background

where Z is the atomic number of atom A , r_A is the radial distance from A , and the numerator of the left hand side is the spherically averaged density. This Hamiltonian could then be utilised to solve the Schrödinger equation, to yield the energy. The rest of this section will outline density functional theory (DFT), an alternative philosophy, that uses the electron density as its core building block, instead of the wavefunction.

2.6.1 Early approximations

The total energy of a system can be separated into the kinetic and potential components. As a first approximation, the classical attraction between the electron density and nuclei is given by

$$\hat{V}_{ne}[\rho(r)] = \sum_k^{\text{nuclei}} \int \frac{Z_k}{|r - r_k|} \rho(r) dr \quad (2.44)$$

and the classical electron-electron repulsion is given by

$$\hat{V}_{ee}[\rho(r)] = \frac{1}{2} \iint \frac{\rho(r_1)\rho(r_2)}{|r_1 - r_2|} dr_1 dr_2 \quad (2.45)$$

where both terms together define a classical potential energy. Thomas and Fermi introduced the uniform electron gas (UEG), a fictitious system, composed of an infinite number of electrons moving in an infinite volume of space, over a background of continuous positive charge i.e. this system has a constant non-zero density.¹⁴¹ The kinetic energy of this system is given by

$$\hat{T}_{ueg}[\rho(r)] = \frac{3}{10} (3\pi^2)^{2/3} \int \rho^{5/3}(r) dr \quad (2.46)$$

The density functionals given by *Equations 2.44-2.46*, together with an assumed variational principle, define the first attempt (by Thomas and Fermi) to derive a density

functional theory, independent of a wavefunction. However, this initial theory predicted all molecules to be unstable with respect to their constituent atoms.

The initial failure to establish a density functional theory was due to the assumption of classical behaviour. The electron-electron repulsion term defined by *Equation 2.45* does not treat the effects of correlation or exchange. To correct for this error, the hole function can be introduced, given by

$$\left\langle \Psi \left| \sum_{i < j}^{electrons} \frac{1}{r_{ij}} \right| \Psi \right\rangle = \frac{1}{2} \iint \frac{\rho(r_1)\rho(r_2)}{|r_1 - r_2|} dr_1 dr_2 + \frac{1}{2} \iint \frac{\rho(r_1)h(r_1; r_2)}{|r_1 - r_2|} dr_1 dr_2 \quad (2.47)$$

where the second term on the right-hand side corrects for the error associated with the first term. The hole function is centred on the position of electron 1, r_1 , and evaluated as a function of the remaining spatial coordinates that define r_2 . In the one-electron case, the hole function is the negative of the density, so that the first and second terms of *Equation 2.47* perfectly cancel each other. In the many-electron case, the form of the hole functional is less clear. In general, the purpose of the hole function is to correct for the self-interaction error (arising from the interaction of a density with itself, even in the one-electron case), as well as the errors associated with not including the effects of correlation and exchange.

It was noted by Slater¹⁴² that the contribution of the exchange correction to the classical repulsion term was larger than the correlation correction. It was therefore proposed to ignore the correlation correction and approximate the exchange hole as a sphere of constant potential with a radius that depends on the magnitude of the electronic density at a particular position. Using this approximation, the exchange functional was derived as

$$E_x[\rho(r)] = -\frac{9\alpha}{8} \left(\frac{3}{\pi}\right)^{1/3} \int \rho^{4/3}(r) dr \quad (2.48)$$

This functional is known as Slater exchange, where the α constant is defined to be 1. This constant was treated as empirical, with differing values being derived based on empirical analysis of a range of systems, collectively termed $X\alpha$ calculations.

2.6.2 The Hohenberg-Kohn Theorems

Having outlined some of the early attempts to define a density functional theory, the two foundational theorems from Hohenberg and Kohn can be introduced.¹⁴³ The first is the existence theorem and proves that the ground state density of a system uniquely determines the external potential, and thus the Hamiltonian operator. The second theorem proves that density functional theory is variational, giving support to the early ideas put forward by Thomas and Fermi.

2.6.2.1 The Existence Theorem

To construct the Hamiltonian for a particular system, the charges and positions of the nuclei, and the total number of electrons are required. By integrating over the density, the total number of electrons is obtained. To determine the interaction of the electrons with the nuclei i.e. the external potential, it must be shown that the density (the ground state density in this case), uniquely determines this external potential. The first Hohenberg-Kohn theorem proceeds via *reductio ad absurdum*, where it is shown that an assumption to the contrary produces an impossible result.

2 - Theoretical Background

The first step is to assume that two different external potentials, v_a and v_b can be determined from the same non-degenerate ground state density. These two external potentials appear in their respective Hamiltonians, \hat{H}_a and \hat{H}_b , where each Hamiltonian has a ground state wavefunction and energy eigenvalue associated with it. By the variational theorem, the expectation value of \hat{H}_a over the wavefunction b must be greater than the true ground state energy associated with wavefunction a. This is represented by

$$E_{0,a} < \langle \Psi_{0,b} | \hat{H}_a | \Psi_{0,b} \rangle \quad (2.49)$$

This expression can be rewritten as

$$\begin{aligned} E_{0,a} &< \langle \Psi_{0,b} | \hat{H}_a - \hat{H}_b + \hat{H}_b | \Psi_{0,b} \rangle \\ &< \langle \Psi_{0,b} | \hat{H}_a - \hat{H}_b | \Psi_{0,b} \rangle + \langle \Psi_{0,b} | \hat{H}_b | \Psi_{0,b} \rangle \\ &< \langle \Psi_{0,b} | \hat{v}_a - \hat{v}_b | \Psi_{0,b} \rangle + E_{0,b} \end{aligned} \quad (2.50)$$

where the final line of *Equation 2.50* is equivalent to

$$E_{0,a} < \int [\hat{v}_a(r) - \hat{v}_b(r)] \rho_0(r) dr + E_{0,b} \quad (2.51)$$

as the external potentials \hat{v} are one-electron operators. The labels a and b are arbitrary, so equivalently

$$E_{0,b} < \int [\hat{v}_b(r) - \hat{v}_a(r)] \rho_0(r) dr + E_{0,a} \quad (2.52)$$

By summing *Equations 2.51* and *2.52* the impossible result

$$E_{0,a} + E_{0,b} < E_{0,b} + E_{0,a} \quad (2.53)$$

occurs, which states that sum of the energies corresponding to wavefunctions a and b is less than itself. Therefore, it must be true that the ground state density uniquely determines the external potential. This is the Hohenberg-Kohn existence theorem.

2.6.2.2 The Variational Theorem

The first Hohenberg-Kohn theorem establishes that if one has in their possession a density, this density will uniquely determine an external potential, and thus the Hamiltonian, and thus the energy. So, having a candidate wavefunction and Hamiltonian in hand, the energy is evaluated, according to

$$\langle \Psi_{\text{cand}} | H_{\text{cand}} | \Psi_{\text{cand}} \rangle = E_{\text{cand}} \geq E_0 \quad (2.54)$$

which, as per the variational theorem of MO theory, will be greater than or equal to the true ground state energy. This demonstrates that the density obeys a variational principle, which is the second Hohenberg-Kohn theorem.

2.6.3 Kohn-Sham Theory

A crucial breakthrough in providing a practical prescription for carrying out DFT calculations was proposed by Kohn and Sham in 1965.¹⁴⁴ The key idea was to take as a starting point a fictitious system of non-interacting electrons, that have the same ground state density as some real system of interest, the electrons of which are interacting. The Hamiltonian for this non-interacting system can be simply expressed as a sum of one-electron operators and has eigenfunctions that are Slater determinants of the individual one-electron eigenfunctions. Furthermore, the eigenvalues for such a system are the sum of the one-electron eigenvalues.

As a starting point, the energy functional for the non-interacting systems can be divided into the various energetic components. This is given by

$$E[\rho(r)] = T_{\text{ni}}[\rho(r)] + V_{\text{ne}}[\rho(r)] + V_{\text{ee}}[\rho(r)] + \Delta T[\rho(r)] + \Delta V_{\text{ee}}[\rho(r)] \quad (2.55)$$

2 - Theoretical Background

where the first, second and third terms correspond to the kinetic energy of the non-interacting electrons, the electron-nuclear attraction potential energy and the classical electron-electron repulsion energy, respectively. The final two terms correct for the assumption of a non-interacting system, with the first of these correcting the kinetic energy deriving from the interacting nature of the electrons in the real system, and the second correcting for the assumption of classical electron-electron interaction.

Equation 2.55 can be rewritten as an orbital expression, given by

$$E[\rho(r)] = \sum_i^N \left(\left\langle \chi_i \left| -\frac{1}{2} \nabla_i^2 \right| \chi_i \right\rangle - \left\langle \chi_i \left| \sum_k^{\text{nuclei}} \frac{Z_k}{|r_i - r_k|} \right| \chi_i \right\rangle \right) + \sum_i^N \left\langle \chi_i \left| \frac{1}{2} \int \frac{\rho(r')}{|r_i - r'|} dr' \right| \chi_i \right\rangle + E_{xc}[\rho(r)] \quad (2.56)$$

where N refers to the total number of electrons, and the density has been expressed as

$$\rho = \sum_{i=1}^N \langle \chi_i | \chi_i \rangle \quad (2.57)$$

The final term of *Equation 2.56* is a catch-all term for the energy resulting from correction of the kinetic energy due to the difference between the interacting and non-interacting system, the self-interaction error correction, as well as the effects of quantum mechanical correlation and exchange. Using variational calculus, the set of orbitals χ_i that minimise the energy are located, resulting in a set of pseudo eigenvalue equations, given by

$$\hat{h}_i^{\text{KS}} \chi_i = \varepsilon_i \chi_i \quad (2.58)$$

These are the Kohn-Sham (KS) equations, where the one-electron KS operator is given by

2 - Theoretical Background

$$\hat{h}_i^{KS} = -\frac{1}{2}\nabla_i^2 - \sum_k^{\text{nuclei}} \frac{Z_k}{|r_i - r_k|} + \int \frac{\rho(r')}{|r_i - r'|} dr' + \hat{V}_{xc} \quad (2.59)$$

where the final term

$$\hat{V}_{xc} = \frac{\delta E_{xc}}{\delta \rho} \quad (2.60)$$

is a functional derivative that can be thought of as the one-electron operator, that when acting on the KS Slater determinant, returns E_{xc} .

Analogous to the approach taken in HF theory to determine the orbital coefficients, a secular equation is solved, but in this case, the Fock matrix elements are replaced by the $K_{\mu\nu}$ matrix elements, given by

$$K_{\mu\nu} = \left\langle \phi_\mu \left| -\frac{1}{2}\nabla^2 - \sum_k^{\text{nuclei}} \frac{Z_k}{|r - r_k|} + \int \frac{\rho(r')}{|r - r'|} dr' + \hat{V}_{xc} \right| \phi_\nu \right\rangle \quad (2.61)$$

A final point to make on the KS procedure is that the density is required for calculation of the secular matrix elements, but the density is determined from the orbitals that result from the procedure. Therefore, the KS procedure must be carried out using an iterative SCF approach.

2.6.4 Functional Classes

The functional dependence of the exchange-correlation energy on the electron density is expressed as an interaction between the electron density and a quantity called the energy density, ε_{xc} , which is dependent on the density (and is usually given as a sum of exchange and correlation energy parts). This is given by

$$E_{xc}[\rho(r)] = \int \rho(r) \varepsilon_{xc}[\rho(r)] dr \quad (2.62)$$

Furthermore, the electron density is usually expressed in terms of an effective radius, given by

$$r_s(r) = \left(\frac{3}{4\pi\rho(r)} \right)^{1/3} \quad (2.63)$$

This effective radius is defined as the radius required to contain exactly one electron, with the sphere defined by this radius having the same density throughout. Finally, in order to account for spin in DFT, individual spin functions of the α and β spin densities are utilised. The spin densities at any position r are expressed as

$$\zeta(r) = \frac{\rho^\alpha(r) - \rho^\beta(r)}{\rho(r)} \quad (2.64)$$

2.6.4.1 Local Density Approximation (LDA)

The idea behind LDA functionals is that the value of the energy density at some position can be calculated exclusively from the value of the electron density at that position i.e. the local value of the density. As a result, the density must be single valued at every position. LDA functionals deriving from the uniform electron gas (UEG) are the only functionals that meet this requirement, due to the density of the UEG having the same value at every position. Invoking the UEG is not equivalent to assuming that the electron density of the real molecule of interest is constant through space. It is instead an assumption that the exchange-correlation energy density at every position in space for the molecule is the same as it would be for the UEG having the same density as is found at that position.

2 - Theoretical Background

The LDA approximation can be extended to the spin-polarised regime using

$$\varepsilon_x[\rho(r), \zeta] = \varepsilon_x^0[\rho(r)] + \{\varepsilon_x^1[\rho(r)] - \varepsilon_x^0[\rho(r)]\} \left[\frac{(1 + \zeta)^{4/3} + (1 - \zeta)^{4/3} - 2}{2(2^{1/3} - 1)} \right] \quad (2.65)$$

where the superscript zero is the Slater exchange energy density given by

$$\varepsilon_x^0[\rho(r)] = -\frac{9\alpha}{8} \left(\frac{3}{\pi} \right)^{1/3} \rho^{1/3}(r) \quad (2.66)$$

and the superscript one energy density is the analogous expression deriving from a consideration of the UEG composed of only electrons of like-spin. For a spin-unpolarised system, the second term on the right-hand side goes to zero. Therefore, *Equation 2.65* represents a general form of the exchange energy density, known as the local spin density approximation (LSDA).

Having considered the exchange energy, a treatment of correlation energy can now be considered. Ceperley and Alder calculated the total energies of a set of UEGs of different densities to a high numerical accuracy.¹⁴⁵ By subtracting the known analytical exchange energies from these total energies, the correlation energies of these UEGs were calculated. Using these results, Vosko, Wilk and Nusair designed local functionals of the density that used several different fitting schemes.¹⁴⁶ The two functional forms that have seen the widest use are VWN and VWN5. LSDA calculations that combine Slater exchange and VWN correlation energy are referred to as the SVWN method.

2.6.4.2 (Meta)-Generalised Gradient Approximation

The generalised gradient approximation (GGA) defines the class of functionals that depend both on the density and the gradient of the density. This class of functional is constructed by adding a correction term to the LDA functional, given by

$$\varepsilon_{x/c}^{\text{GGA}}[\rho(r)] = \varepsilon_{x/c}^{\text{LSD}}[\rho(r)] + \Delta\varepsilon_{x/c} \left[\frac{|\nabla\rho(r)|}{\rho^{4/3}(r)} \right] \quad (2.67)$$

where the correction term to the exchange or correlation LDA function is dependent on the dimensionless reduced gradient, rather than the absolute gradient itself.

The first GGA exchange functional that saw widespread use was the Becke exchange functional, abbreviated as 'B'¹⁴⁷, given by

$$\Delta\varepsilon_x^{\text{B}} = -\beta\rho^{1/3} \frac{x^2}{1 + 6\beta x \sinh^{-1} x} \quad (2.68)$$

where

$$x = \frac{|\nabla\rho|}{\rho^{4/3}} \quad (2.69)$$

This functional incorporates a single empirical parameter β , the value of which was optimised by fitting to the exactly known exchange energies of the six noble gas atoms He through Rn. As well as Becke exchange, there have been other GGA exchange functionals developed, that contain no empirically optimised parameters. Instead, they are based on rational functional expansions of the reduced gradient. Two examples of these are B88 and PBE (Perdew, Burke and Ernzerhof).^{148,149}

Moving on to corrections to the LDA correlation energy, numerous GGA correlation functionals have also been developed. Two prominent examples of these include P86

and LYP (Lee, Yang and Parr).^{150,151} The latter example, LYP, rather than correcting the LDA expression, calculates the correlation energy from scratch, utilising four empirical parameters. It is often combined with B exchange to produce the BLYP exchange-correlation functional.

Given that the gradient of the density has been introduced as a second term in a Taylor-like expansion, a logical next step is then to include the second derivative of the electron density, the Laplacian. Functionals of this dependence are termed meta-GGA functionals. The first meta-GGA exchange functional was proposed by Becke and Roussel (BR)¹⁵², with Proynov, Salahub and co-workers proposing the first correlation functional (Lap).¹⁵³ It was found that numerically stable calculations of the Laplacian of the density were quite a technical challenge, and so an alternative formalism was proposed, one that depended on the kinetic energy density, given by

$$\tau(r) = \sum_i^{\text{occupied}} \frac{1}{2} |\nabla \psi_i(r)|^2 \quad (2.70)$$

Although functionals such as BR include a dependence on the Laplacian, as well as τ , developers tend to discard the Laplacian in more modern functionals. One example of such a functional that has seen wide use is the TPSS exchange-correlation functional.¹⁵⁴

2.6.4.3 Hybrid Methods

By using the Hellmann-Feynman theorem, one can show that the exchange-correlation energy of a system can be calculated as

$$E_{xc} = \int_0^1 \langle \Psi(\lambda) | V_{xc}(\lambda) | \Psi(\lambda) \rangle d\lambda \quad (2.71)$$

2 - Theoretical Background

where a smooth conversion between a non-interacting system ($\lambda = 0$) to a fully interacting system ($\lambda = 1$) is carried out. In the non-interacting limit, there is no correlation energy to consider, with the only component of V being exchange. The exchange energy of the non-interacting system may be calculated exactly, given that the Slater determinant of KS orbitals is the exact wavefunction for the non-interacting Hamiltonian. As the electron-electron interaction is switched on, the remaining energy (correlation) is approximated using a density functional approximation. This is given by the expression

$$E_{xc} = (1 - a)E_{xc}^{DFT} + aE_x^{HF} \quad (2.72)$$

where a is a percentage of Hartree-Fock exchange energy. This approach is called the adiabatic connection method. Using LSDA exchange-correlation, and assuming a value of 0.5 for a , Becke proposed the half-and-half (H&H) density functional.¹⁵⁵ This was one of the first attempts at implementing a hybrid functional (due to the inclusion of DFT and HF exchange).

Given that inclusion of a single optimisable parameter gave improved results, a logical next step was to introduce additional empirical parameters. In this vein, Beck developed a three-parameter expression, given by

$$E_{xc}^{B3PW91} = (1 - a)E_x^{LSDA} + aE_x^{HF} + b\Delta E_x^B + E_c^{LSDA} + c\Delta E_c^{PW91} \quad (2.73)$$

where a , b and c are parameters with values of 0.20, 0.72 and 0.81, respectively. This functional form was given the name B3PW91.¹⁵⁶ The GGA correlation functional, PW91, is designed to provide a correction to the LSDA correlation energy. By replacing this functional with the LYP correlation functional, which is designed to calculate the full correlation energy, Stevens proposed the B3LYP functional.¹⁵⁷ The functional expression for B3LYP is given as

2 - Theoretical Background

$$E_{xc}^{B3LYP} = (1 - a)E_x^{LSDA} + aE_x^{HF} + b\Delta E_x^B + (1 - c)E_c^{LSDA} + cE_c^{LYP} \quad (2.74)$$

where the empirical parameters have the same value as B3PW91. Besides these three-parameter models, there have been a number of one-parameter models, such as the B1PW91 and PBE0 functionals.^{158,159} The parameter in PBE0 dictating the amount of HF exchange (25%) was chosen based on perturbation theory arguments, and not empirically optimised. Hence, the name, PBE0, refers to the fact that there are “zero” parameters. Finally, the Truhlar group have developed a set of functionals that are heavily empirical, containing 25-60 parameters that have been fitted to experimental data. These functionals are collectively referred to as the Minnesota functionals. One example that features heavily in this thesis is the M06-2X hybrid functional, which contains 54% Hartree-Fock exchange.¹⁶⁰

2.6.4.4 Double-hybrid Methods

There also exists a class of functional that includes a MP2-like energy correction, which utilises the Kohn-Sham DFT orbitals and energies to carry out this MP2 calculation. Functionals of this type are called double-hybrid functionals. A general expression, similar in form to hybrid functional expressions, is given by

$$E_{xc}^{DHDFT} = (1 - a)E_x^{DFT} + aE_x^{HF} + (1 - b)E_c^{DFT} + bE_c^{MP2} \quad (2.75)$$

where the empirical parameter b dictates the fraction of MP2 correlation energy that is included. One of the first examples of a double-hybrid functional was B2PLYP, developed by Grimme, which builds upon the B88 and LYP functionals.¹⁶¹ Two other notable example are the PBE0-DH functional, which builds upon the PBE0 functional, and PWPB95.^{162,163} Although double-hybrid functionals do provide improved results, the N^5 computational dependence limits their use with large systems. Furthermore,

the basis set convergence is slower than regular DFT, given the inclusion of the MP2 term.

2.6.5 Dispersion Corrections

DFT in its standard formalism does not describe dispersion forces. For example, between rare gas atoms, many functionals predict purely repulsive interactions, while others fortuitously describe a weak stabilising interaction, but fail to describe the correct long-range behaviour. Dispersion is a long range interaction relative to covalent bonding interactions and thus may not be significant for smaller molecules. However, as molecules become larger, the individually small dispersive interactions become numerous and thus increasingly important.

The pre-parameterised methods from Grimme have become the most widely used dispersion corrections for routine applications. The earliest model from Grimme included a R^{-6} energy term for each atom pair, with an atom-dependent C6 parameter.¹⁶⁴ This has been refined to include higher-order terms, as well as making the parameters depend on the atomic environment. These dispersion corrected methods are denoted D/D2/D3. The original zero-damping function has also been replaced with finite damping, as proposed by Becke and Johnson (BJ).¹⁶⁵ This method is denoted as DFT-D3(BJ), as it was seen to improve the description of medium-range electron correlation effects. The D4 correction is the latest iteration from Grimme, and was found to improve on the D3 scheme in the case of polar, organometallic and ionic systems.¹⁶⁶

2.6.6 Advantages and Disadvantages of DFT

Density functional theory optimises the electron density, while MO theory optimises a wavefunction. If one wanted to calculate a particular molecular property using DFT, how that property depends on the density needs to be known. In other words, one needs to have a particular functional of the density for that property. On the other hand, in order to determine a molecular property in MO theory, one only requires the correct quantum mechanical operator.

The formal scaling behaviour of DFT is no worse than N^3 , where N is the number of basis functions. This is an improvement over HF theory by a factor of N , while being an improvement over other correlation methods by multiple factors of N . DFT also can take advantage of basis sets that are not contracted Gaussians. The density can be represented using an auxiliary basis set, meaning that other options are available for the basis functions, including Slater-type functions (STO). Fewer STOs are required, given that they have correct cusp behaviour at the nuclei. Furthermore, symmetry can be taken advantage of more readily, leading to a greater speed up in calculations. A final point on the computational efficiency of DFT is that the convergence with respect to basis set size is more rapid than HF and correlated MO theories. Therefore, DFT calculations are usually seen to be converged at the polarized triple- ζ level.

To close out this section on density functional theory, the topic of systematic improvability must be discussed. In MO theory, there is a clear and defined path to the exact solution of the Schrödinger equation. One could construct a wavefunction from a linear combination of all possible configurations in principle, and using an infinite basis set, evaluate the exact energy of a system. For density functional theory

2 - Theoretical Background

however, a rough ordering of the classes of functional in terms of increasing quality is $\text{LSDA} < \text{GGA} < \text{meta-GGA} < \text{Hybrid} < \text{Double-hybrid}$. This ordering, referred to as Jacob's Ladder of DFT (Figure 2.3), is based on experiment and observation over the few decades that DFT has been in use. For a thorough benchmarking study of over 200 functionals, across all classes, see the cited review from Goerigk and Grimme¹⁶⁷, where the relative ordering of Jacob's Ladder is supported, and recommendations within each class of functional are given.

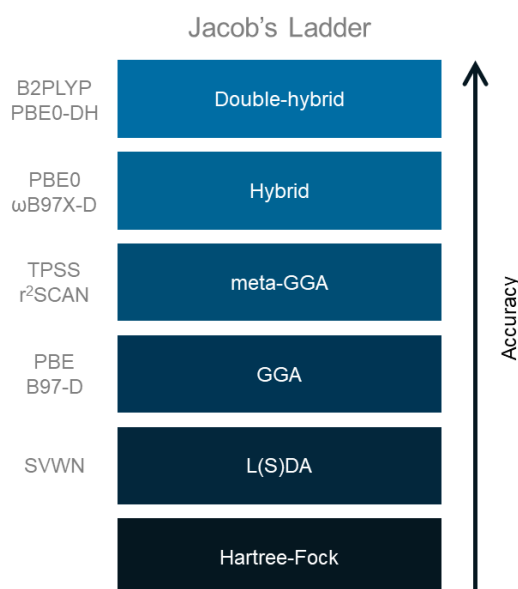


Figure 2.3: Approximate functional class ordering, according to Perdew's "Jacob's Ladder". Examples of each class of functional are given to the left of the figure.

2.7 Basis Sets

Each molecular orbital is expressed as a linear combination of basis functions. The relative contribution of each function to a particular molecular orbital i.e. the coefficients, are determined from the iterative SCF process. Within HF theory, the HF limit of accuracy is reached using an infinite basis set. In practice however, this is not feasible, and so there has been much research into the exact functional form of basis

sets, that allow one to approach the HF limit arbitrarily close, in the most computationally efficient manner. This section will outline the major considerations associated with basis sets and their development, namely the size, functional form and chemical utility.

2.7.1 Slater- vs Gaussian-type orbitals

Slater-type orbitals (STO) were the original basis functions of choice in the historical development of basis sets. This is due to them having a number of features that cause them to resemble hydrogenic atomic orbitals quite closely. In particular, they exhibit the correct cusp behaviour at the nucleus. In the framework of *ab initio* HF theory however, the four-index integrals cannot be solved analytically, when the basis functions are STOs. This requirement, that they be solved numerically, places significant limitations on their use. To overcome this, Boys proposed changing the radial decay of STOs from e^{-r} to e^{-r^2} , therefore converting these functions to Gaussian-type functions.¹⁶⁸ The functional form of a normalised Gaussian-type orbital (GTO) in atom-centred cartesian coordinates is given by

$$\phi(x, y, z; \alpha, i, j, k) = \left(\frac{2\alpha}{\pi}\right)^{3/4} \left[\frac{(8\alpha)^{i+j+k} i! j! k!}{(2i)! (2j)! (2k)!}\right]^{1/2} x^i y^j z^k e^{-\alpha(x^2+y^2+z^2)} \quad (2.76)$$

where α controls the width of the GTO, with i, j and k being non-negative integers that dictate the nature of the orbital. When all indices are zero, this corresponds to an s-type orbitals. When exactly one of the indices is equal to one, this corresponds to a p-type orbital with axial symmetry around a single axis. When the sum of the indices is equal to two, this corresponds to a d-type orbital. There are of course six possible ways that these three indices can sum to two, and these six combinations define the six cartesian d functions. The solution of the Schrödinger equation for the hydrogen atom shows that only five functions are required to span the z component of the orbital

2 - Theoretical Background

angular momentum for $l = 2$. These five functions are derived from linear combinations of the six cartesian functions and are referred to as the canonical d functions. Different Gaussian basis sets use different definitions of the d functions.

2.7.2 Contracted Gaussian Functions

There are certain features of GTOs that, when utilised individually, are not desirable. The first feature of concern is that for s-type functions, GTOs are smooth and differentiable at the nucleus, but hydrogenic atomic orbitals have a cusp. The second feature of concern is that the radial decay of GTOs is too rapid, as a result of having a decay that is exponential in r^2 , rather than r , as is the case with STOs. To overcome these problems, the first basis sets utilised GTOs as building blocks to approximate STOs. In other words, a linear combination of GTOs was used to build up individual basis functions, φ , given by

$$\varphi(x, y, z; \{\alpha\}, i, j, k) = \sum_{a=1}^M c_a \phi(x, y, z; \alpha_a, i, j, k) \quad (2.77)$$

where M is the number of individual GTOs, referred to as primitives. The overall basis function is referred to as a contracted GTO, where the coefficients c are chosen to optimise the shape of the basis function sum and ensure normalisation. These coefficients are termed the contraction coefficients and together with the exponents α of each of the primitives, define a basis function.

Optimal contraction coefficients and exponents for approximating STOs with contracted GTOs were determined by Hehre, Stewart and Pople for a large portion of the periodic table.¹⁶⁹ Using these, a series of basis sets was developed, termed STO-MG (Slater-Type Orbital approximated by M Gaussians). The more primitives

that were employed, the more accurately the contracted Gaussians approximated the STOs. This however results in four-index two-electron integrals that become increasingly more complex to evaluate. In light of this, it was determined that the optimal balance of speed and accuracy was struck for the STO-3G basis set. This basis set is utilised very little in modern electronic structure calculations but was an important stepping stone to more modern basis sets that are used today.

2.7.3 Valence-multiple- ζ & split-valence

When there is only one basis function defined for each type of orbital, core through valence, this is referred to as a minimal or single- ζ basis set. This is the minimum requirement for a basis set. Minimal basis sets are limited, and one possible way to increase the flexibility of a basis set is to decontract it. For example, for the STO-3G basis set, two basis functions for each atomic orbital could be constructed. The first of these could be a contraction of the first two primitive Gaussians used in the STO-3G basis set, while the second basis function could be the third primitive on its own. This type of basis set, where a decontraction has resulted in two basis functions per atomic orbital, is referred to as a double- ζ basis set. Arbitrary decontractions can be carried out, producing a triple- ζ basis set, a quadruple- ζ basis set and so on. A modern family of basis sets that employ such an approach are the cc-pCVXZ ($X = D, T, Q, 5, \dots$) basis sets of Dunning and co-workers.¹⁷⁰ The acronym stands for correlation-consistent polarised Core and Valence (Double/Triple/Quadruple/etc..) Zeta.

The core orbitals are only weakly affected by changes in chemical bonding, while valence orbitals can vary significantly as a function of chemical bonding. Using this fact, so called split-valence basis sets have been developed, where the core orbitals are treated with contracted gaussian functions, while valence orbitals are

decontracted into arbitrarily many functions. This allows significant flexibility in the valence orbitals to react to differing chemical environments. Of the split-valence basis sets, the most popular historically has been the Pople style basis sets.¹⁷¹ Some examples of this family of basis sets include 3-21G, 6-31G and 6-311G. This nomenclature refers to the contraction scheme employed. The first number before the hyphen refers to the number of primitives employed for each contracted gaussian function applied to the core orbitals. The numbers after the hyphen refer to the number of primitives used for the valence functions. If there are two numbers, this is a double- ζ basis set, with three numbers representing a triple- ζ basis set, and so on.

The Pople style basis sets utilise a segmented contraction scheme. This means that there is no crossover in primitives used for orbitals of the same angular momentum. On the other hand, there exists a general contraction scheme that allows the sharing of primitives between orbitals of the same angular momentum. This type of contraction scheme is utilised in the correlation consistent polarised Valence (Double/Triple/etc.) Zeta basis sets of Dunning and co-workers.^{172,173} This family of basis sets are represented by acronyms cc-pVXZ (X = D,T,Q,5,...), where the correlation consistency stems from the fact that these basis sets were optimised for calculations including electron correlation, and not just for HF calculations.

2.7.4 Polarisation functions

The use of atom centred basis functions in molecular calculations, which approximate atomic orbitals, has been shown to not always provide the required mathematical flexibility. For example, if one uses only s and p atom centred basis functions to optimise the geometry of ammonia at the HF level of theory, a planar geometry is predicted to be the minimum energy structure. By adding d functions to the nitrogen

2 - Theoretical Background

basis set, one achieves the correct pyramidalized geometry. This approach, of adding basis functions corresponding to one quantum number of higher angular momentum than the valence orbitals is referred to as adding polarisation functions.

Adding more basis functions comes with a higher computational cost, and early calculations only employed a single set of polarisation functions. Pople and co-workers introduced the *, or “star”, nomenclature to describe polarisation functions. For example, the 6-31G* basis set means that an extra set of d functions have been added to polarise the p functions for heavy atoms (anything after H and He). The 6-311G** basis set means that an extra set of d functions have been added to polarise the p functions, and a set of p functions have been added to polarise the s functions on H and He.¹⁷⁴ A general rule of thumb is that for every set of polarisation functions added, another decontraction step should be carried out in order to obtain a balanced basis set. This philosophy was adopted to add polarisation functions to the basis sets of Dunning and co-workers mentioned above.¹⁷⁵ To accommodate the fact that using more than one set of polarisation functions is necessary in modern calculations, the Pople style basis sets are now more commonly defined with an explicit definition of what functions are included. For example, the 6-31G(d) basis set is equivalent to the 6-31G* basis set. This can be generalised to include more sets of polarisation functions e.g. the 6-31G(3d2fg,2pd) basis set.

2.7.5 Diffuse functions

In cases where electrons are weakly bound and localise far away from the bulk of the density, as is the case for the highest energy molecular orbitals of anions, diffuse or augmentation functions are required. For Pople style basis sets, the “+” symbol indicates the addition of diffuse functions. For example the 6-31+G(d) basis set

implies that heavy atoms have been augmented with a set of s and a set of p functions, while the 6-311++G(3df,2pd) basis set implies that an extra set of s functions have been added to hydrogen. The Dunning style basis sets approach the addition of diffuse functions in a slightly different way. By prefixing the basis set with “aug” e.g. aug-cc-pVTZ, it is implied that one set of diffuse functions is added for each angular momentum present. For aug-cc-pVTZ, diffuse f, d, p and s functions have been added to heavy atoms, while d, p and s functions have been added to H and He.

3 The Diradicaloid Electronic Structure of Dialumenes: a Benchmark Study at the Full CI Limit

3.1 Introduction

From a wavefunction (WF) theory perspective, diradical character is typically an indication of some multi-reference character. This further implies that single-reference WF methods may not be ideal for their calculation and multi-reference methods might instead be preferable. It is also not obvious how accurate DFT methods would be for treating systems with diradical character or even how diradical character should be analyzed with DFT methods. Single-reference wavefunction methods like coupled cluster (CC) have the advantage of a robust treatment of dynamic correlation while being biased towards the quality of the single-determinant reference wavefunction (typically restricted, RHF, or unrestricted Hartree-Fock, UHF). Multi-reference methods on the other hand are more flexible as the reference wavefunction is multiconfigurational (CASSCF), treating static correlation directly, while having drawbacks of either a less accurate treatment of dynamic correlation (multi-reference perturbation theory, for example CASPT2) or being too expensive (multi-reference configuration interaction, for example MRCI). The issue of whether single-reference or multi-reference methodology would be more applicable for a specific system, could in principle be tested by comparing to results at an effective Full Configuration Interaction (FCI) level, using e.g. selected CI or density matrix renormalization group (DMRG) techniques that approach the Full-CI limit by a systematic expansion of the wavefunction. The advantage of such “near Full-CI” WFs is that they are neither biased towards a particular n -particle excitation (like single-reference CC n methods) or by the user-chosen division of the system into an active space, treating static correlation, and an outer space, treating dynamic correlation (like multi-reference methods).

In a previous study carried out by Tuononen and coworkers⁶⁹, the nature of bonding present in the Group 13 (Al-Tl) dimetallenes was investigated (for multiple ligands) and the level of diradical character assessed. For all but the dithallenes, restricted-unrestricted instabilities were identified in the Hartree-Fock wavefunctions, suggestive of singlet diradical character in the lowest energy wavefunction. CASSCF(4,5) as well as CI and CC calculations were utilized and the diradical character was quantified using both CI coefficients as well as natural orbital occupation numbers (NOONs). Both CI- and NOON-based metrics showed a stepwise decrease of diradical character down Group 13, from ~14% for aluminium to ~1% diradical character for thallium. While MP2 was found to predict accurate geometries, natural occupation numbers indicated difficulties in treating reliably the static correlation present. Overall, it was concluded that CCSD(T) and QCISD(T) as well as CAS-based methods are capable of describing the electronic structure of the Group 13 dimetallenes, with DFT methods (B3LYP) offering a cost-effective alternative. However, a more detailed analysis of the behaviour of different methods and whether single-reference or multi-reference methods should be preferred, was not reported. The performance of different functional classes in these systems was also not presented.

In this chapter, the electronic structure of dialumenes is systematically investigated, focusing primarily on the simplest dialumene Al_2H_2 (having the highest diradical character in Group 13), with comparisons drawn to real synthetic examples. The convergence of the electronic structure of Al_2H_2 is analysed up to a practical Full-CI limit, allowing the rigorous benchmarking of the performance of simpler single-reference, multi-reference and DFT-based methods in describing the electronic structure. The performance of the various WFT and DFT methods is discussed for the bond dissociation energy, geometries and electron densities of dialumenes. A decomposition of the DFT errors into density-driven and functional-driven errors

allows additional insight into the nature of these errors. Finally, the calculation and definition of the diradical character using WFT and DFT methods is discussed.

3.2 Methods

The MP2/cc-pVTZ optimised geometries of the transient group 13 dimetallenes, E_2R_2 ($E = \text{Al, Ga, In, Tl}$; $R = \text{H, Me}$) were taken from the previous study carried out by Tuononen.⁶⁹ Most calculations were performed using the cc-pVTZ basis set by Dunning and co-workers¹⁷² (Al,H,C,N,O,Ga) while for heavier elements, (In, Tl), the corresponding valence triple- ζ quasi-relativistic basis set+pseudopotential combination, cc-pVTZ-PP, was used.^{176–178} CCSD and CCSD(T) geometry optimizations of Al_2H_2 and Al_2Me_2 were performed with the CFOUR quantum chemistry program.¹⁷⁹ The larger base-stabilised dialumenes were optimised using RI-MP2 (RI = resolution of the identity approximation)¹⁸⁰, with the exception of the larger synthetic example, where the DLPNO-MP2¹⁸¹ approximation was employed as implemented in the ORCA quantum chemistry program (version 5.0.3).¹⁸² All calculations carried out using ORCA employed the energy convergence threshold of 1×10^{-8} Eh, (“TightSCF” keyword). For both RI- and DLPNO-MP2 calculations, the cc-pVTZ/C triple- ζ quality auxiliary basis set was employed. For the DLPNO-MP2 geometry optimization, the default PNO threshold settings were used ($T_{\text{CutDO}} = 1 \times 10^{-2}$, $T_{\text{CutPNO}} = 1 \times 10^{-8}$). Geometry optimizations at the DFT level were carried out using different functionals: TPSS¹⁵⁴, B3LYP^{146,156,157,183}, and M06-2X¹⁶⁰ functionals, with and without Grimme’s DFT-D3 dispersion correction.¹⁶⁴

Using the cc-pVTZ basis set, the Full-CI limit of Al_2H_2 was systematically approached using three different near-Full-CI methods: the semi-stochastic heat-bath CI method

3 - The Diradicaloid Electronic Structure of Dialumenes: a Benchmark Study at the Full CI Limit

(SHCI)^{184,185}, the iterative configuration expansion CI (ICE-CI)^{139,140} and density matrix renormalization group (DMRG).^{186,187} The SHCI and DMRG calculations were carried out via Dice^{184,185,188} and Block2^{189,190} programs, via the PySCF^{191–193} library through interfaces available in the Python library ASH.¹⁹⁴ The ICE-CI method was carried out using ORCA. CCSD natural orbitals were used as input orbitals to each of these selected CI methods, and for each method, the Full-CI limit was systematically approached as a function of the respective WF expansion parameter.

A range of single point calculations were carried out at both the wave function theory (WFT) and density functional theory (DFT) levels. The ORCA program was employed to carry out the following WFT methods: Hartree-Fock (HF), MP2, CCSD, CCSD(T), CASSCF, CASPT2, NEVPT2, MRCI, and MRCI+Q. ORCA was further utilised to carry out DFT single point calculations. The functionals tested were: PBE¹⁹⁵, TPSS¹⁵⁴, r2SCAN¹⁹⁶, TPSSH¹⁹⁷, B3LYP^{146,156,157,183}, BHandHLYP¹⁵⁵, M06-2X¹⁶⁰, ω B97X-V¹⁹⁸, B2PLYP¹⁶¹ and DSD-PBEP86.¹⁹⁹ Higher order coupled cluster calculations (CCSDT, CCSDT(Q) and CCSDTQ) and first-order densities (CCSD(T) and CCSDT) were calculated using the MRCC program²⁰⁰, via the interface in ASH.

Basis set extrapolations of energies to the complete basis set limit (CBS) were carried out at the RHF-CCSD(T) level of theory, using the keyword Extrapolate(4/5,cc) in the ORCA program which indicates a cc-pVQZ/cc-pV5Z extrapolation. The extrapolation of the HF energy uses the formula:

$$E_{\text{SCF}}^{(X)} = E_{\text{SCF}}^{(\infty)} + A \exp(-\alpha\sqrt{X}) \quad (3.1)$$

where X refers to the cardinal number of the basis set, ∞ refers to the basis set limit and A and α (basis set specific) are constants.^{201,202} While A is fitted, the α parameter is set to 9.19. The extrapolation of the correlation energy uses the formula:

$$E_{\text{corr}}^{(\infty)} = \frac{X^\beta E_{\text{corr}}^{(X)} - Y^\beta E_{\text{corr}}^{(Y)}}{X^\beta - Y^\beta} \quad (3.2)$$

where X and Y are the cardinal numbers of the two basis sets, and $\beta = 3.0$ was used for the 4/5 extrapolations.^{203,204}

Analysis of the topology of the Electron Localisation Function (ELF)^{205–207}, $\eta(r)$, was carried out using the Multiwfn program.²⁰⁸ The wavefunctions were read-in as Molden files of the canonical orbitals (for HF and DFT methods) or natural orbitals (for WFT methods). ELF basin analysis was carried out using a ‘Medium quality grid’ option (as defined in Multiwfn). The average population of each basin was then calculated by integrating over the electron density contained within each basin.

Finally, fractional occupation density (FOD) analysis was carried out using finite temperature (FT) smearing, as implemented in ORCA²⁰⁹, using the TPSS (Tel = 5000 K) functional and the def2-TZVP basis set.^{210,211} The electronic temperature was determined from the (empirical) formula $T_{\text{el}} = 20000 \text{ K} \times a_x + 5000 \text{ K}$, as recommended in the original studies, where the a_x parameter refers to the amount of HF exchange.

3.3 Results & Discussion

Single-reference wavefunction methods require the definition of a reference wavefunction. In practice, this is usually a Hartree-Fock determinant. However, for a molecule with diradical character it is not *a priori* obvious whether a UHF (unrestricted Hartree-Fock) or RHF (restricted Hartree-Fock) reference should be used. In order to assess the suitability of different reference WFs, a comparison at the CCSD(T) level

3 - The Diradicaloid Electronic Structure of Dialumenes: a Benchmark Study at the Full CI Limit

on Al_2H_2 was carried out, as shown in Table 3.1, comparing energies, doubles amplitudes, stability and spin populations.

Table 3.1: Comparison of SCF and CCSD(T) energies (E_H), stability measures, doubles amplitudes, T_1 diagnostic and spin populations for CCSD(T) calculations with different reference wavefunctions for Al_2H_2 .

	SCF Energy	CCSD(T) Energy	Largest Doubles Amplitude	T_1	Al1 / Al2 Spin Populations
RHF	-484.932	-485.116	0.203	0.024	0 / 0
UHF	-484.947	-485.114	0.207	0.109	0.59 / -0.59 ^a (0.18/-0.18) ^b
RKS B3LYP	-485.933	-485.111	0.176	0.016	0 / 0

^aMulliken spin populations of UHF density.

^bMulliken spin populations of UHF-UCCSD density.

Like that originally found by Tuononen⁶⁹, an instability was found for the RHF solution, prompting the search for a stable UHF solution. The UHF solution possesses a considerably lower energy ($\Delta E_{\text{UHF/RHF}} = 9.4 \text{ kcal mol}^{-1}$) than the unstable RHF solution. UHF spin populations on the Al atoms were ± 0.59 electrons, implying convergence to a strongly spin-polarised broken-symmetry (diradical) solution. CCSD(T) calculations were next carried out, using both unstable RHF and stable UHF reference wavefunctions. The RHF-CCSD(T) energy was $1.3 \text{ kcal mol}^{-1}$ lower in energy than the UHF-CCSD(T) energy, despite the instability present in the RHF reference wavefunction. Analysis of the RHF-RCCSD doubles amplitudes reveals a fairly large amplitude of 0.203, and a T_1 singles diagnostic of 0.024. T_1 diagnostics larger than 0.02 have traditionally been interpreted as indicating some multi-reference character,

though in view of the often strong dependence on the reference orbitals, this may also be an indication of the suitability of the reference orbitals themselves. In comparison, UHF-UCCSD results in a similarly large doubles amplitude of 0.207, but a considerably increased T_1 diagnostic of 0.109. Additionally, the UHF-UCCSD spin density (calculated using a CCSD unrelaxed density approximation) results in Mulliken spin populations of ± 0.18 electrons on each Al atom, consistent with exaggerated diradical character, inherited from the UHF reference. An RKS-CCSD(T) calculation was additionally carried out, using canonical Kohn-Sham orbitals obtained with the B3LYP functional. In contrast to RHF, the RKS determinant is stable, and no broken-symmetry UKS solution could be located. The RKS-CCSD(T) energy was found to be 3.1 kcal mol⁻¹ higher in energy than the RHF-CCSD(T) energy. The largest doubles amplitude was found to be 0.176, with a reduced T_1 diagnostic of only 0.016.

Overall, the instability of the RHF solution in combination with the large doubles amplitudes in the CC calculations is suggestive of some static correlation or diradical character in Al₂H₂. For comparison, a doubles amplitude of ~ 0.2 is similar to that found in CCSD calculations of the ozone molecule, a well-known multi-reference problem. However, breaking spin-symmetry by converging to a stable UHF solution clearly results in artefacts, as is evident from a substantially increased T_1 diagnostic in the CC calculation, presumably due to an overestimation of diradical character. The increase in T_1 can be interpreted as arising due to a worse set of reference orbitals (increased weights of singles amplitudes) due to artificial spin polarization arising from the UHF orbitals. It appears that the (unstable) RHF or alternatively a correlated-orbital Kohn-Sham RKS reference is a more suitable choice as a reference wavefunction in CC calculations of dialumenes.

Al_2H_2 clearly possesses some diradical character in its WF based on the large doubles amplitudes, which suggests that single-reference coupled cluster theory might not be an ideal WF expansion. While a multi-reference calculation based on a CASSCF reference is ideally suited to treat such diradical character, the drawback is that the dynamic correlation may not be as well accounted for as in CC theory. Making a direct comparison to the exact Full-CI WF would provide insight into the balance of the static and dynamical correlation effects and whether a single-reference or multi-reference approach is preferable. Al_2H_2 is a sufficiently small system for the Full-CI limit to be approached using either selected CI or DMRG approaches with a small basis set. Here we compare a matrix product state (MPS) wavefunction using the DMRG algorithm to two selected CI approaches: semi-stochastic heat-bath CI method (SHCI) and the iterative configuration expansion CI (ICE-CI). All three WFT types converge to the Full-CI limit as the WF expansion parameters are decreased (ϵ for SHCI and TGen for ICE-CI) or increased (M for number of renormalized states in DMRG).

First, the convergence of an energetic property to the Full-CI limit, the $\text{Al}_2\text{H}_2 \rightarrow 2 \text{AlH}$ ($^1\Sigma^+$) vertical bond dissociation energy (VBDE), was explored. This allowed the investigation of the convergence of the many-body wavefunction for describing the energetics associated with the Al—Al bond. A reasonably large cc-pVTZ basis set was used in these calculations and the Full-CI limit of the BDE of Al_2H_2 was systematically approached using SHCI, DMRG and ICE-CI methods. The Full-CI problem of Al_2H_2 in a cc-pVTZ basis set consists of 28 electrons in 96 orbitals. By invoking the frozen-core approximation this reduces to 8 electrons in 86 orbitals (i.e. a frozen core of 20 electrons in 10 orbitals).

3 - The Diradicaloid Electronic Structure of Dialumenes: a Benchmark Study at the Full CI Limit

For SHCI the ϵ selection threshold was varied from 5×10^{-2} to 6×10^{-6} , for ICE-CI the T_{Gen} threshold was varied from 5 to 4×10^{-5} (the T_{Var} threshold was set to be $T_{\text{Gen}} \times 10^{-7}$) while in the DMRG calculation the M parameter (number of renormalized states) was varied from 50 to 920. All three methods used the same starting orbitals, i.e. natural orbitals from a CCSD/cc-pVTZ unrelaxed density. For SHCI a stochastic PT2 correction (second-order perturbation theory using a stochastic approach) was included.

The results in Figure 3.1 reveal that all three WF-expansion strategies approach the VBDE from below and converge in varying ways towards a Full-CI/cc-pVTZ limit of $\sim 16.8 \text{ kcal mol}^{-1}$. Overall, SHCI, with a perturbation theory correction, was found to be the best method for quickly achieving approximate chemical accuracy as it crossed the 16 kcal mol^{-1} threshold using $\epsilon = 7 \times 10^{-5}$ with a low CPU time (approx. 35 minutes on 1 CPU core). Further decreasing the ϵ threshold resulted in reliable convergence towards $\sim 16.8 \pm 0.1 \text{ kcal mol}^{-1}$ around $\epsilon = 1 \times 10^{-5}$ to 6×10^{-6} with approximately $0.1 \text{ kcal mol}^{-1}$ uncertainty (primarily due to the stochastic perturbation correction). DMRG, gave overall the smoothest convergence of the three methods and convincingly converged to $16.8 \text{ kcal mol}^{-1}$ with an estimated $0.01 \text{ kcal mol}^{-1}$ uncertainty (it crossed the 16 kcal mol^{-1} threshold with $M=300$ in 328 min). ICE-CI (using a configuration expansion), however, was found to converge slower, and the VBDE did not appear to be reliably converged before calculations became intractable (the largest ICE-CI calculation gave a VBDE of $16.3 \text{ kcal mol}^{-1}$). ICE-CI crossed the 16 kcal mol^{-1} threshold with $T_{\text{Gen}} = 9 \times 10^{-5}$ in 174 min.

3 - The Diradicaloid Electronic Structure of Dialumenes: a Benchmark Study at the Full CI Limit

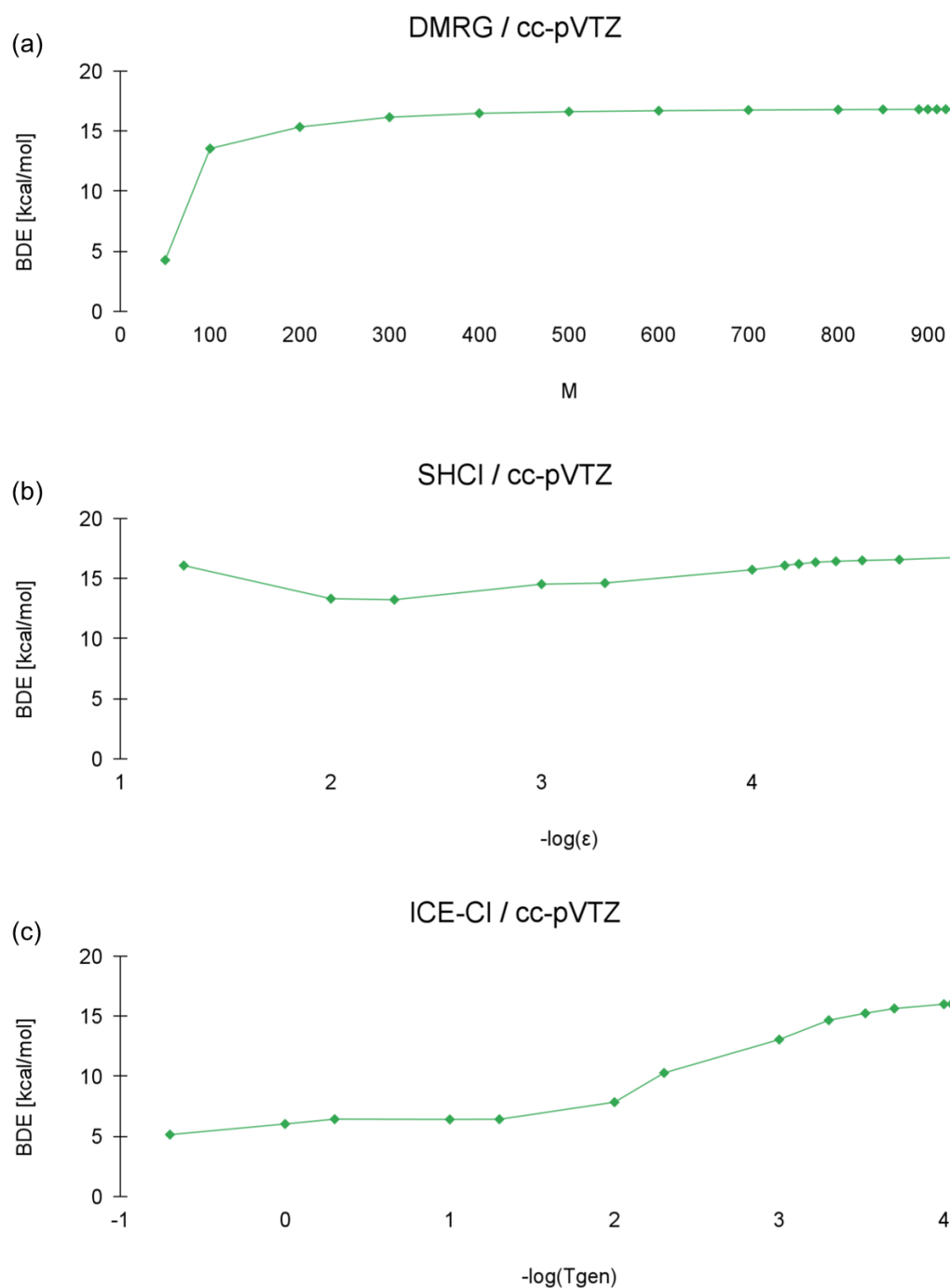


Figure 3.1: Calculation of the vertical bond dissociation energy of Al_2H_2 using DMRG, SHCI or ICE-Cl methods as a function of the respective WF expansion parameters using the cc-pVTZ basis set. (a) DMRG as a function of the M parameter. (b) SHCI with a perturbation theory correction, as a function of the ϵ parameter. (c) ICE-Cl as a function of the T_{Gen} threshold. Input orbitals were CCSD natural orbitals (from an unrelaxed density).

3 - The Diradicaloid Electronic Structure of Dialumenes: a Benchmark Study at the Full CI Limit

Both ICE-CI and SHCI are selected-CI algorithms (ICE-CI selects configurations while SHCI selects determinants) but SHCI additionally utilizes a stochastic perturbation theory correction to estimate the contribution from unselected determinants. Extrapolation schemes for ICE-CI to account for unselected configurations have been suggested¹⁴⁰ but were not considered here. Approximate CI approaches (ICE-CI and SHCI) are additionally not size-consistent, and calculation of a bond dissociation energy is likely especially sensitive to such size-consistency errors. Size-consistency error has been emphasized by Chilkuri and Neese¹⁴⁰ as sometimes dominating the error in the ICE-CI procedure. The perturbation correction in SHCI may be alleviating this size-consistency error. As DMRG has approximate size-consistency²¹² (dependent on orbital basis), this may be the reason for the overall smoother convergence to the FCI limit seen here. Due to the good agreement between SHCI and DMRG and the particularly smooth convergence of the DMRG wavefunction expansion, the Full-CI limit within a cc-pVTZ basis set of the vertical BDE can be confidently estimated to be 16.8 kcal mol⁻¹ with a maximum uncertainty of approx. 0.1 kcal mol⁻¹.

Having established a Full-CI estimate of 16.8 kcal mol⁻¹ for the BDE of Al₂H₂, a comparison of a range of single- and multi-reference wavefunction based methods was carried out (Figure 3.2). Each of these methods were benchmarked against the near Full-CI result from DMRG using the cc-pVTZ basis set. Even though the DMRG/cc-pVTZ result is not at the basis set limit, the WF expansion limit has been effectively reached and can be considered a near-exact result within this orbital basis. This then allows direct comparison to simpler WF methods, provided the same basis set is used.

3 - The Diradicaloid Electronic Structure of Dialumenes: a Benchmark Study at the Full CI Limit

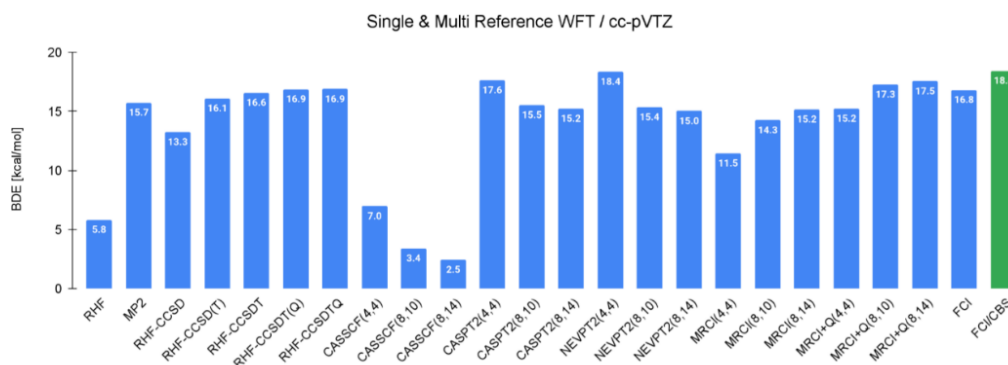


Figure 3.2: Performance of various single- and multi-reference correlated wavefunction theory methods in predicting the bond dissociation energy of Al_2H_2 , compared against the FCI estimate of $16.8 \text{ kcal mol}^{-1}$ (from DMRG and SHCI calculations). All calculations used a cc-pVTZ basis set, except the FCI/CBS estimate which was derived via a CCSD(T) CBS correction. The MRCI calculations used a selection threshold (Tsel) of 0.

Beginning with the single-reference methods, RHF drastically underestimates the BDE by 11 kcal mol^{-1} . Adding dynamic correlation in the form of MP2 gives a much-improved result ($15.7 \text{ kcal mol}^{-1}$), with an error of $1.1 \text{ kcal mol}^{-1}$. Surprisingly, the coupled cluster singles doubles (CCSD) method gives a slightly worse result than MP2 ($13.3 \text{ kcal mol}^{-1}$). Inclusion of perturbative triples (CCSD(T)) further improves the result ($16.1 \text{ kcal mol}^{-1}$), giving an error of only $0.7 \text{ kcal mol}^{-1}$ (i.e. reaching chemical accuracy). Going beyond perturbative triples using CCSDT gave a vertical BDE of $16.6 \text{ kcal mol}^{-1}$, while both CCSDT(Q) and CCSDTQ resulted in a value of $16.9 \text{ kcal mol}^{-1}$. A CCSDTQ coupled cluster expansion is commonly considered a good estimate to Full-CI, and overall, a $0.1 \text{ kcal mol}^{-1}$ agreement between DMRG and CCSDTQ is satisfactory.

Moving to multi-reference methods, CASSCF calculations with active spaces of (4,4), (8,10) and (8,14) were performed for the Al_2H_2 species and corresponding (2,4), (4,5)

and (4,7) spaces were defined for the monomeric AlH species. The CASSCF calculations were found to systematically underestimate the BDE as the active spaces increased. This is somewhat unexpected behaviour but clearly arises due to the almost complete absence of dynamic correlation effects. Adding dynamic correlation in the form of CASPT2 and NEVPT2 improved the results, lying in the region 15-18.4 kcal mol⁻¹ depending on the active space used. The largest CASPT2(8,14) and NEVPT2(8,14) calculations give errors of 1.6-1.8 kcal mol⁻¹. Going beyond multi-reference perturbation theory, MRCI calculations with the same active spaces were also tested, with and without a Davidson size-consistency correction (+Q). The results were found to depend strongly on the Q correction, with accurate results only obtained when the correction was included and with the larger active spaces. Overall, the more elaborate CI treatment of dynamic correlation, however, improves upon CASPT2/NEVPT2, giving a BDE with chemical accuracy (0.5-0.7 kcal/mol error).

The above results highlight the importance of accounting for dynamic correlation reliably for the VBDE of Al₂H₂, and they also demonstrate that size-consistency is critical. Multi-reference methods, somewhat surprisingly, offer seemingly no advantages for describing Al₂H₂, at least not with respect to the bond dissociation energy. Single-reference coupled cluster theory overall seems to offer a reliable systematic convergence with respect to the FCI limit and CCSD(T) is capable of chemical accuracy of Al₂H₂ despite the small diradical character present. MP2 gives a smaller error than CCSD (both methods describe double excitations), which will be demonstrated to be due to some error cancellation (*vide infra*).

Following the assessment of single- and multi-reference based wavefunction methods, a range of density functionals were also tested to predict the VBDE of Al₂H₂.

3 - The Diradicaloid Electronic Structure of Dialumenes: a Benchmark Study at the Full CI Limit

Energies calculated using DFT are usually considered to be converged at the triple- ζ basis set level, whereas wavefunction based methods typically require going to larger basis sets to achieve satisfactory energy convergence. As a result, it would be problematic to compare the BDE calculated at the DFT/cc-pVTZ level of theory to the DMRG/cc-pVTZ Full-CI estimate. To account for this, a complete basis set (CBS) correction of 1.6 kcal mol⁻¹ was derived using extrapolation of CCSD(T) energies with cc-pVQZ and cc-pV5Z basis sets (Figure 3.3). Adding this CBS correction of +1.62 kcal mol⁻¹ to the FCI/cc-pVTZ result gives an estimate of the BDE at the DMRG/CBS limit of 18.4 kcal mol⁻¹, i.e. an effective FCI/CBS estimate.

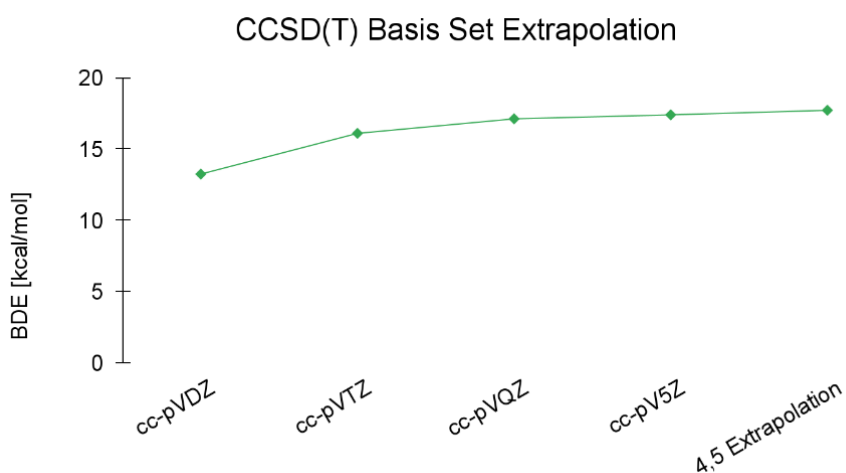


Figure 3.3: Convergence of the Al₂H₂ vertical bond dissociation energy at the RHF-CCSD(T) level as a function of basis set size. Also shown is a basis set extrapolation of the bond dissociation energy using the cc-pVQZ and cc-pV5Z energies. A TZ→CBS correction of 1.62 kcal/mol (i.e. BDE[4,5 Extrapolation] - BDE[cc-pVTZ]) can be derived from these values.

Using the FCI/CBS estimate of 18.4 kcal mol⁻¹ the density functionals for the VBDE (Figure 3.4) can be benchmarked. GGA and meta-GGA functionals (PBE, TPSS and r²SCAN) are found to significantly overestimate the VBDE (3.5-6.4 kcal mol⁻¹). By introducing a small amount (10%) of HF exchange to TPSS, i.e. (TPSSh), the situation

3 - The Diradicaloid Electronic Structure of Dialumenes: a Benchmark Study at the Full CI Limit

is somewhat improved, but an overestimation of $2.7 \text{ kcal mol}^{-1}$ is still observed. Hybrid functionals containing higher amounts of HF exchange (B3LYP, BHandHLYP, M06-2X and ω B97X-V) give VBDEs that instead underestimate the FCI/CBS estimate. Finally, double-hybrid functionals were also tested, B2PLYP and DSD-PBEP86, with the latter overall performing the best, giving a VBDE of $17.0 \text{ kcal mol}^{-1}$ (an underestimation of $1.4 \text{ kcal mol}^{-1}$).

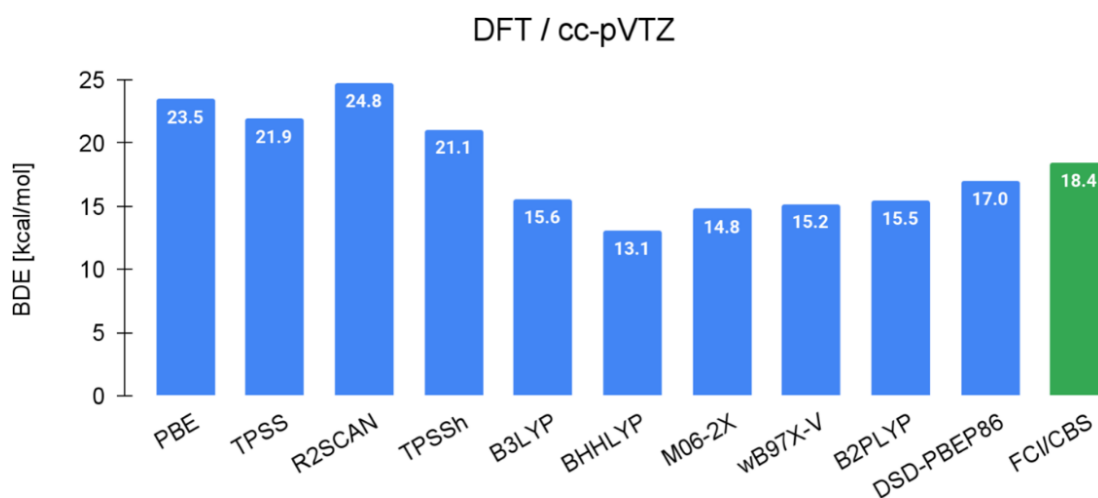


Figure 3.4: Performance of density functionals in predicting the bond dissociation energy of Al_2H_2 at the cc-pVTZ level. The DMRG(8,86)/CBS result is included as a reference, shown in green.

Overall, DFT performs rather poorly for all but the most computationally expensive classes of functionals. Only the double-hybrid functional DSD-PBEP86 can predict the VBDE with an acceptable error (although not quite reaching chemical accuracy). In addition to HF exchange, double-hybrid functionals contain a perturbative second-order correlation contribution, and as already observed, MP2 works surprisingly well to capture most of the dynamic correlation in this system.

So far, the performance of a range of WFT and DFT methods to predict the (vertical) bond dissociation energy of Al_2H_2 has been examined. This benchmark gives some insight into the performance of these methods in terms of describing the electronic structure of Al_2H_2 . However, limiting the comparison to a single reaction energy may not be representative of the overall electronic structure complexity. Previous theoretical analyses have revealed that dialumenes contain rather peculiar $\text{Al}=\text{Al}$ bonding features that might be visible via analysis of the electron density.^{61,69,213} A simple way of benchmarking the quality of the electron density would be to generate the density in real space at the highest possible level of theory and then compare against the density from simpler WF or DFT approximations. Here, it was instead chosen to perform difference density analyses by subtracting the electron density for each method from a reference RHF density. This choice has the advantage that the difference density directly reveals the effects of electron correlation (as single-determinant RHF is defined to have no electron correlation). All calculations utilized the cc-pVTZ basis set which was deemed large enough (this was confirmed by calculating $\text{RHF} \rightarrow \text{CCSD}$ difference density plots with multiple basis sets, see Figure 3.5) to give a reliable electron density (while the total energy will converge slower).

3 - The Diradicaloid Electronic Structure of Dialumenes: a Benchmark Study at the Full CI Limit

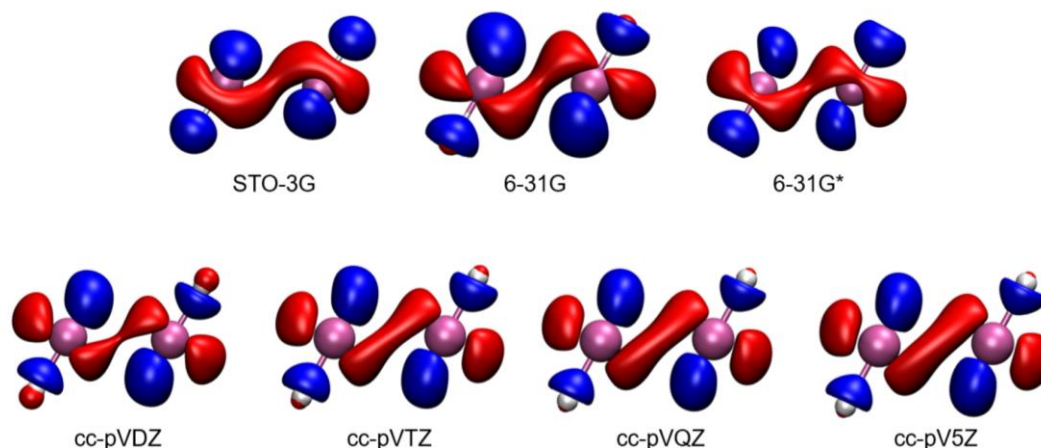


Figure 3.5: Convergence of the CCSD-RHF difference density for basis sets of increasing size/complexity. The difference density between the unrelaxed RHF-CCSD and RHF density was used to demonstrate the convergence of the difference density with respect to basis set size. Red indicates an accumulation of density w.r.t. RHF, and blue indicates a depletion of density (isovalue = ± 0.001).

As it was possible to calculate a DMRG wavefunction with a large M -value of 880 that showed reliable convergence to the FCI-limit for the VBDE, a RHF \rightarrow DMRG ($M=880$) difference density was deemed to be a reliable reference. However, it is noteworthy that all three Full-CI methods (DMRG, ICE-CI and SHCI) gave near identical estimates of the Full-CI density (Figure 3.6).

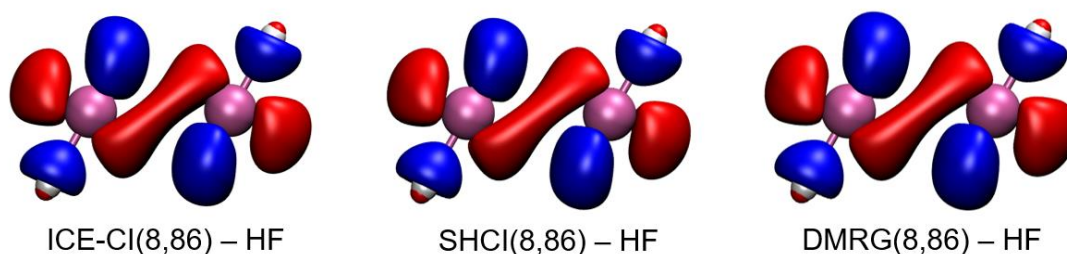


Figure 3.6: Comparison of difference density plots of DMRG ($M = 920$), SHCI($\epsilon = 6 \times 10^{-6}$) and ICE-CI($T_{\text{Gen}} = 4 \times 10^{-5}$) densities, relative to the RHF density. Red indicates an accumulation of density in going from RHF to ICE-CI/SHCI/DMRG while blue indicates a depletion of density (isovalue = ± 0.001).

Figure 3.7 shows the difference density plots for various WFT methods. Significant accumulation of density is found to occur in the bonding region between the Al centres, moving from the uncorrelated RHF WF to the correlated DMRG WF, accompanied by a depletion of density in the lone-pair regions of the aluminium centres as well as the Al–H bonds. This highlights the underbinding of the Al—Al bond by RHF. In comparison, MP2 performs moderately well, with the MP2-RHF difference density showing a similar accumulation and depletion of electron density as DMRG, with effects overall underestimated. The coupled cluster WFs are found to predict highly accurate density changes, with CCSD giving a density that is difficult to visually distinguish from the DMRG reference difference density. Negligible improvements are found by going to CCSD(T) and CCSDT densities, with essentially all densities being visually indistinguishable to the DMRG result. Moving to the multi-reference methods, a CASSCF(4,5) WF gives poor results, predicting only part of the expected density changes, and does so in an unbalanced manner. Increasing the size of the active space to an (8,14) active space, results in further changes but the changes appear somewhat unbalanced. Evidently, accounting for dynamic correlation (e.g. by CCSD) appears to be more important for a consistent treatment of the Al—Al bonding density than explicit treatment of static correlation (as predicted by CASSCF). Accounting for dynamic correlation in a multi-reference WF, i.e. MRCI+Q considerably improves the CASSCF result, as expected.

3 - The Diradicaloid Electronic Structure of Dialumenes: a Benchmark Study at the Full CI Limit

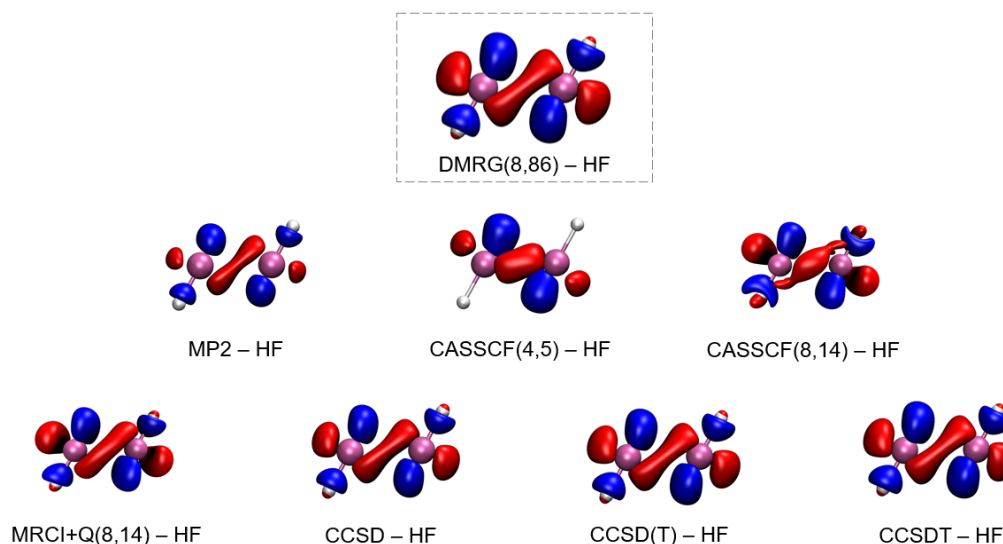


Figure 3.7: Difference density isosurface plots calculated using various correlated WFT methods using the cc-pVTZ basis set, with respect to RHF. An isovalue of 0.001 a.u. was used where the color coding indicates accumulation (red) and depletion (blue) of density w.r.t RHF level. The DMRG density used an M value of 880. Unrelaxed densities were utilized for CCSD, CCSD(T) and CCSDT.

Next, the various density functional approximations were tested. Overall, the quality of the difference densities for all functionals tested was poor compared to the WFT methods, as shown in Figure 3.8. The (meta)-GGA functionals perform best (TPSS in particular), correctly predicting some accumulation of density in the bonding region between the Al atoms and concomitantly partial density depletion from lone pairs and Al—H bonds. However, additional density accumulation around each Al atom is predicted, inconsistent with the DMRG reference. While the TPSSh hybrid description remains qualitatively similar, hybrid functionals with larger amounts of HF exchange lead to less Al—Al bonding density with BHHLYP and M06-2X giving particularly poor descriptions. The range-separated hybrid functional ω B97X-V, one of the best performers for main group thermochemistry¹⁶⁷, performs surprisingly poorly with flawed behaviour in the bonding and lone pair regions. Finally, the double-hybrid functional DSD-PBEP86, was tested, which gave comparable results to PBE, TPSS

3 - The Diradicaloid Electronic Structure of Dialumenes: a Benchmark Study at the Full CI Limit

and TPSSh, highlighting once again the favourable correlation effects from second-order perturbation theory, in line with the moderately good performance of MP2.

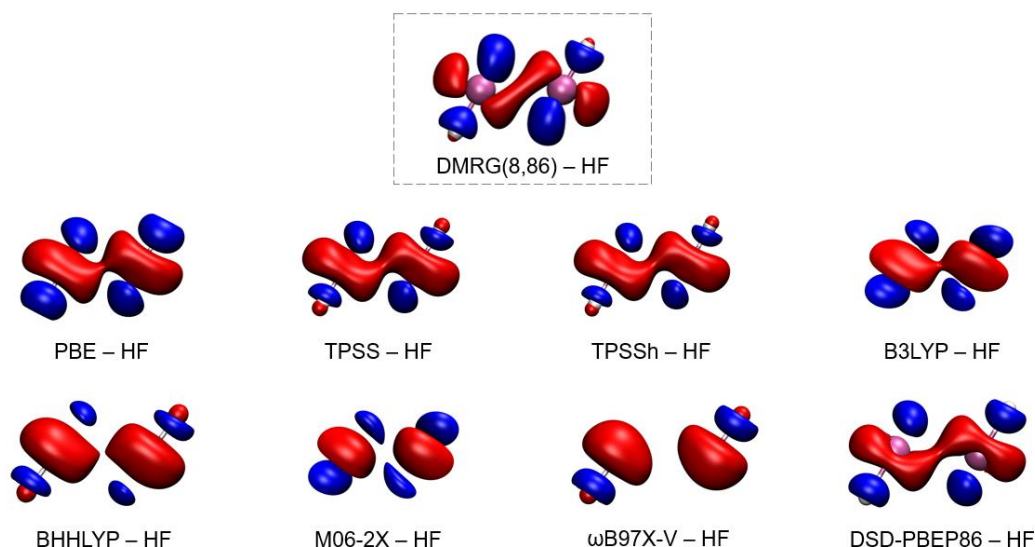


Figure 3.8: Difference density plots of various density functionals, using the RHF density as a reference density. Red indicates an accumulation of density, and blue indicates a depletion of density (isovalue = 0.001 a.u.).

The difference density analysis nicely demonstrates the behaviour of different WF expansions in predicting the correct electronic structure associated with bonding in dialumenes. While difference densities can be quantitatively distinguished by a simple metric such as e.g. integrating over the positive differences, this has the considerable drawback of not distinguishing between the core and valence of the electron density. Previous work has also found such a metric to not be entirely suitable when evaluating density functionals.²¹⁴ Since dialumenes possess particular bonding features, it would be useful to employ quantitative density-based analysis that is sensitive to these features.

A criterion to distinguish so-called classical and non-classical or “slipped” multiple bonds has previously been established by Grützmacher and Fässler²¹³, by using the electron localisation function (ELF). This method was also utilised by Tuononen to investigate the electronic structure of the Group 13 dimetallenes.⁶⁹ Furthermore, in Chapter 4, this method will be utilised to characterise the bonding situation present in the amidophosphine-stabilised dialumene reported by Cowley, as well as two related base-stabilised dialumenes that have been reported by Inoue.^{23,59,61} The ELF function describes the probability of finding two electrons of the same spin in the vicinity of each other (hence reflecting the Pauli principle). Where this probability is calculated to be small, electrons are found to be localised. As a result, electrons of opposite spin can be found in the same location, or in other words, the ELF function provides a means of dividing the valence electron density into bonding and non-bonding pairs (lone pairs). By integrating over these regions of electron density, known as basins, it is possible to determine the number of electrons associated with a particular basin. Local maxima within these basins are referred to as attractors.

ELF isosurfaces were generated for all WFT and DFT methods. In the case of WFT methods, they were generated by Multiwfn through the use of the natural orbitals of each method (via generated Molden files from each program). The ELF isosurface of Al_2H_2 for selected WFT and DFT methods can be found in Figure 3.10 and Figure 3.11, respectively, with the populations of the attractors indicated, along with the basin volumes (in units of \AA^3). As previously found by Tuononen, at the B3LYP/cc-pVTZ level of theory⁶⁹ and from our own work⁶¹, the methods used predict there to be three valence attractors in total. Two of these can be classified as non-bonding electron density localised close to the aluminium centres (A1 and A2). The third attractor is found along the bond axis between the two aluminium centres and can be classified as bonding (A3). Interestingly the shape of the ELF isosurface is virtually

3 - The Diradicaloid Electronic Structure of Dialumenes: a Benchmark Study at the Full CI Limit

indistinguishable between methods when plotted using a typical isovalue of 0.8 a.u. (as has been previously observed²¹⁵), but importantly the populations and volumes of the individual basins differ considerably for each method, and this hence allows the quality of the relevant valence density features from each method to be assessed.

The ELF calculated using the DMRG/cc-pVTZ density was taken as the Full-CI estimate to compare all other methods to. However, further ELF plots calculated with SHCI and ICE-Cl are shown in Figure 3.9 for comparison. On inspection the plots are overall very similar, but DMRG was deemed to be closest to the FCI limit.

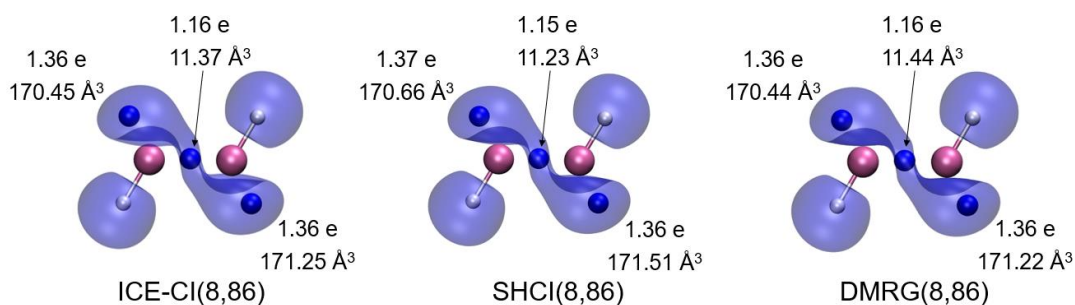


Figure 3.9: Plots of the electron localisation function for DMRG ($M = 920$), SHCI($\epsilon = 6 \times 10^{-6}$) and ICE-Cl($T_{\text{Gen}} = 4 \times 10^{-5}$) (isovalue = 0.80). Relevant attractors are shown as blue spheres, and their electron populations and volumes are given, in units of electrons and cubed angstroms, respectively.

Attractors A1 and A2 were found to have electron populations of 1.36, and attractor A3 was found to have a population of 1.16 electrons. Going to RHF (Figure 3.10), a significant reduction in the population of A3 and a concomitant increase in the populations of A1 and A2 was observed. This is unsurprising, given the results thus far: RHF severely underestimates the BDE and does not describe the density in the bonding region well, predicting more of a localised lone-pair picture of the aluminium centres. MP2 gives a major improvement over RHF, predicting a population of 0.86

3 - The Diradicaloid Electronic Structure of Dialumenes: a Benchmark Study at the Full CI Limit

electrons for attractor A3, but still underestimates the bonding. This moderately good performance of MP2 is in line with the BDE and difference density results. Coupled cluster theory once again gives excellent results, with CCSD(T) predicting highly similar attractor populations and volumes to the DMRG ELF populations, with CCSDT providing negligible improvement. CCSD is also very accurate, clearly more so than MP2, in contrast to the BDE analysis. This suggests that the better performance of MP2 for the BDE (as well as for the geometry as discussed by Tuononen⁶⁹) arises from error cancellations. The multi-reference method MRCI+Q(8,14) as well as CASSCF(8,14) also give results in very good agreement with the DMRG results.

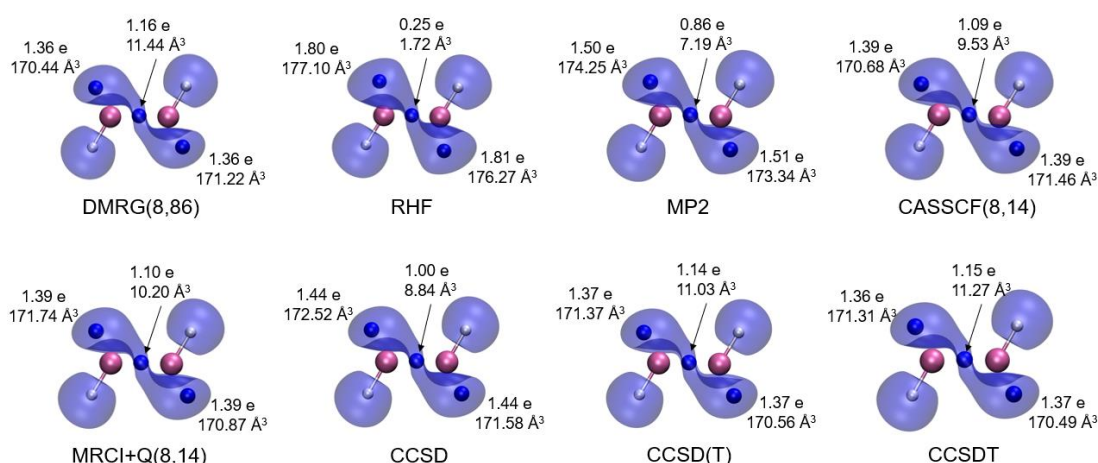


Figure 3.10: Plots of the electron localisation function for various correlated wavefunction theory methods (isovalue = 0.80). Relevant attractors are shown as blue spheres, and their electron populations and volumes are given. Unrelaxed densities were used for the coupled cluster plots.

Moving on to DFT, four functionals (TPSS, B3LYP, M06-2X and DSD-PBEP86) were chosen that contain increasing amounts of HF exchange (0%, 20%, 54% and 72%, respectively). As the ELF plots in Figure 3.11 reveal, as the percentage of HF exchange is increased (up to M06-2X), more localisation onto the aluminium centres is observed, with B3LYP agreeing very well with the previously calculated values from

3 - The Diradicaloid Electronic Structure of Dialumenes: a Benchmark Study at the Full CI Limit

Tuononen.⁶⁹ However, upon going to DSD-PBEP86 (72% HF exchange), similar results to B3LYP are obtained. This is consistent with the difference density analysis above, where the favourable correlation effects from second-order perturbation theory once again come into effect. M06-2X, in line with the difference density analysis, is found to predict poor attractor populations, not so far off the RHF values. Additionally, M06-2X predicts multiple attractors in the A3 bonding region. The reasons for this are not entirely clear (perhaps due to the parameterized nature of this functional), but the results are otherwise in line with the findings from the other electronic structure analyses, and so these attractors were treated as one, given their proximity to each other.

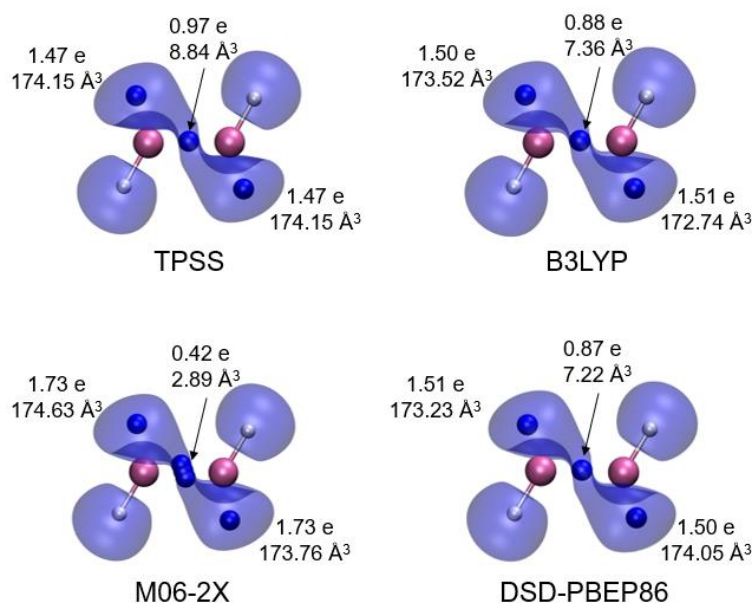


Figure 3.11: Plots of the electron localisation function for selected density functionals having increasing levels of HF exchange (isovalue = 0.80). Relevant attractors are shown as blue spheres, and their electron populations and volumes are given.

As the analyses of the difference density and ELF demonstrate, the tested density functional approximations struggle to give a fully satisfactory description of the electron density of Al_2H_2 , particularly as it relates to the Al—Al bonding. Pure functionals such as TPSS appear to come closest to a correct picture, while hybrid functionals perform notably worse overall. Meanwhile, the WFT-based methods are capable of systematically converging towards the exact result as shown for the difference densities, ELF plots, and the bond dissociation energy (BDE). Encouragingly CCSD(T) is capable of a near-perfect treatment of the electron density (as seen via difference densities and ELF-plots) and reaches chemical accuracy for the BDE (error of $0.7 \text{ kcal mol}^{-1}$).

It would be desirable to get additional insights into how density-based errors as revealed by the difference density and ELF plots translate into energetic errors. Work by Burke and coworkers²¹⁶ has shown that it is possible to divide energetic errors from a density functional approximation (DFA), with respect to the exact result, into density-driven and functional-driven components. A sizeable density-driven error (DE), suggests that the self-consistent DFA is creating artefacts in the density while the functional-error (FE) accounts for the remaining energetic error with respect to the exact energy. The FE and DE are defined by the equations:

$$\begin{aligned}\Delta E_{DFA} &= E_{DFA}[n_{DFA}] - E_{\text{exact}}[n_{\text{exact}}] = FE + DE \\ FE &= E_{DFA}[n_{\text{exact}}] - E_{\text{exact}}[n_{\text{exact}}] \\ DE &= E_{DFA}[n_{DFA}] - E_{DFA}[n_{\text{exact}}]\end{aligned}\tag{3.3}$$

where E_{exact} and n_{exact} refers to the exact energy and density (i.e. Full-CI/CBS). The $E_{DFA}[n_{\text{exact}}]$ term is the most difficult term to calculate as it refers to a non-self-consistent DFA calculation using an exact density. Calculating this term requires solving an inverse Kohn-Sham problem for the exact density and using the resulting

MOs to perform a non-self-consistent calculation with the DFA. In this work the inverse Kohn-Sham problem was solved using the Wu-Yang method²¹⁷ as implemented in the KSpies library.²¹⁸ The DMRG/cc-pVTZ density was used as an approximation to the exact density (n_{exact}). The E_{exact} term was estimated as the sum of DMRG/cc-pVTZ energy and a CCSD(T)/CBS(4,5) basis set correction.

FE and DE analysis was performed for the various density functional approximations for the Al_2H_2 bond dissociation energy reaction. The results are shown in Figure 3.12 and Table 3.2. Overall, it is revealed, unsurprisingly, that the FE is primarily responsible for the error in BDE with the DE error being substantially less. Functionals like TPSS that gave difference density plots and ELF populations closer to the FCI reference are found to have a negligible DE ($-0.03 \text{ kcal mol}^{-1}$), suggesting that the visible real-space density error of TPSS (Figure 3.8) does not translate into a major problem when evaluating energies. Evidently, the functional error ($3.55 \text{ kcal mol}^{-1}$) dominates. Furthermore, the hybrid TPSSh, PBE0 and B3LYP functionals lead to even smaller FEs (between -2.5 and $+2.5 \text{ kcal mol}^{-1}$) while maintaining a relatively small DE (-0.2 to $+0.2 \text{ kcal mol}^{-1}$). Functionals with $>50 \%$ HF exchange such as BHLYP and M06-2X or the range-separated hybrid wB97X-V, however, lead to larger DEs (1.1 - $1.5 \text{ kcal mol}^{-1}$) suggesting these functionals are introducing artefacts to the electron density that will affect reaction energies (in different ways depending on the reaction).

3 - The Diradicaloid Electronic Structure of Dialumenes: a Benchmark Study at the Full CI Limit

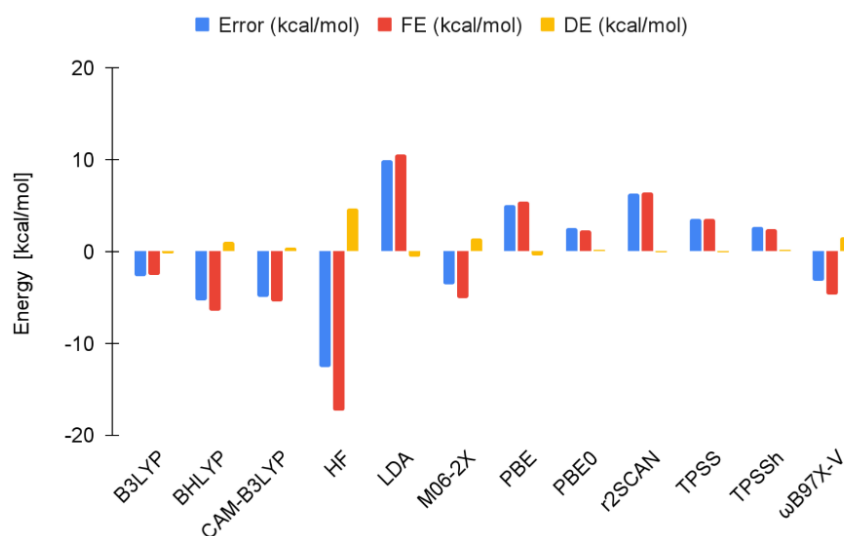


Figure 3.12: Plot of the total BDE errors (w.r.t. the FCI/CBS estimate) and the decomposed functional-driven errors (FE) and density-driven errors (DE).

Both ω B97X-V and M06-2X have relatively small BDE errors (-3.25 and -3.63 kcal mol $^{-1}$) on par with the TPSS functional ($+3.5$ kcal mol $^{-1}$) but these reaction-energy errors arise from error cancellations of large negative FEs (-4.76 and -5.05 kcal mol $^{-1}$) and sizeable DEs ($+1.51$ and $+1.41$ kcal mol $^{-1}$). Finally, perhaps unsurprisingly, the HF method gives the largest DE ($+4.73$ kcal mol $^{-1}$) and the largest FE (-17.3 kcal mol $^{-1}$), which is overall correlated with the inability of HF to give acceptable difference densities and ELF plots, as well as accurate BDEs.

3 - The Diradicaloid Electronic Structure of Dialumenes: a Benchmark Study at the Full CI Limit

Table 3.2: Data used to plot the total BDE errors (w.r.t. the FCI/CBS estimate) and the decomposed functional-driven errors (FE) and density-driven errors (DE).

Method	Error (kcal/mol)	FE (kcal/mol)	DE (kcal/mol)
B3LYP	-2.73	-2.53	-0.20
BHLYP	-5.36	-6.45	1.09
CAM-B3LYP	-5.00	-5.43	0.42
HF	-12.57	-17.30	4.73
LDA	9.99	10.55	-0.56
M06-2X	-3.63	-5.05	1.42
PBE	5.04	5.48	-0.44
PBE0	2.59	2.37	0.22
r2SCAN	6.36	6.39	-0.03
TPSS	3.52	3.55	-0.03
TPSSh	2.65	2.47	0.18
ωB97X-V	-3.25	-4.76	1.51

Overall, the decomposition of the BDE error into density-driven and functional-driven errors is found to be quite revealing of the deficiency of DFAs. It is clearly insufficient to simply look at reaction energies such as the BDE alone for determining whether a functional is describing a molecule accurately.

Finally, the topic of quantifying diradical character in dialumenes will be discussed. As previously outlined by Tuononen and coworkers, diradical character can be quantified using e.g. the CI coefficients of a CI/CASSCF wavefunction or, alternatively, natural orbital occupations of a correlated density matrix. Tuononen performed CASSCF

3 - The Diradicaloid Electronic Structure of Dialumenes: a Benchmark Study at the Full CI Limit

calculations at the CAS(4,5) level with a cc-pVTZ basis set and found a 14 % diradical character based on the CI coefficient metric of the diradical configuration. In this present work, larger active space CASSCF calculations at the ICE-CASSCF level were explored (Figure 3.13).

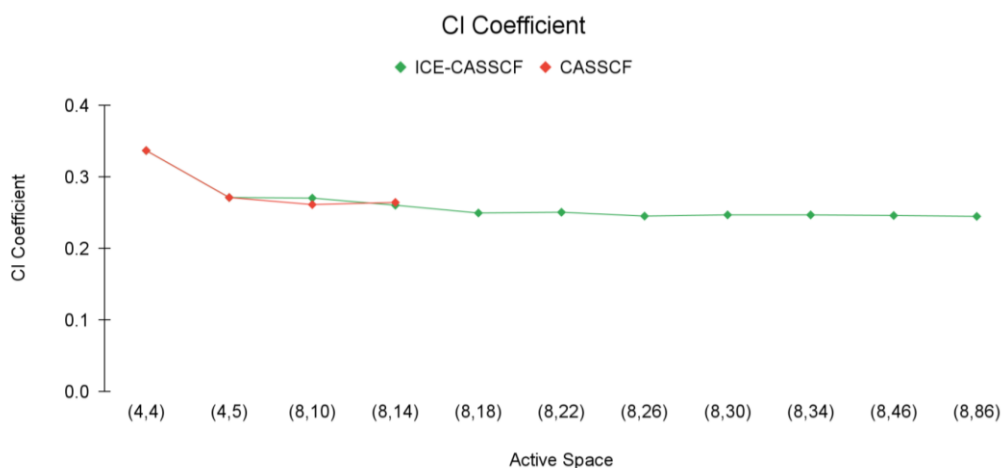


Figure 3.13: Variation of the diradical character of Al_2H_2 , measured via the CI coefficient, as a function of increasing active space in CASSCF and ICE-CASSCF calculations. The ICE-CI Full-CI algorithm was used as a replacement for regular Full-CI algorithm in standard CASSCF, using a T_{Gen} value of 10^{-4} .

In the regular CASSCF calculations, a decreasing trend is observed upon going from a (4,4) active space to a (8,14) active space, with the calculations reproducing Tuononen's CASSCF(4,5) results. Increasing the (4,5) active space to (8,10) or (8,14) led to a small decrease in the CI coefficient by approximately 0.01. The ICE-CI approximation (T_{Gen} threshold of 1×10^{-4}) was found to reproduce the small active space CASSCF results well. The largest calculation performed features the full CAS(8,86) active space and a T_{Gen} threshold of $T_{\text{Gen}} = 1 \times 10^{-4}$, likely very close to the Full-CI limit. A 12% diradical character was predicted using this active space. This corresponds to approximately a 2%-value decrease in diradical character, in comparison to the results obtained when using a (4,5) active space.

3 - The Diradicaloid Electronic Structure of Dialumenes: a Benchmark Study at the Full CI Limit

Natural-orbital based metrics, based on either the occupation of the primary virtual orbital, or a more general polyradical metric such as the one proposed by Head-Gordon²¹⁹ are in a sense preferable as the metrics can be transferable across different WF definitions. They do require, however, diagonalization of the 1-particle density matrix (not always available) and perfect correlation between different metrics is not always found. Analysis of the natural orbital shapes and their occupation numbers do have the advantage of revealing insights into the behaviour of different WFs to describe the diradical character. Natural orbitals obtained by diagonalizing DMRG, SHCI and ICE-CI density matrices were found to be near-identical and can be taken as reference Full-CI quality NOs (Figure 3.14). CCSD(T) natural orbitals were found to be an excellent approximation to them.

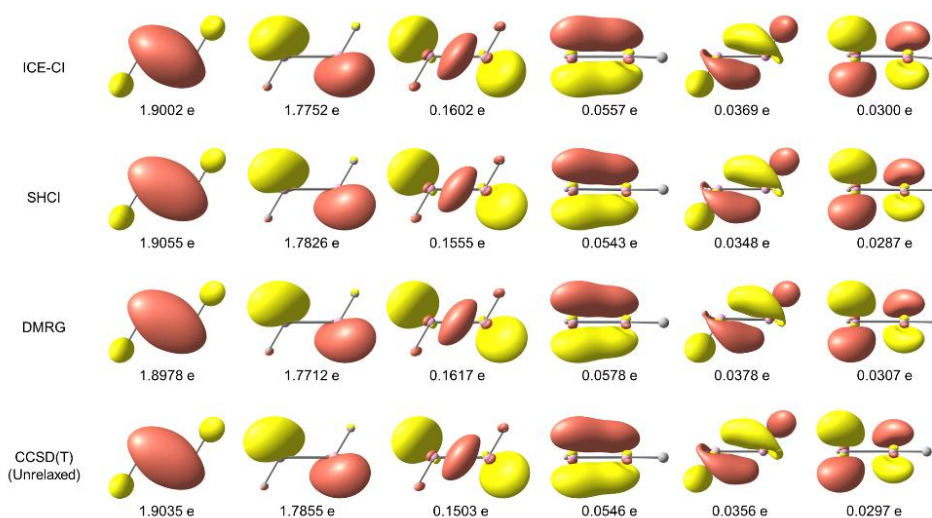


Figure 3.14: Visualisation of selected natural orbitals of Al_2H_2 , with occupations shown below each orbitals, for DMRG ($M = 920$), SHCI($\epsilon = 6 \times 10^{-6}$), ICE-CI($T_{\text{Gen}} = 4 \times 10^{-5}$) and CCSD(T) (unrelaxed density). The orbitals were visualised using an isovalue of 0.05 a.u..

These metrics for diradical character, however, require correlated wavefunction calculations (and for non-variational methods, an approximation to the density) which

are not always feasible options for studying larger molecules (synthetic dialumenes generally feature bulky ligands). Furthermore, neither a CI-based nor NO-based metric is compatible with a DFT-based treatment. In light of this the fractional occupation number weighted density (FOD) approach was explored, as proposed by Grimme and Hansen, which was designed as a robust and cheap method to obtain information on “hot” or strongly correlated electrons in a molecule.^{209,220} This method utilizes finite-temperature fractional occupation DFT, where the visualization of the FOD in real space affords an intuitive picture of localized polyradical character in a molecule. Furthermore, integration of FOD in real space, affords a single number that can be interpreted as a metric for polyradical character.

To demonstrate the suitability of FOD as a diradical metric, FOD-values were calculated for hydride and methyl-substituted transient Group 13 dimetallenes using TPSS and a smearing temperature of 5000 K, as shown in Figure 3.15a. In agreement with Tuonenen’s previous findings, the diradical character decreases as Group 13 is descended and the FOD-numbers are found to correlate well with the CCSD NO occupations (Figure 3.15b).

3 - The Diradicaloid Electronic Structure of Dialumenes: a Benchmark Study at the Full CI Limit

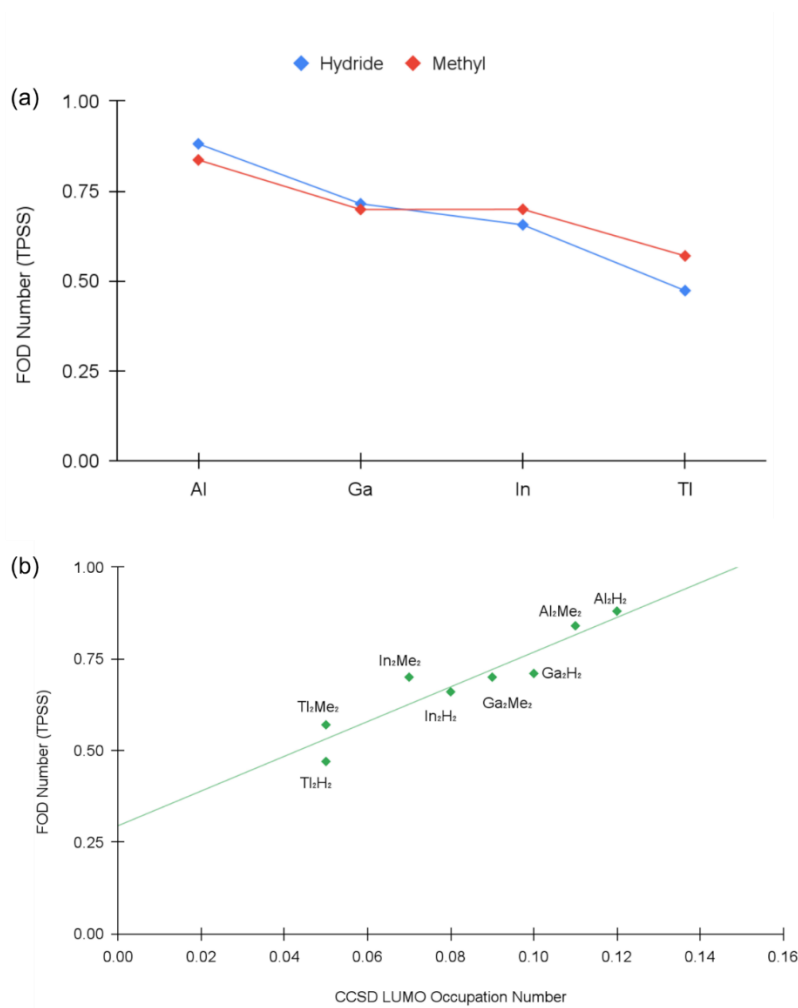
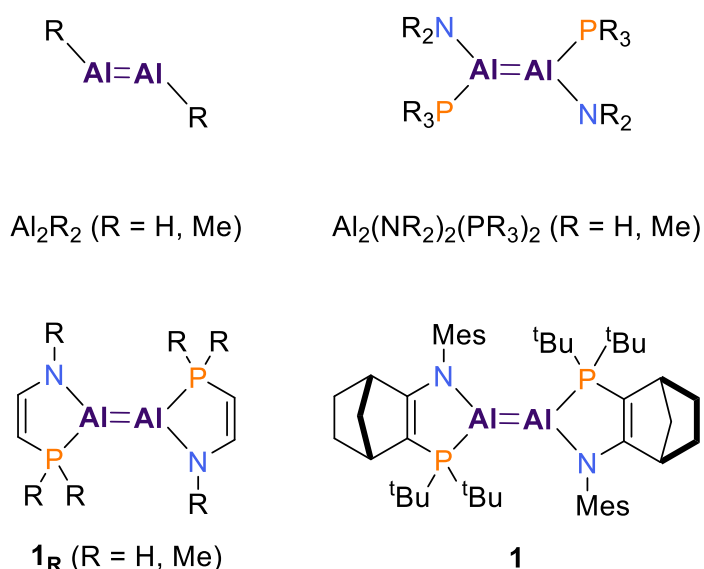


Figure 3.15: (a) Diradical character of the hydride- and methyl-substituted group 13 dimetallenes, measured via the calculation of the number of “hot” electrons, the FOD number (N^{FOD}). The FOD analysis was carried out at the FT-TPSS/def2-TZVP ($T_{\text{el}} = 5000$ K) level of theory. (b) Scatter plot showing correlation of the TPSS-calculated FOD number with the natural occupation of the LUMO calculated at the CCSD (unrelaxed density) level, for the same transient group 13 dimetallenes studied.

These results for the transient dimetallenes are encouraging, as the calculation of the FOD number is far cheaper than the correlated wavefunction methods tested thus far. Although the diradical metrics calculated using the correlated methods are informative at the fundamental electronic structure level, they are not easily extendable to more synthetically realistic systems. The FOD number, on the other hand, can in principle be utilised for any species that can be treated at the DFT-level of theory.²⁰⁹

3 - The Diradicaloid Electronic Structure of Dialumenes: a Benchmark Study at the Full CI Limit

So far, there have only been three examples of base-stabilised dialumenes, and a single example of a base-free dialumene.^{23,59,61,66} Using these as a structural reference point, five model base-stabilised dialumenes (Scheme 3.1) were optimised. These models increased in size and build up to the full system reported by Cowley, **1**, which has an experimental Al=Al bond length of 2.5190(14) Å, taken from the X-ray crystal structure.⁶¹ The transient dialumenes discussed above (Al₂H₂ and Al₂Me₂) were also included for comparison, making a total of seven dialumenes included in this analysis.



Scheme 3.1: Set of dialumenes (transient and base-stabilised) that were studied (Mes = 2,4,6-trimethylphenyl).

The set of seven dialumenes (transient and base-stabilised) were optimised using various DFT methods, with and without dispersion corrections. The Al—Al bond distances are shown in Table 3.3. The Al—Al distance in the dialumenes is found to depend primarily on the ligand, becoming shorter with increased ligand size. Overall, for Al₂H₂, all methods are capable of satisfactory accuracy (compared to a reference

3 - The Diradicaloid Electronic Structure of Dialumenes: a Benchmark Study at the Full CI Limit

value of 2.644 Å, estimated from ICE-CI, see Table 3.5). This reveals that the behaviour of different methods for capturing diradical character or electron density does not translate into appreciably different structural parameters. For the larger dialumenes, however, a larger difference between methods can be seen (compare e.g. TPSS vs. TPSS-D), revealing that treatment of dispersion becomes more important for accurately capturing the local structure of large dialumenes. M06-2X is known to be capable of treating some dispersion directly via its functional form, which explains its satisfactory performance for larger dialumenes, even when employed without a dispersion correction.

Table 3.3: Comparison of the Al-Al bond distance [Å] of the dialumenes in Scheme S1, optimised using three functionals of increasing HF exchange, with and without dispersion.

Structure	TPSS	TPSS-D3	B3LYP	B3LYP-D3	M06-2X	M06-2X-D3
Al₂H₂	2.646	2.644	2.677	2.673	2.669	2.670
Al₂Me₂	2.698	2.691	2.748	2.735	2.758	2.758
Al₂(NH₂)₂(PH₃)₂	2.631	2.636	^a	^a	^a	^a
Al₂(NMe₂)₂(PMe₃)₂	2.591	2.585	2.618	2.603	2.632	2.633
1_H	2.580	2.572	2.642	2.625	2.655	2.655
1_{Me}	2.551	2.540	2.580	2.561	2.581	2.579
1	2.563	2.516	2.595	2.527	2.536	2.535

^a Complete dissociation of the base from the dialumene, PH₃, occurred when attempting to optimize the geometries using the two hybrid functionals.

Table 3.4 compares MP2 calculations (DLPNO-MP2 for the full complex **1**) for dialumenes of increasing size as well as CCSD and CCSD(T) calculations for the smaller Al₂H₂ and Al₂Me₂ species. There is overall good agreement between MP2 and

3 - The Diradicaloid Electronic Structure of Dialumenes: a Benchmark Study at the Full CI Limit

CCSD(T) for Al_2H_2 that one would expect MP2 to be a reasonably accurate structural optimization method for the larger complexes. For the full complex **1** there is also good agreement between DLPNO-MP2 and the dispersion-corrected DFT methods. For Al_2H_2 , higher-order CC calculations at the CCSDT level of theory were additionally carried out, which reduced the Al-Al bond length to 2.647 Å.

Table 3.4: Comparison of the Al-Al bond distance [Å] of the studied dialumenes, optimised using MP2, CCSD and CCSD(T), where feasible. The geometry optimizations were carried out using the cc-pVTZ basis set.

Structure	MP2	CCSD	CCSD(T)	CCSDT
Al_2H_2	2.651	2.657	2.654	2.647
Al_2Me_2	2.715	2.723	2.700	-
$\text{Al}_2(\text{NH}_2)_2(\text{PH}_3)_2$	2.627	-	-	-
$\text{Al}_2(\text{NMe}_2)_2(\text{PMe}_3)_2$	2.565	-	-	-
1_H	2.590	-	-	-
1_{Me}	2.537	-	-	-
1	^a 2.515	-	-	-

^aThe DLPNO-MP2 approximation was employed, and the C & H atoms were treated with the cc-pVDZ basis set to reduce computational cost.

In order to estimate the Al-Al bond length in the Full-CI limit (with the cc-pVTZ basis set), ICE-CI-CASSCF geometry optimizations were also carried out. This was done by performing CASSCF calculations using a complete orbital space (within the frozen-core approximation) of CAS(8,86) but using the ICE-CI selected-CI solver instead of exact Full-CI solver and varying the T_{Gen} selection threshold systematically. The ICE-CI CASSCF calculations were found to converge convincingly with decreasing T_{Gen}

3 - The Diradicaloid Electronic Structure of Dialumenes: a Benchmark Study at the Full CI Limit

threshold, to give an optimized Al-Al bond length of 2.644 Å at $T_{\text{gen}} = 7 \times 10^{-4}$ that remained unchanged at $T_{\text{Gen}} = 2 \times 10^{-4}$. The 2.644 Å bond length is estimated to be of Full-CI/cc-pVTZ quality.

Table 3.5: Comparison of the Al-Al bond length [Å] of Al_2H_2 calculated with ICE-CI-CASSCF with a full orbital space (within frozen-core approximation) of CAS(8,86) and with varying T_{Gen} thresholds.

T_{Gen}	Al-Al bond length (Å)
5E-1	2.643
1E-1	2.642
5E-2	2.642
1E-2	2.644
5E-3	2.643
1E-3	2.643
7E-4	2.644
5E-4	2.644
4E-4	2.644
3E-4	2.644
2E-4	2.644

Having determined a test set of suitable dialumenes, the FOD analysis was carried out (Figure 3.16). Starting with the smallest base-stabilised dialumene, $\text{Al}_2(\text{NH}_2)_2(\text{PH}_3)_2$, a relatively low FOD number of 0.48 was calculated. This increased to 0.62 upon introducing slightly larger methyl substituents. Moving to the dialumene model systems, featuring the bidentate amidophosphine backbone, a steady increase in the FOD numbers was observed, with values of 0.66, 0.73 and 0.90 being

3 - The Diradicaloid Electronic Structure of Dialumenes: a Benchmark Study at the Full CI Limit

calculated for **1_H**, **1_{Me}** and **1**, respectively. Perhaps most strikingly, the FOD number calculated for **1** is very similar to that calculated for Al_2H_2 . Visualization of the FOD for Al_2H_2 and **1** (Figure 15b) reveals relatively similar isosurface shapes, suggesting similar localization of “hot” electrons and demonstrates the overall relevance of Al_2H_2 as a useful model system for this chemistry.

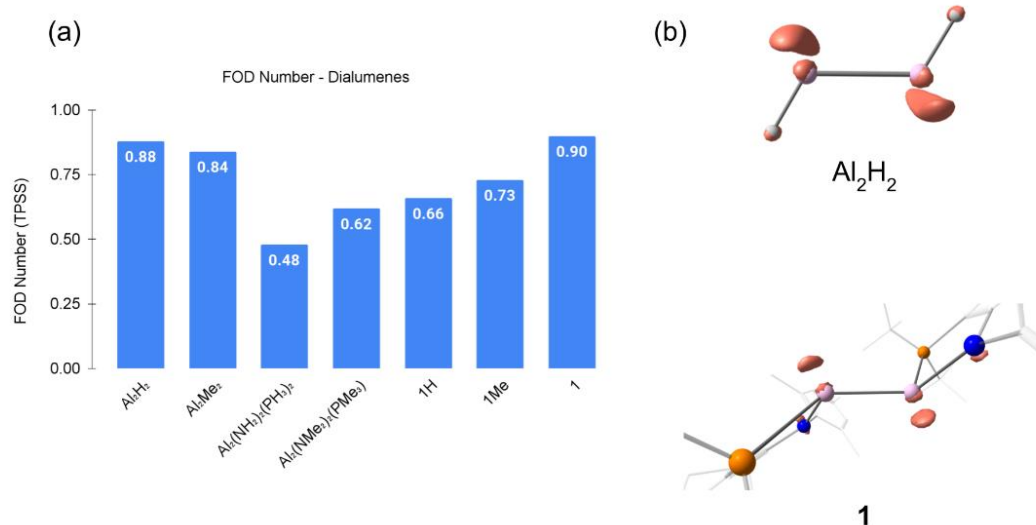


Figure 3.16: (a) Diradical character of the transient and base-stabilised dialumenes, measured via the calculation of the number of “hot” electrons, the FOD number (N^{FOD}). (b) Visualisation of the fractional occupation weighted density at an isovalue of 0.005 a.u. and a grid of 120. The FOD analysis was carried out at the FT-TPSS/def2-TZVP ($T_{\text{el}} = 5000$ K) level of theory.

3.4 Conclusions

An extensive theoretical study was performed on Al_2H_2 , the simplest dialumene. By systematically expanding the wavefunction from a single determinant (RHF) towards an effective Full-CI limit (via DMRG and selected CI approaches) near-exact reference values of the bond dissociation energy as well as properties of the electron

3 - The Diradicaloid Electronic Structure of Dialumenes: a Benchmark Study at the Full CI Limit

density and electron localization function were established. This further allowed a comparison of single-reference WF methods against these properties. Despite the sizeable diradical character present in Al_2H_2 , single-reference coupled cluster theory performs well and CCSD(T) is capable of chemical accuracy for the bond dissociation energy while properties of the density are indistinguishable from the FCI estimates. MP2 performs overall well, better than CCSD for the BDE, however, this must arise from error cancellations in view of the worse Al_2H_2 density seen for MP2. Multi-reference methods are found to offer no advantages over single-reference methods. The importance of the reference determinant in coupled cluster calculations was investigated, the closed-shell RHF determinant was preferred (despite its instability), while a broken-symmetry UHF determinant was found not to be suitable.

Density functional theory methods displayed mixed performance for Al_2H_2 . No functional predicted the BDE satisfactorily, with non-hybrid functionals overestimating and hybrid functionals underestimating it. Interestingly, however, non-hybrid functionals such as TPSS came the closest to capturing the electron density correctly as seen by comparisons of difference density plots and ELF analysis. Furthermore, decomposition of the BDE revealed that non-hybrid functionals give very little density-driven error in comparison to hybrid functionals.

Overall, this analysis would justify the use of non-hybrid functionals such as TPSS for studying dialumenes, in particular the calculations of molecular and electronic structures, while keeping in mind that total energies and hence relative energies may not be very accurate and are best supplemented with single-point coupled cluster calculations (at the CCSD(T) level, with local correlation approximations such as DLPNO when suitable). The combination of TPSS with fractional occupation density

(FOD) is furthermore found to be a cost-effective and useful way of quantifying diradical character in dialumenes, revealing similar trends as a NO-based CCSD metric.

While M06-2X has been a popular functional choice for main group chemistry, including aluminium chemistry, these results suggest that the functional is not describing the electronic structure of the simplest dialumene correctly and is thus unlikely to give correct results for the right reason. Similar problems could be found for the ω B97X-V functional, one of the best performers in recent main group chemistry energy benchmarking.¹⁶⁷ The good track-record of M06-2X in predicting accurate geometries of bulky dialumenes is likely rooted in its capability of describing much of the dispersion effect (without requiring pairwise corrections such as D3/D4), an important aspect of molecules containing bulky ligands.

Finally, one might speculate that the strong focus in recent years on putting the reaction energy front and center when benchmarking density functionals may lead to misleading conclusions about the generalizability and transferability of such benchmarking for molecules with complex electronic structure. The Al_2H_2 compound is small but features considerable electronic structure complexity, which is representative of dialumenes and related congeners in general. As discussed, neither the bond dissociation energy nor geometry is revealing much of the capability of an electronic structure method to capture the correct electronic structure. Recent studies have suggested that many modern density functionals with a track-record for improved energy predictions do not always predict a satisfactory density as well.^{221,222} More systematic benchmarking studies of electron densities of small molecules would be desirable and such studies are starting to appear.^{223–229}

4 Characterisation of a Base-stabilised Dialumene

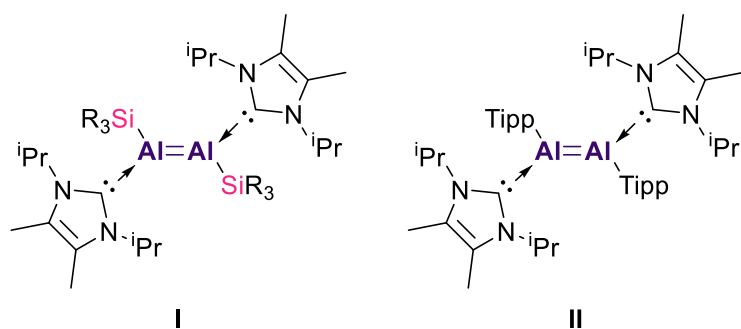
4.1 Introduction

As discussed in Chapter 1, there has been significant progress over the last thirty years or so in overcoming the thermodynamic challenges associated with accessing stable aluminium(I) species. Prototypical neutral compounds such as Schnökel's tetrameric $(\text{Cp}^*\text{Al})_4$ complex and Roesky's NacNacAl(I) species^{43,50} have been more recently complemented by the anionic Al(I) carbene analogues, the anionic aluminyll complexes.^{78,230,231} Sitting alongside these, there exists another class of neutral Al(I) compound, the dialumenes, which are species containing an Al=Al double bond.

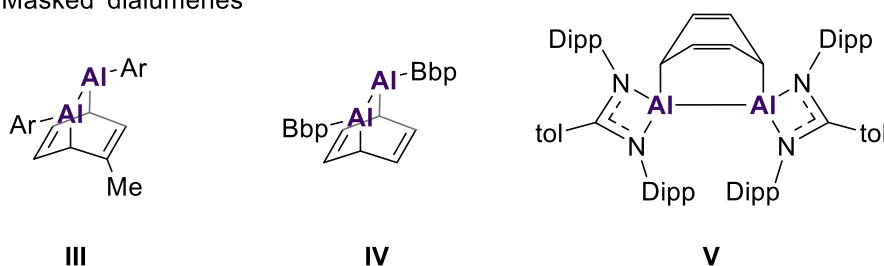
Dialumenes can be split into two categories, free and base stabilised. Although reviewed already, a brief recap is given here for context. Prior to this present work, Inoue and co-workers have reported two examples of base-stabilised dialumenes, of the general formula $(\text{L})\text{RAI}=\text{AIR}(\text{L})$ (L = coordinating base) (Figure 4.1). The first of these, **I**, was a silyl substituted dialumene, stabilised by an N-heterocyclic carbene.²³ An aryl analogue, **II**, was reported three years later.⁵⁹ There have also been reports of so-called “masked” dialumenes, where a presumed *in situ* generated dialumene has reacted with an aromatic solvent molecule such as benzene to form a cycloadduct. Examples of such “masked” species have been reported by Power, Tokito and Bakewell (**III-V**).^{63–65} Only recently though, the very first report of a free dialumene, $\text{Ar}^*\text{Al}=\text{AlAr}^*$ ($\text{Ar}^* = \text{Ar}^* = \text{C}_6\text{H}-2,6-(\text{C}_6\text{H}_2-2,4,6-\text{iPr}_3)_2-3,5-\text{iPr}_2$) has been reported (**VI**), by Power and co-workers (discussed in detail in Chapter 1).⁶⁶ The isolation was achieved by careful analysis of the crystals formed during the reduction of Ar^*AlI_2 . The X-ray crystal structure exhibited the longest Al=Al bond distance reported to date, at 2.648(2) Å.

4 - Characterisation of a Base-stabilised Dialumene

Base-stabilised dialumenes



'Masked' dialumenes



Free dialumenes

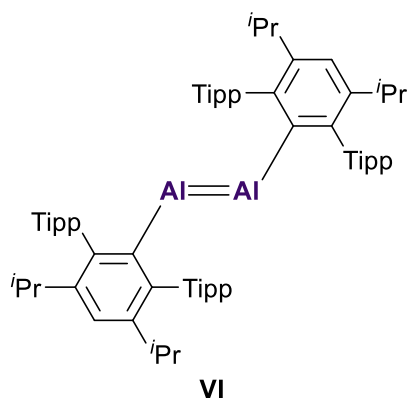
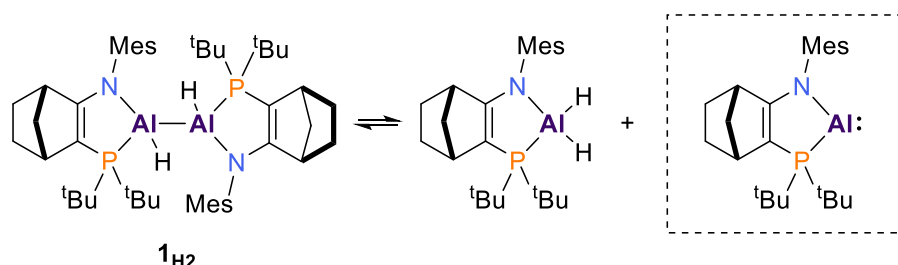


Figure 4.1: Examples of base-stabilised dialumenes (**I-II**) and 'masked' dialumenes (**III-V**) that have been experimentally isolated prior to this study. Tipp = 2,4,6-triisopropylphenyl, Ar = 2,6-(2,6-diisopropylphenyl)phenyl, Bbp= 2,6-(bis(trimethylsilyl)methyl)phenyl, Dipp = 2,6-diisopropylphenyl.

In a previous study from Cowley, the reversible reductive elimination behaviour in Al(II) dihydrides was investigated (Scheme 4.1).⁶² This study utilised a chiral amidophosphine ligand, and was thus useful as a stereochemical reporter, to probe "hidden" reversible reductive elimination processes. This reporting ability of this ligand

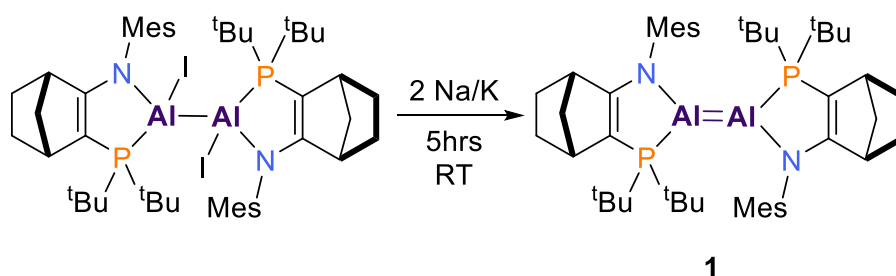
4 - Characterisation of a Base-stabilised Dialumene

was instrumental in implicating a transient aluminyl monomer in the reductive elimination of an Al(II) dihydrodialane.



Scheme 4.1: Implication of a transient N,P-coordinated aluminyl monomer in the reductive elimination of the dihydrodialane, 1_{H_2} .

Given these results, an isolable dialumene species of the same ligand framework was targeted. Dialumene **1** was prepared by reducing the Al(II) diiododialane precursor using a Na/K alloy in THF (Scheme 4.2). This reduction led to a colour change of the solution from yellow to dark purple. Dialumene **1** was crystallised as a dark purple solid from toluene. At 293 K, **1** was observed to decompose over 1-2 days in THF, toluene or hexane.



Scheme 4.2: Preparation of the dialumene **1**.

This chapter will outline the quantum chemical characterisation of this third exemplar of a base-stabilised dialumene. In tandem with experiment, the detailed electronic structure analysis reveals how the amidophosphine ligand is the origin of the unusually weak Al=Al bond, characterised by a low bond dissociation energy and order. The results of this have been published jointly with Cowley and co-workers in a combined experimental and theoretical report in *Angew. Chem. Int. Ed.*⁶¹

4.2 Methods

All electronic structure calculations were carried out using the Gaussian 16 (Revision B.01) program.²³² Initial coordinates of all compounds were extracted from the experimental single-crystal X-ray structures. Geometries were optimised at the M062X-D3/def2-SVP^{160,164,210,211} level of theory without symmetry constraints, and minima were confirmed by the absence of imaginary eigenvalues in the hessian matrix, by way of a frequency calculation performed at the same level of theory. The electronic structure analysis of **1** has been performed on isomer **1C** of the major component from the crystal structure. Geometry optimisations of the other isomers (major and minor component) furnished similar structures with nearly equidistant Al–Al bonds. Single point energy calculations were performed on the optimised geometries at the SMD-B3LYP-D3/6-311G(2d,2p)^{146,156,157,183,233–235} level of theory, utilising the SMD solvation model with benzene as the solvent ($\epsilon=2.2706$). The basis set superposition error in dimeric structures was corrected with the counterpoise method by Boys and Simon.^{236,237} The NBO program (version 6.0) was used to perform Natural Bond Orbital analyses on the optimised structures at the B3LYP-D3/6-311G(2d,2p) level of theory.²³⁸ The topology of the electron density was analysed using QTAIM (quantum theory of atoms in molecules), as implemented in the AIMALL package.²³⁹ NMR shielding tensors were calculated at the SMD-B3LYP-

D3/6-311G(2d,2p) level of theory, using the Gauge-Independent Atomic Orbital (GIAO)^{240–244} method and employing benzene as the solvent ($\epsilon=2.2706$). Analysis of the topology of the Electron Localisation Function (ELF)^{205–207}, $\eta(r)$, was carried out using the Multiwfn program.²⁰⁸ ELF basin analysis was carried out with a grid step size of 0.10 Bohr and by integrating the electron density over the basins, the average population of each basin was obtained. The sum of the synaptic valence basin populations corresponding to the Al-Al bond, $\sum V_i(\text{Al},\text{Al})$ was used as an estimate of the total basin population of the Al-Al bond. Figures of structures and isosurface plots were generated with ChemCraft (Version 1.8)²⁴⁵ and UCSF Chimera (Version 1.15).²⁴⁶

4.3 Results & Discussion

The optimised geometry of **1** is shown in Figure 4.2, along with key bond parameters (see Table 4.1 for a complete list of bond parameters compared to crystal structure data). The calculated bond parameters are in excellent agreement with their crystallographic counterparts. The structure of **1** reveals a highly trans-bent geometry, and an *E*-configuration of the amidophosphine ligand backbone. The amidophosphine ligands enforce narrow N-Al-P bite angles, with calculated values of $\sim 84^\circ$. Furthermore, the calculated Al=Al bond length is 2.514 Å (exptl. 2.519(14) Å), notably shorter than the single bonds in the related Al(II) dihydrodialane (calcd. 2.565 Å, exptl. 2.6586(16) Å)⁶² or Uhl's dialane(4) species $((\text{SiMe}_3)_2\text{HC})_2\text{Al}-\text{Al}(\text{CH}(\text{SiMe}_3)_2)_2$ (2.660(1) Å).⁴¹ The discrepancy between calculated and experimental Al—Al bond length in the Al(II) dihydrodialane has been ascribed previously to intermolecular dispersion interactions in the crystal structure.⁶² The optimised geometries of the dialumenes **I** and **II** were also found to be in excellent agreement with their experimentally determined geometries (Table 4.2 and Table 4.3).^{23,59} The Al=Al bonds in **I** and **II** are notably shorter (calcd. 2.372 Å, exptl. 2.3943(16) and calcd. 2.373 Å,

4 - Characterisation of a Base-stabilised Dialumene

exptl. 2.4039(8) Å for **I** and **II**, respectively) than in **1**. The Al=Al core in **1** is far less planar, with a calculated trans bending angle (θ) of $\sim 50^\circ$, compared to 0° and $\sim 20^\circ$ for **I** and **II**, respectively.

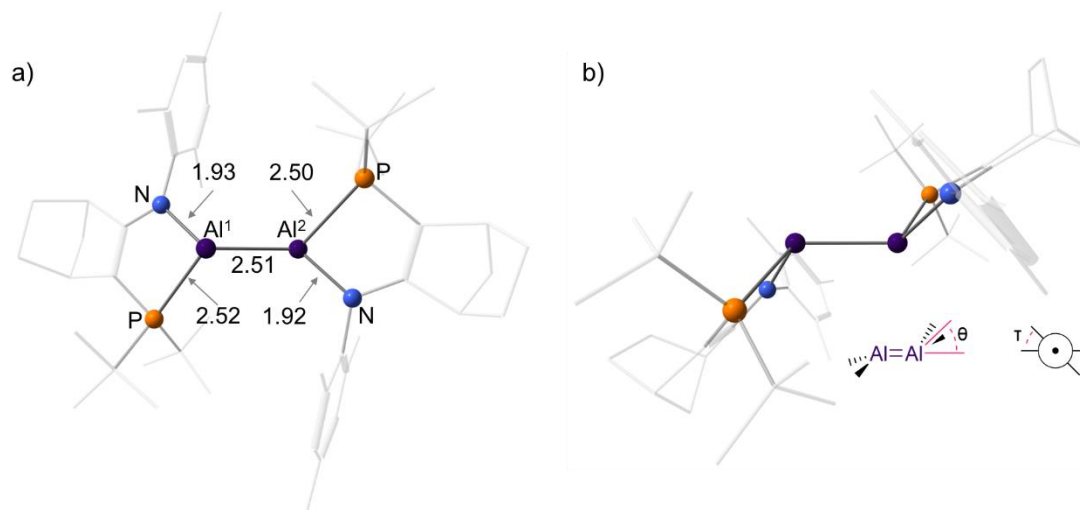
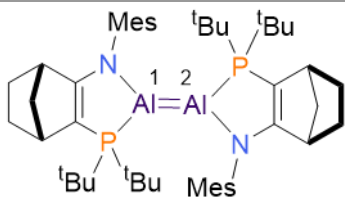


Figure 4.2: Optimised geometry of dialumene **1**, from a) a top down view and b) a side-on view. Key bond parameters are shown, along with the definitions of the trans-bending and twist angle (θ and τ , respectively).

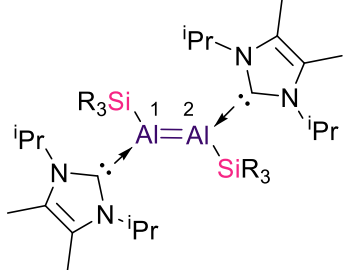
4 - Characterisation of a Base-stabilised Dialumene

Table 4.1: X-ray and calculated bond parameters of dialumene **1**.

	X-Ray	DFT
Al1–Al2 / Å	2.519 (14)	2.514
Al1–N / Å	1.909 (2)	1.925
Al1–P / Å	2.482 (9)	2.523
Al2–N / Å	-	1.924
Al2–P / Å	-	2.504
N–Al1–P / °	84.86 (7)	84.26
N–Al2–P / °	-	84.10
θ	48.82	48.38/53.97
τ	0.00	0.00

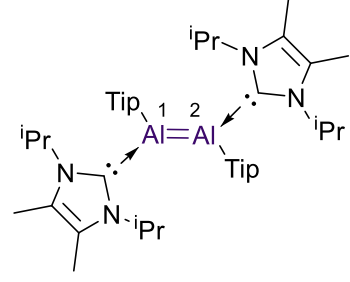
4 - Characterisation of a Base-stabilised Dialumene

Table 4.2: X-ray and calculated bond parameters for dialumene **1**.

	X-Ray	DFT
Al¹–Al² / Å	2.394 (1)	2.372
Al¹–Si / Å	2.494 (1)	2.467
Al¹–C^{NHC} / Å	2.072 (3)	2.081
C^{NHC}–Al¹–Si / °	116.21 (9)	114.95
Si–Al¹–Al²–Si / °	180.00 (7)	180.00
C^{NHC}–Al¹–Al²–C^{NHC} / °	180.00 (1)	180.00
Si–Al¹–Al²–C^{NHC} / °	1.20 (1)	10.02
θ	0.71	7.51/7.51
τ	0.00	0.00

4 - Characterisation of a Base-stabilised Dialumene

Table 4.3: X-ray and calculated bond parameters for dialumene **II**.

	X-Ray	DFT
Al¹–Al² / Å	2.404 (8)	2.373
Al¹–C^{Tip} / Å	2.029 (2)	2.033
Al²–C^{Tip} / Å	2.018 (2)	2.031
Al¹–C^{NHC} / Å	2.060 (2)	2.048
Al²–C^{NHC} / Å	2.042 (2)	2.050
C^{NHC}–Al¹–C^{Tip} / °	110.27 (7)	111.76
C^{NHC}–Al²–C^{Tip} / °	112.84 (7)	109.93
C^{Tip}–Al¹–Al²–C^{Tip} / °	-167.04 (9)	-171.76
C^{NHC}–Al¹–Al²–C^{NHC} / °	-175.54 (8)	-174.56
C^{Tip}–Al¹–Al²–C^{NHC} / °	35.81 (9)	-13.49
C^{NHC}–Al¹–Al²–C^{Tip} / °	-18.39 (9)	27.17
θ	17.25/23.70	14.07/15.84
τ	12.06	7.61

Following the geometrical analysis, a detailed investigation of the bonding and general electronic structure of **1**, **I** and **II** was undertaken. The calculations reveal that the bonding situation in **1** is distinctly different from those in **I** and **II**. In Figure 4.3, a comparison of key natural bond orbitals (NBOs), representing the Al–Al σ and π bonds of all three dialumenes are shown. The overall goal of NBO analysis is to

express the wavefunction in a localised Lewis-like form. This localisation scheme allows the assignment of hybridisation to atomic lone pairs and each atom's contribution to its bond orbitals. This permits, for example, the assignment of the percentage orbital type character (s, p, d, f, etc.), the calculation of partial atomic charges, via a natural population analysis (NPA), or the calculation of Wiberg bond indices (WBI), which can be interpreted as a measure of bond order. Therefore, NBO analysis is useful for the characterisation of the bonding present in **I**, **II** and **1**. Visually, despite **1** retaining apparent π bonding character, there is significant localisation of this orbital on to the aluminium centres. In contrast, the NBOs of **I** and **II** more closely resemble classical π type orbitals i.e. in-phase side-on overlap of p orbitals perpendicular to the molecular plane.

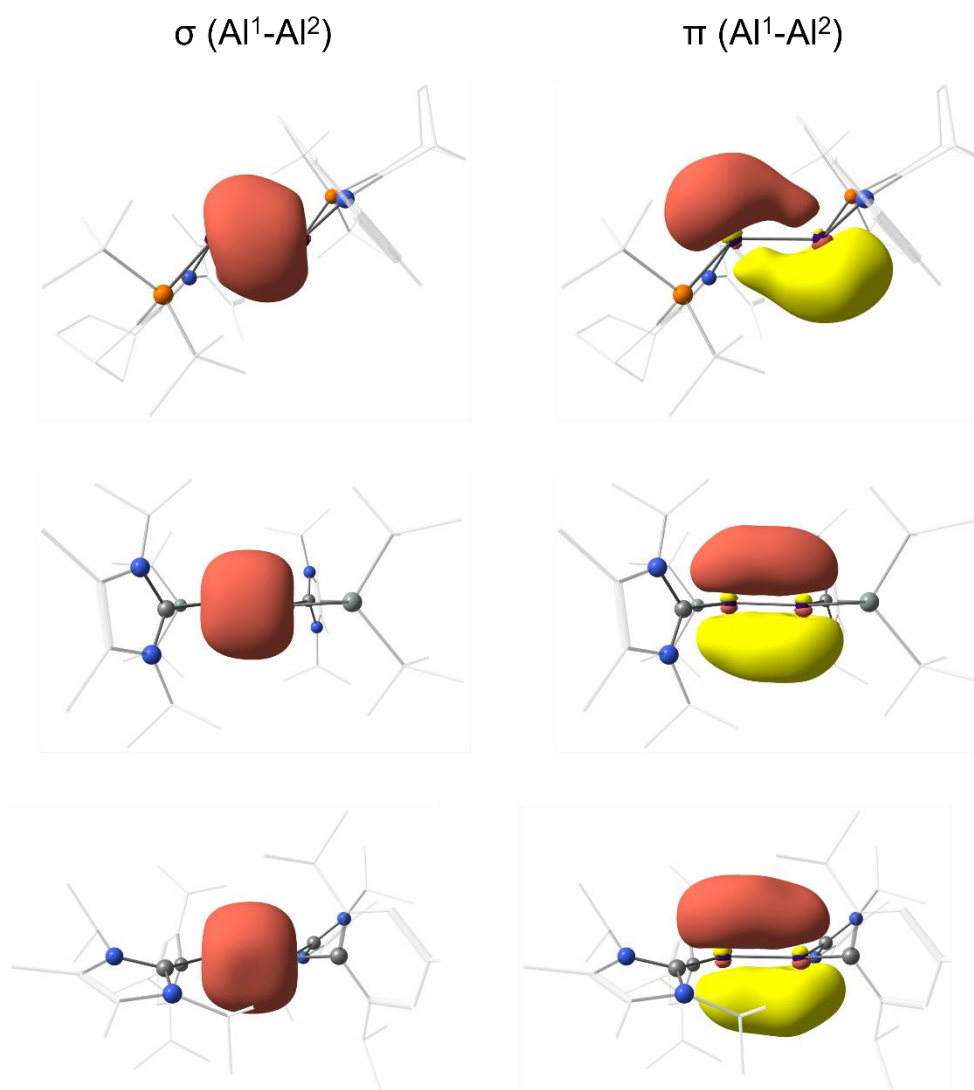


Figure 4.3: Comparison of key NBOs for dialumenes **1** (top), **I** (middle) and **II** (bottom) (Isovalue = 0.036).

This localisation observed for **1** is a result of a second-order Jahn Teller effect¹⁹, rationalised based on the symmetry allowed mixing of the HOMO (π) / LUMO+1 (σ^*) and LUMO (π^*) / HOMO-1 (σ) orbital pairs. On the left hand side of Figure 4.4 are the familiar frontier orbitals of a classical planar E=E double bond, which has D_{2h} symmetry. These orbitals are given the designations σ (a_g , HOMO-1), π (b_{2u} , HOMO), π^* (b_{1g} , LUMO) and σ^* (b_{3u} , LUMO+1). A trans-bending vibration results in symmetry lowering to C_{2h} symmetry, with the orbital designations σ (a_g , HOMO-1), n_- (b_u , HOMO), n_+ (a_g , LUMO) and σ^* (b_u , LUMO+1). The pairs n_- / σ^* and σ / n_+ have the

same symmetry designation in C_{2h} symmetry, while they have differing designations in D_{2h} symmetry, thus preventing mixing of these orbitals.

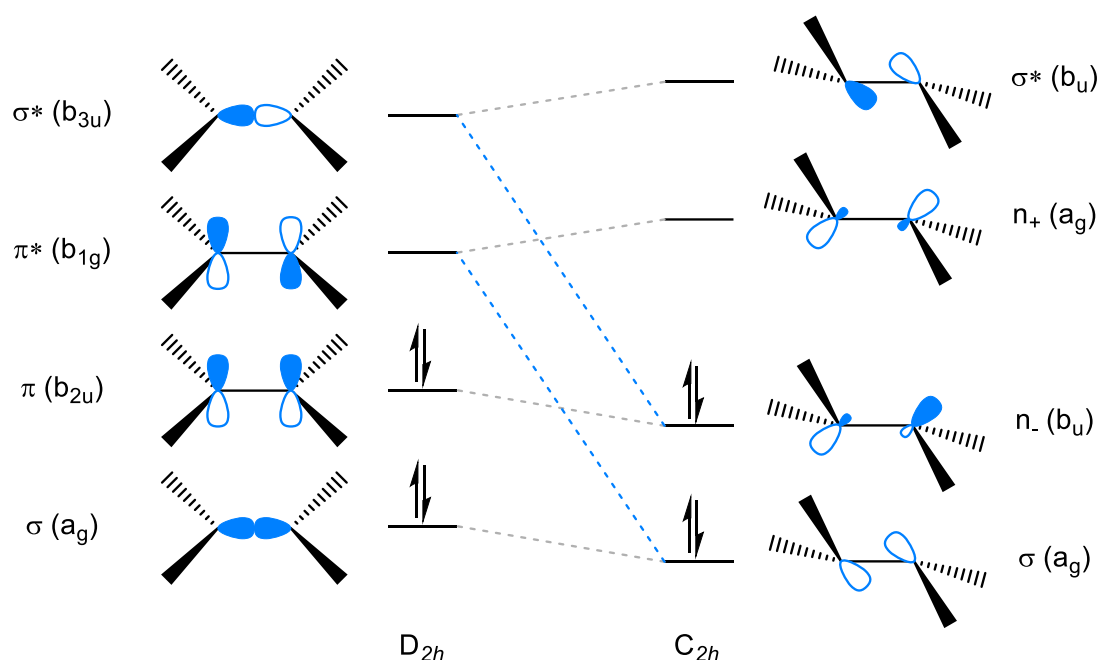


Figure 4.4: Changes in symmetry of frontier orbitals resulting from a *trans*-bending vibration.

The symmetry allowed mixing of the orbitals causes an increase in s-character of the double bond. This increase in s-character is evident from the NBO analysis (Table 4.4). For **1**, a hybridisation of $sp^{4.14}/sp^{3.49}$ (Al^1/Al^2) is calculated for the π bond, corresponding to approximately 20% s-character and 80% p-character. This contrasts with **I** and **II**, where the π bond is constructed from essentially pure p-orbitals. Furthermore, the WBI for the $Al=Al$ bond of **1** is 1.31, compared to 1.67 and 1.54, for **I** and **II**, respectively. Although the WBI is significantly lowered, compared to **I** and **II**, it is still higher than that of the corresponding dihydrodialane, **1**_{H2} with a WBI of 0.91, which is diagnostic of a $Al-Al$ single bond.⁶²

4 - Characterisation of a Base-stabilised Dialumene

Table 4.4: NBO analysis of **1**, **1_{H2}**, **I** and **II**.

	Bond	NPA Charge	Occupancy	Polarisation	Hybridisation	WBI
1	Al ¹ –Al ²	0.56 (Al ¹)	1.77	51% (Al ¹)	sp ^{1.22} (Al ¹)	1.31
		0.66 (Al ²)		49% (Al ²)	sp ^{1.24} (Al ²)	
	Al ¹ –Al ²	0.56 (Al ¹) 0.66 (Al ²)	1.69	51% (Al ¹) 49% (Al ²)	sp ^{4.14} (Al ¹) sp ^{3.49} (Al ²)	1.31
	Al ¹ –P	0.90 (P)	1.91	12% (Al ¹) 88% (P)	sp ^{6.87} (Al ¹) sp ^{2.06} (P)	0.42
	Al ¹ –N	-0.93 (N)	1.92	6% (Al ¹) 94% (N)	sp ^{3.19} (Al ¹) sp ^{2.72} (N)	0.23
	Al ² –P	0.88 (P)	1.91	12% (Al ²) 88% (P)	sp ^{6.03} (Al ²) sp ^{2.12} (P)	0.40
	Al ² –N	-0.94	1.91	5% (Al ¹) 95% (N)	sp ^{3.97} (Al ²) sp ^{2.79} (N)	0.21
1_{H2}	Al ¹ –Al ²	0.90 (Al ¹)	1.92	50% (Al ¹)	sp ^{1.51} (Al ¹)	0.91
		0.91 (Al ²)		50% (Al ²)	sp ^{1.52} (Al ²)	
	Al ¹ –H	-0.45 (H)	1.95	27% (Al ¹) 73% (H)	sp ^{2.43} (Al ¹) sp ^{0.01} (H)	0.72
	Al ² –H	-0.45 (H)	1.95	26% (Al ²) 74% (H)	sp ^{2.44} (Al ¹) sp ^{0.01} (H)	0.72
	Al ¹ –P	0.97 (P)	1.93	17% (Al ²) 83% (P)	sp ^{5.88} (Al ¹) sp ^{2.14} (P)	0.52
	Al ¹ –N	-0.88 (N)	1.92	8% (Al ²) 92% (N)	sp ^{4.91} (Al ¹) sp ^{2.37} (N)	0.28

4 - Characterisation of a Base-stabilised Dialumene

	Al ² –P	0.97 (P)	1.92	17% (Al ²) 83% (P)	sp ^{5.58} (Al ¹) sp ^{2.18} (P)	0.52
	Al ² –N	-0.89 (N)	1.92	8% (Al ²) 92% (N)	sp ^{5.04} (Al ¹) sp ^{2.39} (N)	0.27
I	Al ¹ –Al ²	0.08 (Al ¹) 0.08 (Al ²)	1.92	50% (Al ¹) 50% (Al ²)	sp ^{1.11} (Al ¹) sp ^{1.11} (Al ²)	1.67
	Al ¹ –Al ²	0.08 (Al ¹) 0.08 (Al ²)	1.76	50% (Al ¹) 50% (Al ²)	sp ^{99.99} (Al ¹) sp ^{99.99} (Al ²)	1.67
	Al ¹ –C ^{NHC}	0.05 (C ^{NHC})	1.94	14% (Al ¹) 86% (C ^{NHC})	sp ^{4.82} (Al ¹) sp ^{1.27} (C ^{NHC})	0.49
	Al ¹ –Si	1.17 (Si)	1.93	36% (Al ¹) 64% (Si)	sp ^{1.82} (Al ¹) sp ^{1.97} (Si)	0.88
II	Al ¹ –Al ²	0.49 (Al ¹) 0.49 (Al ²)	1.93	50% (Al ¹) 50% (Al ²)	sp ^{1.03} (Al ¹) sp ^{1.06} (Al ²)	1.54
	Al ¹ –Al ²	0.49 (Al ¹) 0.49 (Al ²)	1.60	50% (Al ¹) 50% (Al ²)	sp ^{99.99} (Al ¹) sp ^{43.39} (Al ²)	1.54
	Al ¹ –C ^{NHC}	-0.01 (C ^{NHC})	1.94	14% (Al ¹) 86% (C ^{NHC})	sp ^{3.66} (Al ¹) sp ^{1.27} (C ^{NHC})	0.55
	Al ¹ –C ^{Tipp}	-0.57 (C ^{Tipp})	1.92	16% (Al ¹) 84% (C ^{Tipp})	sp ^{2.49} (Al ¹) sp ^{2.31} (C ^{Tipp})	0.52
	Al ² –C ^{NHC}	0.00 (C ^{NHC})	1.94	15% (Al ²) 85% (C ^{NHC})	sp ^{3.73} (Al ²) sp ^{1.28} (C ^{NHC})	0.57
	Al ² –C ^{Tipp}	-0.56 (C ^{Tipp})	1.92	17% (Al ¹) 83% (C ^{Tipp})	sp ^{2.52} (Al ²) sp ^{2.34} (C ^{Tipp})	0.52

To further characterise the electronic structure and bonding in **1**, topological criteria, proposed by Grützmacher and Fässler were utilised, which have been used to distinguish between classical and non-classical multiple bonds.²¹³ This topological criterion utilises the Electron Localisation Function (ELF), introduced by Becke and Edgecombe.²⁰⁵ In brief, by making use of the two-electron pair density, it was shown that the probability of finding two electrons of the same spin close to one another is position dependent. This leads to regions of high and low pair probability. If the pair probability is low, the electrons are well localised. The ELF was introduced to provide a measure of this localisation, defined to have the range $0 \leq \text{ELF} \leq 1$, and given by the equation

$$\text{ELF}(\mathbf{r}) = \frac{1}{1 + \chi_{\sigma}^2} \quad (4.1)$$

where

$$\chi_{\sigma}(\mathbf{r}) = \frac{D_{\sigma}(\mathbf{r})}{D_{\sigma}^0(\mathbf{r})} \quad (4.2)$$

is the ratio of the electron localisation of the system of interest ($D_{\sigma}(\mathbf{r})$), to that of the uniform electron gas ($D_{\sigma}^0(\mathbf{r})$). An ELF value close to 1 defines well localised electrons and can identify regions or “basins” of localised core and valence electron density, while an ELF value of $1/2$ corresponds to the uniform electron gas. By integrating over the basins, so-called attractors are revealed, which are local maxima in the ELF. These attractors correspond to electron pairs and can be interpreted in familiar terms as covalent bonds and lone pairs. The synaptic order of a valence attractor refers to the number of connections with core attractors i.e. attractors corresponding to covalent bonds are disynaptic, and attractors corresponding to lone pairs are monosynaptic.²⁰⁷ In classical double bonded systems, there are two disynaptic valence attractors, one above and one below the molecular plane. Furthermore, the ELF isosurface corresponding to these systems is dumbbell shaped. The ELF of

ethene is an example of such a classical double bond (Figure 4.5). An ideal double bond, containing a σ and π component, should have 4 electrons in total. In reality, even in the case of ethene, the respective basin populations sum to only 3.40 electrons (1.70 electrons each). This result is not abnormal, as the value of 4 electrons is based on a classical Lewis picture and thus would only be reached in an idealised bonding scenario.

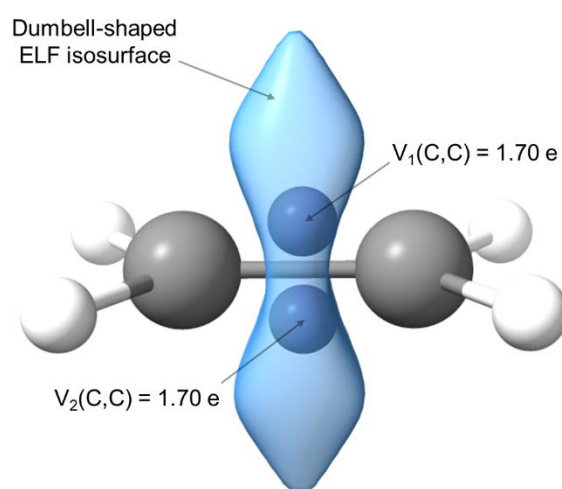


Figure 4.5: Plots of ELF localisation domains (isovalue=0.795 a.u.) along with key valence attractors of the C_2 core of ethene. For clarity, localisation domains corresponding to core domains are excluded. The $C=C$ bond is characterised by the presence of two valence attractors $V_i=(C,C)$ ($i=1,2$), with their respective basin populations summing to 3.40 electrons.

From the ELF analysis of dialumene **1**, quite a different picture than the classical one emerges (Figure 4.6). Three valence attractors (V_{1-3}) are present around the $Al=Al$ core, with their populations summing to 3.76 electrons. V_1 is located on the midpoint of the $Al-Al$ bond axis, with a population of 1.11 electrons, with V_2 and V_3 each located above or below an Al centre, having populations of ~ 1.30 electrons each. This pattern, along with the sigmoidal shape of the ELF isosurface, is characteristic of a “slipped” π -bond and is consistent with that calculated for the parent transient dialumene

species, Al_2H_2 .⁶⁹ In contrast, the ELF analysis of the dialumenes **I** and **II** are more consistent with the classical picture of π bonding. For **I**, only two valence attractors were located around the $\text{Al}=\text{Al}$ core, both having populations of 1.71 electrons. Almost the same situation was found for **II**, with both valence attractors having populations of 1.68 electrons (Figure 4.6). Furthermore, these valence attractors are located above and below the midpoint of the $\text{Al}=\text{Al}$ bond, resulting in more of a dumbbell shaped ELF isosurface, in contrast to the sigmoidal shape observed for **1**.

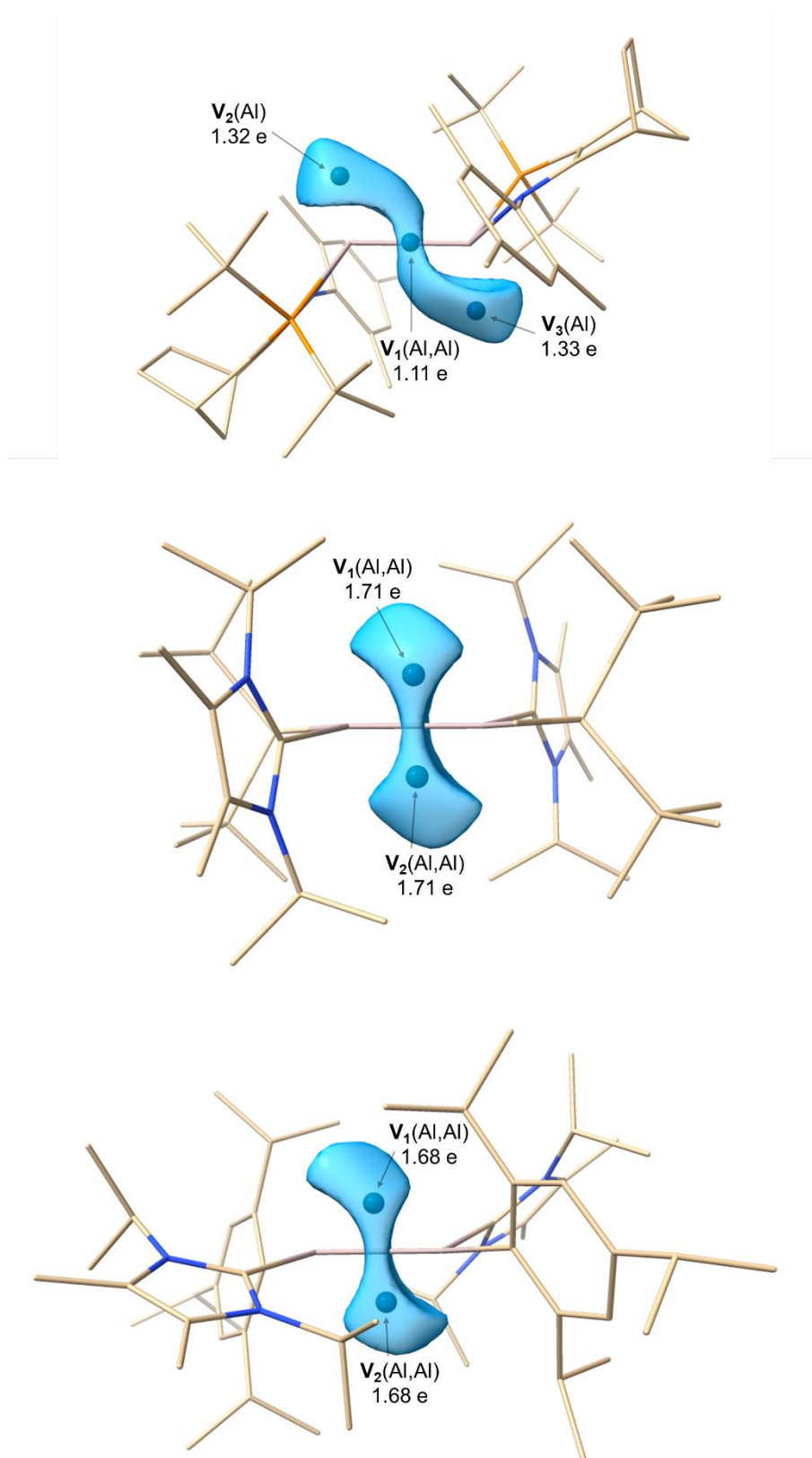


Figure 4.6: Plots of ELF localisation domains (isovalue=0.795 a.u.) along with key valence attractors of dialumenes **1** (top), **I** (middle) and **II** (bottom).

To provide further insight into the bonding of **1**, QTAIM analysis was carried out. In Figure 4.7, the molecular graph of **1** is shown, revealing Al–Al, Al–N and Al–P bond paths (BP, shown as black lines) and bond critical points (BCP, shown as green spheres). The properties of the Al–Al BCP (Table 4.5) are characteristic of weak shared covalent interactions²⁴⁷ ($\rho(r) = 0.052 \text{ e/a}_0^3$, $\nabla^2\rho(r) = -0.058 \text{ e/a}_0^5$ and $H(r) = -0.020 \text{ E}_h/\text{a}_0^3$).

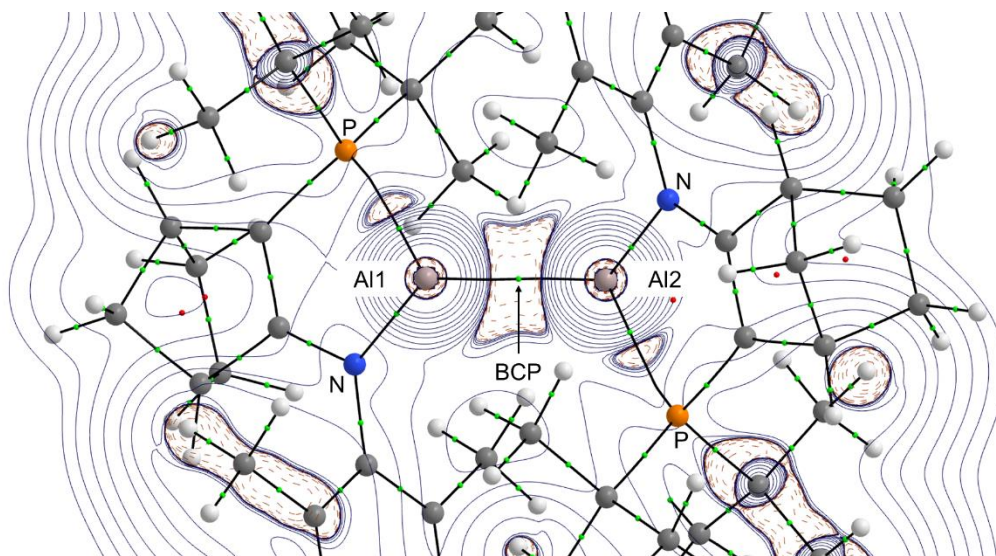


Figure 4.7: Molecular graph of **1**, including a contour plot of the Laplacian $\nabla^2\rho(r)$ of the electron density in the plane containing Al1 and Al2, with the bond critical points (BCP) shown as green spheres, and the ring critical points (RCP) shown as red spheres.

Furthermore, the bond ellipticity parameter can be interpreted as a measure of the π bonding character.²⁴⁷ The ellipticity measures the extent to which density accumulates in a given plane that contains the bond path. It is defined as $\varepsilon = \lambda_1/\lambda_2 - 1$, where $|\lambda_1| \geq |\lambda_2|$, and λ_{1-3} are the curvatures of the density with respect to the three principal axes (one of which is the bond axis of interest). If $\lambda_1 = \lambda_2$, then $\varepsilon = 0$, and the bond is cylindrically symmetrical, with the C—C single bond of ethane or the triple bond of ethyne being classic examples. The ellipticity is a measure of π bonding

character to the limit of a double bond, at which it reaches a maximum value. As a reference point, the ellipticity of the C=C double bond in ethene is approximately 0.33.²⁴⁸

Table 4.5: Selected properties of the bond critical points of **1**. $\rho(r)$ is the electron density (e/a_0^3), $\nabla^2\rho(r)$ is the Laplacian of the electron density (e/a_0^5), λ_n are eigenvalues of the Hessian of $\rho(r)$ (e/a_0^5), ε is the bond ellipticity defined as $(\lambda_1/\lambda_2)-1$, $V(r)$, $G(r)$ and $H(r)$ represent the potential, kinetic and total energy density, respectively (Hartree/ a_0^3).

BCP	$\rho(r)$	$\nabla^2\rho(r)$	λ_1	λ_2	λ_3	ε	$V(r)$	$G(r)$	$H(r)$
Al1–Al2	+0.052	-0.058	-0.037	-0.031	+0.011	+0.195	-0.025	+0.005	-0.020
Al1–N	+0.074	+0.349	-0.115	-0.103	+0.567	+0.112	-0.115	+0.101	-0.014
Al2–N	+0.074	+0.349	-0.114	-0.103	+0.566	+0.111	-0.115	+0.101	-0.014
Al1–P	+0.046	+0.049	-0.041	-0.038	+0.129	+0.081	-0.044	+0.028	-0.016
Al2–P	+0.048	+0.054	-0.044	-0.041	+0.139	+0.062	-0.047	+0.030	-0.017

It is possible for local maxima in the electron density to occur at positions other than those of atomic nuclei. These are termed non-nuclear attractors (NNA) and are topologically indistinguishable from the nuclear maxima. NNAs have well-defined properties, such as an electron population and energy components, and have been referred to as “pseudoatoms” in the literature.²⁴⁷ Interestingly, a NNA was located upon carrying out the QTAIM analysis of dialumene **II** (Figure 4.8). This prevented a direct comparison to the BCP properties of the Al=Al bond in **1**, due to theoretical ambiguities. For example, an ellipticity is individually defined for both BCPs and the single NNA, yet it is unclear how this may be compared to the ellipticity of **1**. Despite this complication, it is of interest that a NNA was located for **II**, with further investigation outside of the scope of this work.

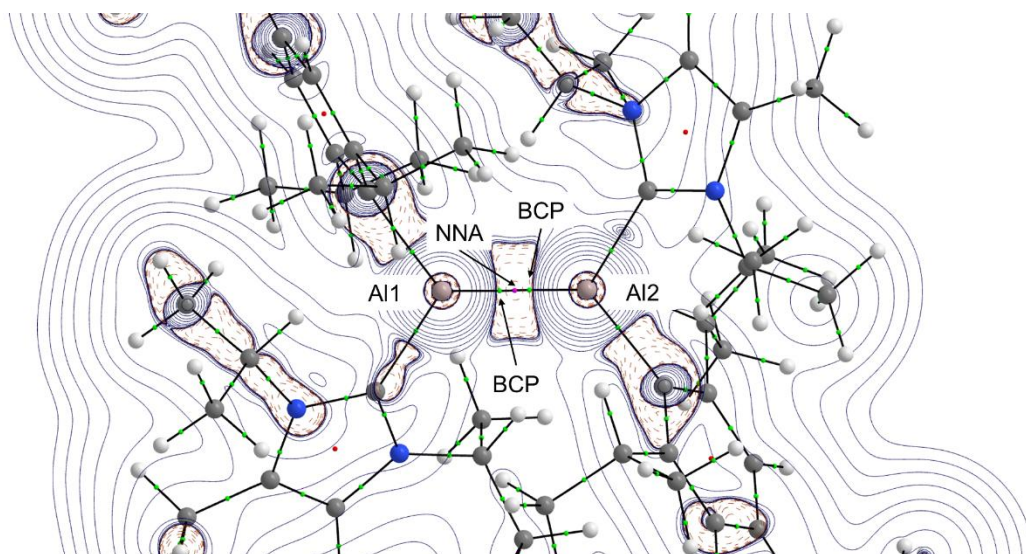


Figure 4.8: Molecular graph of **II**, including a contour plot of the Laplacian $\nabla^2\rho(r)$ of the electron density in the plane containing Al1 and Al2, with the bond critical points (BCP) shown as green spheres, the ring critical points (RCP) shown as red spheres, and the single non-nuclear attractor (NNA) shown as a pink sphere.

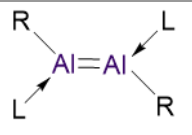
To summarise the electronic structure analysis thus far, the dialumene **1** has a small but significant amount of double bond character. This is evidenced by an Al–Al bond length and bond order that is intermediate between that of a single and double bond. Furthermore, the ELF and QTAIM analysis provide support to this conclusion, from a topological perspective. It is clear that the dialumene **1** is significantly different to **I** and **II**, which can both be categorised as having more of a classical π bond, due to zero or near zero trans-bending that occurs in these structures, as well as the shorter Al–Al bond lengths and larger bond orders.

In order to probe the reasons for the observed variations in bonding amongst **1**, **I** and **II**, calculations were carried out on a set of minimal base-stabilised dialumenes (Table 4.6). A set of hydride, amino, phenyl and silyl substituents were chosen, with the transient dialumenes stabilised by either an NHC (Imidazol-2-ylidene ($C_3H_4N_2$))) or

4 - Characterisation of a Base-stabilised Dialumene

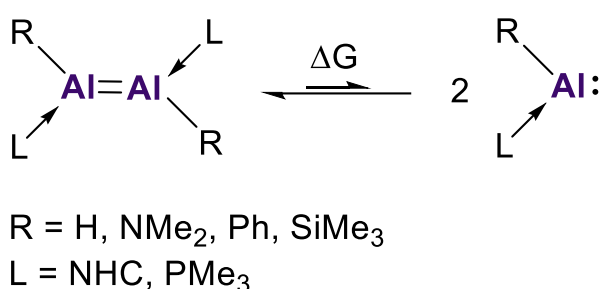
phosphine (PMe_3). The geometries of these structures were observed to depend strongly on the identity of the substituent, as well as the Lewis base employed. When more electropositive substituents are employed, such as SiMe_3 , shorter $\text{Al}=\text{Al}$ bonds, wider $\text{L}-\text{Al}-\text{R}$ angles and more planar structures are observed. On the other hand, when more electronegative or π -donating substituents such as Ph or NMe_2 are employed, longer $\text{Al}=\text{Al}$ bonds, narrower $\text{L}-\text{Al}-\text{R}$ angles and more trans-bent structures are observed. More generally, the dialumenes stabilised by the NHC exhibit shorter $\text{Al}=\text{Al}$ bonds than their PMe_3 stabilised counterparts.

Table 4.6: Calculated structural parameters of model systems. For $\text{M}^1\text{-M}^4$, $\text{L} = \text{NHC}$ (Imidazol-2-ylidene ($\text{C}_3\text{H}_4\text{N}_2$)) and for $\text{M}^5\text{-M}^8$, $\text{L} = \text{PMe}_3$.

	L	R	$\text{Al1-Al2} / \text{\AA}$	$\text{L-Al-R} / ^\circ$	$\theta(\text{Al1}) / \theta(\text{Al2})$	τ
M¹	NHC	H	2.422	101.71	29.59/47.22	17.81
M²	NHC	NMe_2	2.483	91.97	43.06/43.07	0.00
M³	NHC	Ph	2.444	97.10	33.37/53.92	20.54
M⁴	NHC	SiMe_3	2.392	112.08/106.94	19.10/16.34	7.58
M⁵	PMe_3	H	2.446	95.84	46.59/46.59	0.00
M⁶	PMe_3	NMe_2	2.602	99.43	63.46/44.60	19.76
M⁷	PMe_3	Ph	2.469	92.71	50.52/50.43	0.00
M⁸	PMe_3	SiMe_3	2.425	98.72	41.55/41.02	0.00

These structural trends observed for the model dialumene systems mimic those seen for disilenes. It has been observed that for disilenes, the trans-bending angles and $\text{Si}=\text{Si}$ bond distances are correlated with the singlet-triplet energy gaps ($\Delta E(\text{S-T})$) of

the corresponding silylene monomers.²⁴⁹ This was initially studied using qualitative valence bond and molecular orbital theory^{250–252}, and then more quantitatively using *ab initio* methods, by Carter, Goddard, Malrieu and Trinquier (CGMT model).²⁵³ Given these previous results, the bond dissociation energies and monomeric singlet-triplet gaps were calculated for all model dialumenes and plotted (Scheme 4.3, Figure 4.9 and Table 4.7).



Scheme 4.3: Al=Al bond dissociation energy scheme for the set of model systems.

The same linear relationship found for disilenes was observed. As the bond dissociation energy of the dimers increase, the singlet-triplet energetic gaps of the corresponding aluminyl monomers decrease. At one extremity of the spectrum for this set of model systems, the large bond dissociation energy and small singlet-triplet gap of **M**⁴ can be explained by the strong donating ability of the NHC coordinating base, which raises the HOMO of the aluminyl monomer, resulting in a smaller singlet-triplet gap. Conversely, at the other extremity, the small bond dissociation energy and large singlet-triplet gap calculated for **M**⁶ can be explained by the more electronegative or π -donating ability of NMe₂, together with the weaker donating ability of the coordinating base, PMe₃.

4 - Characterisation of a Base-stabilised Dialumene

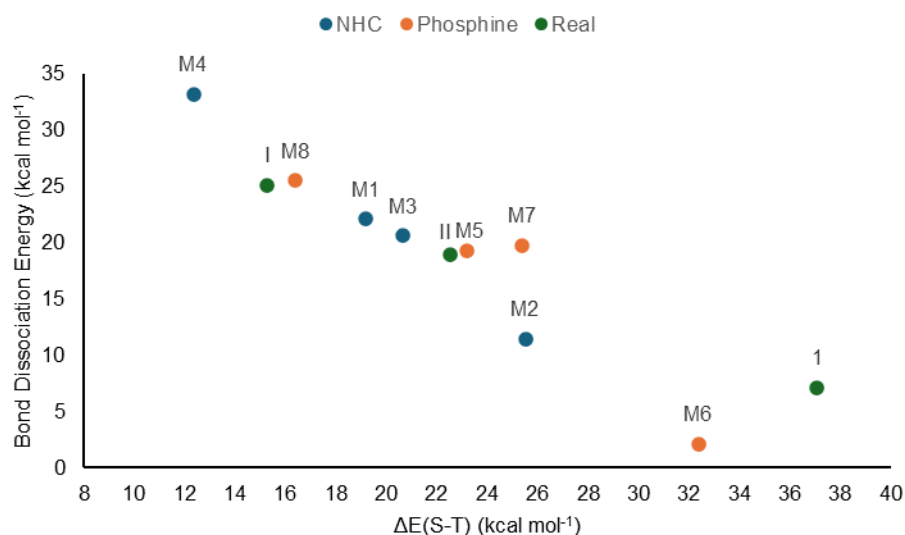


Figure 4.9: Plot of bond dissociation energies (BSSE corrected) and singlet-triplet energy gaps of the singlet monomers (ΔE_{S-T}) for model compounds **M¹-M⁸** and the real dialumenes **1**, **I** and **II**. See Table 4.7 and Table 4.8 for the source data.

Table 4.7: Bond dissociation energies of the model dialumenes **M¹-M⁸**, and adiabatic singlet triplet gaps of the corresponding aluminyll monomeric fragments. A counterpoise correction was applied to account for the basis set superposition error (BSSE).

	ΔG_{298} / kcal mol ⁻¹ Uncorrected	ΔG_{298} / kcal mol ⁻¹ BSSE Corrected	Singlet Monomer ΔE_{S-T} / kcalmol ⁻¹
M¹	23.18	22.09	19.17
M²	13.19	11.46	25.50
M³	22.49	20.60	20.64
M⁴	34.83	33.18	12.34
M⁵	20.23	19.31	23.19
M⁶	4.33	2.11	32.36
M⁷	21.16	19.73	25.38
M⁸	26.96	25.50	16.40

Having analysed the structural and energetic trends of the eight model systems, these findings can then be applied to the synthetic base-stabilised dialumenes (Table 4.8). For dialumene **1**, the extreme trans-bending can be attributed to the electronegative and π -donating NR_2 substituent and narrow bite angle ($\sim 85^\circ$). This results in an increased singlet-triplet gap in the aluminyll monomer, and a lower bond dissociation energy, compared to dialumenes **I** and **II**, where in the case of dialumene **I**, the strong donation of the NHC, together with the silyl substituent, result in the highest bond dissociation energy, and lowest aluminyll singlet-triplet gap. Dialumene **II** falls in between these two extremes, as although it benefits from the strong donating capability of the NHC, the aryl substituent is more electronegative than the silyl substituent utilised in **I**. Therefore, these results indicate that, among the isolated systems, **1** lies at the extreme end of what is considered a double bond, being on the cusp of separating into two monomeric aluminyll fragments, as evidenced by the small bond dissociation energy.

Table 4.8: Bond dissociation energies of the synthetic dialumenes, and adiabatic singlet triplet gaps of the corresponding aluminyll monomeric fragments. A counterpoise correction was utilised to account for the basis set superposition error (BSSE).

	$\Delta G_{298} / \text{kcal mol}^{-1}$ Uncorrected	$\Delta G_{298} / \text{kcal mol}^{-1}$ BSSE Corrected	Singlet Monomer $\Delta E_{\text{S-T}} / \text{kcal mol}^{-1}$
1	9.39	7.09	37.05
I	26.93	25.06	15.28
II	21.38	18.95	22.54

Experimentally, it was found that **1** was predominantly dimeric in solution. At 300 K, one broad signal was observed in the $^{31}\text{P}\{^1\text{H}\}$ NMR spectrum (Figure 4.10a). Given

that the aluminium centres in **1** are stereogenic, when the relative orientation of the methylene (CH₂) bridges are considered, there are three possible diastereomers of *E*-**1**, **A-C**. These three possible diastereomers must have distinct ³¹P NMR signals. **1A** and **1B** are *meso* compounds, due to the centre of inversion, resulting in chemically equivalent phosphorus centres. **1C** on the other hand, has inequivalent phosphorus centres. Therefore, one signal is expected for each of **1A** and **1B**, while two distinct signals are expected for **1C**. To examine this theoretically, the isotropic ³¹P magnetic shielding tensors were calculated, and by using H₃PO₄ as the reference, ³¹P chemical shifts could be obtained. This confirmed the pattern of signals (Figure 4.10b). **1A** was calculated to have identical ³¹P chemical shifts of 15.1 ppm, and **1B** was calculated to have shifts of 16.7 ppm. On the other hand, **1C** was calculated to have ³¹P chemical shifts of 16.1 and 19.3, confirming that the two phosphorus centres in **1C** are in inequivalent stereochemical environments. Experimentally, at 300 K, the broad ³¹P{¹H} resonance indicates that **1A-C** are exchanging in solution. When cooled to 243 K, the broad signal was observed to resolve into two singlets. Upon cooling further to 203 K, the higher field signal was observed to approach coalescence. The dynamic behaviour in solution phase is a result of both intra- and intermolecular exchange processes, with only the former occurring at low temperatures. The two singlets observed at 243 K were assigned to be **1A/B** and **1C**. A “trans-flip” process that is fast on the NMR timescale can invert the stereochemistry at both aluminium centres, interconverting **1A** and **1B**. This generates a time-averaged signal for them. For **1C** however, the trans-flip is a degenerate process (slow on the NMR timescale at 203 K), that exchanges the two inequivalent phosphorus centres. To support these experimental observations, planar transition states were located, corresponding to the “trans-flip” process (Figure 4.10d). The barriers for this process range from 8-11 kcal mol⁻¹, relative to the lowest energy diastereomer **1B**. In the higher temperature regime, at ~300 K, exchange between **1A-C** becomes active through an intermolecular route that scrambles all possible isomers. This occurs through

dissociation of **1** into the aluminyl monomer, which can then recombine to form any of the three diastereomers. This process is possible due to a low bond dissociation energy, which was calculated to be 7.1 kcal mol⁻¹ (Table 4.8). Furthermore, the energies of **1A-C** were calculated to be within 2 kcal mol⁻¹ of each other. This is in line with experiment, as the equilibrium constants could be determined for the intermolecular exchange in the temperature range 188-243 K, providing an estimate of 0.19 ± 0.04 kcal mol⁻¹ for ΔG^0 .

4 - Characterisation of a Base-stabilised Dialumene

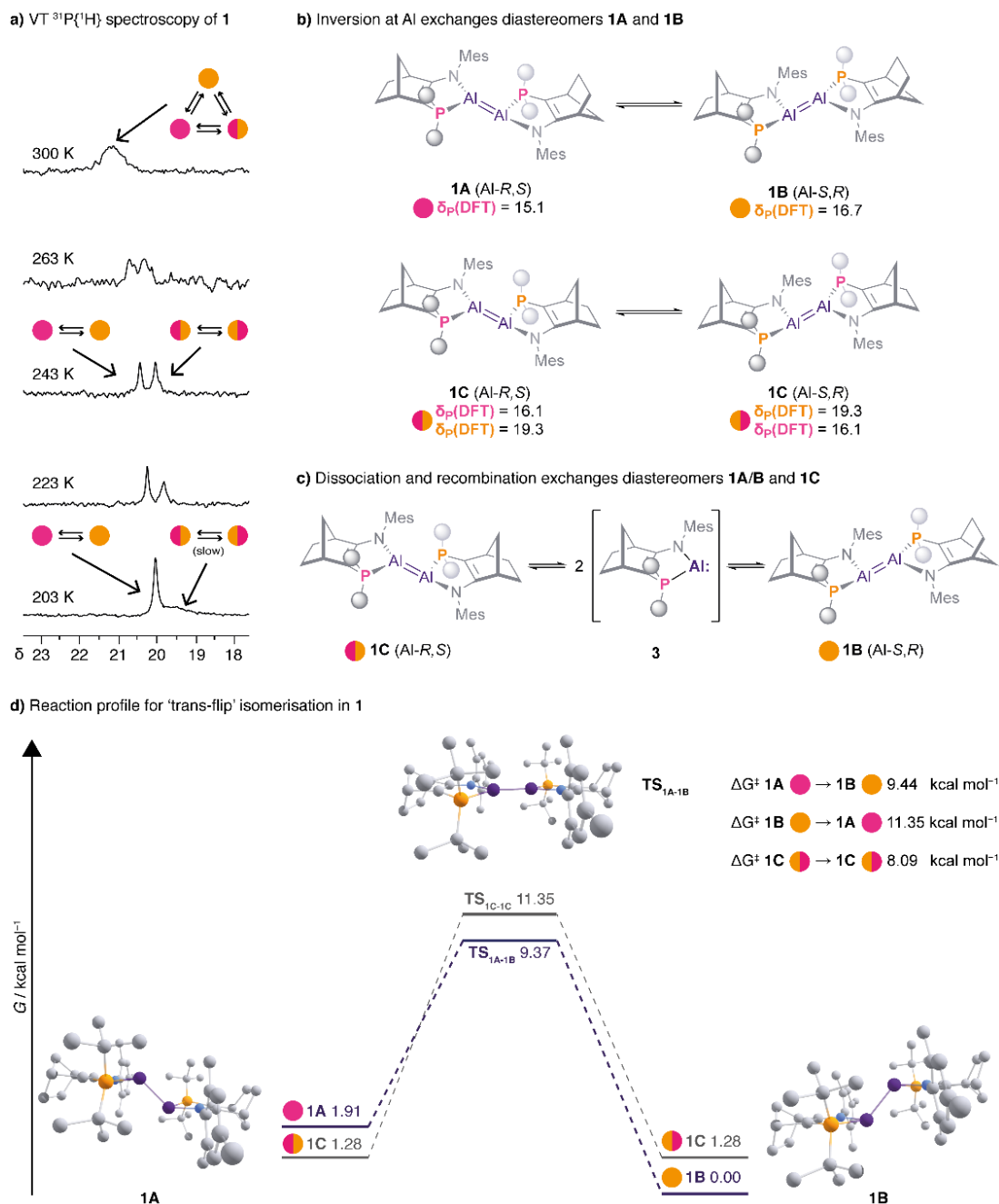


Figure 4.10: a) $^{31}\text{P}\{^1\text{H}\}$ NMR spectra of **1** (161 MHz, $[\text{D}_8]\text{toluene}$) recorded at 203–300 K. b) Inversion at aluminium exchanges **1A** and **1B**, but is degenerate for **1C**. c) Intermolecular dissociation/recombination of **1** exchanges all diastereomers. d) Reaction energy profile for the “trans-flip” in diastereomers **1A–C** at $T = 298.15$ K (geometries optimised at M062X- D3/def2-SVP, energies calculated at B3LYP-D3/6-311G(2d,2p) corrected for C_6H_6 solvent).

4.4 Conclusions

In conclusion, this collaborative study reported the third example of a base-stabilised dialumene, supported by an amidophosphine ligand framework. As well as being the third example, it was also the first example of a dialumene that could reversibly dissociate in solution to the monomeric form. Through a combination of X-ray crystallographic, spectroscopic, and computational analysis, it was revealed that this dialumene has an extremely long and trans-bent Al=Al bond, with a low bond dissociation energy and order. Furthermore, by employing electronic structure analysis techniques such as NBO, QTAIM and ELF, the Al=Al bond was further categorized as being an example of a slipped π bond, contrasting classical π bonded systems, such as Inoue's dialumene **1**. A small systematic study of a set of model systems was carried out, demonstrating the isostructural relationship between dialumenes and disilenes. The following chapter will outline the computational mechanistic work that has been carried out, to investigate the experimentally observed activation of small molecules by **1**.

5 Reactivity of a Base-stabilised Dialumene

5.1 Introduction

Processes such as oxidative addition, reductive elimination and migratory insertion are highly important elementary reactions in organometallic chemistry, with the cleavage of strong σ bonds being a key step. The activation of these σ bonds has traditionally been the domain of transition metals^{254,255}, with the activation of dihydrogen, for example, typically proceeding via a synergistic interaction of the H—H bond with the frontier d-orbitals of the transition metal complex (Figure 5.1). This synergistic interaction involves donation from the σ orbital of H_2 into the frontier d-orbitals of the transition metal complex, with the concomitant donation from these d-orbitals into the σ^* orbital of H_2 .

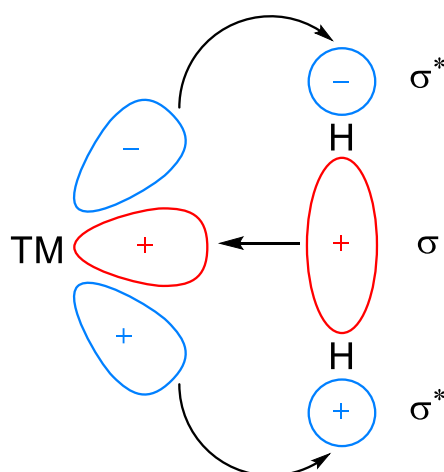


Figure 5.1: Interaction of dihydrogen with the frontier d-orbitals of a transition-metal (TM) complex.

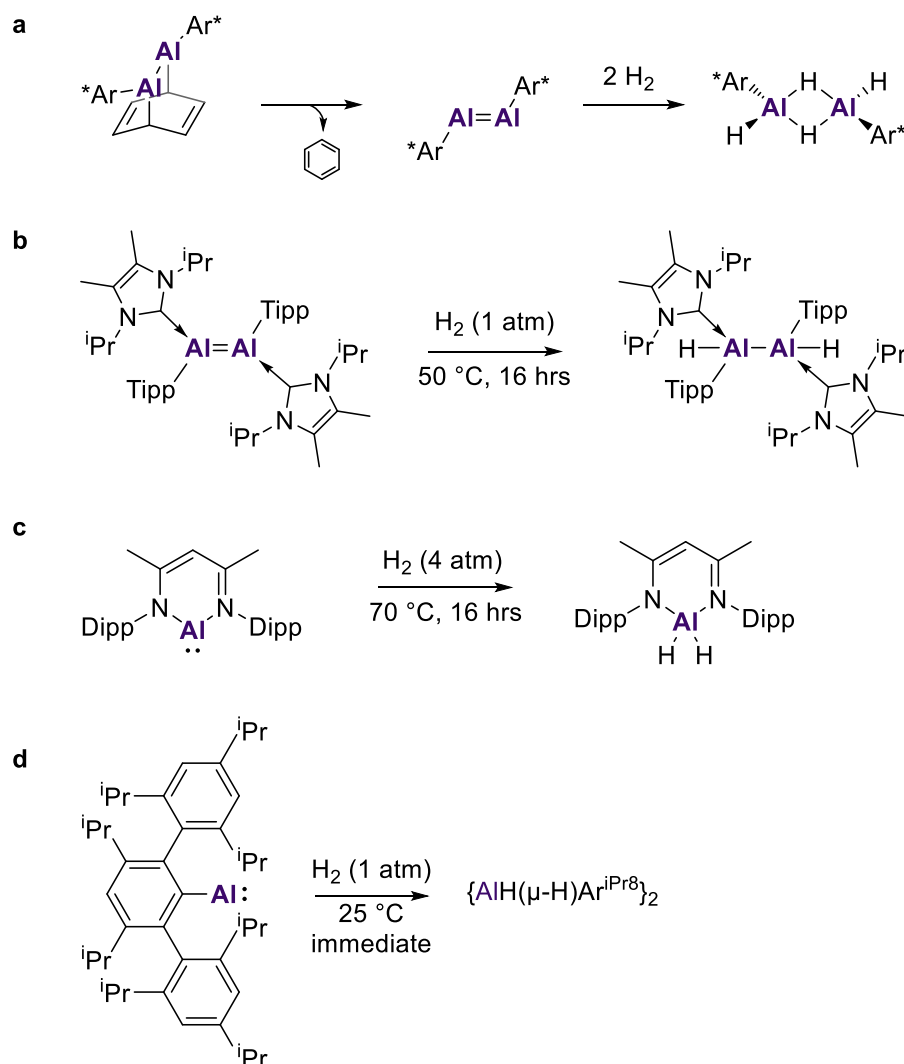
However, Power's seminal review highlighted how the chemistry of the heavier main group complexes bears similarities to that of transition metal complexes.¹ These similarities include open coordination sites and modest energetic gaps between

frontier molecular orbitals, permitting these main group complexes to undergo fundamental oxidative addition and reductive elimination reactions. The first report of dihydrogen activation by a main group compound came from Power, where a digermene, $\text{Ar}'\text{GeGeAr}'$ ($\text{Ar}' = 2,6\text{-diisopropylphenyl}$) was shown to add one, two and three equivalents of dihydrogen.²⁷ Since this milestone in main group chemistry, the activation of dihydrogen has been utilised as a benchmark reaction, to assess the reactive capability of novel main group complexes. This is due to its non-polarity, high bond enthalpy and industrial relevance. Theoretical studies often accompany reports of new oxidative additions, however the mechanisms considered typically assume a monomeric main group complex reacting with one equivalent of substrate. Furthermore, the frontier orbitals involved are assumed to mimic those of a transition metal complex. However, several low oxidation state main group complexes have been shown to be dimeric in solution or the solid state. Therefore, simple addition of $\text{E}-\text{H}$ bonds across the two metal centres must be considered as a mechanistic possibility when studying these complexes.

In the area of low oxidation main group chemistry, aluminium has been shown to exhibit high levels of reactivity with small molecules.^{3,46} There have been reports of both monomeric and dimeric Al(I) complexes, but there are few investigations into the mechanistic details of the reactivity that these species undergo. As discussed in previous chapters, dialumenes are neutral Al(I) dimers, containing an $\text{Al}=\text{Al}$ double bond. Due to the inherent instability of these low-oxidation state dimers, partially due to the presence of a small amount of diradicaloid character⁶⁹ (see Chapter 3), the initial reports were of so called masked dialumenes, which had reacted with aromatic solvents to yield the corresponding cycloadducts. One such example was reported by Tokito.²⁵⁶ This complex was shown to eliminate benzene, to yield a transient $\text{Al}=\text{Al}$ intermediate, which can react with dihydrogen under mild conditions (1 atm, 25 °C, 5

hours) (Scheme 5.1a). The hydrogenated product is dimeric and features both terminal and bridging hydrides. Inoue has reported two isolable dialumenes, stabilised by a N-heterocyclic carbene, and differing in the other substituent. The first reported base-stabilised dialumene featured a bulky silyl substituent, and was relatively planar, while the second featured a bulky aryl substituent, resulting in a more trans-bent and twisted structure.^{23,59} The latter of these was shown to react with dihydrogen at elevated conditions of 50 °C over a period of 16 hours (Scheme 5.1b), while the former exhibited no reactivity (decomposition was observed).⁵⁹ Despite the reactivity observed for Inoue's dialumene, there were challenges associated with characterizing the exact nature of the hydrogenated product. Due to the quadrupolar nature of the Al nucleus, no (Al—)H signals could be observed in the ¹H NMR spectrum. This, in addition to distinct iso-propyl signals observed, akin to that seen for the monomeric Al(III) dihydride, led to the conclusion that complete hydrogenation and cleavage of the Al—Al bond could not be ruled out. In addition to activation across two centres, there have been examples of dihydrogen activation by monomeric Al(I) complexes. The prototypical NacNacAl(I) species has been shown by Nikonov to activate dihydrogen (4 atm, 70 °C, overnight, Scheme 5.1c)⁵¹. Furthermore, the monomeric ⁱPr⁸ArAl(I) complex, reported by Power, requires milder conditions (1 atm, 25 °C, immediate) (Scheme 5.1d).²⁵⁷ In fact, in a more recent report from Power, the long sought after transient dialumene, ⁱPr⁸ArAl=ArⁱPr⁸, has been isolated in the solid state.⁶⁶ Despite decomposition to the monomer in solution, density functional theory calculations revealed that the activation of dihydrogen preferentially occurs via the dimer. A Gibbs Free Energy activation barrier of only 17.4 kcal mol⁻¹ was calculated, which contrasted with a barrier of 45.9 kcal mol⁻¹ calculated for activation at the monomer. Given that the reaction proceeds immediately at conditions of 25 °C and 1 atm, this is therefore strong evidence for activation of H₂ at the dimer in solution.

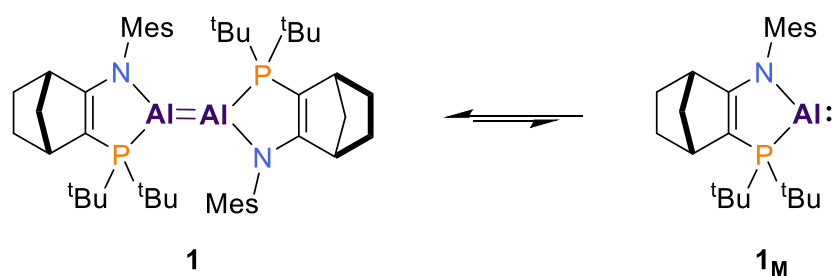
5 - Reactivity of a Base-stabilised Dialumene



Scheme 5.1: Examples of monomeric and dimeric Al(I) activations of dihydrogen.

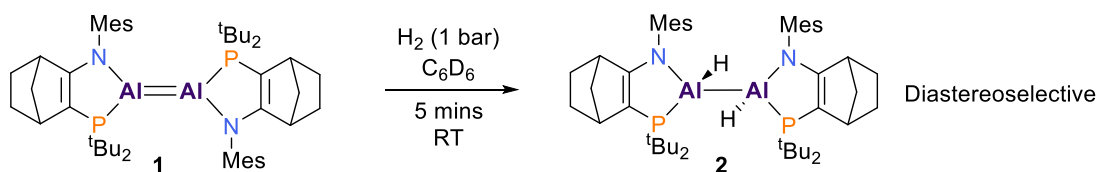
In Chapter 4, the computational characterization of the third exemplar of a base-stabilised dialumene, **1**, was discussed (Scheme 5.2). It was established that in solution, **1** reversibly dissociates to its monomeric form, **1_M**, enabled by a low bond dissociation energy.⁶¹ A key aspect of this complex is the supporting N,P-ligands, which act as stereochemical reporters. This ligand framework has been critical in revealing the structure and reactivity of low oxidation state aluminium complexes previously.^{61,62}

5 - Reactivity of a Base-stabilised Dialumene



Scheme 5.2: Previously reported dialumene **1** that exists in equilibrium with its corresponding aluminyl monomer, **1_M**.

The Cowley group sought to utilise the unique reporting capabilities of the amidophosphine (N,P) ligand framework. Previously, interconversion between diastereomers by reversible reductive elimination was revealed.⁶² This was enabled by the stereochemistry of the N,P ligand, which helped to uncover these “hidden” processes. Thus, by exploiting these reporting capabilities, insight into the reactivity of **1** was hoped to be gained. It was found that **1** reacted with dihydrogen at room temperature rapidly and quantitatively, to selectively form only two of six possible diastereomers of the dihydrodialane **2** (Scheme 5.3), *vide infra*. This contrasts with Inoue’s base-stabilised dialumenes, which do not react with H₂ or only react above 50 °C⁵⁹, but is consistent with the observed rapid reactivity of ⁱPr⁸ArAl(I) at 25 °C.^{66,257}

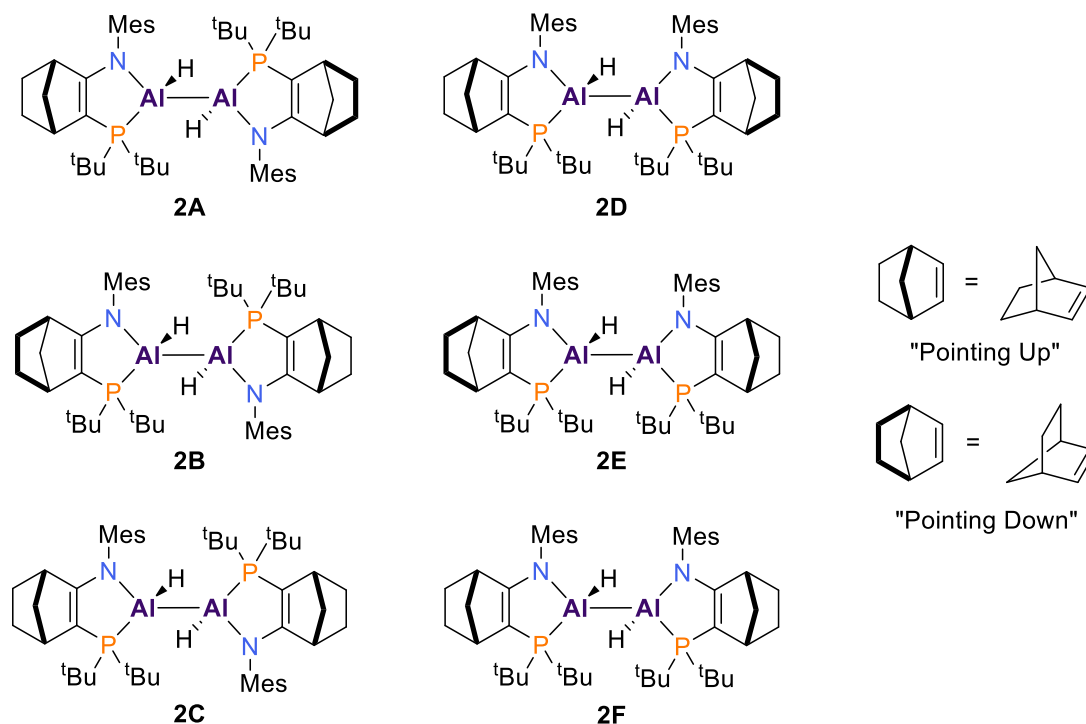


Scheme 5.3: Reaction of dialumene **1** with dihydrogen to form dihydrodialane **2**.

The dihydrodialane **2**, can exist as 6 possible diastereomers (**2A-F**), arising from the stereogenic aluminium centres and the stereocentres in the ligand backbone

5 - Reactivity of a Base-stabilised Dialumene

(Scheme 5.4).^{61,62} The isomers **2A-C** have the phosphine donors *anti* to each other, while the isomers **2D-F** have the phosphine donors *syn* to each other. Within these two subsets, the relative orientation (pointing up or down) of the methylene bridge of the norbornene backbone differentiates the individual isomers.⁶²

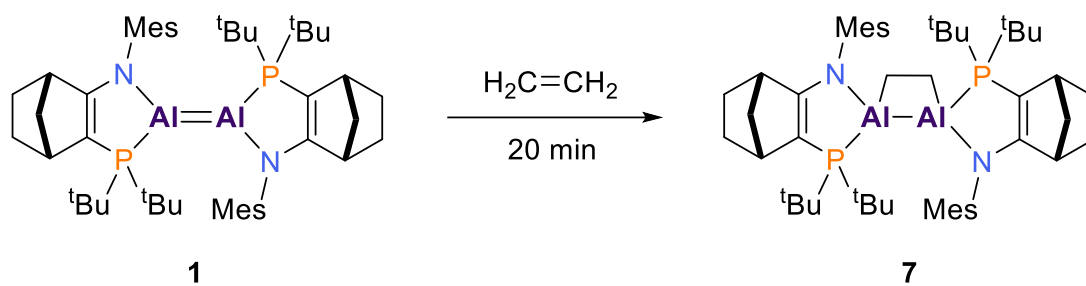


Scheme 5.4: The six possible diastereomers of the dihydrodialane **2**. Clarification of the relative orientations of the methylene bridges is shown on the right of the scheme.

The immediate product mixture upon reacting with H_2 was found to contain only two of the six possible diastereomeric products. These products were **2F** and either **2D** or **2E** although the latter could not unambiguously be distinguished by $^{31}\text{P}\{^1\text{H}\}$ or ^1H NMR spectroscopy, as evidenced by following the reaction using ^1H and $^{31}\text{P}\{^1\text{H}\}$ NMR. The initial product mixture equilibrated over 72 hrs to one containing all six possible diastereomeric products, **2A-F**, and then one containing only **2A-C** after 4 weeks.⁶²

5 - Reactivity of a Base-stabilised Dialumene

Like the previously reported dialumenes from Inoue⁵⁹, it has been shown that **1** can react with alkenes and alkynes to form four-membered aluminacycles. At ambient conditions, **1** was found to react with ethene rapidly (5-20 mins) to yield the dialuminacyclobutane **7** by formal [2+2] cycloaddition of the Al=Al and C=C bonds (Scheme 5.5).⁶¹ Signals for three distinct diastereomers were revealed by ³¹P{¹H} NMR spectroscopy, as a result of the locking of the stereogenic aluminium centres enforced by their cyclic structures. These structures have an *anti*-configuration of the amidophosphine backbone.



Scheme 5.5: Reactivity of **1** with ethene.

This chapter outlines the computational mechanistic work that was carried out to study the reaction of **1** with dihydrogen and ethene. More specifically, the activation of these substrates at the monomer and dimer will be explored and compared. In the case of dihydrogen, this investigation will be extended to the monomeric DippNacNacAl(I) complex, to probe whether the currently accepted mechanistic paradigm for the activation of small molecules by main group carbenoid species is suitable. Finally, the role of the small biradicaloid character known to be present in dialumenes (as explored by Tuononen⁶⁹ previously and expanded upon in Chapter 3) will be investigated in the reactivity with ethene. This was previously hinted at as a possibility

for transient dialumene species, but not explored as of yet for synthetic base-stabilised examples.⁶⁸

5.2 Methods

All electronic structure calculations were carried out using the Gaussian 16 (Rev. B.01), ORCA 4.2.1 and Amsterdam Density Functional 2023.101 (ADF) program suites.^{232,258–260} All geometries were optimised at the M062X-D3/def2-SVP^{160,210,211} level of theory using the Gaussian program, in the absence of symmetry constraints. The D3 version of Grimme's atom-pairwise dispersion correction was utilised including its original damping function.¹⁶⁴ Harmonic frequency calculations on optimised geometries were performed at the same level of theory as above. Minima and transition states were confirmed by the absence or presence of one imaginary eigenvalue in the Hessian matrix, respectively. The connectivity between minima and transition states was confirmed by distorting the geometry of the transition state along the imaginary vibrational mode of the reaction coordinate followed by subsequent unconstrained geometry optimisations. The frequency calculations also provided thermal and entropic corrections to the total energy in gas phase at $T = 298.15$ K and $p = 1$ atm within the rigid-rotor/harmonic oscillator (RRHO) approximation. The "ultrafine" grid option was used for numerical integrations, which is the default setting in Gaussian16 (Rev. B.01). Single point energy calculations were performed on optimised geometries at the B3LYP-D3/def2-TZVPP^{146,156,157,183} level of theory, in conjunction with the SMD solvation model²³³ and solvent parameters corresponding to those of benzene ($\epsilon=2.2706$). The basis set superposition error in dimeric structures was corrected with the counterpoise method by Boys and Simon.²³⁶

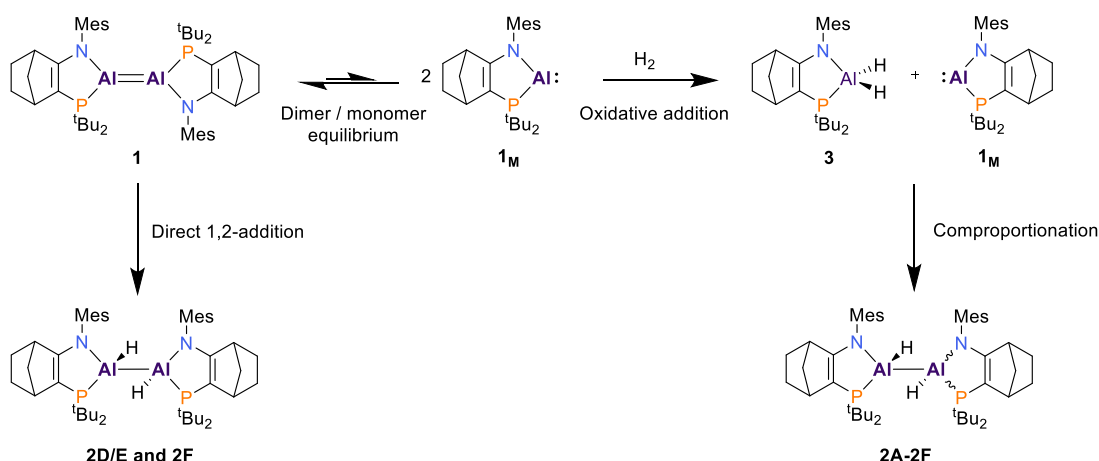
To be consistent with previous calculations (Chapter 4), bonding analyses were performed at the B3LYP-D3/6-311G(2d,2p) level of theory.^{234,235} The NBO program (version 6.0) was used to perform Natural Bond Orbital analyses on the optimised structures²³⁸ The AIMALL tool was used for topological QTAIM analyses of the electron density.²³⁹ DLPNO-CCSD(T) single-point energy calculations were performed using the ORCA program, in order to validate the chosen DFT methodology in selected cases. These calculations utilised the def2-TZVPP basis set in conjunction with the def2/J universal auxiliary basis set of Weigand. The RIJCOSX approximation was used to accelerate evaluation of Coulomb and HF exchange integrals. The def2-TZVPP/C correlation fitting auxiliary basis was employed for the Resolution of Identity (RI) used in the TrafoStep.^{261–264} In this work DLPNO-CCSD(T) calculations were performed on the basis of NormalPNO settings with the following default cut-off values: TCutMKN 10^{-3} , TCutPairs 10^{-3} , TCutPNO 3.33×10^{-7} . All calculations used the “VeryTightSCF” convergence criteria. The Morokuma/Ziegler energy decomposition analysis (EDA) was carried out using ADF, at the PBE0/TZP (all electron basis set) level of theory, employing Grimme’s D3 dispersion correction with Becke-Johnson damping.^{159,165,265} The EDA analysis was carried out in conjunction with the activation strain model.²⁶⁶ Finally, molecular structures and orbital isosurfaces were generated and visualised with the ChemCraft program.²⁴⁵

5.3 Results & Discussion

5.3.1 Oxidative addition of H₂

For the activation of dihydrogen, two plausible mechanisms must be considered (Scheme 5.6). The first is direct 1,2-addition of dihydrogen to the double bond of **1** i.e. a two-centre activation. This possibility is supported by previous experimental and

theoretical work carried out by Inoue and Rieger on a highly trans-bent and twisted iminodisilene species.²⁶⁷ The iminodisilene was shown to activate dihydrogen rapidly at room temperature. NMR and X-ray analysis indicated a stereospecific trans-hydrogenation of the double bond. A theoretical study revealed that the steric congestion of the bulky ligands induced a twist in the Si=Si bond, favourably pre-arranging the frontier orbitals for facile *anti*-addition of dihydrogen. Given that in Chapter 4, it was found that the structural trends of dialumenes mirror that of disilenes, it is reasonable to assume that a similar mechanism for the activation of dihydrogen by **1** may be operative.

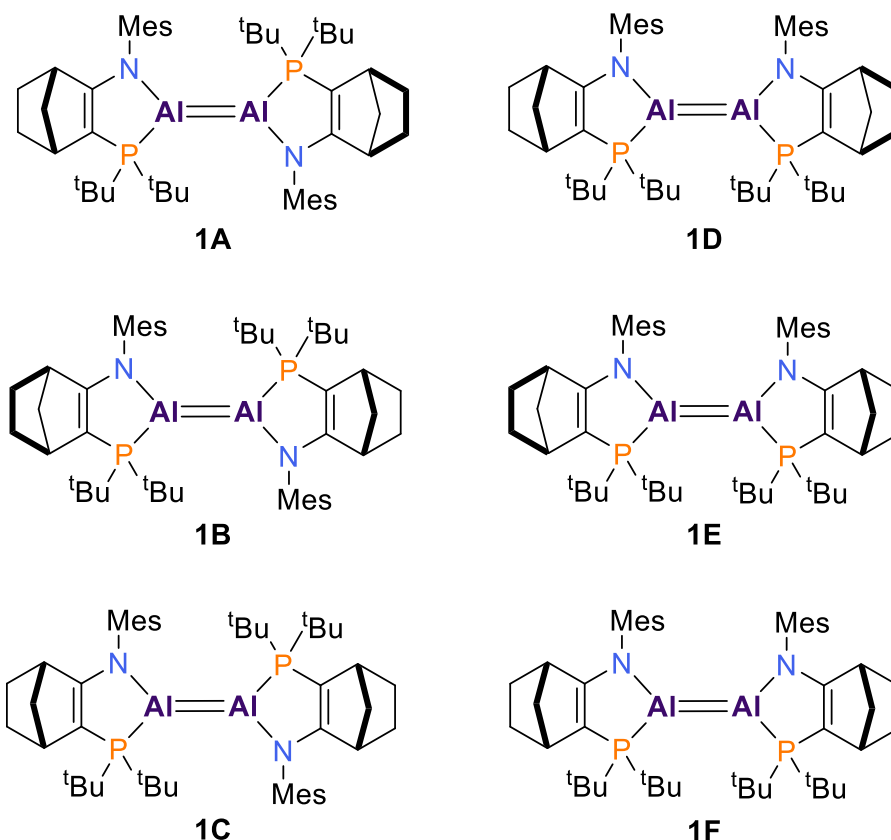


Scheme 5.6: Possible pathways to the dihydrodialane **2**.

The second possibility involves the dissociative equilibrium of **1**, generating two alumanyl monomers, **1_M**. Subsequent oxidative addition to one monomer yields the Al(III) dihydride **3**, which can then comproportionate with **1_M** to generate **2**. This latter pathway is unlikely in this present context, as treatment of **1** with 2 equivalents of pre-prepared **3** rapidly generates all six diastereomeric products, **2A-F**. Furthermore, theoretical work by Cao has investigated the activation of dihydrogen by the monomeric NacNacAl(I) complex (Scheme 5.1c).²⁶⁸ Consistent with the forcing

conditions (4 atm H₂, 70 °C, 16 hrs) required for this reaction to occur, Gibbs Free Energy activation barriers of >30 kcal mol⁻¹ were calculated. Thus, a direct 1,2-addition to the double bond is most likely, based on the above experimental and theoretical evidence.

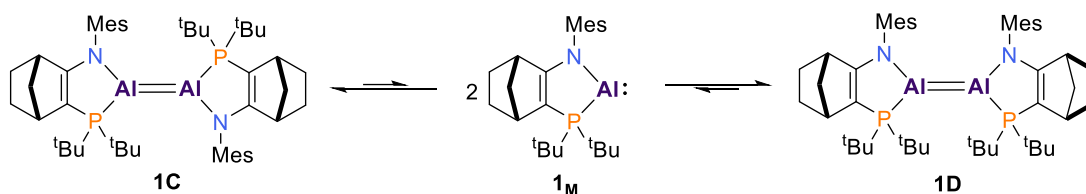
To gain insight into the details of the above reaction and the observed selectivity, DFT and *ab initio* calculations were carried out. Analogous to the different isomers of the dihydrodialane products **2A-F**, the dialumene **1** also exists as six possible diastereomers, plus their enantiomers (Scheme 5.7). The isomers **1A-C** have the phosphine donors *anti* to each other i.e. they are *E* isomers, while the isomers **1D-F** have the phosphine donors *syn* to each other i.e. they are *Z* isomers. Within these two subsets, the relative orientation of the methylene bridge of the norbornene backbone differentiates the individual isomers.

Scheme 5.7: The six possible diastereomers of the dialumene **1**.

Firstly, the calculations place the three *E* isomers of **1** within a narrow energetic window around the most stable isomer (*E*)-**1B** (ΔG_{298} : (*E*)-**1A** +2.1 kcal mol⁻¹; (*E*)-**1C** +1.3 kcal mol⁻¹), whilst all of the (*Z*)-isomeric forms lie higher in energy ((*Z*)-**1D** +5.7 kcal mol⁻¹; (*Z*)-**1E** 5.9 kcal mol⁻¹; (*Z*)-**1F** 4.8 kcal mol⁻¹). Therefore, all six diastereomers are thermodynamically accessible at room temperature, with the calculations predicting an energy span of only 5.9 kcal mol⁻¹. Interconversion between the diastereomers is presumed to proceed via dissociation into **1_M** and recombination as any of the diastereomers (Scheme 5.8).⁶¹ This is supported by the calculation of a low bond dissociation energy in Chapter 4 (ΔG_{298} of +7.1 kcal mol⁻¹, corrected for basis set superposition error).⁶¹ Rotation around the Al=Al axis can be excluded as a possibility. Relaxed potential energy surface scans were carried out, which provided

5 - Reactivity of a Base-stabilised Dialumene

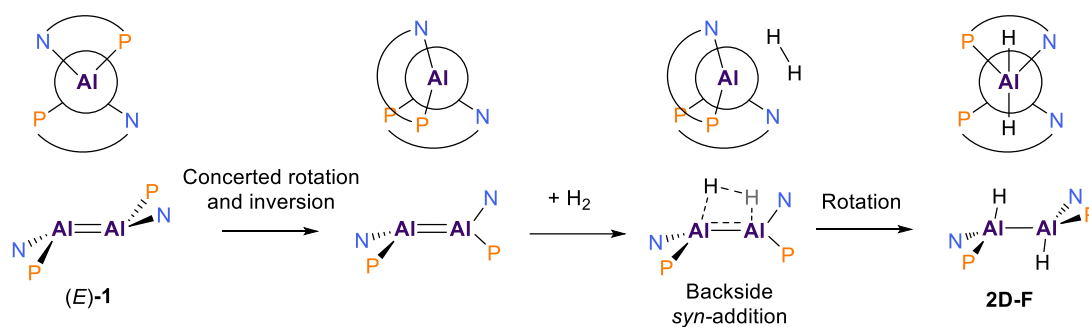
a lower-bound estimate of 50 kcal mol⁻¹ for the rotation. This is unsurprising, given the heavily trans-bent nature of **1**, coupled with the bulky substituents.



Scheme 5.8: Example of interconversion between isomers **1C** and **1D**, via initial dissociation into two equivalents of the Al(I) monomer **1M**, followed by recombination.

Having hypothesised that the most plausible mechanistic scenario is direct 1,2-addition of dihydrogen to the double bond, two main possibilities arise within this context. The first possibility is the concerted *syn*-addition of H₂ across the Al=Al bond, which directly converts **1A-C** into the experimentally observed **2D-F**. In the context of this work, a *syn*-addition will be defined as per the IUPAC Gold Book definition, as well as work from Baines^{269,270} – stereochemical arrangements corresponding to torsion angles between 0° and ±90°. This definition will be applied to the discussion of the transition states, specifically the H-Al-Al-H dihedral angle. To achieve *syn*-addition, concerted partial rotation and concomitant inversion of one aluminium centre must occur before addition of H₂ to provide the correct stereochemistry in the resulting product, due to the significant pyramidalization at the Al centres in **1** (Scheme 5.9).

5 - Reactivity of a Base-stabilised Dialumene



Scheme 5.9: Necessary mechanistic steps to achieve *syn*-addition of H_2 to the $\text{Al}=\text{Al}$ bond of $(E)\text{-1}$, to produce the observed products (2D/E and 2F). Newman projections, viewed down the $\text{Al}-\text{Al}$ axis (right to left) are shown above each structure, to help visualise the mechanistic steps.

Once addition to the “backside” (defined in Scheme 5.9) of the $\text{Al}=\text{Al}$ bond is complete, the stereochemistry is locked in place, preventing further inversion, with a final rotation of the $\text{Al}-\text{Al}$ single bond yielding the desired product with the hydrogen atoms *trans* to each other. A shorthand for the below discussed transition states is noted here; they are labelled according to the starting material and product formed. For example, the conversion of $(E)\text{-1A}$ to 2F proceeds through transition state $\text{TS}(\text{A-F})$, and so forth. All energies are reported relative to the lowest lying dialumene isomer $(E)\text{-1B}$.

The energetic cost for backside *syn*-addition to $(E)\text{-1A}$ is significant, proceeding with a barrier of $28.7 \text{ kcal mol}^{-1}$ (Figure 5.2), giving product 2F , with both of the P and N pairs lying on the same side of the $\text{Al}=\text{Al}$ bond. Although DLPNO-CCSD(T) gives an energetic barrier that is somewhat higher ($33.6 \text{ kcal mol}^{-1}$), both barriers are inconsistent with a reaction that proceeds rapidly at room temperature.

5 - Reactivity of a Base-stabilised Dialumene

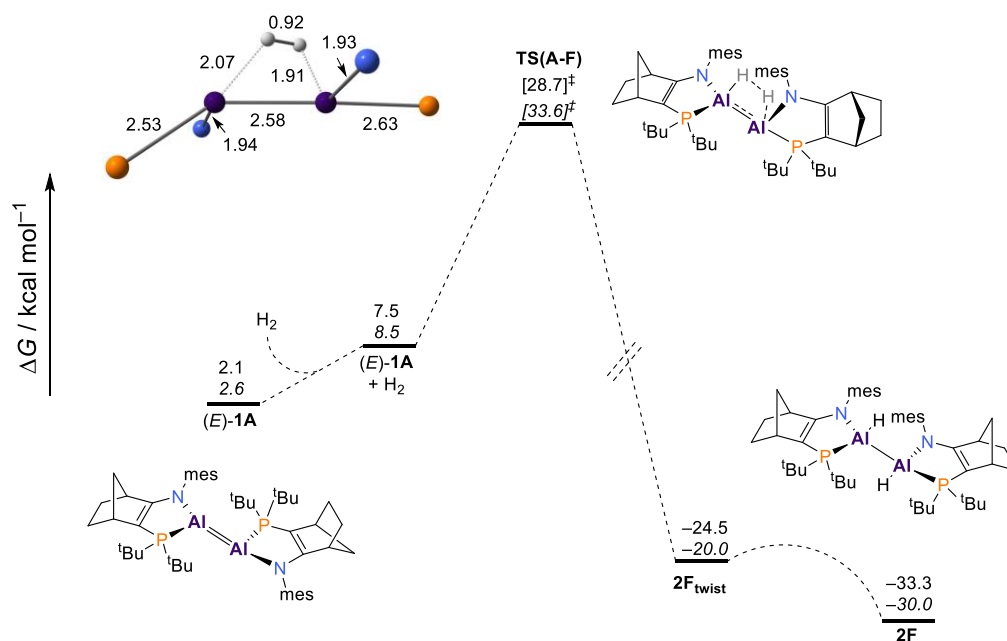


Figure 5.2: Computed reaction energy profile for backside *syn*-addition of H₂ to (*E*)-**1A**. Gibbs Free Energies (in kcal mol⁻¹) are given at $T = 298$ K and $p = 1$ atm relative to (*E*)-**1B** at the SMD(benzene)-B3LYP-D3/def2-TZVPP//M062X-D3/def2-SVP and DLPNO-CCSD(T)/def2-TZVPP/M062X-D3/def2-SVP (in *italics*) levels of theory.

Prior to the formation of **2F**, where the hydrogen atoms are trans to each other, a twisted intermediate, **2F_{twist}**, was located (Figure 5.3), lying 8.5 kcal mol⁻¹ higher in energy than **2F**. The dihedral angle defined by H-Al-Al-H is 86.9 ° in **2F_{twist}**, compared to a dihedral angle of 156.3 ° in **2F**. Furthermore, the Al—Al bond length in **2F_{twist}** is 0.04 Å shorter, while the Al—H bond lengths are consistent across both structures, at 1.61 Å.

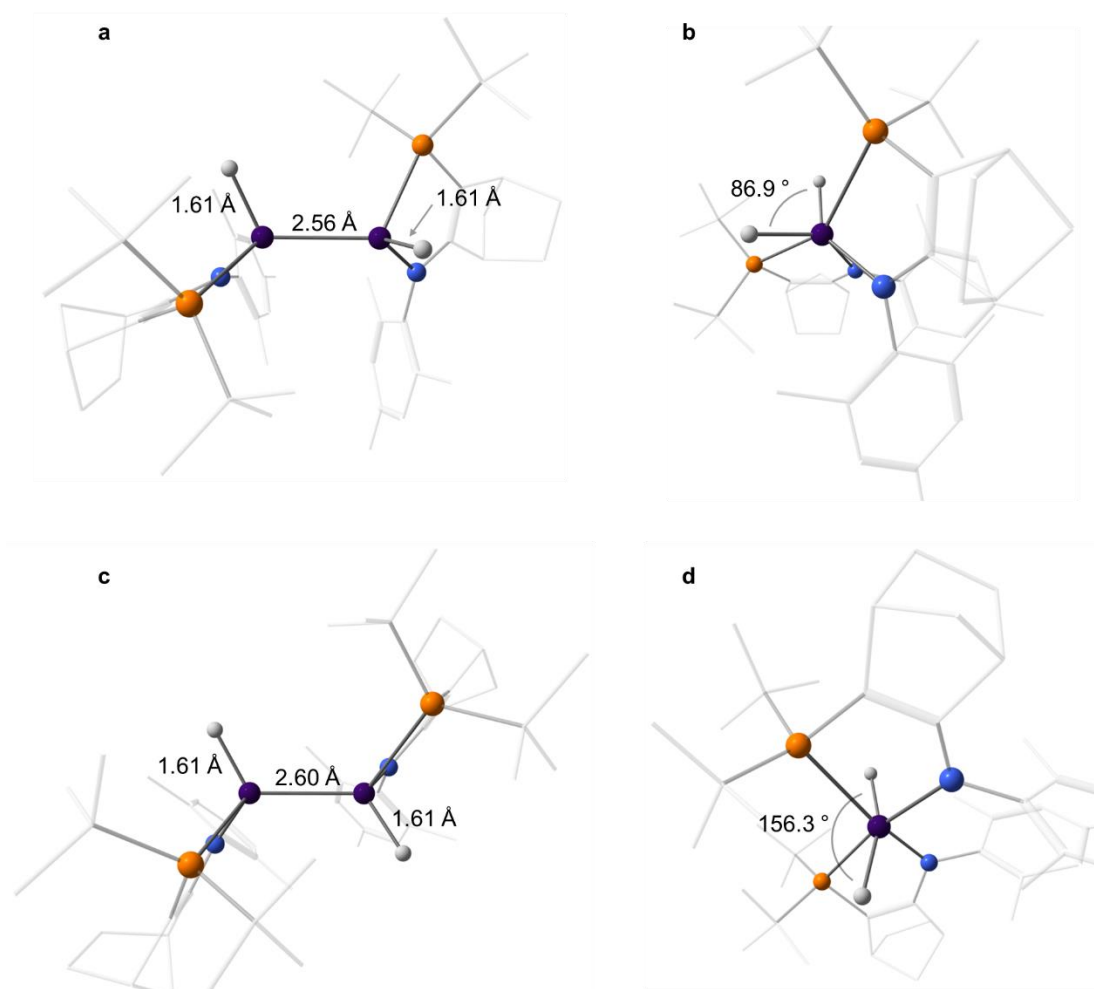


Figure 5.3: a) Front view of $2F_{\text{twist}}$ b) Side-on view of $2F_{\text{twist}}$ c) Front view of $2F$ d) Side-on view of $2F$.

Frontside *syn*-addition to (*E*)-**1B** results in **2F'**, the enantiomer of **2F**, proceeding with a slightly lower, but still sizeable barrier of 25.9 kcal mol⁻¹ (Figure 5.4). The analogous process for (*E*)-**1C** and (*E*)-**1C'** (the enantiomer of **1C**) results in products **2D** and **2E**, through barriers of 27.5 and 27.1 kcal mol⁻¹, respectively (Figure 5.5 and Figure 5.6).

5 - Reactivity of a Base-stabilised Dialumene

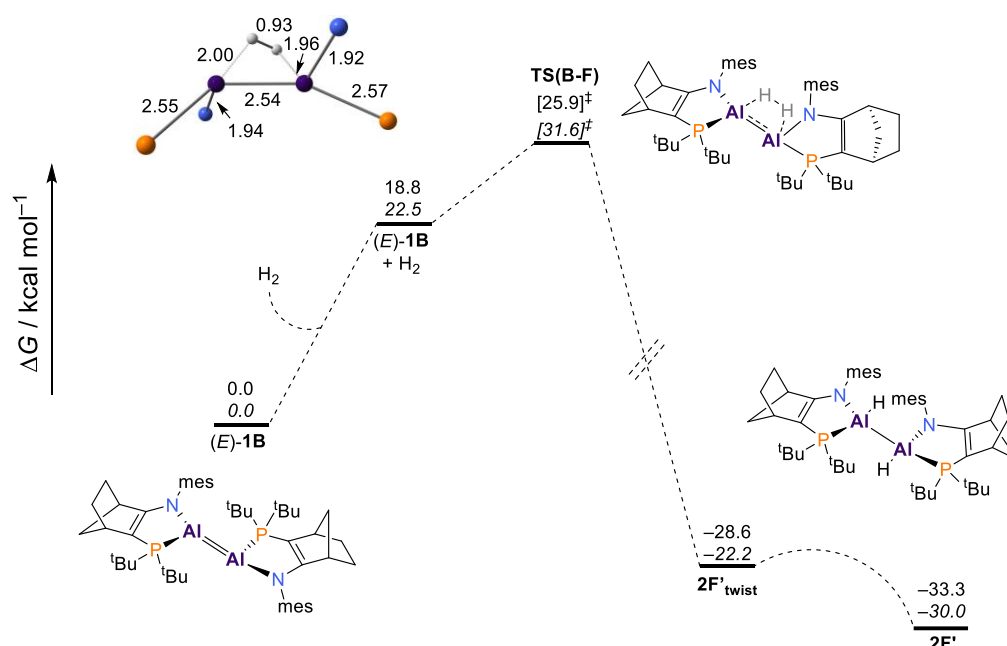


Figure 5.4: Computed reaction energy profile for backside *syn*-addition of H₂ to (E)-1B. Gibbs Free Energies (in kcal mol⁻¹) are given at $T = 298$ K and $p = 1$ atm relative to (E)-1B at the SMD(benzene)-B3LYP-D3/def2-TZVPP//M062X-D3/def2-SVP and DLPNO-CCSD(T)/def2-TZVPP/M062X-D3/def2-SVP (in *italics*) levels of theory.

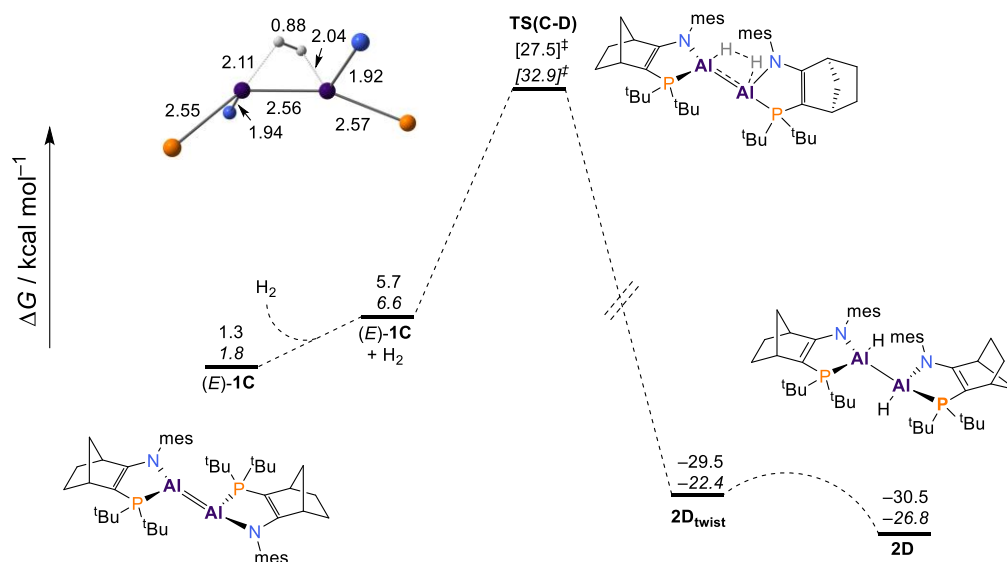


Figure 5.5: Computed reaction energy profile for backside *syn*-addition of H₂ to (E)-1C. Gibbs Free Energies (in kcal mol⁻¹) are given at $T = 298$ K and $p = 1$ atm relative to (E)-1B at the SMD(benzene)-B3LYP-D3/def2-TZVPP//M062X-D3/def2-SVP and DLPNO-CCSD(T)/def2-TZVPP/M062X-D3/def2-SVP (in *italics*) levels of theory.

5 - Reactivity of a Base-stabilised Dialumene

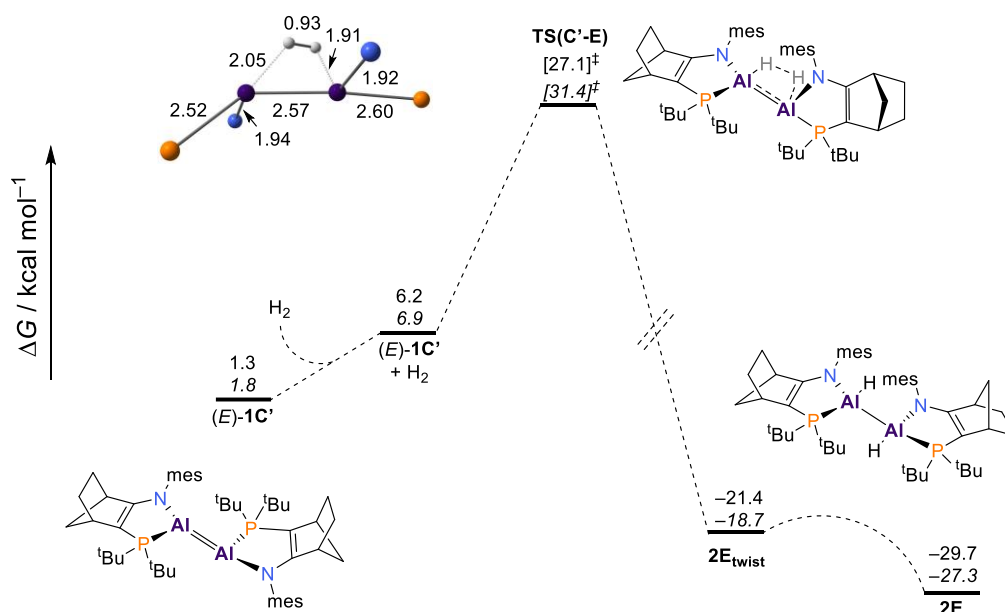


Figure 5.6: Computed reaction energy profile for backside *syn*-addition of H₂ to (*E*)-**1C'**. Gibbs Free Energies (in kcal mol^{−1}) are given at $T = 298$ K and $p = 1$ atm relative to (*E*)-**1B** at the SMD(benzene)-B3LYP-D3/def2-TZVPP//M062X-D3/def2-SVP and DLPNO-CCSD(T)/def2-TZVPP/M062X-D3/def2-SVP (in *italics*) levels of theory.

Calculation of the barriers for front- and backside *syn*-addition to (*E*)-**1F**, resulting in product **2A**, were found to be energetically inaccessible at ambient conditions, with barriers in excess of 25 kcal mol^{−1} (Figure 5.7 and Figure 5.8). This is consistent with the observation that the initial product mixture only contains products **2D** or **2E**, and **2F**. Given that the barriers of the above reactions are collectively in excess of 25 kcal mol^{−1} (both at the DFT and DLPNO-CCSD(T) level of theory), it can be concluded that *syn*-addition of H₂ to **1** is kinetically inaccessible.

5 - Reactivity of a Base-stabilised Dialumene

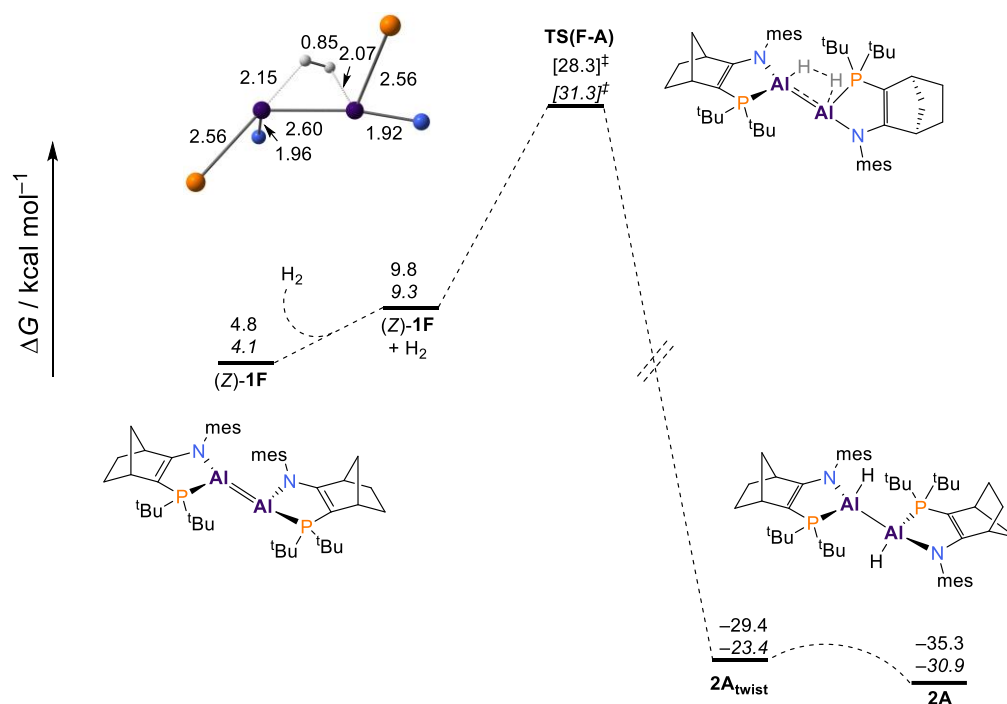


Figure 5.7: Computed reaction energy profile for backside *syn*-addition of H_2 to $(Z)\text{-1F}$. Gibbs Free Energies (in kcal mol⁻¹) are given at $T = 298$ K and $p = 1$ atm relative to $(E)\text{-1B}$ at the SMD(benzene)-B3LYP-D3/def2-TZVPP//M062X-D3/def2-SVP and DLPNO-CCSD(T)/def2-TZVPP/M062X-D3/def2-SVP (in *italics*) levels of theory.

5 - Reactivity of a Base-stabilised Dialumene

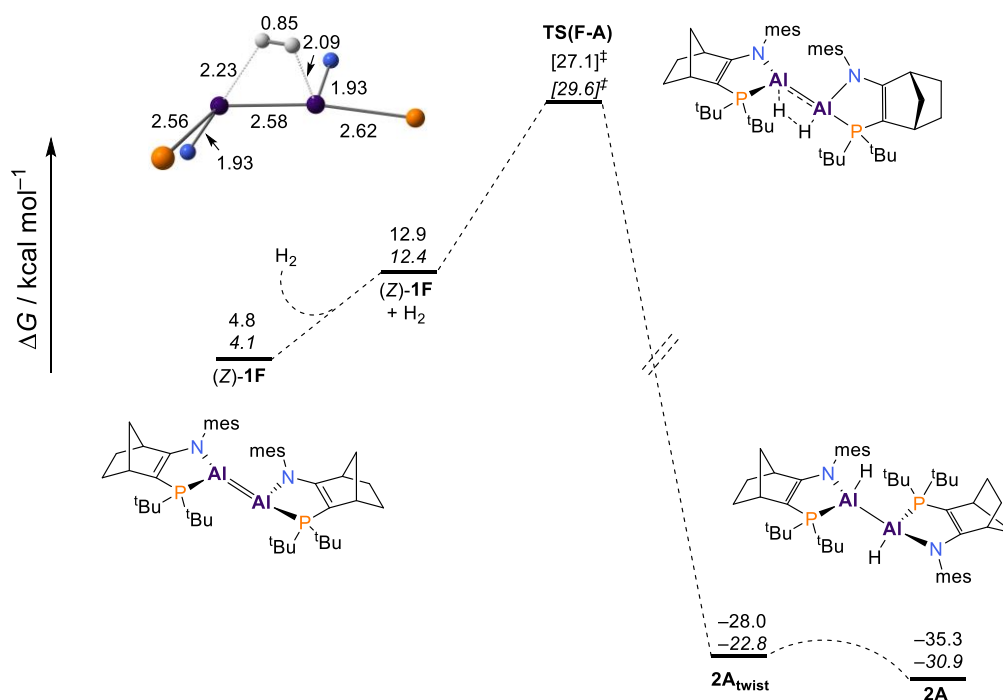
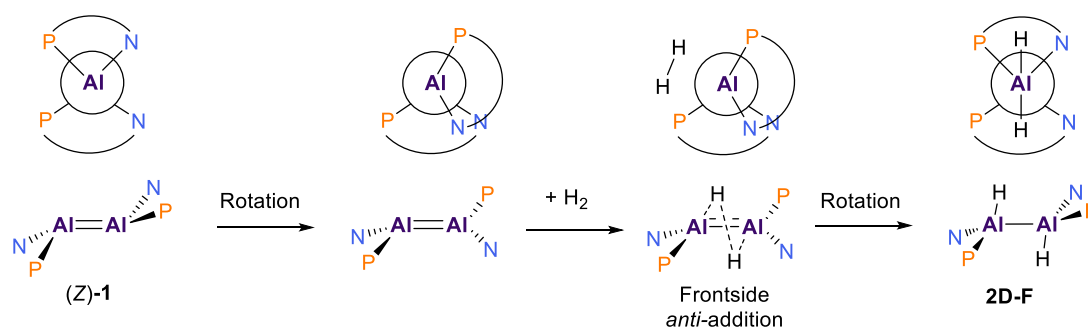


Figure 5.8: Computed reaction energy profile for frontside *syn*-addition of H₂ to (Z)-1F. Gibbs Free Energies (in kcal mol⁻¹) are given at $T = 298$ K and $p = 1$ atm relative to (E)-1B at the SMD(benzene)-B3LYP-D3/def2-TZVPP//M062X-D3/def2-SVP and DLPNO-CCSD(T)/def2-TZVPP/M062X-D3/def2-SVP (in *italics*) levels of theory.

Having established that *syn*-addition of H₂ to any of the isomers of **1** comes with prohibitively high activation barriers – inconsistent with the experimentally observed reaction times – the alternative *anti*-addition pathway was then explored. In order to access the observed products **2D-F**, partial rotation of the Al=Al bond is required (Scheme 5.10). Once dihydrogen has been added to the pyramidalized aluminium centres (both units rotated against one another), the stereochemistry is locked in, and partial rotation (in the opposite direction of the initial rotation) yields the final product with the hydrogen atoms *trans* to each other. However, this places stereochemical constraints on the mechanism: the observed products **2D**, **2E** or **2F** must result from concerted anti-addition to the (Z)-isomers **1D-F**. The requirement of only a partial

5 - Reactivity of a Base-stabilised Dialumene

rotation without inversion at one Al centre in this case implies a more favourable process, on the basis of a geometric strain argument.



Scheme 5.10: Necessary mechanistic steps to achieve *anti*-addition of H₂ to the Al=Al bond of (Z)-1, to produce the observed products (**2D/E** and **2F**). Newman projections, viewed down the Al-Al axis (right to left) are shown above each structure, to help visualise the mechanistic steps.

This is indeed the case, as evidenced by the calculated energetic barriers. Concerted *anti*-addition of dihydrogen to (Z)-**1D** to give the product **2D** proceeds through a facile barrier of 20.3 kcal mol⁻¹ (Figure 5.9). Likewise, addition to (Z)-**1E** and (Z)-**1F** proceeds through barriers of 18.3 and 18.5 kcal mol⁻¹, respectively (Figure 5.10 and Figure 5.11). The energetic separation between the barriers for addition to **1D** and **1E** are sufficiently sizeable to discriminate between the resulting products and consolidate selective formation of diastereomers **2E** and **2F**.

5 - Reactivity of a Base-stabilised Dialumene

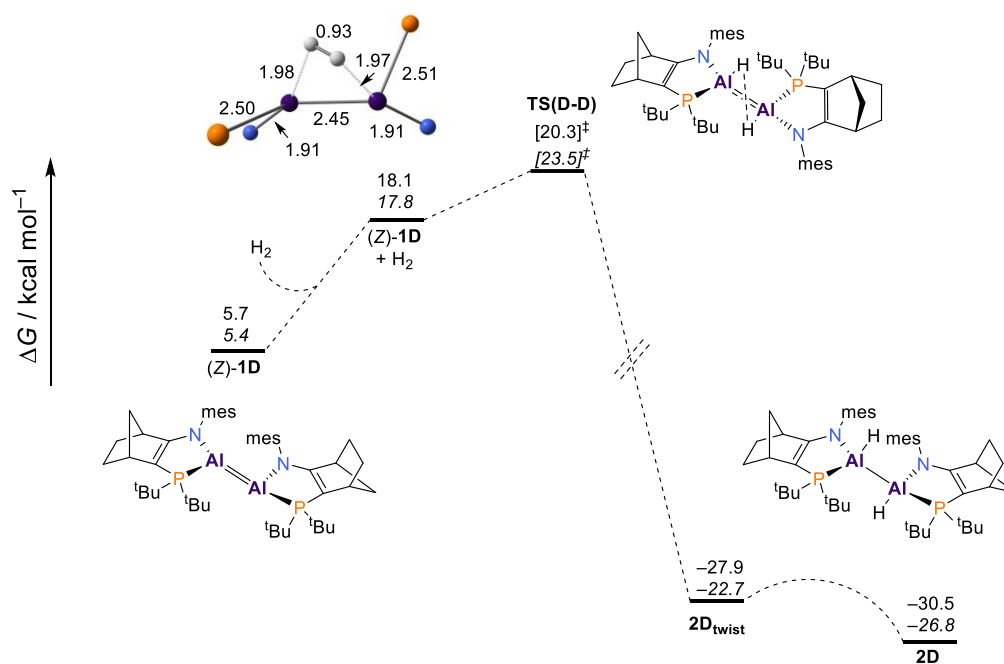


Figure 5.9: Computed reaction energy profile for *anti*-addition of H₂ to (Z)-1D. Gibbs Free Energies (in kcal mol⁻¹) are given at $T = 298$ K and $p = 1$ atm relative to (E)-1B at the SMD(benzene)-B3LYP-D3/def2-TZVPP//M062X-D3/def2-SVP and DLPNO-CCSD(T)/def2-TZVPP/M062X-D3/def2-SVP (in *italics*) levels of theory.

5 - Reactivity of a Base-stabilised Dialumene

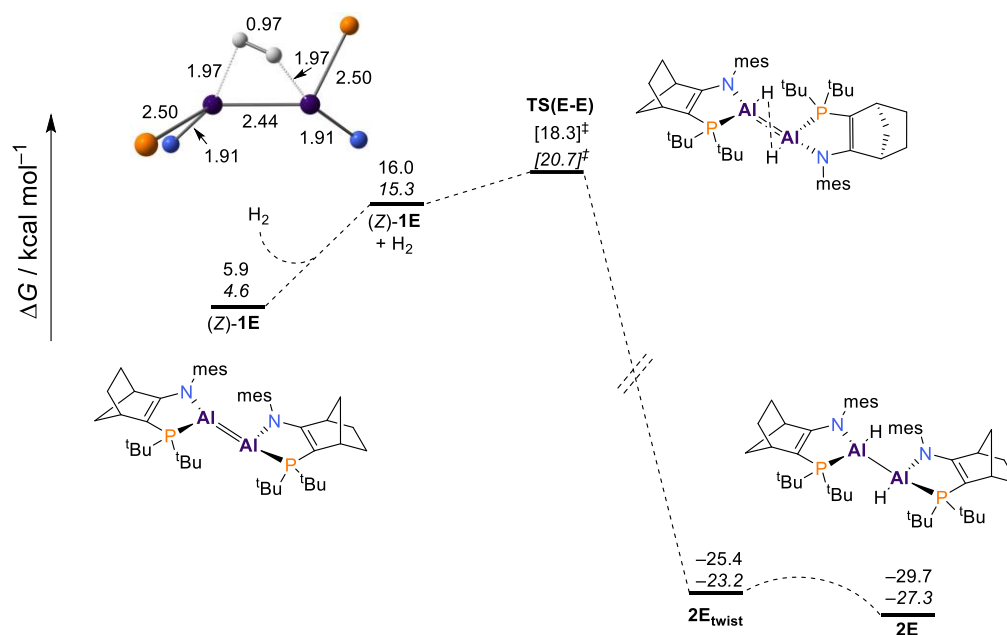


Figure 5.10: Computed reaction energy profile for *anti*-addition of H_2 to $(Z)\text{-1E}$. Gibbs Free Energies (in kcal mol^{-1}) are given at $T = 298 \text{ K}$ and $p = 1 \text{ atm}$ relative to $(E)\text{-1B}$ at the SMD(benzene)-B3LYP-D3/def2-TZVPP//M062X-D3/def2-SVP and DLPNO-CCSD(T)/def2-TZVPP/M062X-D3/def2-SVP (in *italics*) levels of theory.

5 - Reactivity of a Base-stabilised Dialumene

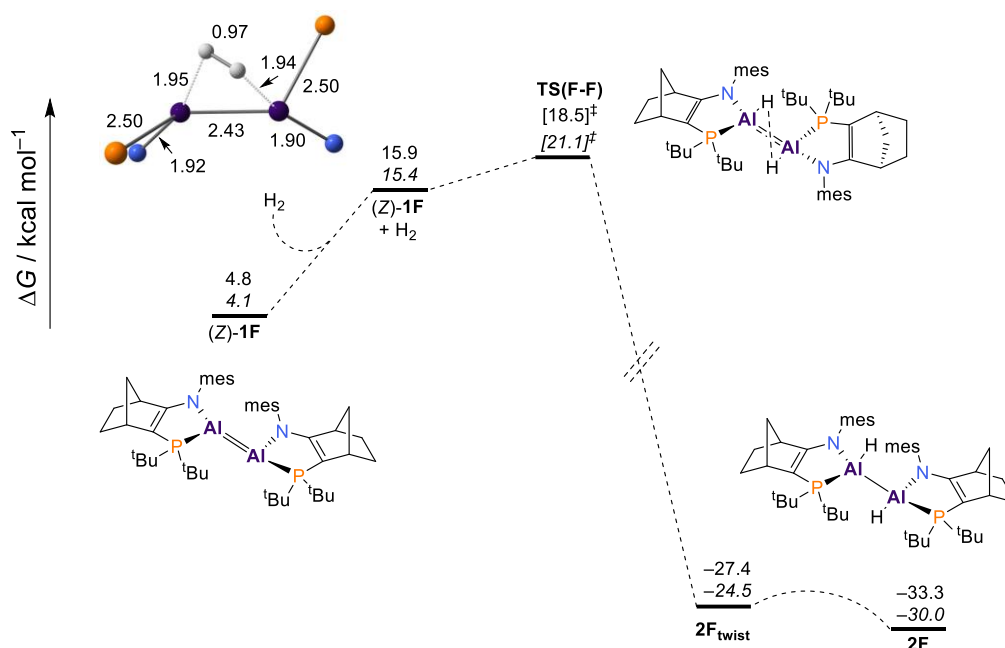


Figure 5.11: Computed reaction energy profile for *anti*-addition of H_2 to **(Z)-1F**. Gibbs Free Energies (in kcal mol^{-1}) are given at $T = 298 \text{ K}$ and $p = 1 \text{ atm}$ relative to **(E)-1B** at the SMD(benzene)-B3LYP-D3/def2-TZVPP//M062X-D3/def2-SVP and DLPNO-CCSD(T)/def2-TZVPP/M062X-D3/def2-SVP (in *italics*) levels of theory.

Finally, concerted *anti*-addition to **1A-C** was calculated to occur via barriers of 22.2-26.0 kcal mol^{-1} , which although not being as energetically high as calculated for the *syn*-addition, still renders these pathways not competitive (Figure 5.12, Figure 5.13 and Figure 5.14). A note aside here is that for **TS(C-C)**, there were issues with convergence of the transition state optimisation. Analytical frequencies were calculated for a partially optimised transition state, producing a single imaginary mode. Therefore, this structure was deemed trustworthy for subsequent analysis.

5 - Reactivity of a Base-stabilised Dialumene

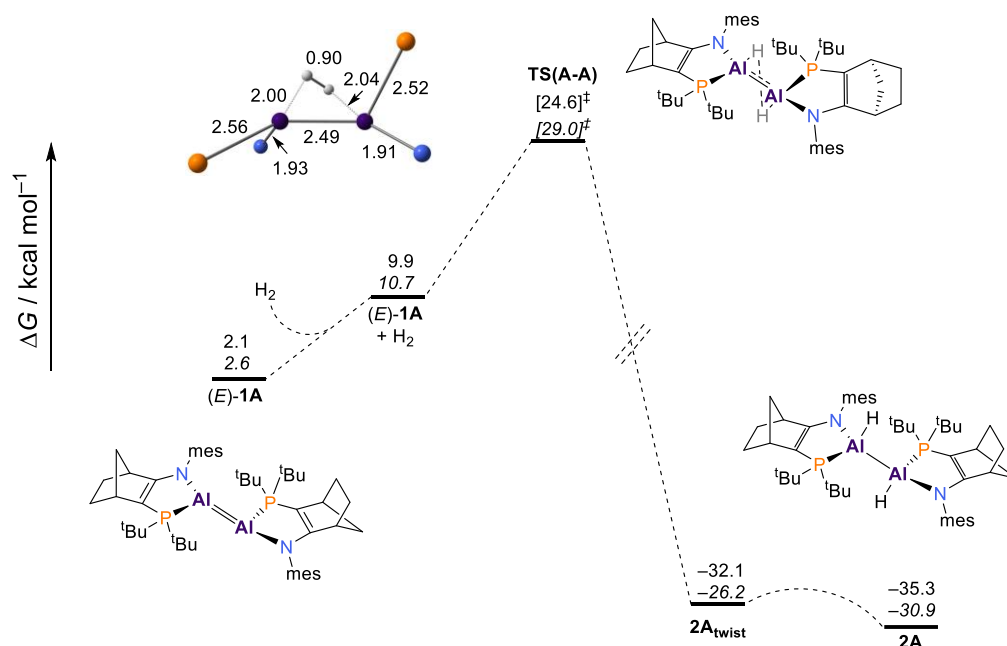


Figure 5.12: Computed reaction energy profile for *anti*-addition of H_2 to $(Z)\text{-1A}$. Gibbs Free Energies (in kcal mol^{-1}) are given at $T = 298 \text{ K}$ and $p = 1 \text{ atm}$ relative to $(E)\text{-1B}$ at the SMD(benzene)-B3LYP-D3/def2-TZVPP//M062X-D3/def2-SVP and DLPNO-CCSD(T)/def2-TZVPP/M062X-D3/def2-SVP (in *italics*) levels of theory.

5 - Reactivity of a Base-stabilised Dialumene

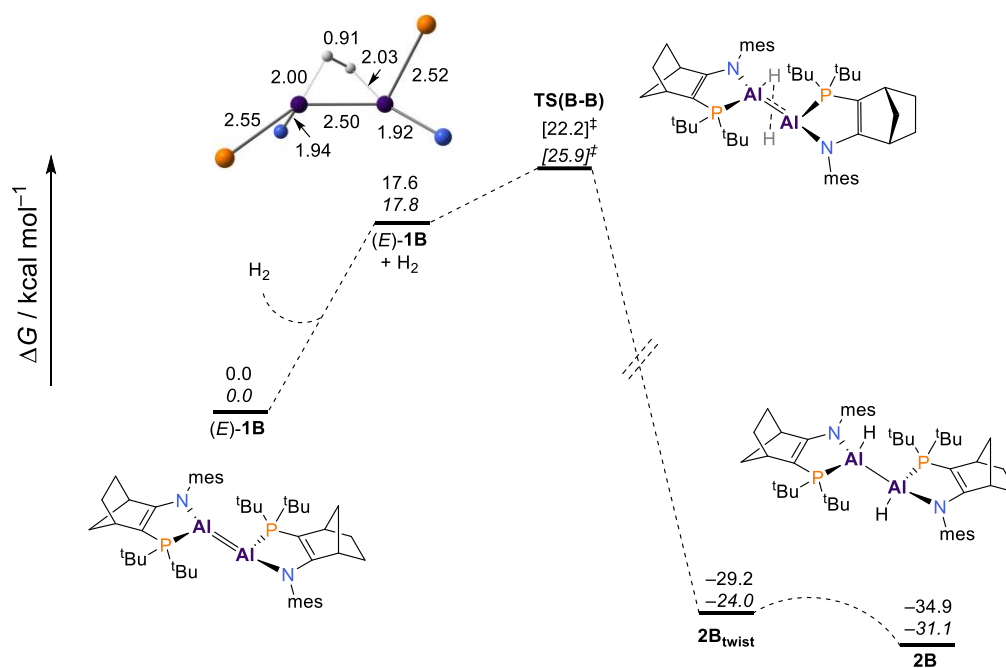


Figure 5.13: Computed reaction energy profile for *anti*-addition of H₂ to (Z)-1B. Gibbs Free Energies (in kcal mol⁻¹) are given at $T = 298$ K and $p = 1$ atm relative to (E)-1B at the SMD(benzene)-B3LYP-D3/def2-TZVPP//M062X-D3/def2-SVP and DLPNO-CCSD(T)/def2-TZVPP/M062X-D3/def2-SVP (in *italics*) levels of theory.

5 - Reactivity of a Base-stabilised Dialumene

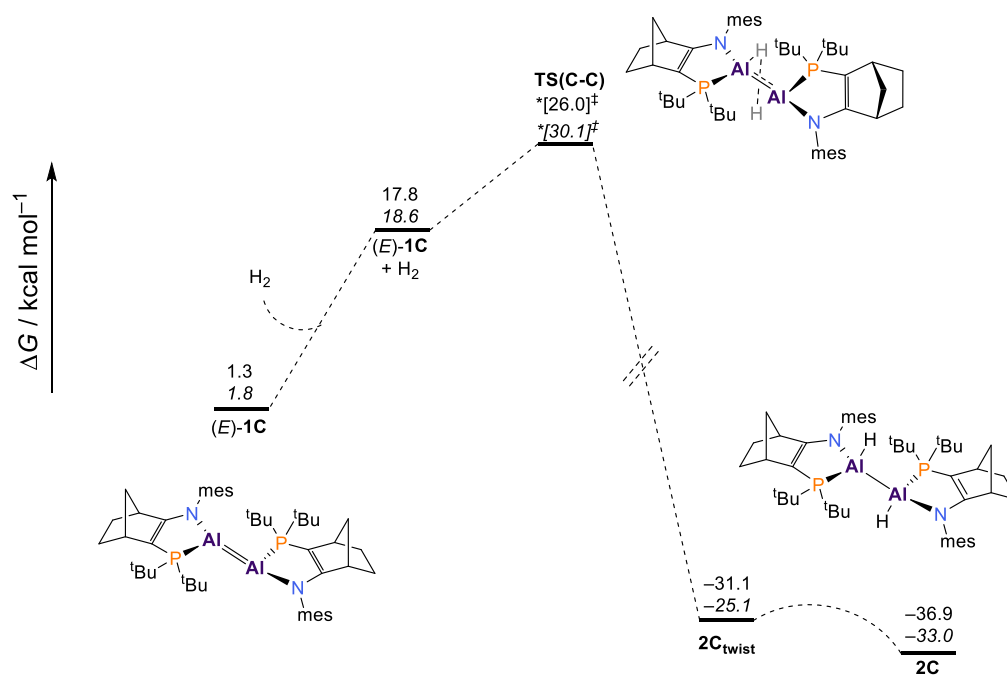


Figure 5.14: Computed reaction energy profile for *anti*-addition of H₂ to (E)-1C. Gibbs Free Energies (in kcal mol⁻¹) are given at $T = 298$ K and $p = 1$ atm relative to (E)-1B at the SMD(benzene)-B3LYP-D3/def2-TZVPP//M062X-D3/def2-SVP and DLPNO-CCSD(T)/def2-TZVPP/M062X-D3/def2-SVP (in *italics*) levels of theory. *partially optimised transition state

It has now been established that anti-addition to the Z-isomers of **1** constitutes the most favourable mechanistic pathway to access the experimentally observed products, with the calculations having identified that it is specifically **2E** and **2F** that form. It was found that the alternative *syn*-addition of H₂ to both the *E* and *Z* isomers of **1** consistently gives kinetically inaccessible activation barriers in excess of 25 kcal mol⁻¹. These findings were further supported by DLPNO-CCSD(T) calculations, that gave good agreement with the DFT calculated energetic barriers.

To gain further insight into these results, **TS(F-F)** was chosen as a representative example to study in more detail, from a geometric and electronic structure point of view. The optimized geometry of **TS(F-F)** reveals that the dihydrogen bond is

significantly activated (0.97 Å), through donation and backdonation interactions with the Al=Al unit. This is evident from visual examination of the frontier molecular orbitals of **TS(F-F)** (Figure 5.15). The HOMO and LUMO correspond to the π and π^* orbitals of the “slipped” Al=Al bond, resulting from the admixture of the $\pi(\text{Al}-\text{Al})$ and $\sigma^*(\text{Al}-\text{Al})$ orbitals.¹⁹ The twisted geometry of the transition state enforces localisation of electron density on the Al centres.

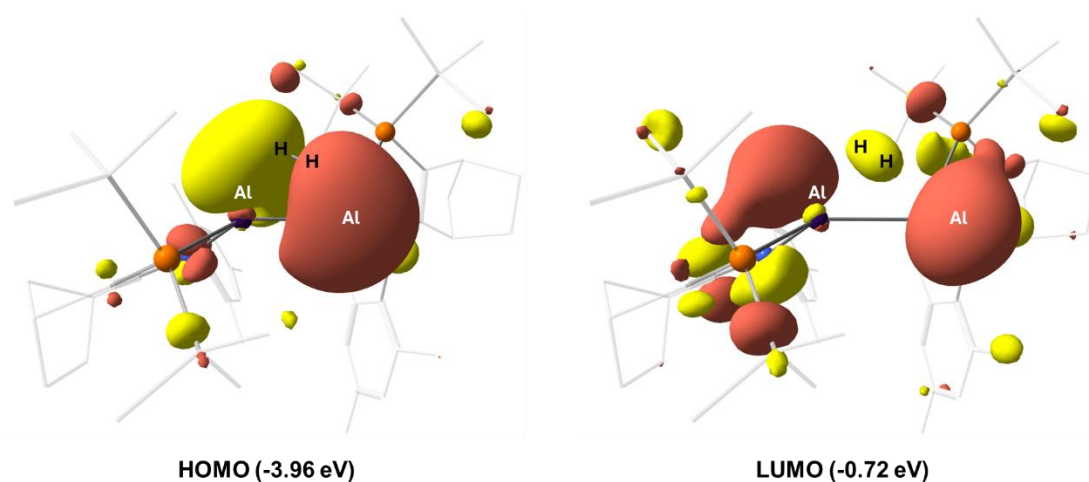


Figure 5.15: DFT-calculated HOMO and LUMO (B3LYP-D3/6-311G(2d,2p), isovalue 0.036 a.u.) in the transition state **TS(F-F)**, which are consistent with a bonding interaction between the two reacting fragments.

In addition to visual inspection of the canonical Kohn-Sham frontier orbitals, natural bond orbital calculations (NBO) were carried out, to gain insight into the donor-acceptor interactions taking place in the transition state, via analysis of the fragment interaction terms from second order perturbation theory (Figure 5.16a). The stabilisation energy, $E^{(2)}$ associated with donation from $\pi(\text{Al}-\text{Al})$ to $\sigma^*(\text{H}-\text{H})$ in **TS(F-F)** is 347 kcal mol⁻¹. A second donation from $\sigma(\text{H}-\text{H})$ to $\pi^*(\text{Al}-\text{Al})$ has a much smaller magnitude of only 21 kcal mol⁻¹. The dominant term is consistent with substantially weakened Al—Al and H—H bonds in the transition state, evidenced by the natural

5 - Reactivity of a Base-stabilised Dialumene

bond orbital electron populations of $1.05\ e^-$ and $0.5\ e^-$, respectively. This is supported by the optimised structural parameters and calculated NPA charges (Figure 5.16b and Figure 5.16c). Appreciable activation of the H—H bond is evident from the bond length of $0.97\ \text{\AA}$, and a build-up of negative charge on each hydrogen atom ($-0.16 / -0.18$ electrons).

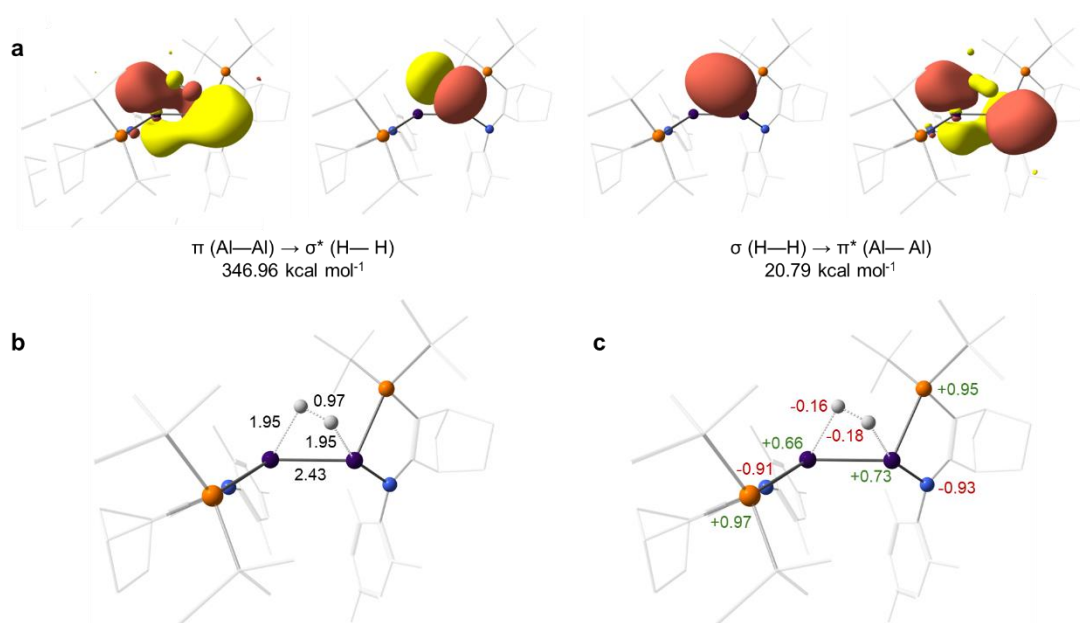


Figure 5.16: Summary of key results of the NBO and structural analysis of **TS(F-F)** (B3LYP-D3/6-311G(2d,2p)). (a) Dominant donor/acceptor orbitals (isovalue $0.036\ \text{au}$) along with corresponding 2nd order perturbative interaction energies $E^{(2)}$ and orbital occupancies. (b) Molecular connectivity with selected bond lengths in Å. (c) NPA charges.

In order to put these stabilisation energies from the donor-acceptor interactions in perspective, Table 5.1 provides the corresponding data for **TS(A-A)** and **TS(F-A)**. For **TS(A-A)**, the stabilisation energy, associated with donation from $\pi(\text{Al—Al})$ to $\sigma^*(\text{H—H})$ is $117.48\ \text{kcal mol}^{-1}$, while the stabilisation energy associated with donation from $\sigma(\text{H—H})$ to $\pi^*(\text{Al—Al})$ is $11.25\ \text{kcal mol}^{-1}$. In contrast, for **TS(F-A)**, stabilisation energies of 53.10 and $0.80\ \text{kcal mol}^{-1}$ for the $\pi(\text{Al—Al})$ to $\sigma^*(\text{H—H})$ and $\sigma(\text{H—H})$ to

$\pi^*(\text{Al—Al})$, respectively, were calculated. What is clear from these results is that **TS(F-F)**, and more broadly speaking, the transition states corresponding to anti-addition to **1D-F** provide ideal geometries for H_2 addition due to maximising overlap between the lobes of the frontier orbitals of **1D-F** and H_2 .

Table 5.1: Survey of key NBO donor/acceptor pairs for examples of the transition states, corresponding to *anti*- and *syn*-addition to either an *E* or *Z* diastereomer. Energies shown have units of kcal mol^{-1} .

	$\pi (\text{Al—Al}) \rightarrow \sigma^* (\text{H—H})$	$\sigma (\text{Al—Al}) \rightarrow \pi^* (\text{H—H})$
TS(A-A)	117.48	11.25
TS(F-A)	53.10	0.80
TS(F-F)	346.96	20.79

Considering further alternative mechanisms, a stepwise addition of dihydrogen to the Al=Al bond was calculated to be kinetically inaccessible, having a barrier of $42.0 \text{ kcal mol}^{-1}$ (Figure 5.17). This is consistent with the experimentally observed stereoselectivity, as initial activation at one aluminium centre via this mechanism would permit rotation about the Al—Al vector, therefore potentially destroying the stereoselectivity. This mechanistic possibility resembles that reported for the initial step for dihydrogen activation by multiply bonded Ge and Sn compounds²⁹, and a similar step has also been explored for addition to a (*Z*)-diiminodisilene species.²⁶⁷

5 - Reactivity of a Base-stabilised Dialumene

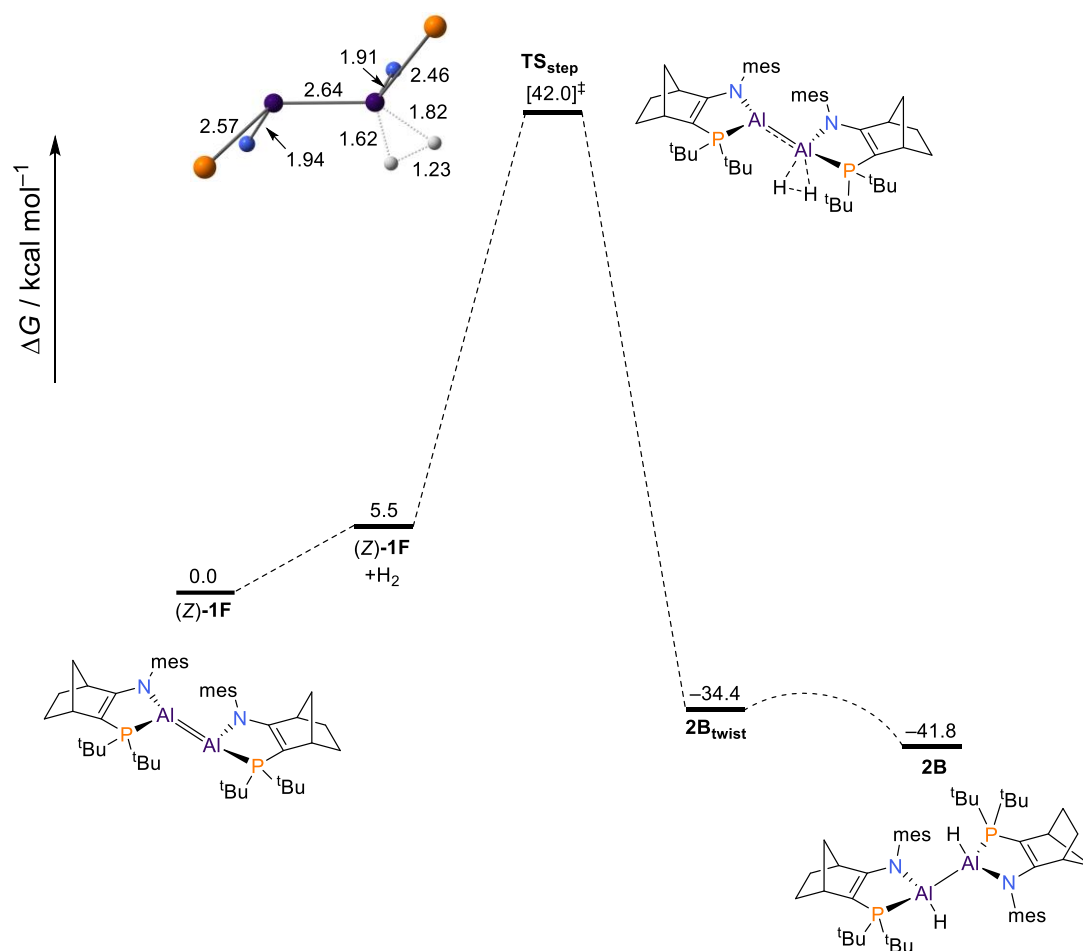


Figure 5.17: Computed reaction energy profile for stepwise addition of H_2 to $(Z)\text{-1F}$. Gibbs Free Energies (in kcal mol $^{-1}$) are given at $T = 298$ K and $p = 1$ atm at the SMD(benzene)-B3LYP-D3/def2-TZVPP//ONIOM(M062X-D3/def2-SVP:UFF) level of theory. ONIOM was utilised due to issues with convergence of the transition state.

As discussed in the previous sections, the direct 1,2-addition mechanistic possibility has been explored. The second possibility outlined above involves the dissociative equilibrium of **1**, generating two alumanyl monomers, **1_M**. Subsequent oxidative addition to the Al(I) centre of **1_M** yields the Al(III) dihydride **3**, which can then comproportionate with **1_M** to generate **2** (Scheme 5.6). Concerted oxidative addition to **1_M** to yield **3** was calculated to proceed via a prohibitively high Free Energy barrier of 38.6 kcal mol $^{-1}$ (Figure 5.18). The DLPNO-CCSD(T) activation barrier was calculated to be 40.3 kcal mol $^{-1}$, in good agreement with DFT. Therefore, despite the

5 - Reactivity of a Base-stabilised Dialumene

reversible dissociation of **1** to **1_M** shown to be operative at room temperature, the monomeric alumanyl would not be able to react with dihydrogen under these ambient conditions. This result is consistent with the previously calculated energetic span that was in excess of 30 kcal mol⁻¹ for H₂ activation by the NacNacAl(I) system (Scheme 5.1c).²⁶⁸

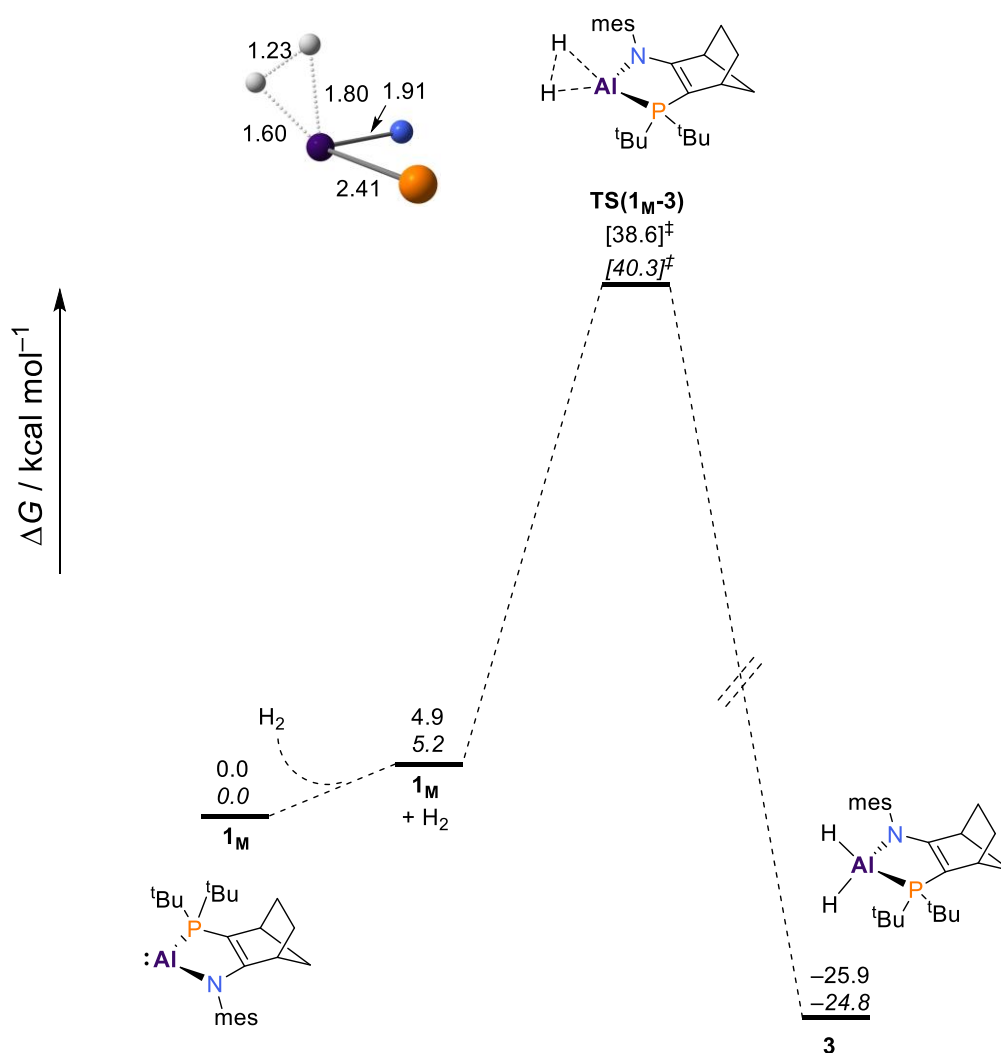


Figure 5.18: Computed reaction energy profile for addition of H₂ to **1_M**. Gibbs Free Energies (in kcal mol⁻¹) are given at $T = 298$ K and $p = 1$ atm at the SMD(benzene)-B3LYP-D3/def2-TZVPP//M062X-D3/def2-SVP and DLPNO-CCSD(T)/def2-TZVPP/M062X-D3/def2-SVP (in *italics*) levels of theory.

5 - Reactivity of a Base-stabilised Dialumene

In order to further corroborate the above mechanistic and orbital analysis, an activation strain and energy decomposition analysis was carried out. The overall bonding energy between two molecular fragments can be represented by the following equation:

$$\Delta E = \Delta E_{strain} + \Delta E_{int} \quad (5.1)$$

The energy required to distort the fragments from their equilibrium geometries to the geometries that they attain in the interacting molecule is given by the strain energy, ΔE_{strain} , which is offset by the stabilising interaction energy ΔE_{int} . The interaction energy can be further decomposed into contributions stemming from electrostatic interaction (ΔE_{elec}), Pauli repulsion (ΔE_{Pauli}), orbital interaction (ΔE_{orb}) and dispersion energy (ΔE_{disp}), given by the following equation:

$$\Delta E_{int} = \Delta E_{elec} + \Delta E_{Pauli} + \Delta E_{orb} + \Delta E_{disp} \quad (5.2)$$

The electrostatic term is the quasi-classical electrostatic interaction between the unperturbed charge densities of each fragment, involving attraction to the nuclei. The Pauli repulsion term, involving same-spin electrons, accounts for steric repulsion, arising from destabilising interactions between the occupied orbitals of the fragments. The orbital term accounts for charge transfer, polarisation, and electron-pair interactions upon relaxation of the fragment orbitals. Finally, a stabilising dispersion energy term is added.

In Table 5.2, the strain (ΔE_{strain}) and interaction (ΔE_{int}) energies for selected transition states, representative of the different mechanisms discussed above (*syn*-addition, *anti*-addition and monomeric activation), are shown. For the activation of dihydrogen at the monomer, the strain energy is significant, at 48.95 kcal mol⁻¹. The primary source of this strain originates from the dihydrogen fragment (41.76 kcal mol⁻¹), which is rather unsurprising, given the significant activation of this bond (1.23 Å). Similar

results have been found for the activation of dihydrogen by an aluminyl anion monomer by Schaefer.²⁷¹ This strain energy is offset by an interaction energy between dihydrogen and the dialumene of $-24.11 \text{ kcal mol}^{-1}$, yielding an overall bonding energy of $24.84 \text{ kcal mol}^{-1}$. For the activation at the dimer, the overall strain energies were found to be smaller, mainly due to a less pronounced activation of dihydrogen (e.g. 0.97 \AA for **TS(F-F)**). Of the dimeric activations, the interaction energies were found to be most stabilising for **TS(F-F)**. Interestingly, the interaction energy in **TS(1_M-3)** was calculated to be $2.32 \text{ kcal mol}^{-1}$ more stabilising than **TS(F-F)**, due to more stabilising electrostatic and orbital terms, which help to counteract a large Pauli repulsion term. However, this interaction energy is largely offset by the more destabilising strain energy, with $48.95 \text{ kcal mol}^{-1}$ calculated for **TS(1_M-3)** and $24.59 \text{ kcal mol}^{-1}$ calculated for **TS(F-F)**. Overall, the most significant result is that the overall energy (ΔE) is smallest for *anti*-addition to the Z isomer, **1F**, consistent with the energetic barriers and orbital analysis results discussed above (canonical and NBO).

Table 5.2: Activation strain and energy decomposition analysis of selected transition states. All energies stated have units of kcal mol^{-1} . The fragments are defined as the H_2 molecule and the dialumene **1**.

	ΔE_{strain}			ΔE_{int}	ΔE_{elec}	ΔE_{pauli}	ΔE_{orb}	ΔE_{disp}	ΔE
	[Al]	H ₂	Total						
TS(A-A)	21.00	6.83	27.84	-16.17	-30.11	63.07	-46.15	-2.98	11.67
TS(F-A)	18.86	3.53	22.40	-8.80	-24.87	63.01	-43.96	-2.98	13.60
TS(F-F)	10.90	13.69	24.59	-21.79	-38.19	79.87	-59.97	-3.50	2.80
TS(1_M-3)	7.19	41.76	48.95	-24.11	-71.27	175.26	-127.88	-0.22	24.84

As outlined in the introduction, the initial product mixture equilibrated over 72 hrs to one containing all six possible diastereomeric products, **2A-F**. After 4 weeks, the product mixture contained only the thermodynamic products, **2A-C**.⁶² The calculated activation barriers for anti-addition of H₂ to **1A-C** (~24-26 kcal mol⁻¹) and **1D-F** (~18-20 kcal mol⁻¹) are consistent with the kinetic products **2D-F** being observed immediately, with the thermodynamic products **2A-C** appearing over 72 hrs, at room temperature. The equilibration to only the thermodynamic products **2A-C** after 4 weeks necessitates the interconversion between **2D-F** and **2A-C**, via disproportionation of **2D-F** to the Al(I) and Al(III) monomers, followed by comproportionation to **2A-C**. In Figure 5.19, this process has been modelled for interconversion between products **2F** and **2A**. Using **2F** as the reference, reductive elimination of an Al—H bond takes place (**TS_{redel}**) via an activation barrier of 24.7 kcal mol⁻¹. This generates an encounter complex between the Al(I) and Al(III) dihydride monomers ($\Delta G = +17.6$ kcal mol⁻¹). Scrambling between the different diastereomers can then occur, to give any of the six possibilities, **2A-F**. Oxidative addition of an Al—H bond can occur (**TS_{oxadd}**) via a local Free Energy activation barrier of 13.2 kcal mol⁻¹. However, the overall energetic span of this process, starting from **2F** is 30.8 kcal mol⁻¹. This is an appreciable activation barrier to overcome, consistent with the time period of 4 weeks required to equilibrate. Comparing the structures of **TS_{redel}** and **TS_{oxadd}** (which are the exact same process in opposite directions), the Al—H bond distances are appreciably different, at 1.84 and 2.09 Å, respectively. Furthermore, the Al—Al bond distances are 2.47 and 2.84 Å for **TS_{redel}** and **TS_{oxadd}**, respectively. The larger activation of these bonds in **TS_{oxadd}** accounts for the greater activation barrier (30.8 vs 24.7 kcal mol⁻¹).

5 - Reactivity of a Base-stabilised Dialumene

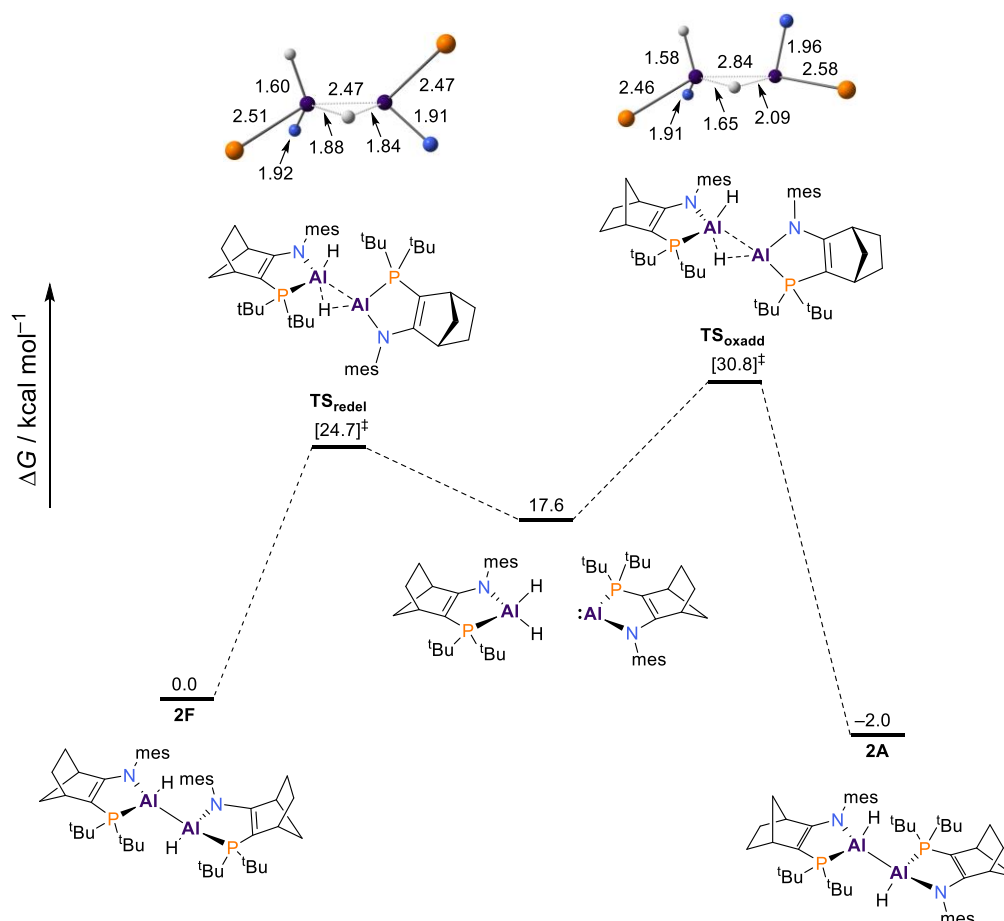


Figure 5.19: Computed reaction energy profile for dis- and comproportionation of **2F**. Gibbs Free Energies (in kcal mol^{-1}) are given at $T = 298 \text{ K}$ and $p = 1 \text{ atm}$ at the SMD(benzene)-B3LYP-D3/def2-TZVPP//M062X-D3/def2-SVP.

It has now been established that oxidative addition of dihydrogen to **1** preferentially proceeds via a concerted anti-addition to the $\text{Al}=\text{Al}$ double bond, with the addition to the corresponding alumanyl monomer **1_M** proceeding via a prohibitively high barrier. This result is notable, since it represents a digression from the current mechanistic understanding of how H_2 is added to $\text{Al}(\text{I})$ centres. The question arises as to whether such a mechanistic scenario can be extended to other related systems, by invoking a monomer-dimer equilibria. Thus, these systems could potentially react via a loosely bound dimeric intermediate. Several examples in the literature give hints that this may be warranted. Power has shown that the monomeric $^{\text{iPr}_8}\text{ArGa}(\text{I})$ ($^{\text{iPr}_8}\text{Ar} = \text{C}_6\text{H}-2,6-$

(C₆H₂-2,4,6-ⁱPr₃)₂-3,5-ⁱPr₂) is unreactive with dihydrogen, whereas the digallene ⁱPr⁴ArGaGaArⁱPr⁴ (ArⁱPr⁴ = C₆H₃-2,6-(C₆H₃-2,6-ⁱPr₂)₂) reacts readily under mild conditions (1 atm of H₂ at 25 °C).⁶⁸ More recently, the analogous aluminyl monomer ⁱPr⁸ArAl(I) was reported to react readily with dihydrogen, with calculations predicting a kinetically inaccessible barrier. A loose association into an encounter complex was thus proposed, prior to reaction with dihydrogen.²⁵⁷ Since this study, the corresponding transient dialumene has been successfully isolated in the solid state, providing further evidence that association in solution to the dimer prior to reactivity is in fact a distinct possibility.⁶⁶ This is supported by calculations that predict a kinetically accessible barrier of 17.4 kcal mol⁻¹ for 1,2-addition at the dimer. This calculated barrier is consistent with the activation barriers calculated for *anti*-addition to **1**. The above studies from Power thus provide ample reason to extend this present study to other systems.

The prototypical monomeric Al(I) species from Roesky, NacNacAl(I) (**4_M**) was reported by Nikonov to react with dihydrogen at 70 °C over 16 hrs to afford the Al(III) dihydride, **5** (Scheme 5.1b).^{50,51} Previous computational mechanistic work from Cao and Toro-Labbé has only considered addition to the monomer.^{268,272} In these studies, the addition was calculated to proceed through a concerted asynchronous mechanism, where polarisation of the H—H bond takes place via nucleophilic attack from one aluminium centre to capture a proton, followed by attack of the p orbital of aluminium by the hydride to form the second Al—H bond. The barrier for this process was calculated by Cao to be 37.5 kcal mol⁻¹ using B97-D²⁶⁸ and by Toro-Labbé to be 36.7 kcal mol⁻¹ using M06-2X.²⁷² These calculations were repeated for this present study, and a barrier of 41.5 kcal mol⁻¹ was calculated (Figure 5.20). Both the calculated energetic barrier and concerted asynchronous nature of the transition state is comparable to that of **1_M** discussed above (Figure 5.18). Thus, for both **1_M** and **4_M**, the

barrier to H₂ activation is prohibitively high under the mild experimental conditions and would not proceed in the absence of elevated conditions.

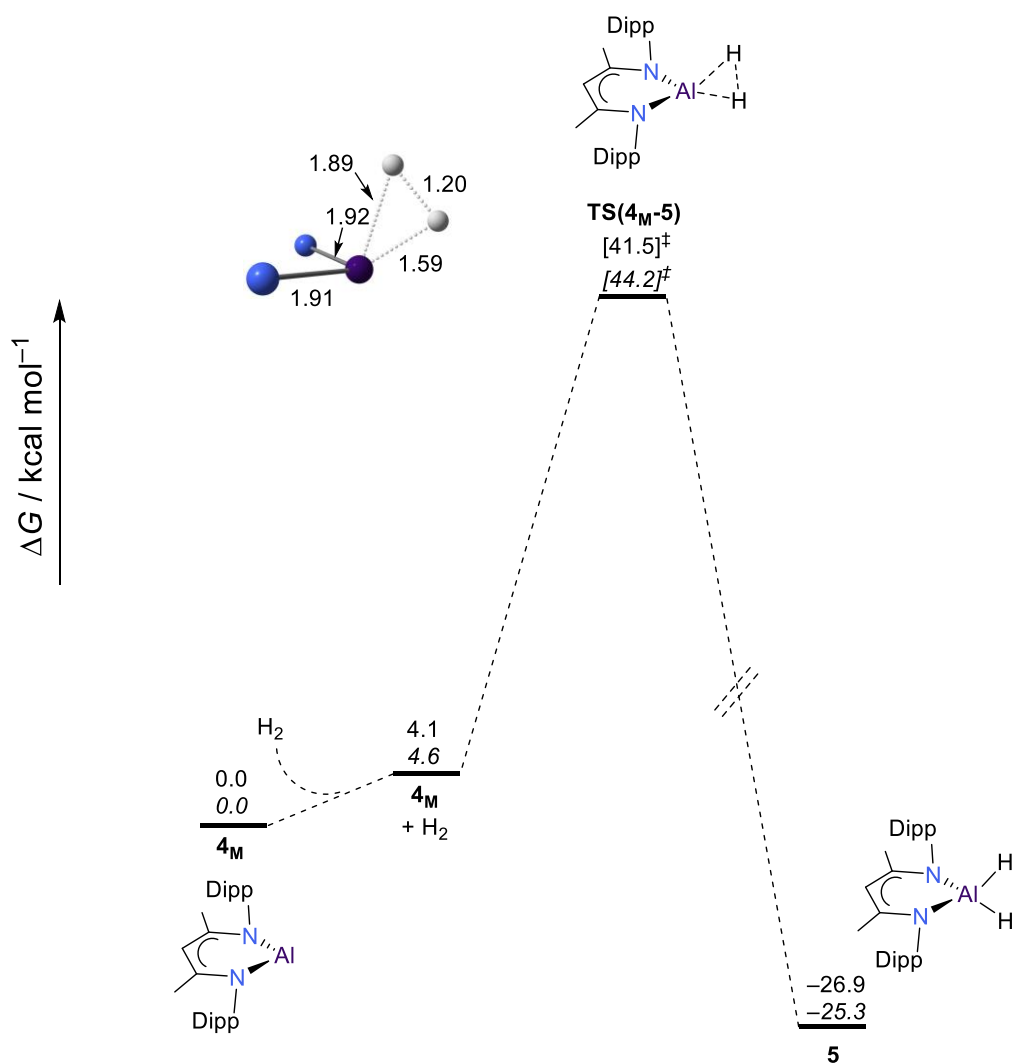
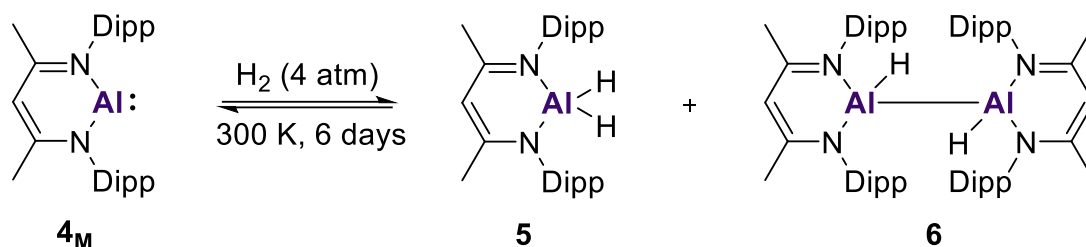


Figure 5.20: Computed reaction energy profile for addition of H₂ to monomeric **4_M**. Gibbs Free Energies (in kcal mol⁻¹) are given at $T = 298$ K and $p = 1$ atm at the SMD(benzene)-B3LYP-D3/def2-TZVPP//M062X-D3/def2-SVP and DLPNO-CCSD(T)/def2-TZVPP/M062X-D3/def2-SVP levels of theory.

When the reaction of **4_M** was repeated in the same solvent (C₆H₆) and at the same pressure of dihydrogen (4 bar) as Nikonov⁵¹, monitoring by ¹H NMR revealed that elevated temperatures were not necessary for the reaction to occur. The reaction was

5 - Reactivity of a Base-stabilised Dialumene

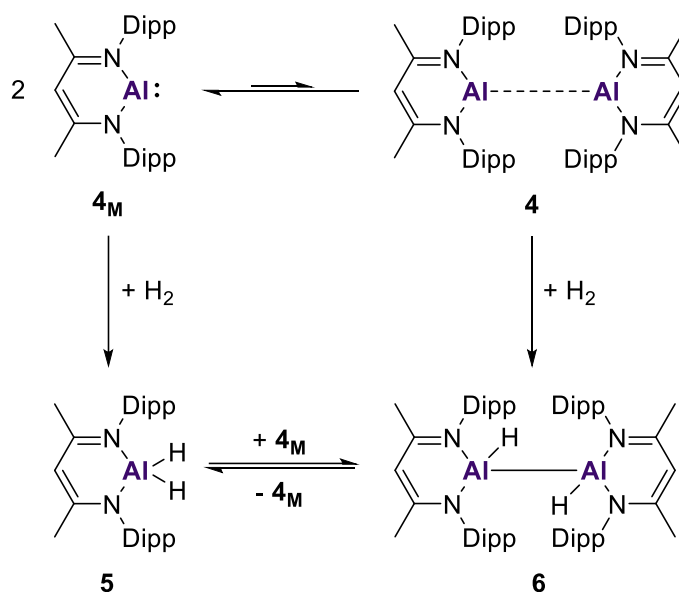
found to proceed at 300 K, with initial formation of **5** and the Al(II) dihydrodialane **6** (Scheme 5.11). After 6 days at room temperature, 10 % of **4_M** remained and 73 % of **5** and 17 % of **6** had been formed.



Scheme 5.11: Reaction of **4_M** with H₂ at 300 K, in C₆H₆.

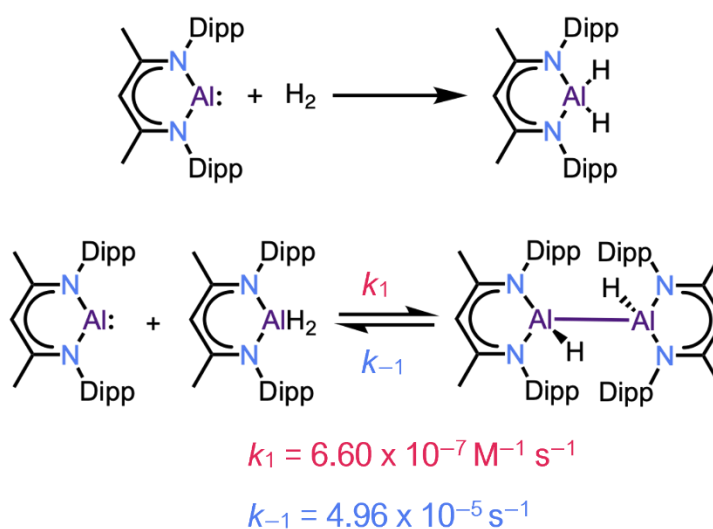
Given that direct activation at the monomer is kinetically inaccessible (Figure 5.20), it was then hypothesised that a lower energy pathway, proceeding via a loosely associated dimeric complex, could exist (Scheme 5.12). It was speculated that the steric bulk of the Dipp substituents of the NacNac ligand framework would hinder formation of an Al=Al double bond, but at the same time support formation of a dimeric encounter complex through dispersion stabilisation. Activation of H₂ would proceed via direct activation of the H—H bond at both aluminium centres of the dimeric complex **4** to form the Al(II) dihydrodialane **6**, followed by disproportionation to **4_M** and **5** (Scheme 5.12). Experimentally, it has been previously reported by Nikonov that **6** exists in equilibrium with **4_M** and **5** via a reversible oxidative addition / reductive elimination, thereby allowing full conversion to **5**.⁵¹

5 - Reactivity of a Base-stabilised Dialumene



Scheme 5.12: Possible pathways for the reaction of 4_M with H_2 .

To support this alternative hypothesis, the Cowley group repeated the reaction of 4_M with H_2 and monitored its kinetics under room temperature conditions. Kinetic rate constants for the individual steps of the comproportionation / disproportionation reactions of the Al(I) and Al(III) species were obtained in a separate reaction (Scheme 5.13).



Scheme 5.13: Kinetic rate constants measured at room temperature for the individual steps of the comproportionation / disproportionation reactions of 4_M , **5** and **6**.

5 - Reactivity of a Base-stabilised Dialumene

By utilising these rate constants, a kinetic model was fitted and the evolution of the expected concentrations over time were plotted (Figure 5.21, solid coloured lines). It is immediately apparent that the kinetic model does not fit the experimental data points. The model predicts an accumulation of the Al(III) dihydride over time, due to the very small rate constant for the comproportionation reaction, with only a small increase in the concentration of the Al(II) dihydrodialane to a stable level predicted. In the experiment however, the concentration of the Al(II) dihydrodialane was seen to increase at a greater rate than formation of the Al(III) dihydride initially. Thus, H_2 addition to the Al(I) monomer, followed by Al—H addition to form the Al(II) dihydrodialane cannot account for the observed kinetics.

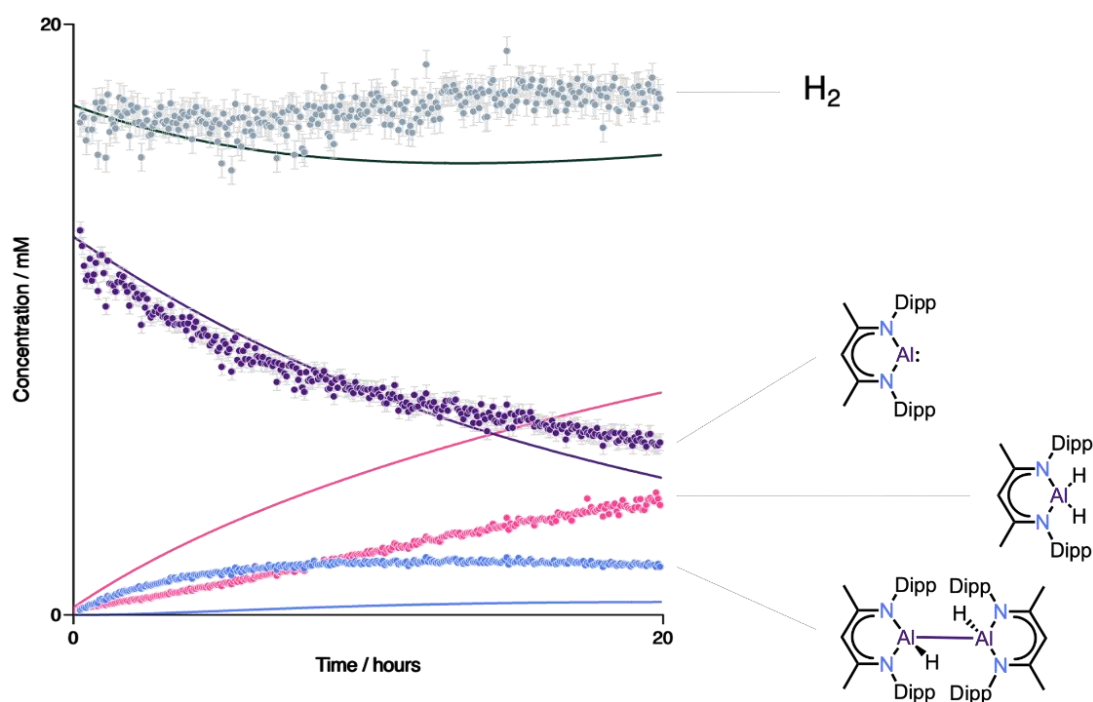


Figure 5.21: Kinetic model study (carried out by the Cowley group), modelling the reaction of **4_M** with H_2 , assuming Al—H addition, following the addition of H_2 to **4_M**. The solid coloured lines represent the predicted concentrations as a function of time, while the coloured points represent the observed experimental concentrations as a function of time.

It was found that a model that involves a pre-equilibrium of the monomeric and dimeric NacNacAl(I) followed by addition of H_2 to the NacNacAl(I) dimeric species and subsequent disproportionation to **4_M** and **5** fits the kinetic model far more closely (Figure 5.22). Formation of the Al(II) dihydrodialane, and a plateau of this species as it undergoes the expected disproportionation reaction is predicted. This is more consistent with experiment, as the equilibrium of the disproportionation reaction lies more towards the products i.e. the Al(I) and Al(III) monomeric species, as evidenced by the kinetic rate constants for the individual steps.

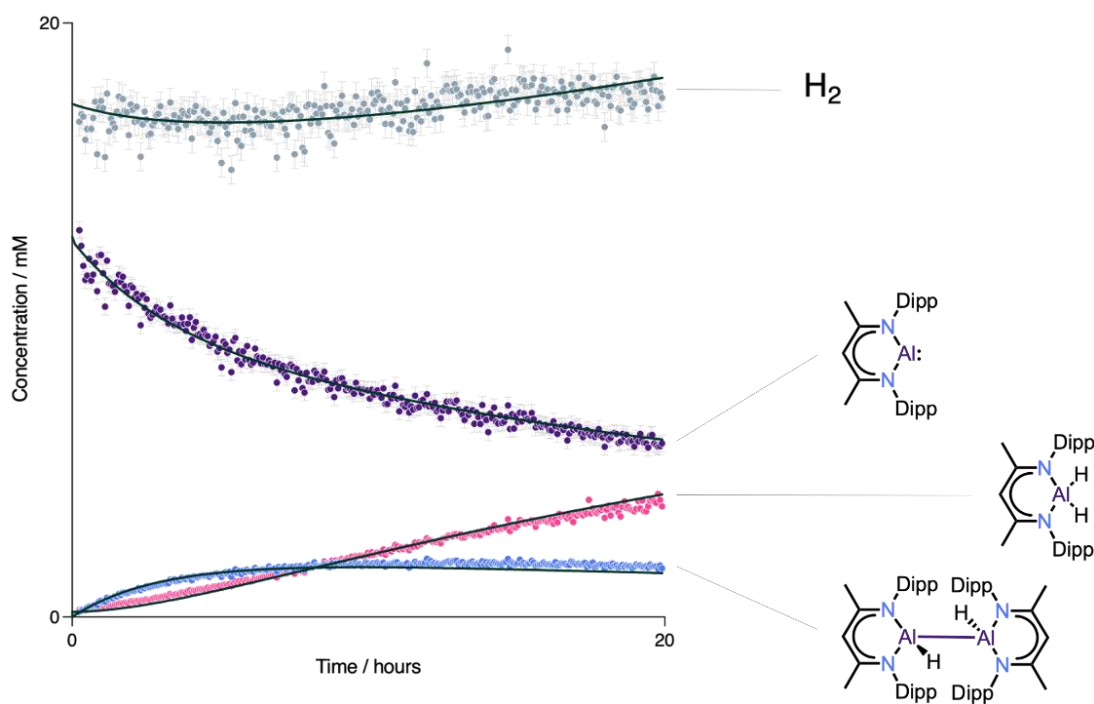


Figure 5.22: Kinetic study modelling the reaction of **4_M** with H_2 , assuming oxidative addition of H_2 to a loosely bound encounter complex, followed by disproportionation to **5** and **4_M**. The solid coloured lines represent the predicted concentrations as a function of time, while the coloured points represent the observed experimental concentrations as a function of time.

The calculations show that the loosely bound dimeric species **4** is energetically accessible under the reaction conditions, with a low-energy transition state, **TS(4_M-4)**

located for the dimerization (Figure 5.23 and Figure 5.24). In the optimised geometry of **4**, the two NacNacAl(I) fragments are strongly trans-bent and twisted with respect to each other, with bond distance between the Al centres of 2.72 Å (Figure 5.24). All attempts to locate an untwisted structure were unsuccessful, due to the steric bulk afforded by the Dipp residues.

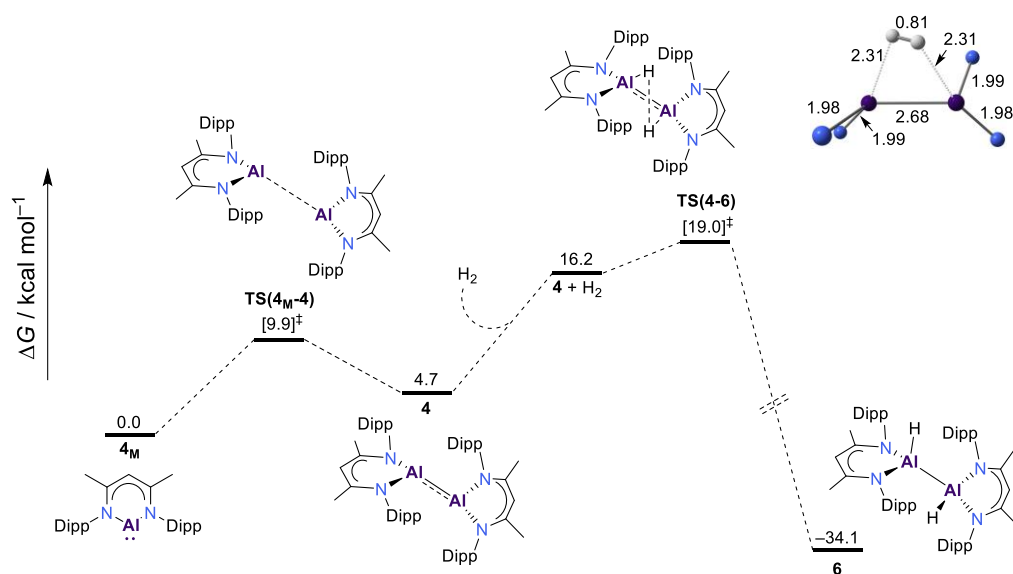


Figure 5.23: Computed reaction energy profile (B3LYP-D3/def2-TZVPP//M062X/def2-SVP corrected for benzene solvent) for the hydrogenation of NacNacAl(I) dimer **4** into anti-**6**_{twist}. Relative Gibbs Free Energies (in kcal mol⁻¹) are given at $T = 298$ K relative to monomeric **4**_M.

The oxidative addition of dihydrogen to **4**, following dimerization was found to occur via an energetic span of 19.0 kcal mol⁻¹ (Figure 5.23), to yield **6**, which has a relative Gibbs Free Energy of -34.1 kcal mol⁻¹. Due to the twisted nature of **4**, it is already pre-organised for dihydrogen activation via **TS(4-6)**, in contrast to **1**, which required rotation of the Al=Al core to achieve sufficient frontier orbital overlap. Although **4** is referred to as a dimeric species in this text, it is recognised that it is more akin to an encounter complex. This is supported by the calculated Al—Al bond distances, compared across complexes **4** (2.72 Å), **TS(4-6)** (2.68 Å) and **6** (2.61 Å) (Figure 5.24).

5 - Reactivity of a Base-stabilised Dialumene

As the Al—Al single bond in **6** forms, the bond distance contracts, rather than elongates. Despite this, **TS(4-6)** clearly shows clear activation of H₂ across the two aluminium centres in a well-defined transition state.

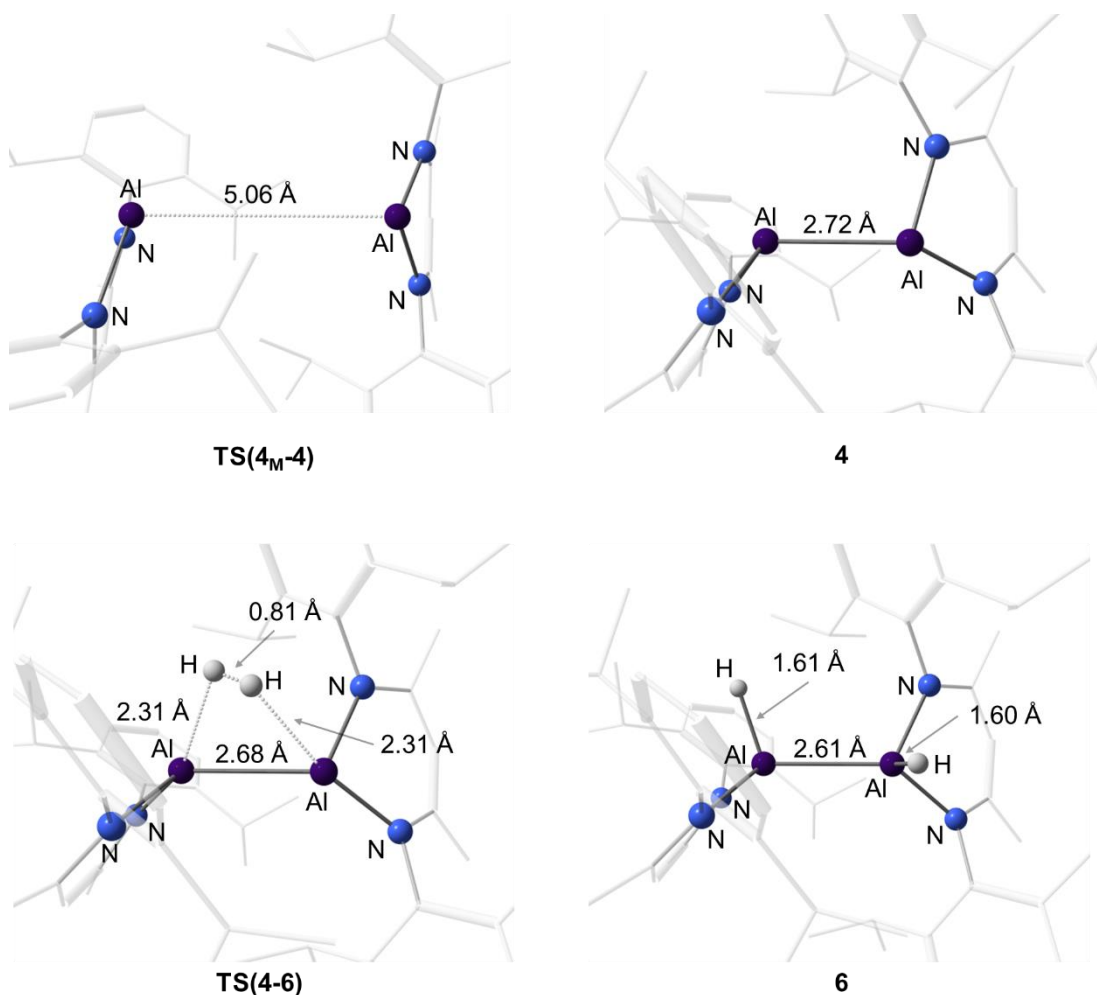


Figure 5.24: Optimised geometries of **TS(4_M-4)**, **4**, **TS(4-6)** and **6**.

Finally, to support the experimentally observed equilibrium⁵¹ and to access **5**, the reversible reductive elimination / oxidative addition of an Al—H bond of **5** to the Al(I) centre of **4_M** was investigated. Cao has previously attempted to locate a transition state for this process, however all attempts were unsuccessful.²⁶⁸ A transition state for this process has been successfully located in this present work, coming with an

activation enthalpy of 29.9 kcal mol⁻¹ from **6** to form **5** and **4_M** (Figure 5.25). Enthalpies are reported for this process as the entropic penalty was significant, on the order of 21.8 kcal mol⁻¹. This is possibly due to errors in describing the vibrational entropy. Low vibrational normal modes are not well described by the rigid rotor harmonic oscillator approximation. Quasi harmonic vibrational entropy approaches, as proposed by Cramer, Truhlar and Grimme were employed to attempt to remedy this.^{273,274} However, the entropic penalty was relatively unaffected by applying these corrections, reducing the penalty by only 0.4 kcal mol⁻¹ to 21.4 kcal mol⁻¹. The enthalpic barrier to oxidative addition is 24.2 kcal mol⁻¹, relative to the encounter complex. The geometry of the transition state, **TS_{redel}**, contains two NacNacAl(I) monomeric fragments twisted with respect to each other, similar to **4**. The Al—H distance is significantly elongated to 1.85 Å, from 1.59 Å in **5**. The hydride being transferred is situated in a bridging position between the two aluminium centres, with the twisted geometry allowing efficient transfer to the empty p orbital of the opposite aluminium centre. These calculations are in reasonable agreement with the results from Nikonov⁵¹, where at room temperature, the oxidative addition of the Al—H bond results in an equilibrium mixture of **4_M**, **5** and **6**. However, upon heating to 50 °C, disproportionation to **4_M** and **5** occurs, indicating an entropy driven reaction. Upon returning to room temperature, the mixture returned to the initial equilibrium containing **4_M**, **5** and **6**.

5 - Reactivity of a Base-stabilised Dialumene

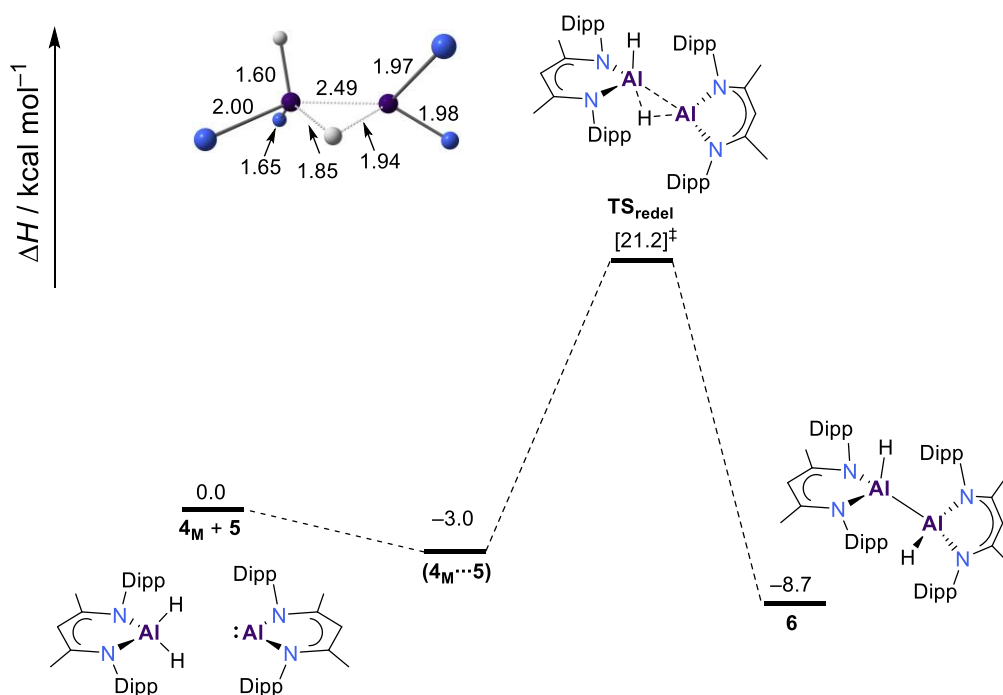
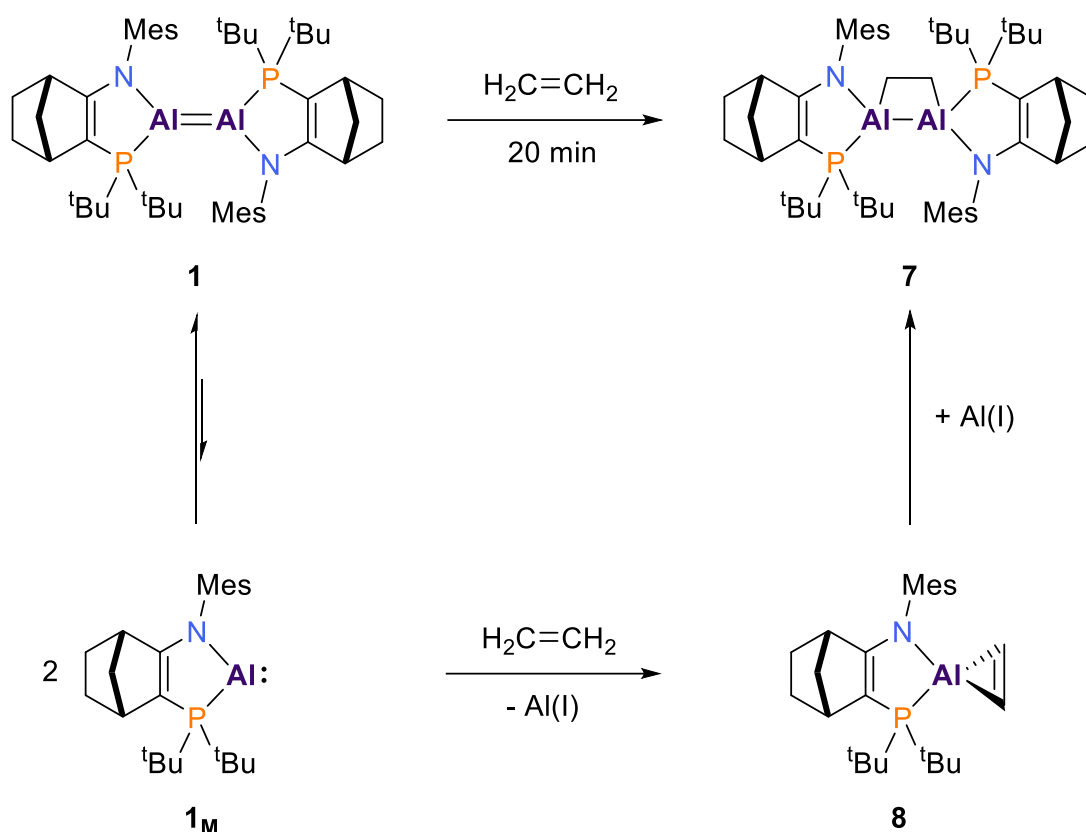


Figure 5.25: Computed reaction energy profile for oxidative addition of **5** to **4_M**. Enthalpic energies (in kcal mol^{-1}) are given at $T = 298 \text{ K}$ and $p = 1 \text{ atm}$ at the SMD(benzene)-B3LYP-D3/def2-TZVPP//M062X-D3/def2-SVP level of theory.

5.3.2 Cycloaddition – A Biradicaloid Mechanism

As discussed in the introduction, **1** was shown to react rapidly (5-20 mins) with ethene at room temperature, generating the dialuminacyclobutane, **7** (Scheme 5.5). This final section will explore the mechanistic possibilities of this reactivity. Given the low bond dissociation energy of the Al=Al double bond in **1**, both activation at the monomer and dimer are conceivable (Scheme 5.14). In the case of the activation at the monomer, initial dissociation of **1** into two equivalents of **1_M** must occur. This is followed by a formal [2+1] cycloaddition of ethene to one equivalent of **1_M**, followed by a comproportionation step between **1_M** and **8** to yield the dialuminacyclobutane, **7**.

5 - Reactivity of a Base-stabilised Dialumene



Scheme 5.14: Possible reaction pathways for the formal [2+2] cycloaddition of ethene to **1**.

This monomeric pathway will be explored first (Figure 5.26). Initial dissociation of **1** into two equivalents of **1_M** is $10.2 \text{ kcal mol}^{-1}$ endergonic. Exchange of one equivalent of **1_M** with C_2H_4 then results in an encounter complex that sits at $16.9 \text{ kcal mol}^{-1}$. Formal [2+1] cycloaddition between **1_M** and C_2H_4 can then occur via **TS(1_M-8)** to form the aluminacyclopropane **8**, which is $4.5 \text{ kcal mol}^{-1}$ endergonic. To complete the reaction and form the dialuminacyclobutane **7**, a final comproportionation step between **8** and previously released **1_M** must occur. This was calculated to proceed via a transition state, **TS(8-7)**, sitting at $14.9 \text{ kcal mol}^{-1}$. This step was calculated to be strongly exergonic, with the dialuminacyclobutane **7** having a relative Gibbs Free Energy of $-26.9 \text{ kcal mol}^{-1}$, making it the thermodynamic product. Overall, the rate determining step on this reaction pathway is the [2+1] cycloaddition between **1_M** and C_2H_4 , having a barrier of $28.3 \text{ kcal mol}^{-1}$, which is incompatible with the experimental

5 - Reactivity of a Base-stabilised Dialumene

conditions and reaction time ($T = 298$, $t = 20$ mins). Having established the inaccessibility of the monomeric pathway, activation at the dimer can now be considered.

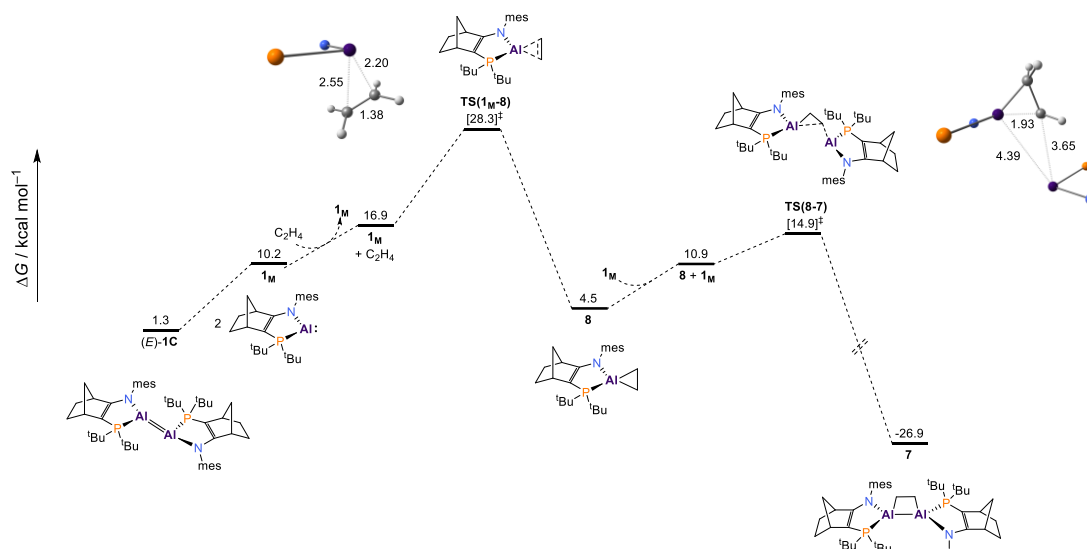


Figure 5.26: Computed reaction energy profile for formal [2+2] cycloaddition of C_2H_4 to (E) -**1C**, via [2+1] cycloaddition to **1M**, followed by comproportionation between **8** and **1M**. Gibbs Free Energies (in kcal mol^{-1}) are given at $T = 298$ K and $p = 1$ atm at the SMD(benzene)-B3LYP-D3/def2-TZVPP//M062X-D3/def2-SVP.

It has been shown through high-level quantum chemical calculations, in Chapter 3 and previous work from Tuononen and Power⁶⁹ that dialumenes possess a small amount of open-shell singlet biradicaloid character (~12-15 %). This finding has been used to rationalise the observed cycloaddition of a putative dialumene from Power with toluene.⁶⁸ In this study, preliminary calculations of the reaction of a model dialumene $ArAlAlAr$ ($Ar = C_6H_3-2,6-Me_2$) with propene was carried out. This reaction was found to proceed via a stepwise mechanism, where the first transition state contained a dangling $H_3CC(H)C(H)_2^-$ moiety (Figure 5.27). Subsequent stability analysis of the wavefunction located a restricted-unrestricted instability, indicative of

5 - Reactivity of a Base-stabilised Dialumene

a broken symmetry, biradicaloid ground state. Unpaired spin populations were located on Al1 (+0.25), Al2 (-0.47) and C2 (+0.27) of the dangling olefin.

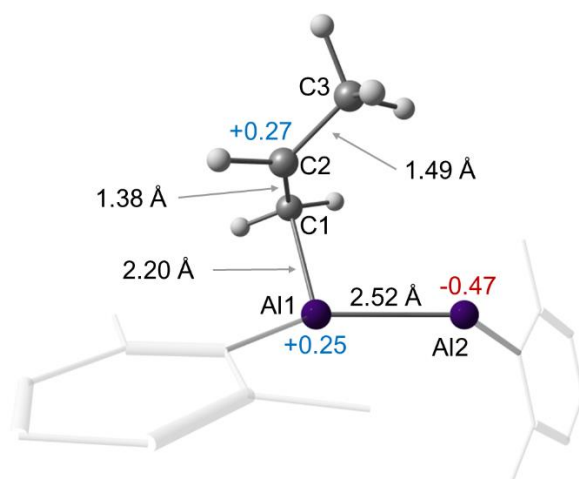


Figure 5.27: Optimised geometry of the transition state for the stepwise addition of propene to ArAlAlAr , with key structural parameters shown. Reproduced from Tuononen and Power study for the purpose of comparison.⁶⁸ Spin populations are shown in blue and red.

No such theoretical work has been carried out on a synthetically realised base-stabilised dialumene to date. Therefore, the possibility of a stepwise, open-shell biradicaloid mechanism for the addition of ethene to the dialumene **1** has been investigated herein. Using the broken-symmetry formalism²⁷⁵, the singlet potential energy surface was scanned, successfully locating **TS1_{step}**, which models the initial association of ethene **1** (Figure 5.28). The resulting antiferromagnetically coupled singlet biradicaloid intermediate ($M_s = 0$) contains a dangling $\text{H}_2\text{CCH}_2\cdot$ radical moiety, with C(1) bound to Al(1) (Figure 5.29). The $\langle S^2 \rangle$ value of 0.94 is diagnostic of minimal overlap of the magnetic orbitals and weak antiferromagnetic coupling between the α -spin electron located on C(2) and the β -spin electron located on Al(2). This interpretation is reinforced by Mulliken spin populations of +0.93 and -0.74 located on C(2) and Al(2), respectively. Spin densities of key structures are shown in Figure 5.29.

Subsequent radical recombination can then occur via **TS2**_{Step}, which requires an inversion of the aluminium centre, to yield the final dialuminacyclobutane **7**. The barrier for the initial association of ethene was calculated to be 18.5 kcal mol⁻¹, while the overall energetic span for radical recombination was calculated to be 21.5 kcal mol⁻¹, making the latter step rate determining. A span of 21.5 kcal mol⁻¹ is consistent with a reaction that proceeds at ambient conditions. However, the broken symmetry method utilised always suffers from a degree of spin contamination from higher spin states (the triplet state with $M_s = 0$ in this case).²⁷⁶ This spin contamination influences total energies, as it stems from the broken symmetry wavefunction. Several spin-projection procedures have been proposed to eliminate the spin contamination. Yamaguchi has proposed the approximate spin projection (AP) procedure, based on the Heisenberg-Hamiltonian.^{277–280} A spin-projected energy of the singlet state can be obtained without the spin contamination using the equation

$$E_{AP-BS}^{LS} = \alpha E_{U-BS}^{LS} - \beta E_U^{HS} \quad (5.3)$$

where

$$\alpha = \frac{\langle S^2 \rangle_U^{HS} - \langle S^2 \rangle_{Exact}^{LS}}{\langle S^2 \rangle_U^{HS} - \langle S^2 \rangle_{U-BS}^{LS}} \quad (5.4)$$

$$\beta = \frac{\langle S^2 \rangle_{U-BS}^{LS} - \langle S^2 \rangle_{Exact}^{LS}}{\langle S^2 \rangle_U^{HS} - \langle S^2 \rangle_{U-BS}^{LS}} \quad (5.5)$$

$$\beta = \alpha - 1 \quad (5.6)$$

This method provides the AP energy for the unrestricted broken symmetry (U-BS) singlet state. By applying this method, a reduction in the activation barrier from 21.5 to 19.5 kcal mol⁻¹ was achieved. These results, in combination with Power's previous

5 - Reactivity of a Base-stabilised Dialumene

work⁶⁸ thus confirm the viability of an open-shell stepwise biradicaloid pathway for the addition of ethene to a dialumene species, at ambient conditions.

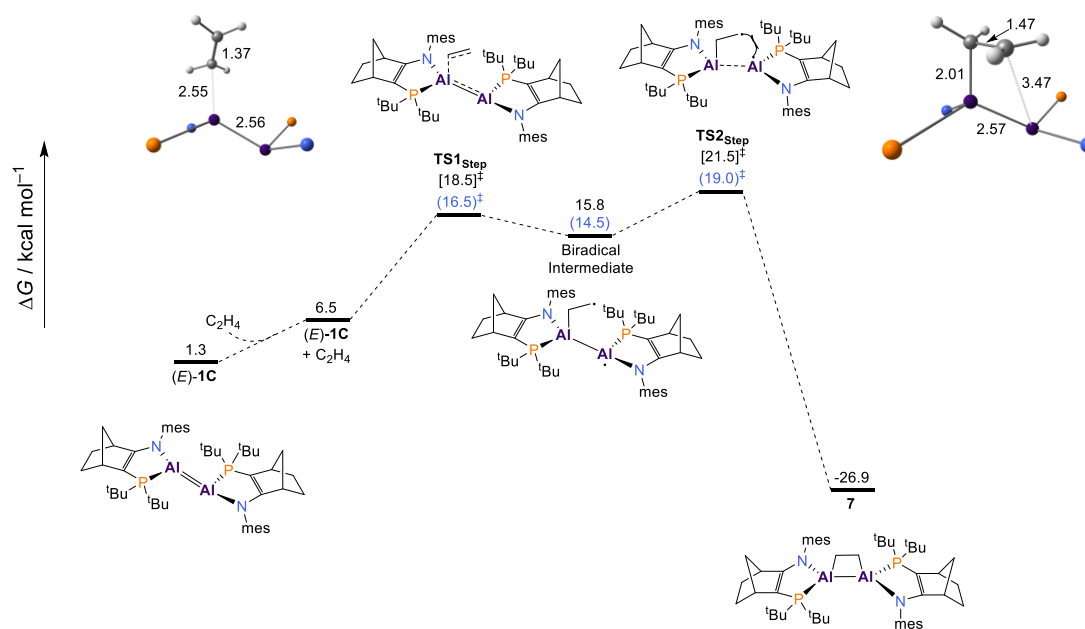


Figure 5.28: Computed reaction energy profile for formal [2+2] cycloaddition of C_2H_4 to (E) -**1C**, via an open-shell stepwise biradicaloid mechanism. Gibbs Free Energies (in kcal mol^{-1}) are given at $T = 298 \text{ K}$ and $p = 1 \text{ atm}$ at the SMD(benzene)-UB3LYP-D3/def2-TZVPP//UM062X-D3/def2-SVP. Spin projected relative energies are shown in blue rounded brackets.

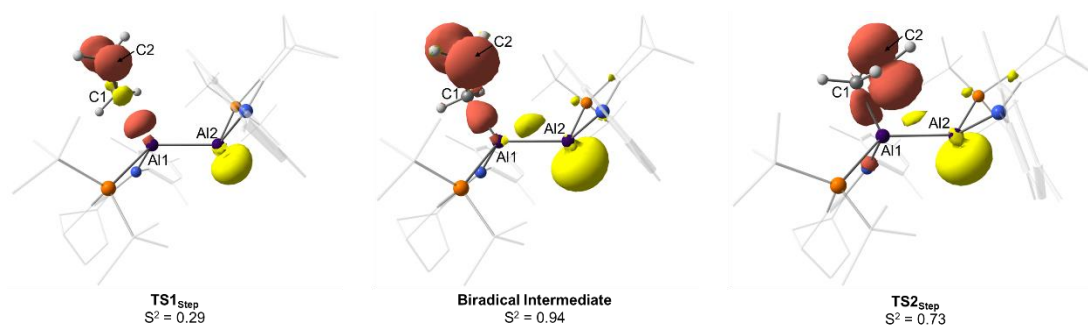


Figure 5.29: Spin density plots of key transition states and intermediates along the open-shell stepwise biradicaloid pathway for the addition of ethene to **1** (Figure 5.28). Isovalue = 0.005 a.u.. Alpha spin density shown in red, and beta spin density shown in yellow.

5.4 Conclusions

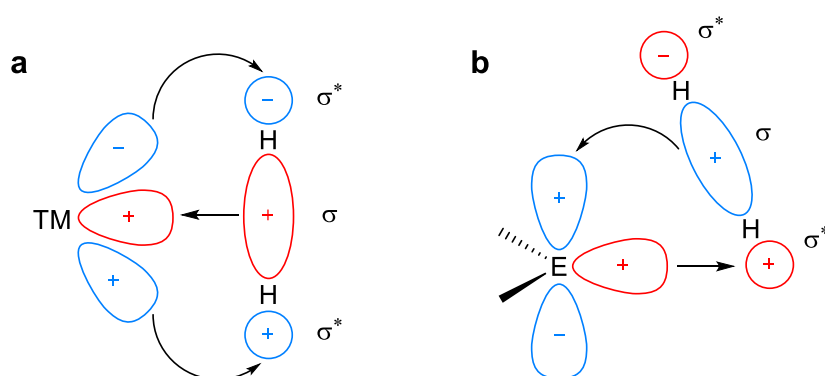
In summary, this computational mechanistic work has demonstrated that oxidative addition of dihydrogen occurs preferentially via a concerted *anti*-addition to the *Z* isomers of dialumene **1**. The concerted addition to the monomeric aluminyl **1_M** was further shown to be kinetically inaccessible under the ambient experimental conditions. Given these results, the investigation was extended to the prototypical NacNacAl(I) system from Roesky, **4_M**. Association to the loosely bound dimer **4** and subsequent dihydrogen activation across the Al=Al vector was theoretically shown to be more facile than direct monomeric activation by **4_M**, followed by subsequent comproportionation to the dihydrodialane **6**.

In an extension to this work, the possibility of a stepwise biradicaloid mechanism for the formal [2+2] cycloaddition of ethene to **1** has been investigated. It has been demonstrated that such a pathway exists, and furthermore, is kinetically favoured over an alternative closed-shell monomeric pathway. In tandem with experiment, this quantum chemical work has highlighted the importance of considering the full spectrum of the monomer-dimer equilibrium in the activation of small molecules by low-oxidation state aluminium compounds.

6 FLP-type cooperativity in an alkali metal aluminyl complex: proposal of a hydride rebound mechanism

6.1 Introduction

The activation of dihydrogen is a reaction of fundamental importance, across both industry and academia.⁹⁴ This area, and more broadly speaking, industrial chemical processes, have traditionally been dominated by late transition metal (TM) systems. As discussed in the previous chapters, due to the growing scarcity of many of these late TM systems, there has been significant research efforts into developing main group metal systems.^{1,2} A common design strategy that has been employed by workers in this field has been attempting to mimic the frontier orbital symmetries and energetic gaps observed in TM systems (Scheme 6.1).

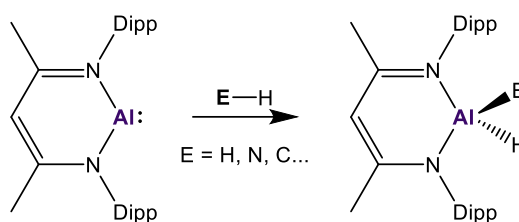


Scheme 6.1: a) The interaction of H_2 with the frontier d-orbitals of a transition metal (TM) complex b) The interaction of H_2 with the p-orbital and lone pair of a monomeric main group carbenoid species (E = main group element).

Neutral aluminium(I) carbene-like compounds, such as Roesky's $\text{Nacnac}^{\text{Dipp}}\text{Al(I)}$ system have displayed a range of bond activating capabilities, including the activation of

6 - FLP-type cooperativity in an alkali metal alumanyl complex: proposal of a hydride rebound mechanism

dihydrogen (Scheme 6.2).³ This reactivity was explored in Chapter 5, together with the reactivity of Cowley's dialumene system. Gaining a fundamental understanding of this reactivity, down to the electronic structure level, is essential in order to aid in the development of non-TM systems that exhibit useful reactivity.



Scheme 6.2: The activation of a range of E-H bonds by the prototypical complex $\{\text{HC}(\text{MeCDippN})_2\}\text{Al}$ ($\text{Nacnac}^{\text{Dipp}}\text{Al}$, where $\text{Dipp} = 2,6\text{-}i\text{Pr}_2\text{C}_6\text{H}_3$).

As reviewed in Chapter 1, in 2018, the very first report of a nucleophilic anionic alumanyl Al(I) complex appeared, from Aldridge and Goicoichea.⁷⁸ This species was shown to exist in solution and the solid state as the “contacted dimeric pair”, where stabilisation was provided by the bulky xanthene based diamido ligand with its aryl side groups favourably interacting with the partner alkali metal, potassium (Figure 6.1).

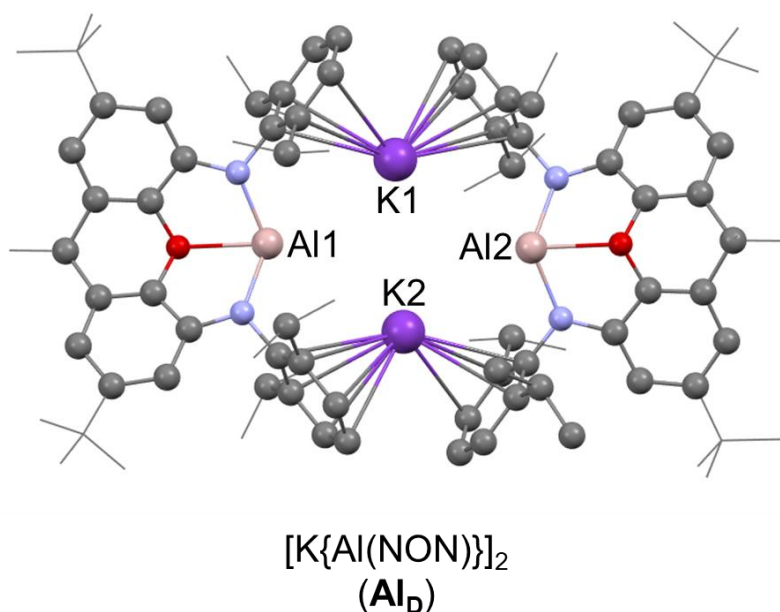
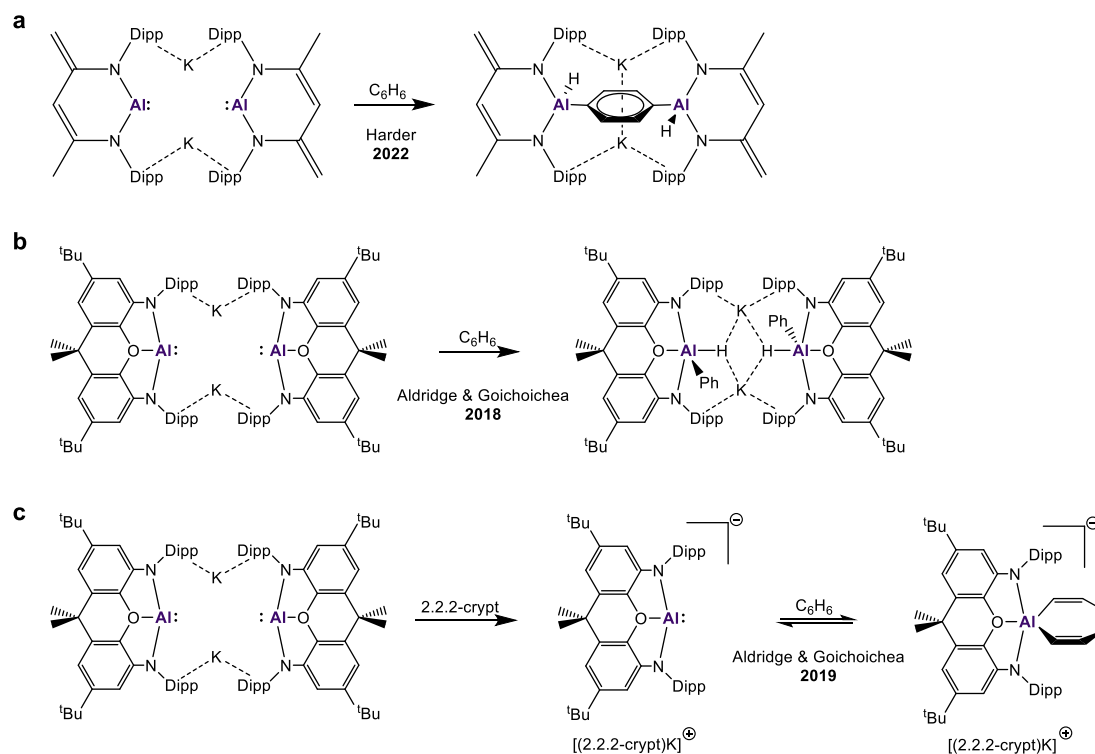


Figure 6.1: X-ray crystal structure of $[K\{Al(NON)\}]_2$ (NON = 4,5-bis(2,6-diisopropylanilido)-2,7-di-tert-butyl-9,9-dimethylxanthene), labelled as **Al_D**.

The thermodynamically favourable two-electron oxidation has been reported for all alumanyl complexes.²³¹ Importantly, it has been stressed in the literature that the partner alkali metal may not simply be a stabilising spectator in much of this reactivity. For example, Harder has demonstrated the dual activation of benzene in the *para* positions, by the $[K_2\{Al^{(BDI)Dipp-H}\}]_2$ complex (Scheme 6.3a). The potassium cations are boosting the reactivity of the independent monomers through favourable non-covalent interactions, while helping to sustain the structural integrity of the dimeric product.⁸³ It has also been shown that **Al_D**, when in the contacted dimeric pair form, undergoes the thermally promoted oxidative addition of a C—H bond of benzene, retaining the dimeric state in solution (Scheme 6.3b).⁷⁸ Conversely, the “naked” alumanyl anion, where the potassium cation has been sequestered by the cryptand 2.2.2-crypt, has been shown to oxidatively insert into a C—C bond of benzene, at room temperature, with reversibility achieved upon heating (Scheme 6.3c).⁸⁰ Overall, these reactions indicated that both the presence of the alkali metal and the

6 - FLP-type cooperativity in an alkali metal aluminyl complex: proposal of a hydride rebound mechanism

aggregation state of the complex may alter the course of the reactivity quite significantly.

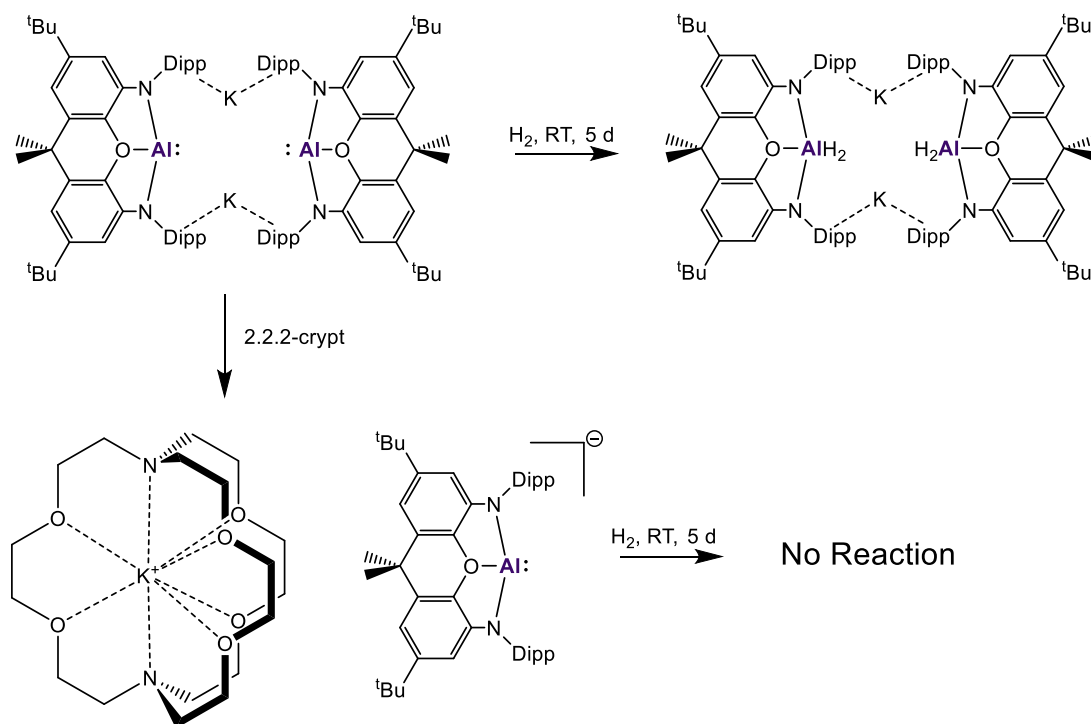


Scheme 6.3: Examples of synergistic activity of aluminyl anions.

Continuing with this theme, it has been previously shown that Al_D can activate two equivalents of dihydrogen, at room temperature, over a time period of 5 days.⁷⁸ However, when the potassium counterion is sequestered by a 2,2,2-cryptand species, no reactivity with dihydrogen is observed, at same reaction conditions. This differing reactivity observed in the presence or absence of the partner alkali metal has hinted at a possible cooperative effect of the cation. This is consistent with reports from Harder, Coles and Mulvey, where the influence of the alkali metal cation on the reactivity and structural outcomes has been highlighted.^{87,88,281} Furthermore, a

6 - FLP-type cooperativity in an alkali metal aluminyl complex: proposal of a hydride rebound mechanism

cooperative activation of H₂ goes against the classical view of single-centre reactivity observed for related neutral Al(I) species, such as $\text{Nacnac}^{\text{Dipp}}\text{Al(I)}$.³



Scheme 6.4: Reaction of two equivalents of H₂ with $[\text{K}\{\text{Al}(\text{NON})\}]_2$ to afford $[\text{K}\{\text{Al}(\text{NON})\text{H}_2\}]_2$, and lack of reactivity with $[\text{Al}(\text{NON})][\text{K}(2,2,2\text{-crypt})]$.

Previous computational mechanistic work on this precise system has been carried out by Schaefer and co-workers, to determine whether a cooperative effect from the K⁺ ions was exerted in the activation of H₂.²⁷¹ In order to reduce the computational cost, the ligand was truncated i.e. the tBu and iPr groups were replaced with methyl groups. This was shown to be a reasonable approach, based on benchmarking carried out against the full system. It was concluded in this work that there was no cooperative effect exerted by the K⁺ ions. The activation of H₂ at the monomeric aluminyl anion and the contacted dimeric pair were calculated to proceed via analogous concerted oxidative addition transition states (Figure 6.2, **TS_M** and **TS_{D-I}**), with no appreciable difference in the calculated activation barriers (~30 kcal mol⁻¹). Both **TS_M** and **TS_{D-I}**

6 - FLP-type cooperativity in an alkali metal aluminyl complex: proposal of a hydride rebound mechanism

are characterised by a high level of asynchronicity in the Al—H bond formation and feature an appreciably activated H—H bond (1.17 and 1.08 Å, respectively). Furthermore, accurate single point energies at the DLPNO-CCSD(T)/def2-TZVP level of theory were calculated, to corroborate the DFT-calculated activation barriers.

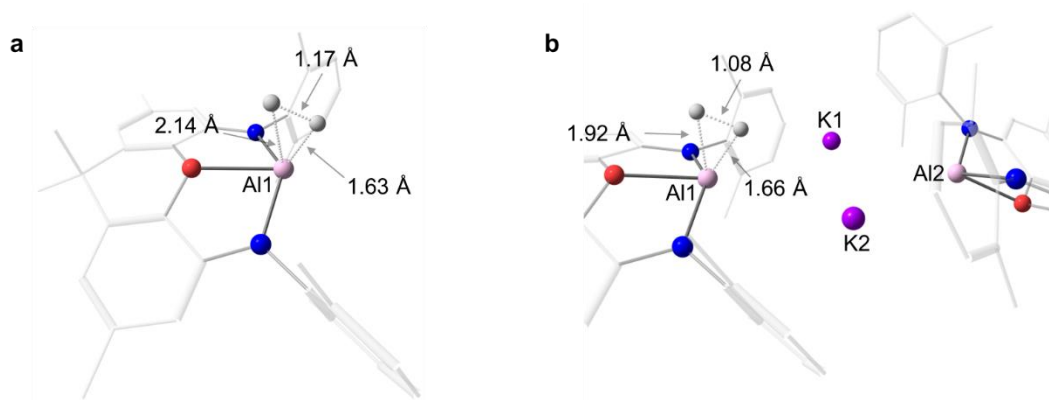


Figure 6.2: Optimized geometries (M062X/def2-SVP) of (a) **TS_M** and (b) **TS_{D-I}** reported by Schaefer and co-workers²⁷¹ along with key bond distances (in Å).

Recall that when the potassium cation is sequestered by a 2,2,2-cryptand species, no reactivity with H₂ is observed. However, reactivity at the contacted dimer pair proceeds at room temperature over 5 days. This new experimental result is inconsistent with Schaefer's conclusions i.e. that the contacted dimer pair activates H₂ via the same concerted oxidative addition mechanism as the aluminyl anion monomer. Given this, it is worth examining what has been stated in the literature, in relation to this exact reactivity. Following the initial report of **Al_b** and its reactivity with H₂, Hinz and Breher stated, in a highlight article of Aldridge's initial work: "The mechanism for this transformation would be an interesting target for computational studies as various pathways are imaginable, including a frustrated Lewis pair FLP-type activation of H₂ between the basic Al⁻ and an acidic K⁺ site".²⁸² Schaefer's

computational study concludes that: “It has been suggested that a frustrated Lewis pair-type reaction for the activation of H₂ may take place in these systems, however, attempts to obtain a suitable TS for such a transformation were unsuccessful”.²⁷¹ Thus, an FLP-like mechanism has been proposed as a possibility, but attempts so far (by Schaefer) to locate such a pathway, have been unsuccessful. With this in mind, this chapter describes work that aims to build upon the existing computational results and provide fresh insight into this reactivity.

6.2 Methods

All electronic structure calculations were carried out using the Gaussian 16 (G16, revision B.01, C.02), Amsterdam Density Functional 2023.101 (ADF) and ORCA (version 5.0.2)¹⁸² program packages.^{232,260} Unconstrained optimisations of ground-state and transition-state geometries and subsequent analytical frequency calculations were carried out using G16 at the DFT level using the TPSS Meta-GGA exchange correlation functional¹⁵⁴, as well as the M06-2X hybrid exchange correlation functional¹⁶⁰, in conjunction with Ahlrich’s def2-SVP basis set.^{210,211} All optimized stationary points were characterized by their analytical second derivatives, with minima having only positive eigenvalues and transition states having one imaginary eigenvalue. The nature of transition states was confirmed via intrinsic reaction coordinate (IRC) calculations in both forward and reverse direction of the reaction coordinate.²⁸³ Subsequent geometry optimisations of the IRC endpoints yielded the nearest minima linked by a transition state. The frequency calculations also provided thermal and entropic corrections to the total energy in gas phase at $T = 298.15$ K and $p = 1$ atm within the rigid-rotor/harmonic oscillator (RRHO) approximation. To reduce computational cost, the geometry optimisations were carried out using the model complexes **Al_M** and **Al_D**, in which the ^{*i*}Pr and ^{*t*}Bu groups were replaced by methyl

groups (Table 6.1). This truncation of the xanthene ligand has previously been shown to be a justified choice for the present aluminyl system²⁷¹, which was confirmed by comprehensive benchmark studies, *vide infra*. An ultrafine integration grid, corresponding to a pruned grid of 99 radial shells and 590 angular points per shell, was used for all calculations. Single-point calculations for accurate energies and electronic structure analyses were performed using the M062X global hybrid exchange correlation functional in conjunction with Ahlrich's def2-TZVPP basis set. Dispersion effects were accounted for by Grimme's D3 correction,¹⁶⁴ while effects on the energy due to the presence of solvent were incorporated by utilising the SMD solvation model with benzene as the solvent ($\epsilon=2.2706$)²³³, corrected for a reference concentration in solution of 1 mol L⁻¹. DLPNO-CCSD(T) single-point energy calculations were also performed using the ORCA program, in order to validate the chosen DFT methodology.^{261,262} These calculations utilised the def2-TZVP basis set of Weigand, with the def2-QZVPP/C auxiliary basis employed. The Normal PNO (default) threshold settings were used ($T_{\text{CutPairs}} = 1 \times 10^{-4}$, $T_{\text{CutPNO}} = 3.33 \times 10^{-7}$). Extended Transition State Natural Orbital for Chemical Valence (ETS-NOCV)²⁸⁴ and Voronoi deformation density (VDD) charge analyses²⁸⁵ were carried out using ADF at the TPSS/TZP²⁶⁵ level of theory (all-electron basis set), employing Grimme's D3 dispersion correction with Becke-Johnson damping.¹⁶⁵ The Zlm Fit²⁸⁶ density fitting scheme in combination with the Becke integration grid^{287,288} was used, at *Excellent* quality. The Morukuma/Ziegler Energy Decomposition Analysis (EDA) was also employed in conjunction with the Activation Strain Model (ASM).²⁶⁶ The NBO program (version 6.0) was used to perform Natural Bond Orbital analyses on the optimised structures.²³⁸ The topology of the electron density was analysed using the Quantum Theory of Atoms in Molecules (QTAIM)²⁸⁹, as implemented in the AIMALL package.²³⁹ Figures of optimized geometries were generated with ChemCraft (Version 1.8).²⁴⁵

6 - FLP-type cooperativity in an alkali metal aluminyl complex: proposal of a hydride rebound mechanism

Table 6.1: Comparison of different size models for **Al_M** and **Al_D** used in this study.

	#atoms	#electrons	#basisfunctions
Al_M (full model)	113	380	1028
Al_M (truncated model)	71	268	692
Al_D (full model)	228	796	2104
Al_D (truncated model)	144	572	1432

6.3 Results & Discussion

Prior to investigating the apparent cooperativity present in the activation of H₂ by **Al_D**, the validity of the chosen method for geometry optimisations was examined. As mentioned above, in the previous study from Schaefer, a truncation of the xanthene ligand was shown to be a justified choice, in which the ⁱPr and ^tBu groups were replaced by methyl groups.²⁷¹ Comprehensive structural benchmarking was carried out to validate this. Two functionals were tested, TPSS (the functional employed in this work) and M062X (the functional employed by Schaefer), with and without dispersion corrections (D3BJ). The TPSS functional has been shown to describe the geometries and electronic structures of other main group systems well.²⁹⁰ More generally, meta-GGA functionals are recommended and typically sufficient for geometry optimisations.²⁹¹ Key X-ray and DFT-optimised structural parameters are shown in Table 6.2. The results indicate that the inclusion of a dispersion correction causes an over-contraction of the key bond distances, relative to their non-dispersion counterparts. Furthermore, M062X accounts for short to medium range dispersive interactions, where TPSS does not. This effect is observed in the present case, where for example, the contraction of the Al1—Al2 bond distance is not as pronounced as observed for TPSS (6.353 Å (TPSS) vs 6.169 Å (TPSS-D3BJ) and 6.121 Å (M062X)

6 - FLP-type cooperativity in an alkali metal aluminyl complex: proposal of a hydride rebound mechanism

vs 6.101 Å (M062X-D3)). Overall, TPSS, in the absence of a dispersion correction, provided the best agreement with structural parameters chosen from the X-ray crystal data.

Table 6.2: Comparison of key DFT-optimised and crystallographic bond distances (Å°) and angles (°) for complex $[K\{Al(NON)\}]_2$ (**Alb**).

	X-ray	DFT			
		TPSS (truncated)	TPSS-D3BJ (truncated)	TPSS (full)	TPSS-D3BJ (full)
$[K\{Al(NON)\}]_2$ (Alb)					
Al1–Al2	6.627(1)	6.353	6.169	6.647	6.307
Al1...K1	4.070(1)	3.675	3.667	3.954	3.699
Al1...K2	3.844(1)	3.881	3.635	3.926	3.690
Al1–N1	1.956(2)	2.034	2.002	2.036	2.019
Al1–N2	1.963(2)	2.012	2.013	2.034	2.019
Al1–O1	2.279(2)	2.155	2.131	2.213	2.194
N1–Al1–N2	128.1(1)	126.1	122.5	129.2	128.9
		M062X (truncated)	M062X-D3 (truncated)	M062X (full)	M062X-D3 (full)
Al1–Al2	6.627(1)	6.121	6.101	6.288	6.252
Al1...K1	4.070(1)	3.663	3.653	3.820	3.801
Al1...K2	3.844(1)	3.699	3.683	3.789	3.765
Al1–N1	1.956(2)	1.991	1.990	1.989	1.987

6 - FLP-type cooperativity in an alkali metal aluminyl complex: proposal of a hydride rebound mechanism

Al1–N2	1.963(2)	1.998	1.997	1.995	1.993
Al1–O1	2.279(2)	2.138	2.137	2.227	2.229
N1–Al1–N2	128.1(1)	120.7	120.5	122.2	121.9

Having validated the chosen protocol for geometry optimisations, the mechanism for the activation of H₂ was then investigated. To act as a reference point, the concerted oxidative addition of H₂ to **Al_M** was also calculated. The Gibbs Free Energy reaction profile for this process is shown in Figure 6.3, with the relevant optimised structures shown in Figure 6.4. Starting from the **Al_M** and H₂ molecules at infinite separation, the encounter complex (**Al_M** + H₂) was calculated to be 3.1 kcal mol⁻¹ endergonic. Approach of the H₂ molecule in the equatorial plane of **Al_M** and subsequent activation of H₂ occurs via a barrier of 31.6 kcal mol⁻¹ (**TS_M**). This calculated barrier is consistent with previous computational work from Cao and co-workers, who investigated the activation of H₂ by related but neutral Al(I) systems.²⁶⁸ Along the forward reaction coordinate, the Al(III) dihydride product, **Al_M-H₂**, is generated, yielding an overall exergonic reaction energy of -35.4 kcal mol⁻¹. These DFT-calculated relative Gibbs Free Energies were found to be in excellent agreement with the DLPNO-CCSD(T) calculated values (within 1 kcal mol⁻¹). Overall, the calculated activation barrier is inconsistent with a reaction that proceeds at room temperature over a period of 5 days, implying that another mechanism is likely to be operative.

6 - FLP-type cooperativity in an alkali metal aluminyl complex: proposal of a hydride rebound mechanism

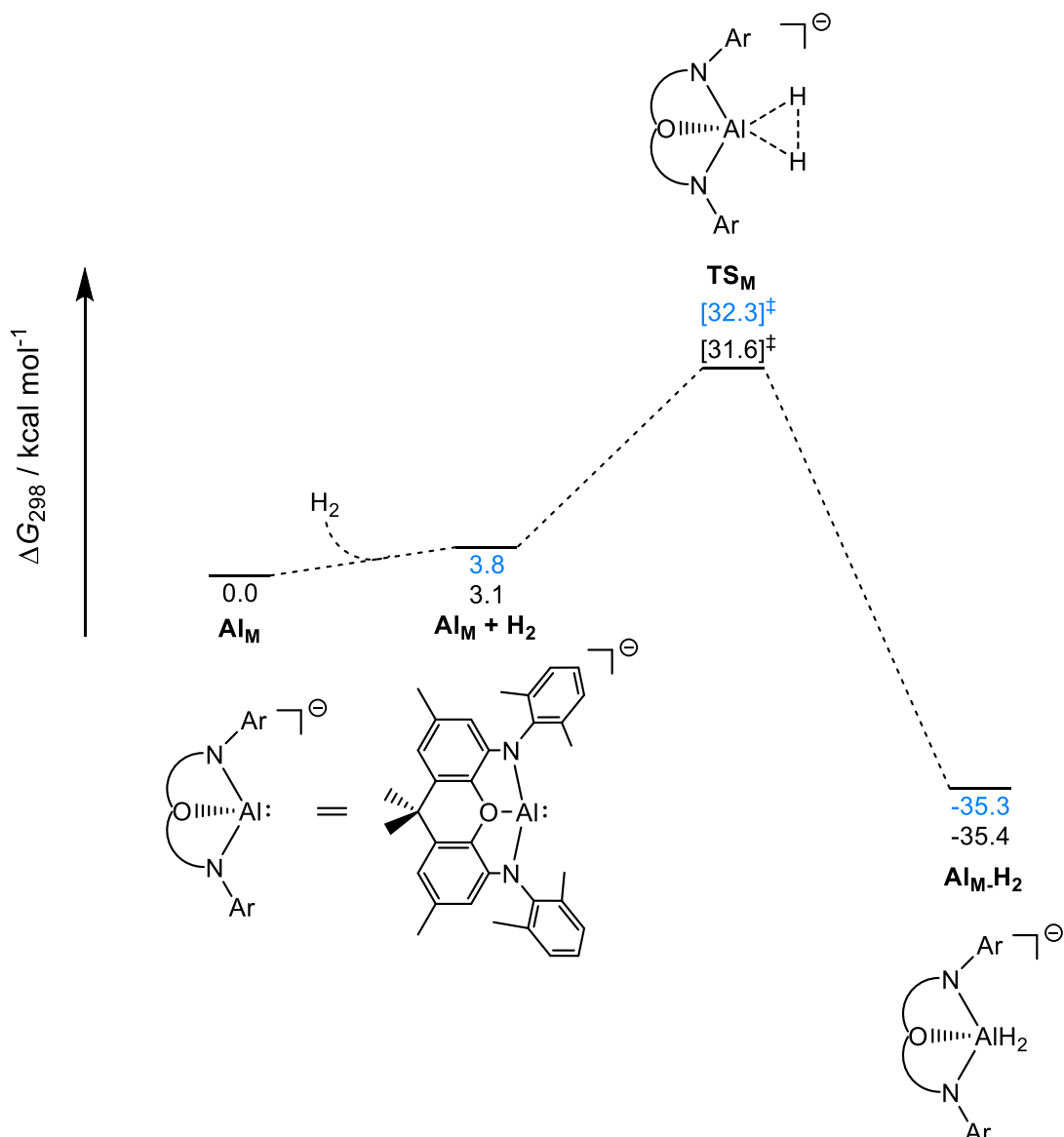


Figure 6.3: Gibbs Free Energy profile for activation of H_2 by the anionic aluminyl monomer Al_M , calculated at the SMD(benzene)-M062X-D3/def2-TZVPP//TPSS/def2-SVP level of theory. Relative Gibbs energies calculated at the SMD(benzene)-DLPNO-CCSD(T)//TPSS/def2-SVP level of theory are shown in blue.

The key optimised structures of this reaction profile are shown in Figure 6.4. In the encounter complex, $\text{Al}_\text{M} + \text{H}_2$, dihydrogen is situated above and perpendicular to the molecular plane of Al_M , with a $\text{Al}-\text{H1}$ bond distance of 3.57 Å. Along the intrinsic reaction coordinate, dihydrogen migrates to the equatorial plane of Al_M . In the transition state, TS_M , the $\text{H}-\text{H}$ bond is appreciably activated, with a bond distance of

6 - FLP-type cooperativity in an alkali metal aluminyl complex: proposal of a hydride rebound mechanism

1.16 Å. Furthermore, there is a clear asynchronicity in the forming Al—H bonds, with bond distances of 1.97 Å and 1.64 Å calculated for Al—H1 and Al—H2, respectively. This is consistent with the related activation of H₂ by the neutral $\text{NacNac}^{\text{Dipp}}\text{Al}$ species, where a concerted but asynchronous activation of dihydrogen has been calculated previously, by Cao²⁶⁸, as well as the results involving Cowley's N,P-stabilised aluminylene, presented in Chapter 5 of this thesis.

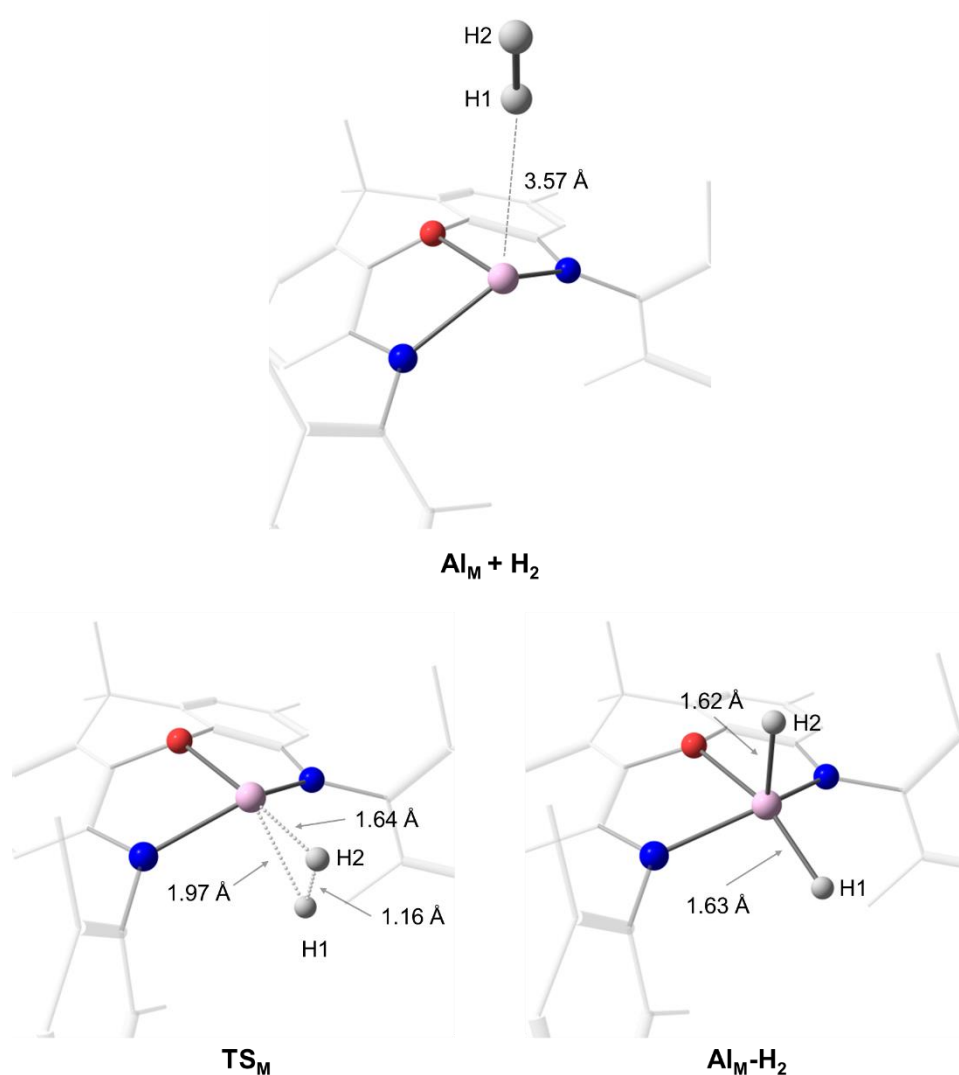


Figure 6.4: Optimized geometries (TPSS/def2-SVP) of $\text{Al}_M + \text{H}_2$, TS_M and $\text{Al}_M\text{-H}_2$ with key bond distances shown.

The transition state features the dihydrogen approaching the Al centre in the equatorial plane. This contrasts with the previous work by Schaefer (Figure 6.2, **TS_M**) where dihydrogen is activated above the molecular plane, reminiscent of an electrophilic activation of H₂, while the transition state calculated in this present work is more akin to a nucleophilic activation. It is noted that due to the more diffuse nature of the Al lone pair in aluminyl anion complexes, compared to carbenes²⁹², the line between electrophilic and nucleophilic activation is not entirely clear. However, this terminology will be employed here to draw a distinction between the two transition states. To investigate this, the electrophilic and nucleophilic concerted oxidative addition mechanism were calculated, using the same methodology employed by Schaefer (for comparative purposes). The electrophilic activation (**TS_M-Electro**) was found to proceed via a *higher* activation barrier (35.6 kcal mol⁻¹) than that calculated for the nucleophilic activation (31.6 kcal mol⁻¹). This is consistent with the increased nucleophilicity of the formally anionic Al(I) centre, compared to neutral Al(I). The DFT-calculated values are in excellent agreement with the DLPNO-CCSD(T) activation barriers. This result is significant, as it demonstrates that in the work by Schaefer, not only was the concerted oxidative addition mechanism calculated inconsistent with the experimental reaction conditions of 5 days at room temperature, but it was also a less energetically favourable *type* of concerted oxidative addition. This has been shown using the same methodology as employed by Schaefer, to provide a fair comparison.

6 - FLP-type cooperativity in an alkali metal aluminyl complex: proposal of a hydride rebound mechanism

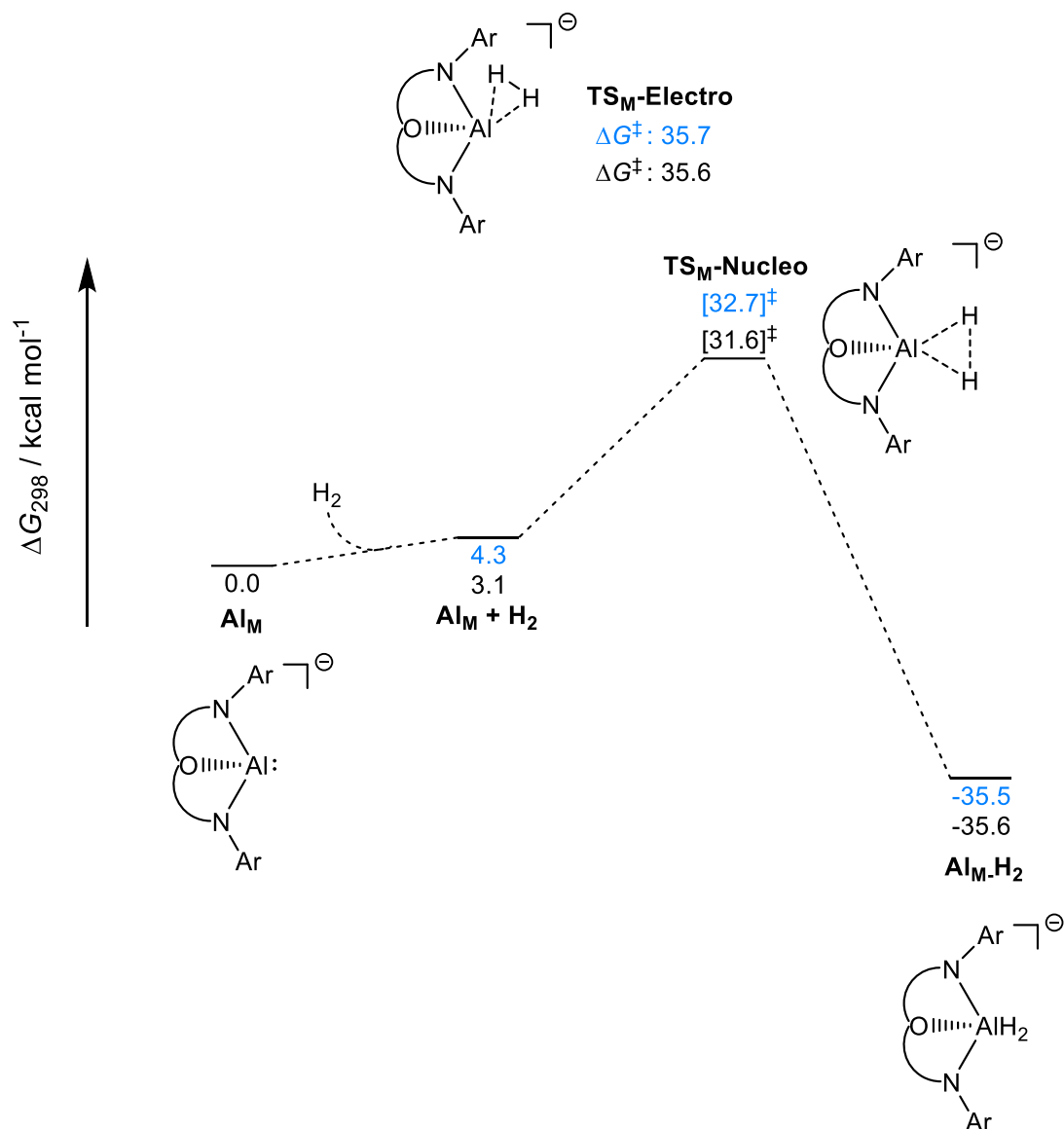


Figure 6.5: Gibbs Free Energy profile for activation of H_2 by the anionic aluminyl monomer Al_M , calculated at the SMD(benzene)-M062X-D3/def2-TZVPP//M062X/def2-SVP level of theory. Relative Gibbs energies calculated at the SMD(benzene)-DLPNO-CCSD(T)//TPSS/def2-SVP level of theory are shown in blue.

6 - FLP-type cooperativity in an alkali metal aluminyl complex: proposal of a hydride rebound mechanism

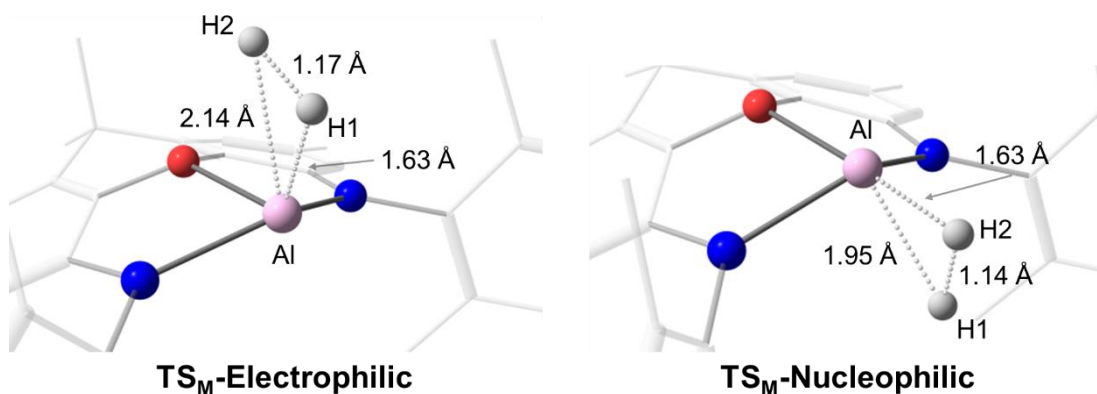


Figure 6.6: Optimized geometries (M062X/def2-SVP) of the transition states for the concerted electrophilic and nucleophilic oxidative addition mechanism, with key bond distances shown.

It has now been established that a concerted oxidative addition mechanism proceeds with an activation barrier that is inconsistent with the experimental reaction conditions. As discussed in the introduction, Hinz and Breher have previously postulated an FLP-type mechanism for the reaction under investigation.²⁸² Furthermore, Schaefer has even suggested this as a mechanistic possibility. However, all attempts by Schaefer to locate such a transition state were unsuccessful.²⁷¹ This was investigated further in this work, for the activation of H₂ by **Al_D**. A transition state has been located, that proceeds with a significantly lower activation barrier than the concerted oxidative addition mechanism. Furthermore, clear cooperative action between the metal centres is demonstrated. The Gibbs Free Energy reaction profile for this mechanism is shown in Figure 6.7, with key optimised structures shown in Figure 6.8 and Figure 6.9.

6 - FLP-type cooperativity in an alkali metal aluminyl complex: proposal of a hydride rebound mechanism

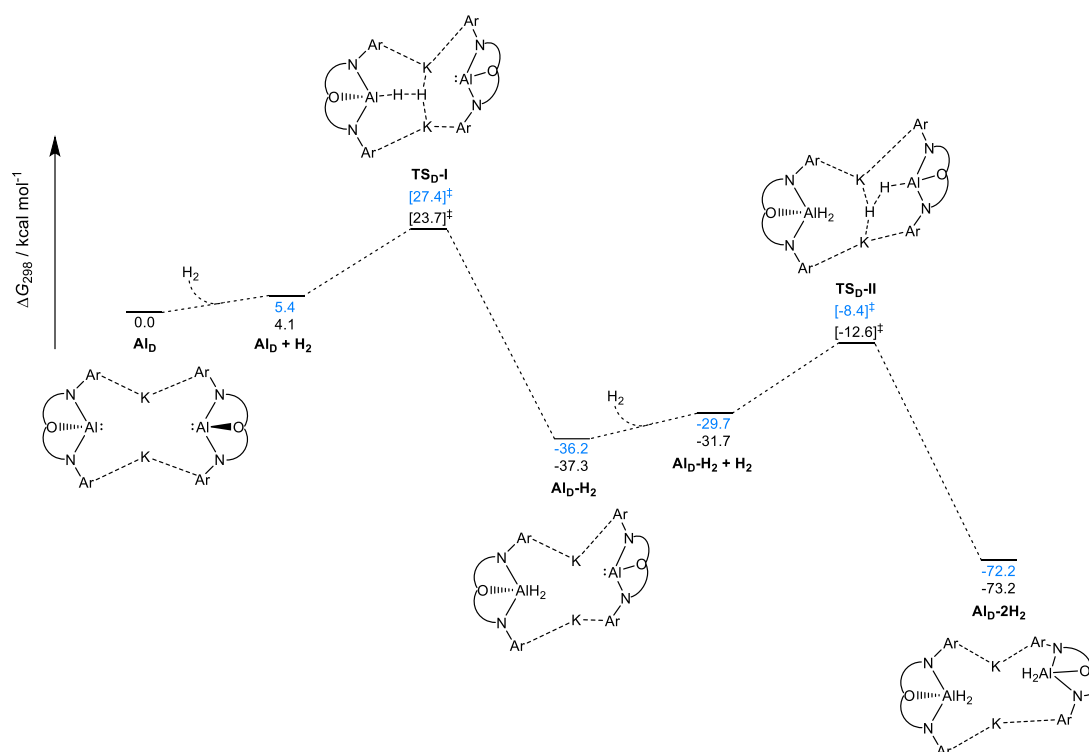


Figure 6.7: Gibbs Free Energy profile for activation of H_2 by the aluminyl contacted dimer pair Al_D , calculated at the SMD(benzene)-M062X-D3/def2-TZVPP//TPSS/def2-SVP level of theory. Relative Gibbs energies calculated at the SMD(benzene)-DLPNO-CCSD(T)//TPSS/def2-SVP level of theory are shown in blue.

Relative to the separated reactants, Al_D and H_2 , the encounter complex $\text{Al}_\text{D} + \text{H}_2$, was calculated to be $4.1 \text{ kcal mol}^{-1}$ endergonic. Dihydrogen is situated at the approximate midpoint between the two aluminium centres (4.29 \AA ($\text{Al1}\cdots\text{H1}$) and 4.60 \AA ($\text{Al2}\cdots\text{H2}$)), above the two potassium centres (3.37 \AA ($\text{K1}\cdots\text{H1}$) and 3.50 \AA ($\text{K2}\cdots\text{H1}$)). At the transition state, $\text{TS}_\text{D-I}$, dihydrogen interacts in an end-on fashion with the Al(I) centre, adopting a side-on bridging position between both K^+ ions. The activation barrier was calculated to be $23.7 \text{ kcal mol}^{-1}$ (a significant reduction of $7.9 \text{ kcal mol}^{-1}$, relative to the concerted oxidative addition process). The $\text{H}-\text{H}$ bond, at 1.23 \AA , is appreciably activated, more so than observed in the concerted oxidative mechanism (1.16 \AA). Furthermore, the $\text{Al1}-\text{H1}$ bond is already partially formed (1.81 \AA). The $\text{H2}-\text{K}$ bond distances are relatively equidistant at 2.50 \AA (K1) and 2.57 \AA (K2).

6 - FLP-type cooperativity in an alkali metal aluminyl complex: proposal of a hydride rebound mechanism

Inspection of the intrinsic reaction coordinate in the forward direction reveals that the Al1—H1 shifts downward into position, while the potassium cations “hold on to” to the more hydridic hydrogen atom, H2 (*vide infra*). Subsequent “hydride rebound” of H2 on to the aluminium centre then occurs, to form the Al(III) dihydride product, **Al_D-H₂**. The reaction energy for the addition of the first equivalent of dihydrogen was calculated to be -37.3 kcal mol⁻¹. The Al—H2 distance, at 1.67 Å in **Al_D-H₂** is elongated, relative to the Al—H2 distance, at 1.64 Å. This is due to the partial activation of the Al—H2 bond by the two potassium centres.

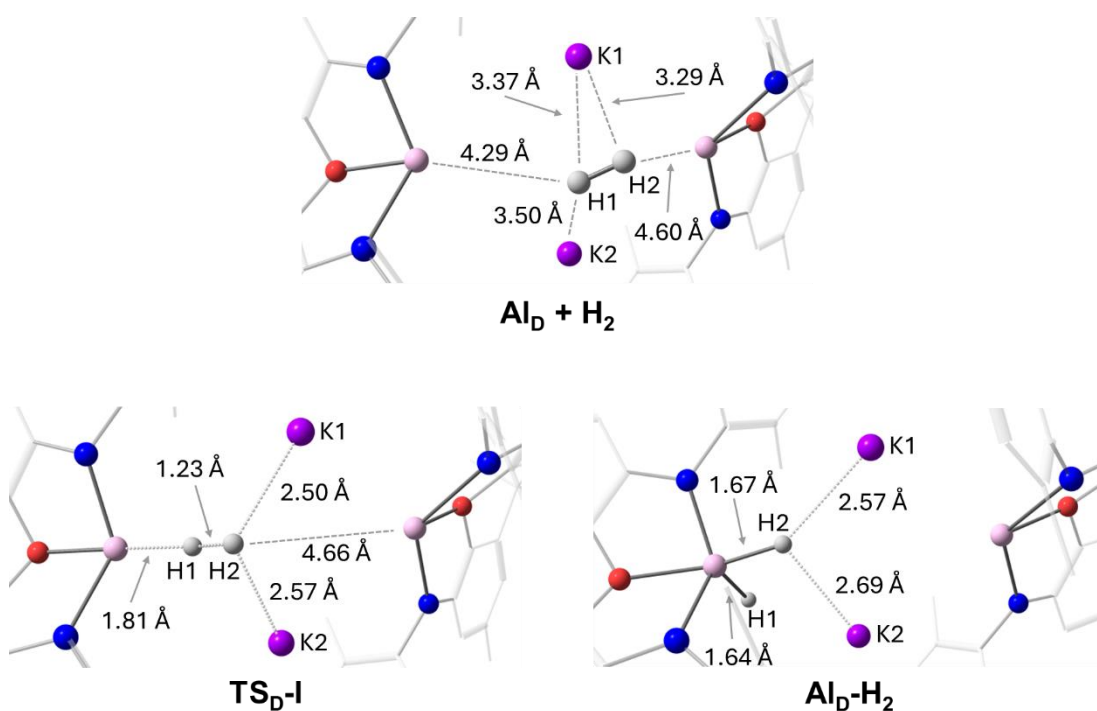


Figure 6.8: Optimized geometries (TPSS/def2-SVP) of **Al_D + H₂**, **TS_D-I** and **Al_D-H₂** with key bond distances shown.

The activation of a second equivalent of dihydrogen was calculated to proceed via the analogous mechanism, with a calculated activation barrier of 24.7 kcal mol⁻¹, essentially identical to the first barrier (within the error of the method). Furthermore,

the key structural parameters of the $K_2Al(H_2)$ unit at the transition state, **TS_{D-II}**, are almost identical to that observed for **TS_{D-I}**, with the H3—H4 bond distance calculated to be 1.22 Å, the Al2—H3 distance calculated to be 1.80 Å, and the H4—K1 and H4—K2 distances calculated to be 2.56 and 2.50 Å, respectively.

The DFT-calculated activation barriers and the DLPNO-CCSD(T) calculated values are in relatively good agreement. However, it is recognised that the agreement is not as good as that observed for the concerted oxidative addition process to the monomeric species, **Al_M** (Figure 6.3). Despite this, the *relative* barriers still indicate that **TS_{D-I}** provides access to a lower energy pathway than previous calculations have shown.²⁷¹ Furthermore, in the previous study from Schaefer, DLPNO-CCSD(T)/def2-TZVP calculated energies were also utilised to validate the DFT-calculated barriers (although only electronic energies were reported). Thus, a fair comparison of this work to the previous work is made.

6 - FLP-type cooperativity in an alkali metal aluminyl complex: proposal of a hydride rebound mechanism

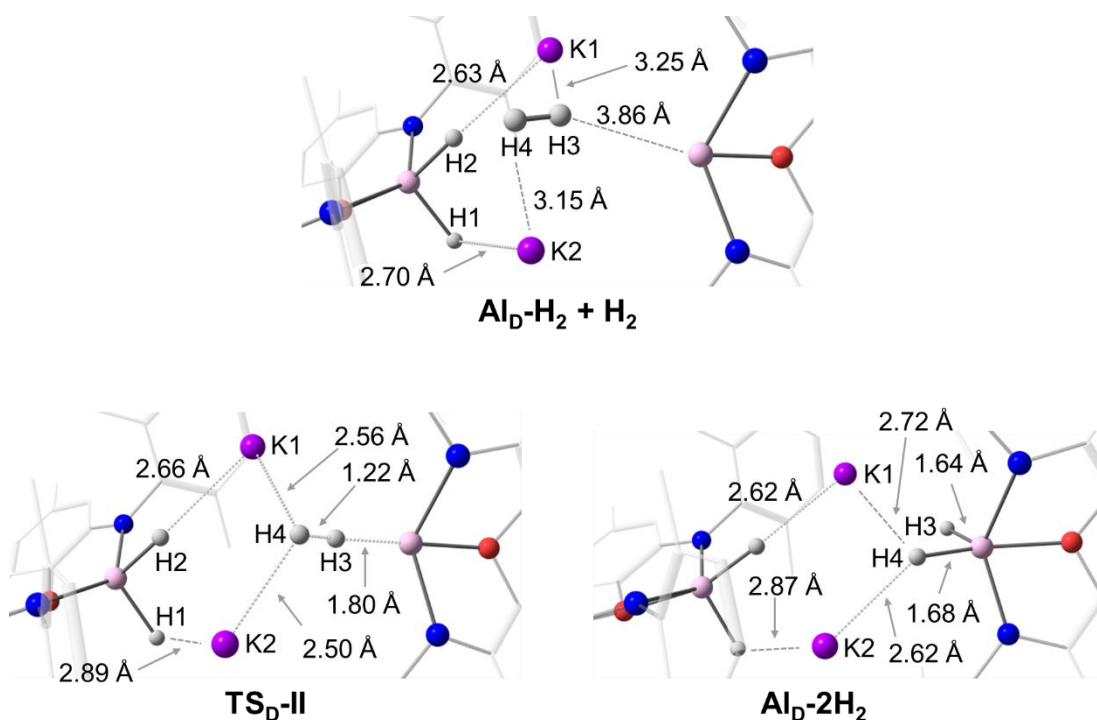


Figure 6.9: Optimized geometries (TPSS/def2-SVP) of $\text{Al}_\text{D}\text{-H}_2 + \text{H}_2$, $\text{TS}_\text{D-II}$ and $\text{Al}_\text{D}\text{-2H}_2$ with key bond distances shown.

This new mechanism for the activation of H_2 by Al_D can be compared to previously calculated FLP-type processes in the literature. In 2018, Stephan reported that an FLP-type mechanism was likely operative in the activation of H_2 by the $[\text{KCH}_2\text{C}_6\text{H}_5]_2$ dimer, or a related lithium phosphide (Figure 6.10).²⁹³ By comparing the structures of the TS from Stephan and $\text{TS}_\text{D-I}$, there are clear parallels. The H—H axis is aligned head-on with the carbanion or Al(I) centre, while interacting side-on with the two potassium cations. The carbanion or Al(I) centres are acting as the Lewis base, while the potassium cations are acting together as the Lewis acid. Thus, there is structural precedent in the literature for this FLP-type transition state, in addition to the energetically accessible barrier calculated.

6 - FLP-type cooperativity in an alkali metal aluminyl complex: proposal of a hydride rebound mechanism

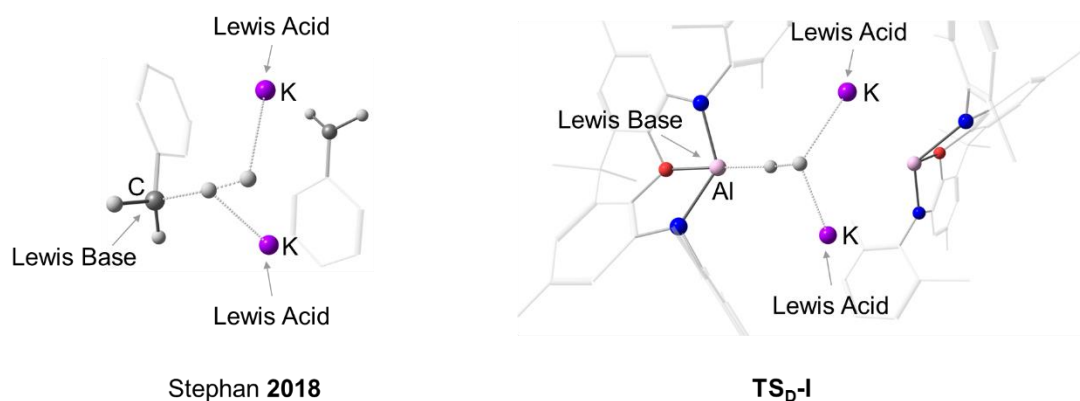


Figure 6.10: Comparison between the transition state calculated by Stephan²⁹³ and TS_{D-I}.

The new FLP-type mechanism was also successfully located using the methodology employed by Schaefer (M062X/def2-SVP) for the geometry optimisations (Figure 6.11). The optimised geometries of the two transition states are shown in Figure 6.12. The activation barriers, at 22.7 (first addition) and 23.4 kcal mol⁻¹ (second addition) are almost identical, and the overall structural features are essentially the same, as that calculated using the chosen level of theory for this study (TPSS/def2-SVP).

6 - FLP-type cooperativity in an alkali metal alumanyl complex: proposal of a hydride rebound mechanism

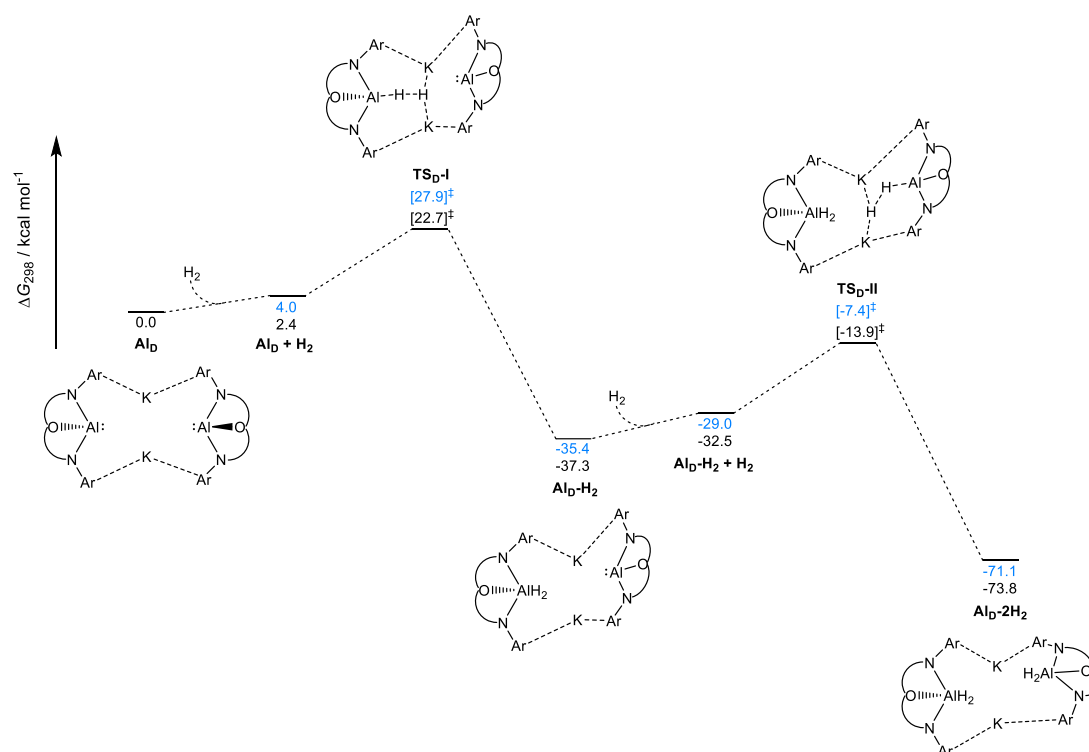


Figure 6.11: Gibbs Free Energy profile for activation of H₂ by the alumanyl contacted dimer pair **Al_D**, calculated at the SMD(benzene)-M062X-D3/def2-TZVPP//M062X/def2-SVP level of theory. Relative Gibbs energies calculated at the SMD(benzene)-DLPNO-CCSD(T)//TPSS/def2-SVP level of theory are shown in blue.

This result is significant, as it demonstrates that even when employing Schaefer's methodology, the FLP-type mechanism could still be located, with broadly identical structural and energetic features. Furthermore, the FLP-type mechanism once again affords a more energetically accessible pathway, compared to the experimentally inconsistent concerted oxidative addition mechanism. Having established that the FLP-type process is not dependent on the chosen methodology in this work, the detailed electronic structure analysis carried out will now be discussed.

6 - FLP-type cooperativity in an alkali metal aluminyl complex: proposal of a hydride rebound mechanism

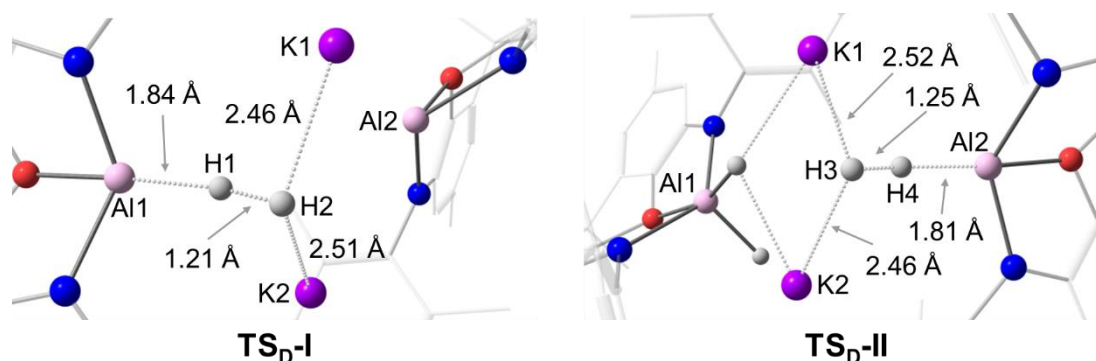


Figure 6.12: Optimized geometries (M062X/def2-SVP) of **TS_{D-I}** and **TS_{D-II}** with key bond distances shown.

One of the well-known charge analysis schemes is the Voronoi deformation density (VDD) analysis. The charge Q , of an atom A , is computed by spatial integration of the electronic density over the Voronoi cell of atom A . The charge Q can be interpreted as a measure of charge flow, that upon chemical bonding, flows either into ($Q_A < 0$) or out of ($Q_A > 0$) the Voronoi cell of atom A . This method therefore provides the capability to follow the electronic charge flow in a chemically intuitive way. One common method of utilising VDD atomic charges is to analyse the change in the charges, ΔQ_A , upon interaction of two molecular fragments. In Figure 6.13 and Figure 6.14 the relevant changes in VDD atomic charges (ΔQ) for each of the transition states are summarised. From analysis of ΔQ for the relevant atoms of the monomeric transition state (Figure 6.13), it is evident that as the metal fragment is permitted to interact with the dihydrogen fragment, a significant amount of electronic charge flows onto H1 (-162 milli-electrons), marking it as the hydridic species in the transition state. H2 is clearly marked as the protic species, evidenced by the charge flow of +70 milli-electrons occurring upon interaction of the dihydrogen and aluminyl fragments.

6 - FLP-type cooperativity in an alkali metal aluminyl complex: proposal of a hydride rebound mechanism

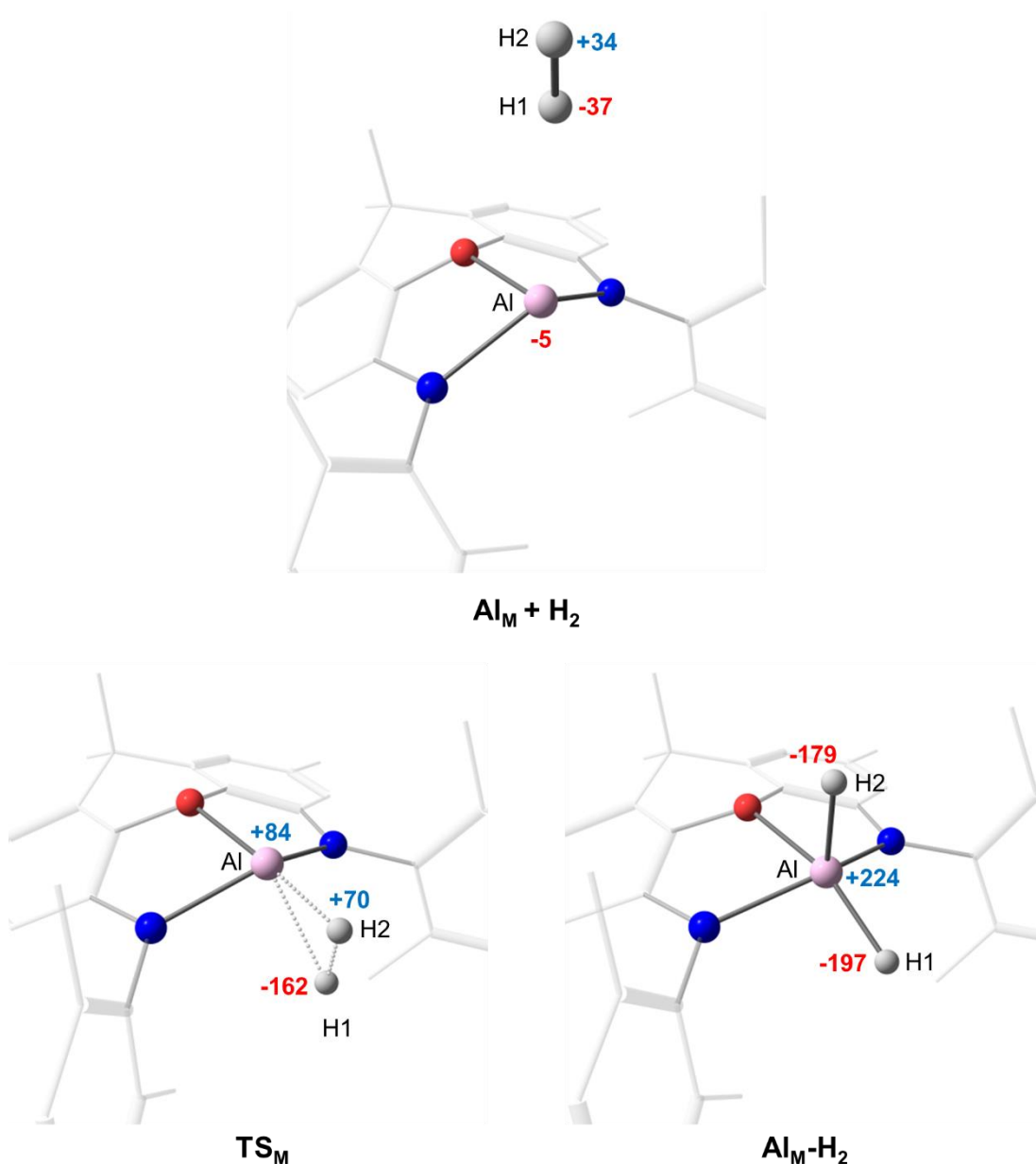


Figure 6.13: Change in Voronoi deformation density (VDD) atomic charge, ΔQ (in milli-electrons), for $\text{Al}_M + \text{H}_2$, TS_M and $\text{Al}_M\text{-H}_2$. $\Delta Q > 0$ (blue) indicates charge flow out of the Voronoi cell of an atom, and $\Delta Q < 0$ (red) indicates charge flow into the Voronoi cell of an atom, due to the interaction between the molecular fragments.

Moving to the FLP-type mechanism (Figure 6.14), the more activated H—H bond is evident from analysis of the ΔQ s. This large separation of charges upon interaction of the metal fragment with the H_2 fragment gives support to the description of this

6 - FLP-type cooperativity in an alkali metal aluminyl complex: proposal of a hydride rebound mechanism

transition state as an FLP-type transition state. The ΔQ for H₂ in **TS_D-I** is -334 milli-electrons, while the Al centre experiences a ΔQ of +61 milli-electrons. The two potassium centres experience ΔQ s of +7 and +26 milli-electrons, for K1 and K2 respectively. This reflects the differing K \cdots H₂ bond distances. Similar results are found for the VDD charge analyses of the transition states for the second activation of H₂ (Figure 6.15).

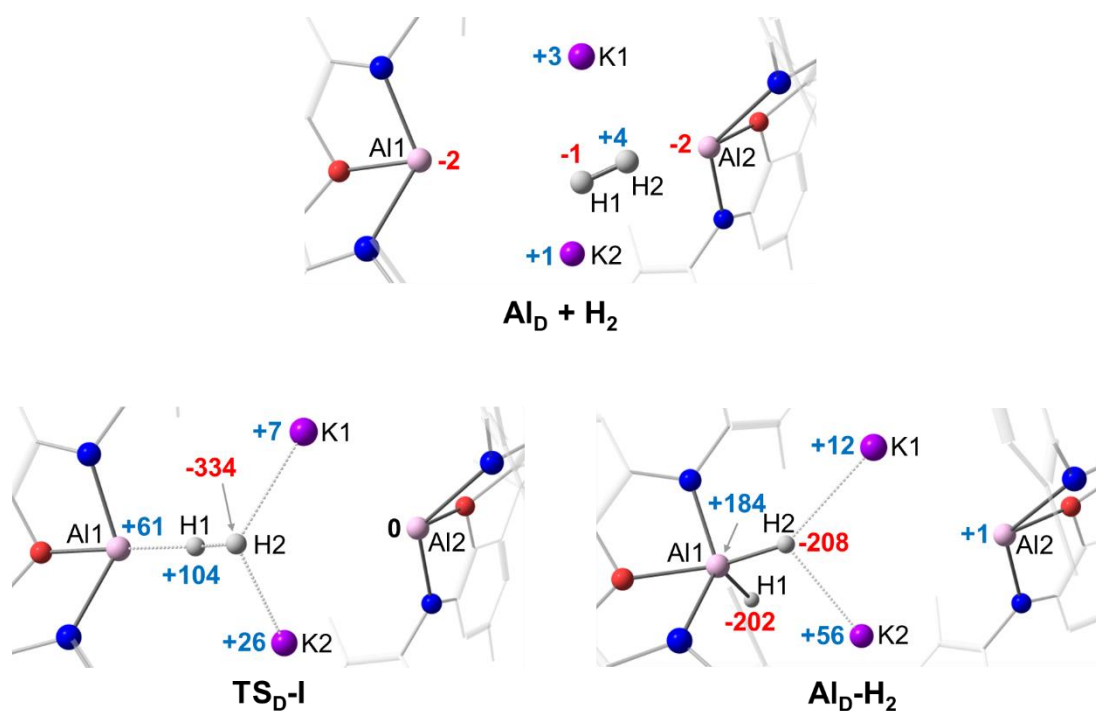


Figure 6.14: Change in Voronoi deformation density (VDD) atomic charge, ΔQ (in milli-electrons), for **Al_D** + H₂, **TS_D-I** and **Al_D-H₂**. $\Delta Q > 0$ (blue) indicates charge flow out of the Voronoi cell of an atom, and $\Delta Q < 0$ (red) indicates charge flow into the Voronoi cell of an atom, due to the interaction between the molecular fragments.

6 - FLP-type cooperativity in an alkali metal aluminyl complex: proposal of a hydride rebound mechanism

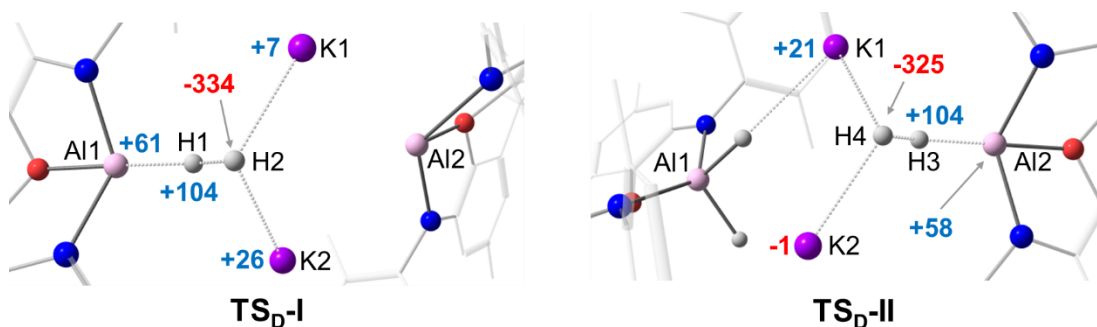


Figure 6.15: Change in Voronoi deformation density (VDD) atomic charge, ΔQ (in milli-electrons), for TS_D-I and TS_D-II . $\Delta Q > 0$ (blue) indicates charge flow out of the Voronoi cell of an atom, and $\Delta Q < 0$ (red) indicates charge flow into the Voronoi cell of an atom, due to the interaction between the molecular fragments.

In order to gain further insight into the interactions present, and to complement the VDD charge analysis, an activation strain and energy decomposition analysis (ASM-EDA), also known as the distortion/interaction model, was carried out.²⁹⁴ The overall bonding energy between two molecular fragments can be represented by the following equation:

$$\Delta E_{bond} = \Delta E_{strain} + \Delta E_{int} \quad (6.1)$$

The energy required to distort the fragments from their equilibrium geometries to the geometries that they attain in the interacting molecule is given by the strain energy, ΔE_{strain} , which is offset by the stabilising interaction energy ΔE_{int} (Figure 6.16).

6 - FLP-type cooperativity in an alkali metal aluminyl complex: proposal of a hydride rebound mechanism

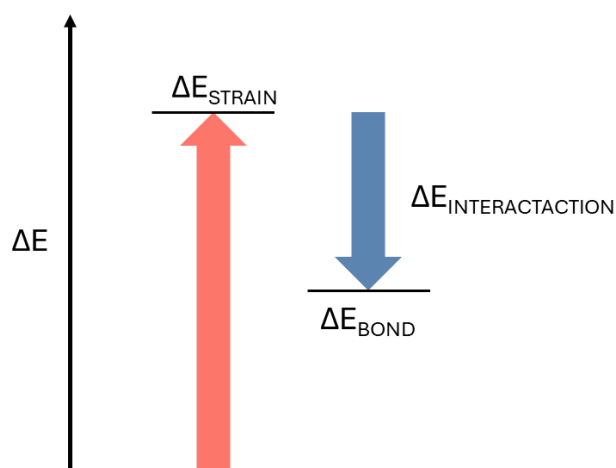


Figure 6.16: Visual representation of the overall bonding energy between molecular fragments.

The interaction energy can be further decomposed into contributions stemming from electrostatic interaction (ΔE_{elec}), Pauli repulsion (ΔE_{Pauli}), orbital interaction (ΔE_{orb}) and dispersion energy (ΔE_{disp}), given by the following equation:

$$\Delta E_{int} = \Delta E_{elec} + \Delta E_{Pauli} + \Delta E_{orb} + \Delta E_{disp} \quad (6.2)$$

The electrostatic term is the quasi-classical electrostatic interaction between the unperturbed charge densities of each fragment. The Pauli repulsion term accounts for steric repulsion, arising from destabilising interactions between the occupied orbitals of the fragments. The orbital term accounts for charge transfer, polarisation, and electron-pair interactions. Finally, a stabilising dispersion energy term is added.

Shown in Table 6.3 are the strain (ΔE_{strain}) and the interaction (ΔE_{int}) energies for each of the transition states studied. First, focussing on **TS_M**, most of the total strain energy comes from the activation of the H—H bond. The stabilizing interaction energy is less than half the magnitude of the total strain energy, resulting in an overall high activation barrier. Decomposition of the interaction energy into its various contributions demonstrates that although there is significant stabilization from the orbital term (-

6 - FLP-type cooperativity in an alkali metal aluminyl complex: proposal of a hydride rebound mechanism

116.7 kcal mol⁻¹) and the electrostatic term (-62.7 kcal mol⁻¹), the repulsive Pauli term largely cancels out this effect (163.9 kcal mol⁻¹).

Table 6.3: Activation strain and energy decomposition analysis of the transition states for the monomeric and dimeric pathways. All energies stated have units of kcal mol⁻¹.

	ΔE_{strain}			ΔE_{int}	ΔE_{elec}	ΔE_{pauli}	ΔE_{orb}	ΔE_{disp}
	[Al]	H ₂	Total					
TS_M	4.48	33.82	38.30	-18.85	-62.70	163.91	-116.72	-3.34
TS_{D-I}	5.57	41.52	47.08	-33.48	-43.33	126.57	-113.51	-3.21
TS_{D-II}	6.85	41.32	48.17	-32.97	-43.75	129.31	-115.15	-3.38

For **TS_{D-I}** there is an increase in the strain experienced by both H₂ and **Al_D**, leading to an overall higher strain energy than in the monomeric case (47.1 kcal mol⁻¹). The difference in energy for the aluminyl fragment is only marginal, however, and as already observed structurally, the activation of the H—H bond is larger in the dimeric case. Despite this larger strain energy, the interaction energy was calculated to be almost twice as stabilising ($\Delta E_{\text{int}} = -33.5$ kcal mol⁻¹) than that observed for the monomeric transition state **TS_M**. Decomposition of the interaction energy term for **TS_{D-I}** reveals that this effect can mainly be attributed to loss of Pauli repulsion, although this is accompanied by a reduction in electrostatic stabilization. This reduction in electrostatic stabilization for **TS_{D-I}** is likely due to the less favourable, end-on orientation of dihydrogen, reducing the electrostatic interaction between the Al(I) centre and the more hydridic hydrogen atom, compared to **TS_M**. The orbital and dispersion terms are largely the same as for **TS_M**. In summary, there is a 22.7 kcal mol⁻¹ total electrostatic stabilization loss compared to monomeric case, however a reduction of Pauli repulsion by 37.3 kcal mol⁻¹ more than compensates for this. For

TS_{D-II}, the same trends are broadly observed, with the total strain energy being slightly larger (1.2 kcal mol⁻¹ increase compared to first **TS_{D-I}**) and a slightly less stabilizing interaction energy (0.5 kcal mol⁻¹ decrease relative to **TS_{D-I}**).

The activation strain and energy decomposition analysis above was performed on a single point on the intrinsic reaction for each of the reactions considered i.e. the transition states. It has been stated in the literature that analysis of a single stationary point should be interpreted with care, as the energetic components involved are highly dependent on the position of the studied point on the IRC.²⁹⁵ An acceptable comparison *can* be made when reactions are compared at a consistent geometry. In Figure 6.17, the comparative activation strain and energy decomposition analysis for the H₂ activation as a function of the H···H bond distance along the IRC to the transition state and several steps after is shown. In order to reliably compare the two processes i.e. the concerted oxidative addition to **Al_M** to the FLP-type addition to **Al_D** (the first addition of H₂), a comparable distance of 1.2 Å (an approximate average of the H···H distance in **TS_M** and **TS_{D-I}**) was chosen arbitrarily on each of the respective intrinsic reaction coordinates. Coincidentally, in the case of **Al_D**, this is the point corresponding to the transition state, whereas for **Al_M** it is a single step past the transition state on the IRC. The relevant activation strain and energy decomposition analysis data for this comparable point is shown in Table 6.4.

6 - FLP-type cooperativity in an alkali metal aluminyl complex: proposal of a hydride rebound mechanism

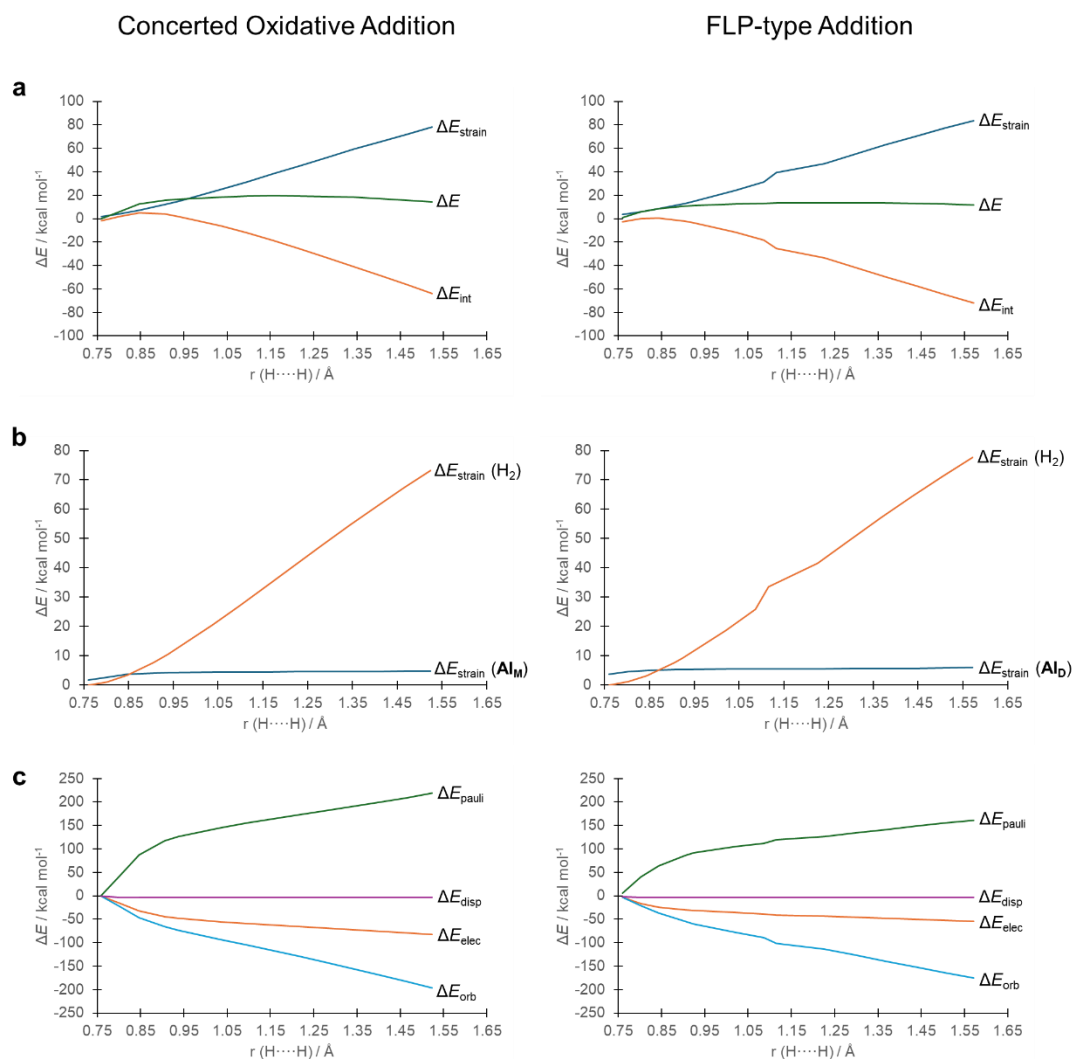


Figure 6.17: Comparative activation strain and energy decomposition analysis for the H₂ activation by **Al_M** (left panels) and **Al_D** (right panels), as a function of the H···H bond distance along the IRC up to the transition states, and several steps after. a) Plot of the total strain energy, interaction energy and the overall change in energy ($\Delta E = \Delta E_{\text{strain}} + \Delta E_{\text{int}}$). b) Decomposition of the total strain energy into the strain energy of H₂ and **Al_X** (X= M, D). c) Decomposition of the interaction energy into its various components.

Unsurprisingly, the overall strain energy along the concerted oxidative addition pathway increases to 45.3 kcal mol⁻¹, which is a 7.0 kcal mol⁻¹ increase, relative to the transition state. This is almost entirely due to the increased H···H distance, with only a negligible change observed for the monomer, **Al_M**. The interaction energy decreases by 7.1 kcal mol⁻¹, in comparison to the transition state. This is due to a net stabilisation,

6 - FLP-type cooperativity in an alkali metal aluminyl complex: proposal of a hydride rebound mechanism

stemming from the electrostatic and orbital terms, which cancel out a 9.1 kcal mol⁻¹ increase in the Pauli repulsion. Despite this more stabilising interaction energy, the increased strain energy essentially cancels out this net gain in stabilisation. Overall, these results indicate that whether one compares the two structures containing comparable H···H distances, or the two transition states (**TS_M** and **TS_{D-I}**), the conclusions are the same: a) The concerted oxidative addition process has a less stabilising interaction energy, due to a significantly larger Pauli repulsion term, in comparison to the FLP-type process b) the strain energy is dominated by the activation of H₂, with **Al_D** requiring more distortion than **Al_M**.

Table 6.4: Activation strain and energy decomposition analysis for the monomeric and dimeric pathways, at a comparable HH bond distance of 1.2 Å. All energies stated have units of kcal mol⁻¹.

IRC Point at 1.2 Å (H···H)	ΔE_{strain}			ΔE_{int}	ΔE_{elec}	ΔE_{pauli}	ΔE_{orb}	ΔE_{disp}
	[Al]	H ₂	Total					
Concerted Oxidative Addition	4.53	40.77	45.30	-25.91	-66.23	173.03	-129.39	-3.32
FLP-type Addition	5.57	41.52	47.08	-33.48	-43.33	126.57	-113.51	-3.21

The Extended Transition State / Natural Orbitals for Chemical Valence (ETS-NOCV) charge and energy decomposition scheme offers further insight into the deformation density, which is partitioned into different symmetry components of the chemical bonding interaction between defined fragments. The energy contributions ΔE_{orb} to the total bond energy is calculated for each specific orbital interaction between fragments, giving insight in the orbital interactions. A breakdown of key deformation densities

6 - FLP-type cooperativity in an alkali metal aluminyl complex: proposal of a hydride rebound mechanism

contributing to the orbital term in both **TS_M** and **TS_{D-I}** is presented in Figure 6.18 and Figure 6.19, respectively.

6 - FLP-type cooperativity in an alkali metal alumanyl complex: proposal of a hydride rebound mechanism

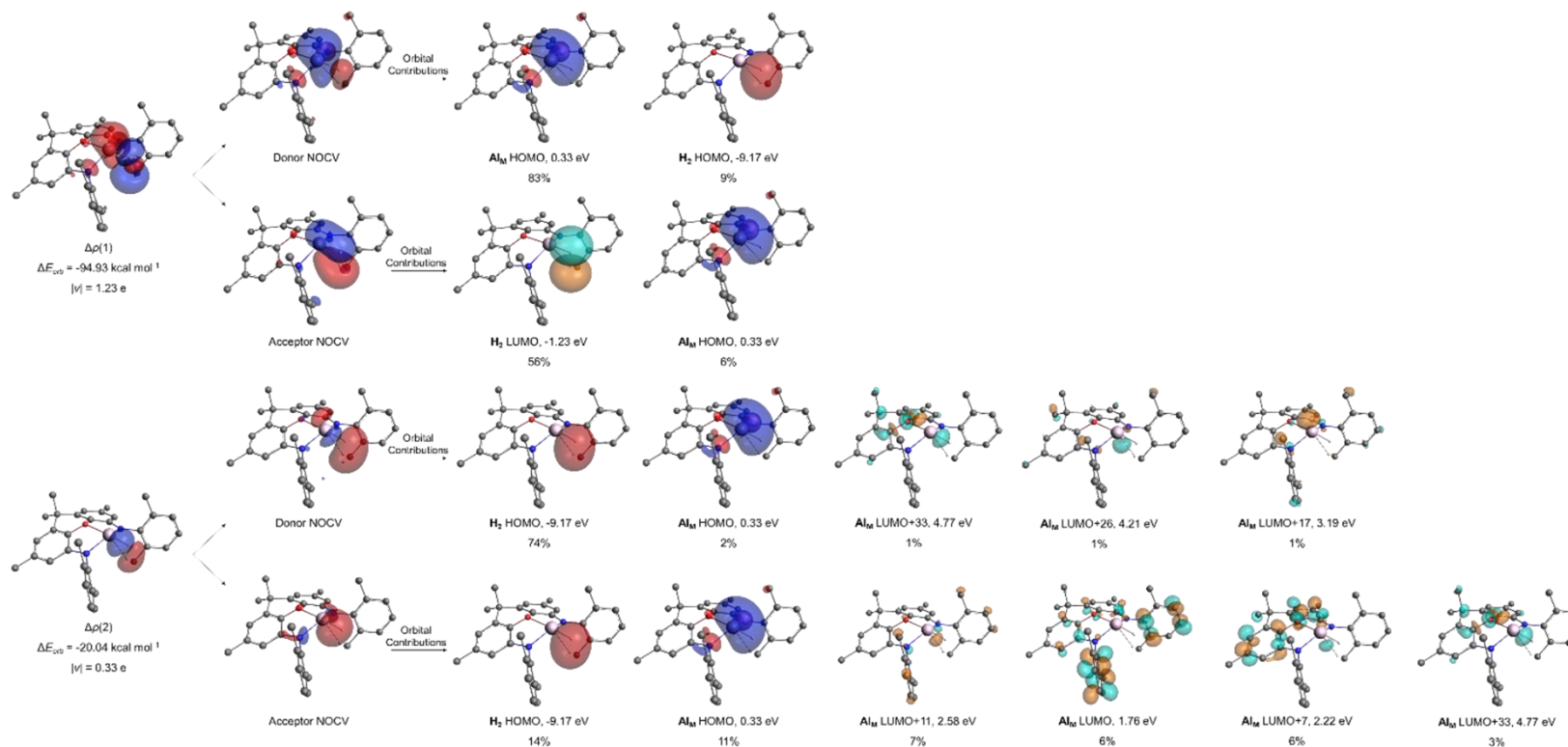


Figure 6.18: Breakdown of the most significant deformation density (charge flow is red to blue) that contributes to ΔE_{orb} for **TS_M**. Chemically relevant fragment orbitals that compose the donor and acceptor NOCV orbitals are shown, along with their energies and percentage contributions. The deformation densities were visualised using an isovalue of 0.002 au, and the orbitals were visualised using an isovalue of 0.04 au.

6 - FLP-type cooperativity in an alkali metal alumanyl complex: proposal of a hydride rebound mechanism

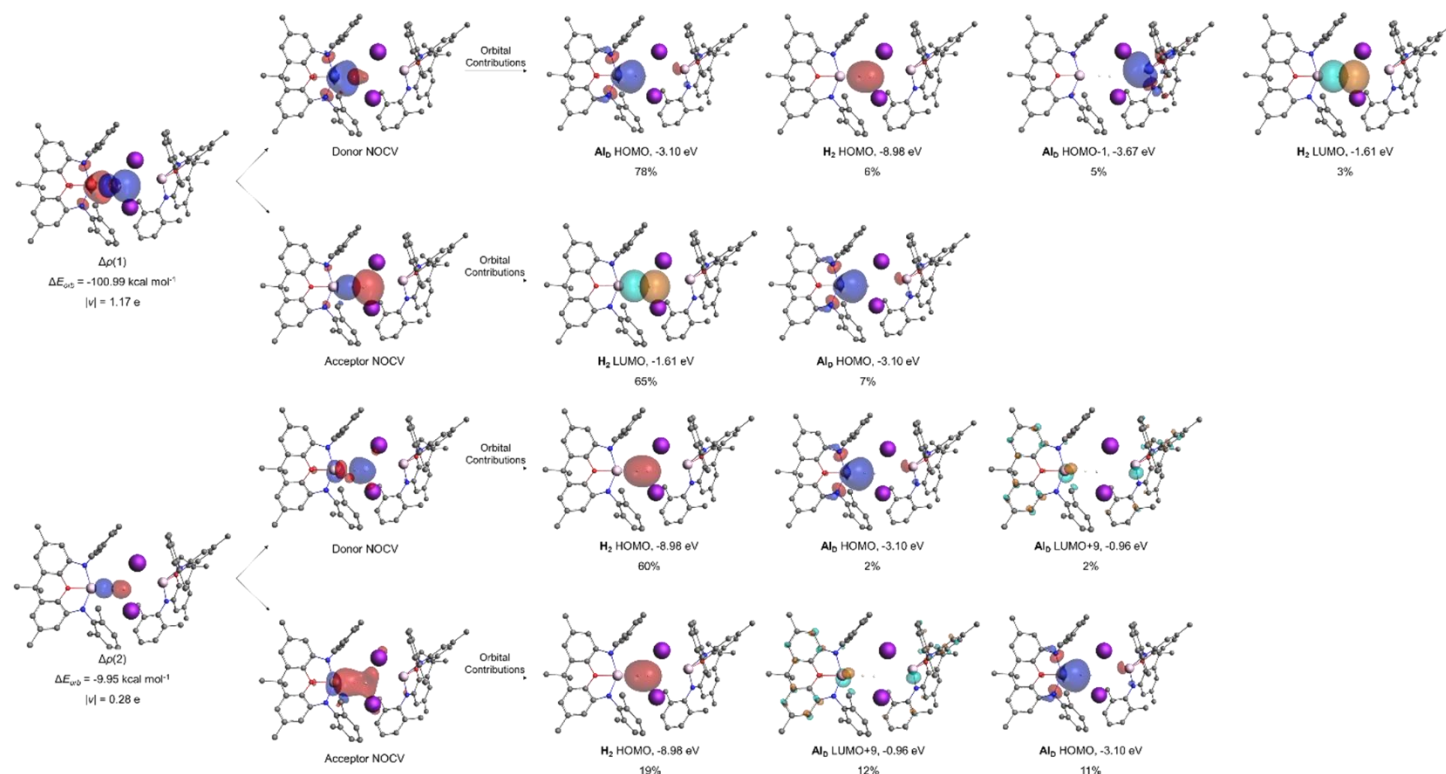


Figure 6.19: Breakdown of the most significant deformation densities (charge flow is red to blue) that contributes to ΔE_{orb} for **TS_{D-I}**. Chemically relevant fragment orbitals that compose the donor and acceptor NOCV orbitals are shown, along with their energies and percentage contributions. The deformation densities were visualised using an isovalue of 0.002 au, and the orbitals were visualised using an isovalue of 0.04 au.

A natural bond orbital (NBO) analysis was carried out on **TS_M**, **TS_{D-I}**, and **TS_{D-II}** to provide insight into the key interactions present at these transition states, via analysis of the fragment interaction terms from second order perturbation theory. The stabilisation energies, $E^{(2)}$, associated with donor-acceptor interactions within the two FLP-type transition states are given in Figure 6.20 and Figure 6.21. The Lewis structure localised by the NBO analysis contains a hydride and an Al—H bond, in the case of **TS_{D-I}**. The dominant interaction for **TS_{D-I}**, with a magnitude of 129.4 kcal mol⁻¹, is the donation from the lone pair type orbital of the hydridic species into the σ^* of the Al—H bond that is already partially formed at the transition state. This acceptor orbital has a population of 0.44 electrons. Furthermore, there are donations from this same lone pair type orbital into the empty s orbital of each of the potassium atoms. In the case of **TS_{D-I}**, the donation into the 4s orbital of K1 has an energy of 9.75 kcal mol⁻¹, with this orbital having an occupation of 0.13 electrons. A smaller donation of 4.19 kcal mol⁻¹ was also observed for the 4s orbital of K2, with this orbital having an occupation of 0.10 electrons. Although both interactions are relatively small in magnitude, they provide further support to the connotation of cooperativity between the metal centres in both transition states. The high negative charge localisation on the hydridic species, as indicated by the Voronoi charges (and NBO charges below), can be stabilised or dissipated by the empty s-orbitals of the two potassium cations.

6 - FLP-type cooperativity in an alkali metal aluminyl complex: proposal of a hydride rebound mechanism

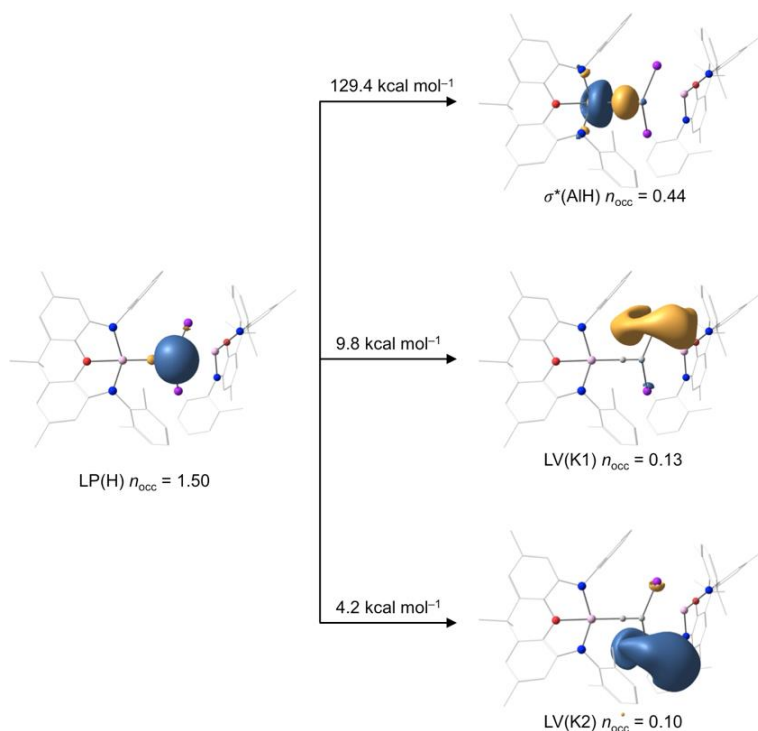


Figure 6.20: Second order perturbation theory analysis of the Fock matrix from NBO, showing the most relevant donor-acceptor interactions taking place at the reaction site in **TS_{D-I}**. An isovalue of 0.05 au was used for visualisation.

The same analysis of **TS_{D-II}** revealed an almost identical picture. The dominant interaction between the lone pair type orbital of the hydridic species and the σ^* of the Al—H bond has a magnitude of 127.5 kcal mol⁻¹, with the acceptor orbital having a population of 0.44 electrons (identical to **TS_{D-I}**). The donation into the 4s orbital of K2 has a magnitude of 10.9 kcal mol⁻¹. This is in contrast to **TS_{D-I}**, where the analogous donation (of similar magnitude) occurs into the 4s orbital of K1. This is simply explained by the Al—K bond distances. In **TS_{D-I}**, K1 is closer (2.50 Å) than K2 (2.57 Å) to Al1, while in **TS_{D-II}**, K1 is further away (2.56 Å) than K2 (2.50 Å) from Al2. Finally, there is a smaller donation of 4.20 kcal mol⁻¹ into the 4s orbital of K1, almost identical that observed in **TS_{D-I}**.

6 - FLP-type cooperativity in an alkali metal aluminyl complex: proposal of a hydride rebound mechanism

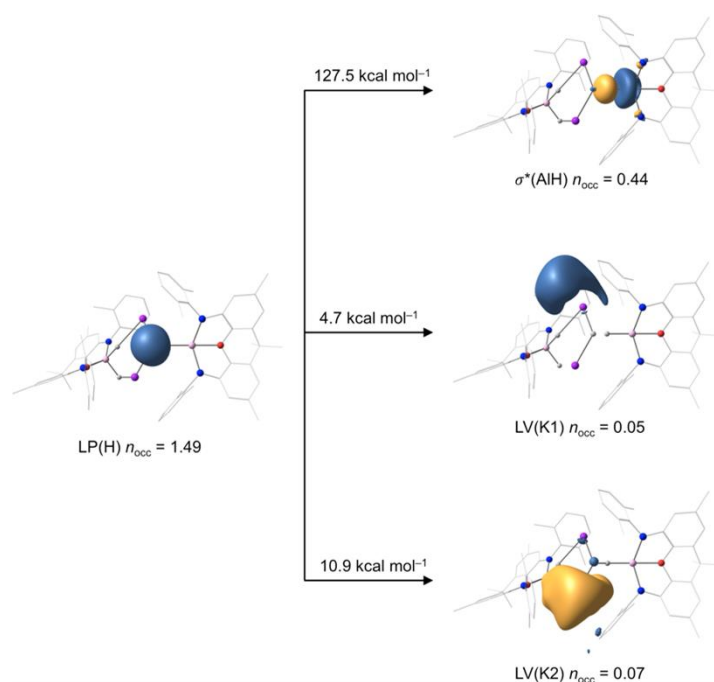


Figure 6.21: Second order perturbation theory analysis of the Fock matrix from NBO, showing the most relevant donor-acceptor interactions taking place at the reaction site in **TS_{D-II}**. An isovalue of 0.05 au was used for visualisation.

Relevant natural population charges and Wiberg bond indices were also collected for **TS_M**, **Al_M-H₂**, **TS_{D-I}**, **TS_{D-II}**, **Al_D-H₂** and **Al_D-2H₂** as shown in Figure 6.22 and Figure 6.23 (charges given in milli-electrons to be consistent with the presentation of Voronoi charges above). For **TS_M**, the NPA charges predict negative charges on both hydrogen atoms and in line with the Voronoi charge analysis, significantly more negative charge is calculated to be present on H1. There is also a high degree of positive charge on the aluminium (+967 milli-electrons) atom, consistent with oxidative addition occurring (+717 milli-electrons on Al centre in **Al_M**). The appreciable activation of the H—H bond is also evident from the WBI of 0.29, coupled with the WBIs of 0.60 and 0.64 for Al—H1 and Al—H2, respectively.

6 - FLP-type cooperativity in an alkali metal aluminyl complex: proposal of a hydride rebound mechanism

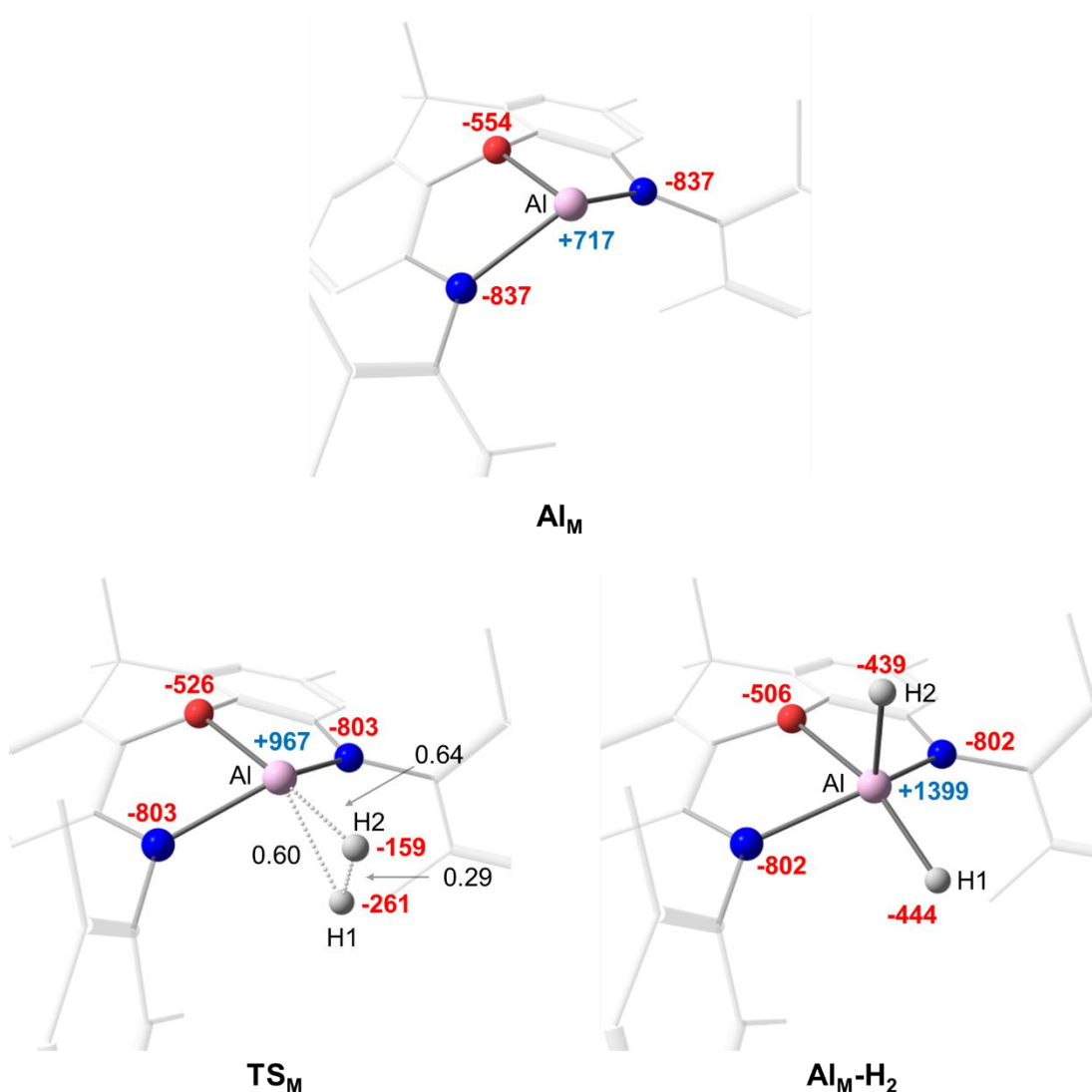


Figure 6.22: Relevant NPA charges (positive charges shown in blue, negative charges shown in red) and Wiberg bond indices (shown in black) of Al_M , TS_M and Al_M-H_2 . Charges are given in units of milli-electrons.

Moving to the dimer (Figure 6.23), the NPA charges predict both hydrogen atoms to be negative in TS_D-I , with more negative charge located on H1. This is consistent with the VDD charge analysis, that marked H1 as being more hydridic in nature than H2. Furthermore, the WBI of H1—H2 is 0.25, slightly less than that predicted in TS_M , in line with the higher degree of bond activation observed structurally for TS_D-I . In the intermediate Al_D-H_2 , H2 has a slightly more negative charge associated with it, and

6 - FLP-type cooperativity in an alkali metal aluminyl complex: proposal of a hydride rebound mechanism

the Al1—H2 bond has a WBI of 0.62, lower than that predicted for Al1—H1. This is consistent with partial activation of Al1—H2 by the potassium centres. In Figure 6.24, relevant NPA charges and WBIs were also collected for the transition state associated with the second activation of H₂, with almost identical results obtained.

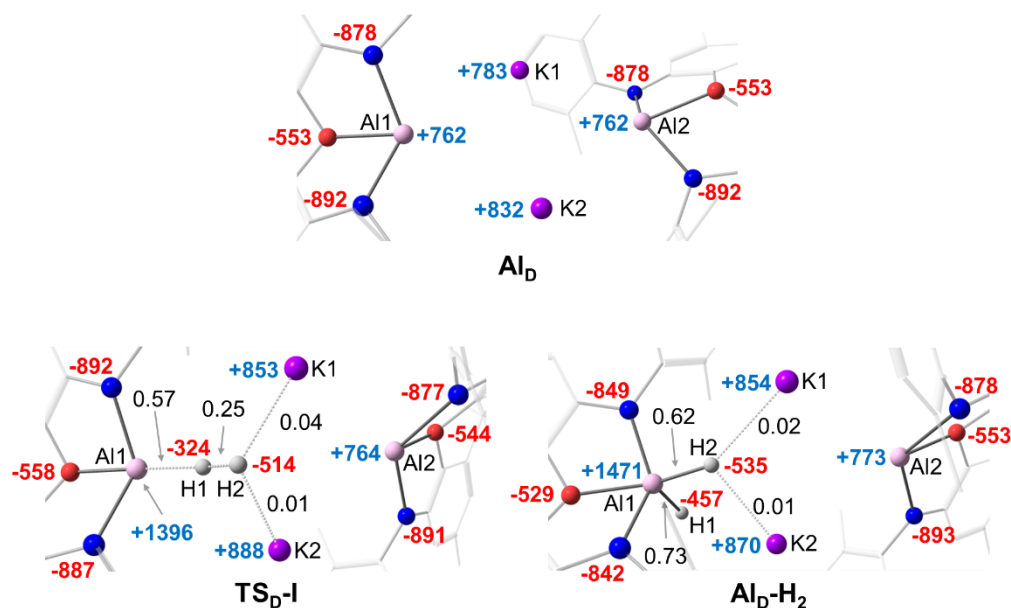


Figure 6.23: Relevant NPA charges (positive charges shown in blue, negative charges shown in red) and Wiberg bond indices (shown in black) of Al_D , $\text{TS}_D\text{-I}$ and $\text{Al}_D\text{-H}_2$. Charges are given in units of milli-electrons.

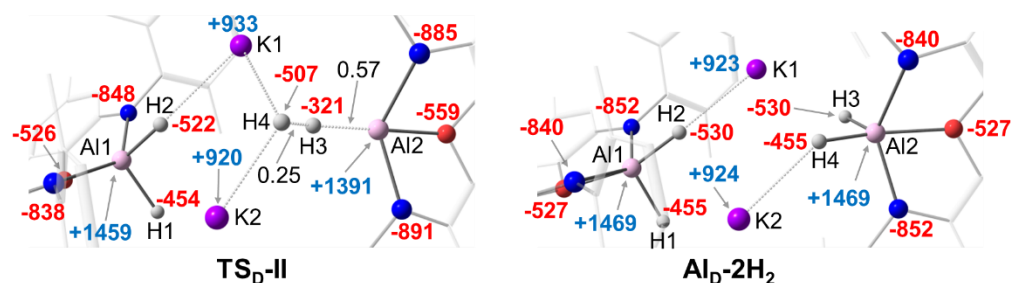


Figure 6.24: Relevant NPA charges (positive charges shown in blue, negative charges shown in red) and Wiberg bond indices (shown in black) of $\text{TS}_D\text{-II}$ and $\text{Al}_D\text{-2H}_2$. Charges are given in units of milli-electrons.

Finally, QTAIM analysis was carried out, to further characterise the main features of relevant stationary points. Shown in Figure 6.25 to Figure 6.28 are the molecular graphs of **TS_{D-I}**, **TS_{D-II}**, **Al_D-H₂** and **Al_D-2H₂** with Table 6.5 summarising selected properties of relevant bond critical points (BCP). The analysis of the properties of the Al1—H1 BCP indicate that the bond is almost fully formed at the transition state. This is evidenced by the accumulation of electron density $\rho(r)$ ($+0.061 \text{ e/a}_0^3$) and the near-zero value of $\nabla^2\rho(r)$ ($+0.003 \text{ e/a}_0^5$), where a negative value usually indicates that a bond is characterised by a high degree of covalency. As expected, the H2...K interactions can be characterised as being closed-shell ionic interactions, with low values of $\rho(r)$, positive values of $\nabla^2\rho(r)$ and near zero values of the local energy density $H(r)$.²⁹⁶ Finally, despite the H1—H2 bond being significantly activated at the transition state, the BCP indicates that there is still a non-negligible amount of covalent character present, characterised by a relatively high value of $\rho(r)$, negative value of $\nabla^2\rho(r)$ and a negative $H(r)$.

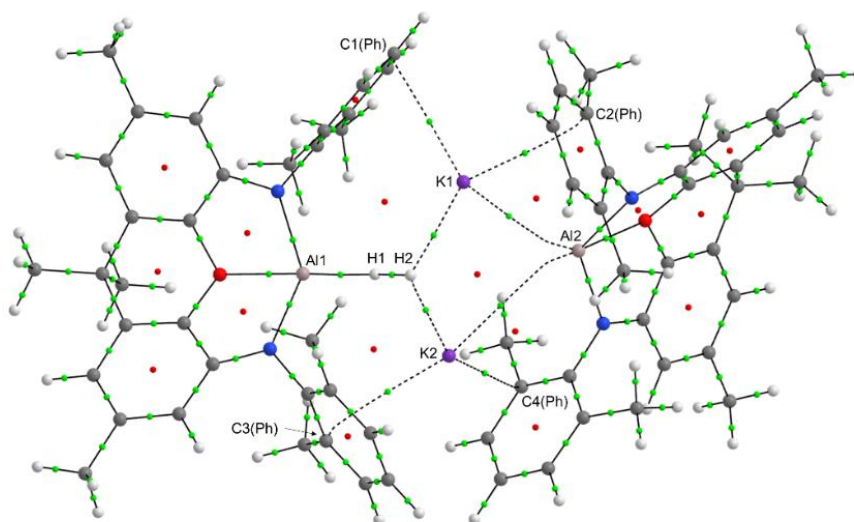


Figure 6.25: QTAIM molecular graph of **TS_{D-I}** (M062X-D3/def2-TZVPP//TPPS/def2-SVP) with bond critical points (BCP) and ring critical points (RCP) shown as green and red spheres, respectively. Bond paths are shown as solid and dotted lines.

6 - FLP-type cooperativity in an alkali metal aluminyl complex: proposal of a hydride rebound mechanism

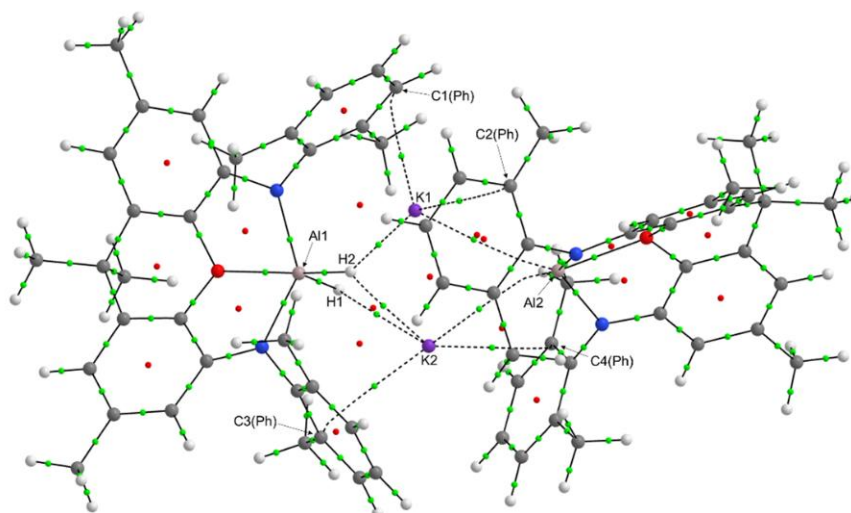


Figure 6.26: QTAIM molecular graph of **AlD-H₂** (M062X-D3/def2-TZVPP//TPPS/def2-SVP) with bond critical points (BCP) and ring critical points (RCP) shown as green and red spheres, respectively. Bond paths are shown as solid and dotted lines.

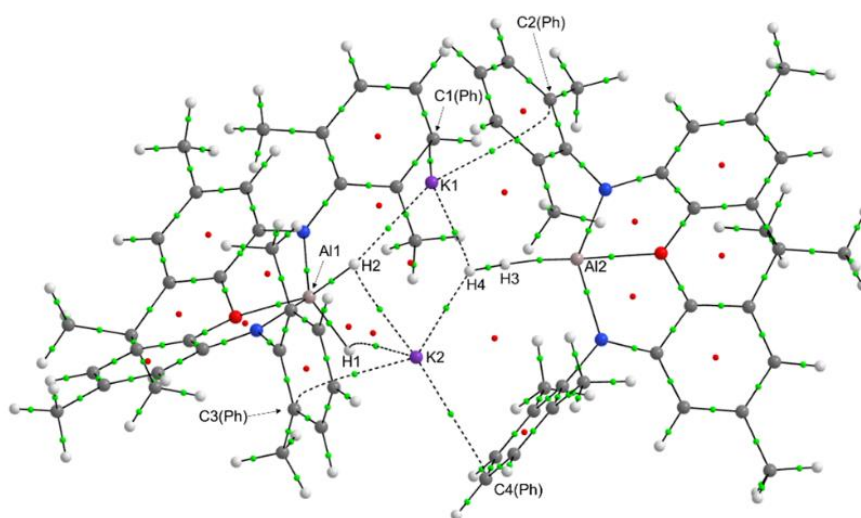


Figure 6.27: QTAIM molecular graph of **TSd-II** (M062X/def2-TZVPP//TPPS/def2-SVP) with bond critical points (BCP) and ring critical points (RCP) shown as green and red spheres, respectively. Bond paths are shown as solid and dotted lines.

6 - FLP-type cooperativity in an alkali metal aluminyl complex: proposal of a hydride rebound mechanism

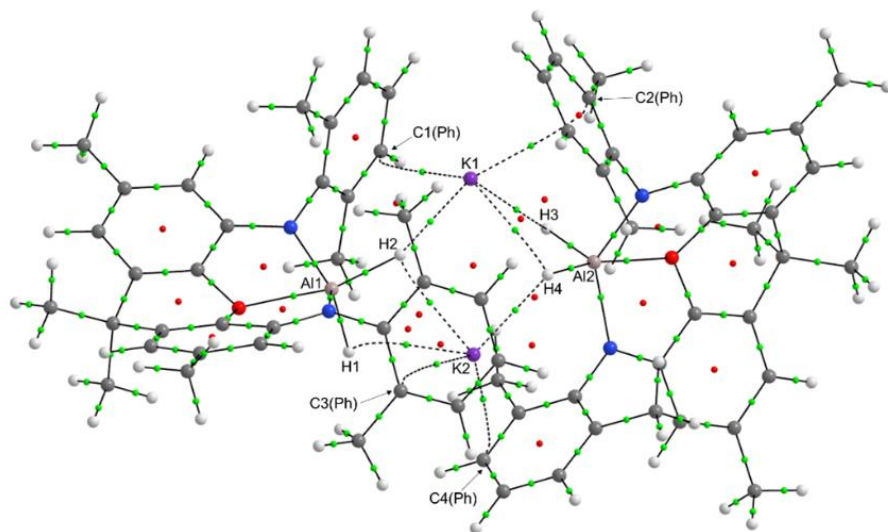


Figure 6.28: QTAIM molecular graph of $\text{Al}_2\text{-}2\text{H}_2$ (M062X/def2-TZVPP//TPPS/def2-SVP) with bond critical points (BCP) and ring critical points (RCP) shown as green and red spheres, respectively. Bond paths are shown as solid and dotted lines.

6 - FLP-type cooperativity in an alkali metal aluminyl complex: proposal of a hydride rebound mechanism

Table 6.5: Selected properties of the bond critical points (BCP) of **TS_{D-I}**, **TS_{D-II}**, **Al_D-H₂** and **Al_D-2H₂**. $\rho(r)$ is the electron density (e/a_0^3), $\nabla^2\rho(r)$ is the Laplacian of the electron density (e/a_0^5), λ_n are eigenvalues of the Hessian of $\rho(r)$ (e/a_0^5), ε is the bond ellipticity defined as $(\lambda_1/\lambda_2)-1$ and $V(r)$, $G(r)$ and $H(r)$ represent the potential, kinetic and total energy density, respectively (E_h/a_0^3).

	BCP	$\rho(r)$	$\nabla^2\rho(r)$	λ_1	λ_2	λ_3	ε	$G(r)$	$V(r)$	$H(r)$
TS_{D-I}	Al1 - H1	+0.061	+0.003	-0.063	-0.052	+0.117	+0.212	+0.025	-0.050	-0.025
	K1 - H2	+0.016	+0.050	-0.014	-0.013	+0.076	+0.061	+0.011	-0.010	+0.001
	K2 - H2	+0.015	+0.050	-0.013	-0.008	+0.071	+0.560	+0.011	-0.010	+0.001
	H1 - H2	+0.084	-0.065	-0.159	-0.159	+0.253	+0.006	+0.021	-0.058	-0.037
	Al2 - K1	+0.009	+0.017	-0.004	-0.004	+0.025	+0.055	+0.004	-0.003	0.000
	Al2 - K2	+0.006	+0.010	-0.003	-0.002	+0.015	+0.079	+0.002	-0.002	0.000
	K1 - C1(Ph)	+0.007	+0.028	-0.005	-0.001	+0.033	+7.208	+0.006	-0.004	+0.001
	K1 - C2(Ph)	+0.008	+0.032	-0.006	-0.002	+0.039	+2.565	+0.006	-0.005	+0.001
	K2 - C3(Ph)	+0.006	+0.022	-0.004	-0.001	+0.027	+3.152	+0.004	-0.003	+0.001
	K2 - C4(Ph)	+0.007	+0.027	-0.005	-0.001	+0.032	+6.733	+0.005	-0.004	+0.001

6 - FLP-type cooperativity in an alkali metal aluminyl complex: proposal of a hydride rebound mechanism

Al-TS_{D-II}	Al1 - H1	+0.072	+0.200	-0.107	-0.105	+0.411	+0.017	+0.070	-0.089	-0.020
	Al1 - H2	+0.064	+0.178	-0.092	-0.088	+0.358	+0.044	+0.060	-0.075	-0.015
	K1 - H2	+0.011	+0.036	-0.009	-0.008	+0.053	+0.057	+0.008	-0.006	+0.001
	K2 - H1	+0.009	+0.029	-0.006	-0.003	+0.038	+1.053	+0.006	-0.005	+0.001
	K2 - H2	+0.011	+0.036	-0.008	-0.006	+0.051	+0.297	+0.008	-0.006	+0.001
	K1 - H4	+0.015	+0.051	-0.013	-0.008	+0.072	+0.575	+0.011	-0.010	+0.001
	K2 - H4	+0.016	+0.050	-0.014	-0.013	+0.077	+0.043	+0.011	-0.010	+0.001
	Al2 - H3	+0.061	+0.009	-0.064	-0.053	+0.125	+0.213	+0.027	-0.052	-0.025
	H3 - H4	+0.084	-0.065	-0.160	-0.159	+0.254	+0.006	+0.021	-0.059	-0.037
	K1 - C1(Ph)	+0.007	+0.029	-0.005	-0.001	+0.035	+6.664	+0.006	-0.004	+0.002
	K1 - C2(Ph)	+0.006	+0.024	-0.004	0.000	+0.028	+7.957	+0.005	-0.003	+0.001
	K2 - C3(Ph)	+0.009	+0.033	-0.007	-0.002	+0.042	+2.082	+0.007	-0.005	+0.002
	K2 - C4(Ph)	+0.008	+0.030	-0.005	-0.001	+0.037	+4.373	+0.006	-0.005	+0.002
Al_D-H₂	Al1 - H1	+0.072	+0.200	-0.107	-0.105	+0.412	+0.019	+0.070	-0.089	-0.019

6 - FLP-type cooperativity in an alkali metal aluminyl complex: proposal of a hydride rebound mechanism

	Al1 - H2	+0.063	+0.179	-0.091	-0.087	+0.356	+0.046	+0.060	-0.075	-0.015
	K1 - H2	+0.013	+0.044	-0.011	-0.011	+0.065	+0.035	+0.009	-0.008	+0.001
	K2 - H2	+0.012	+0.039	-0.009	-0.007	+0.056	+0.305	+0.008	-0.007	+0.002
	K2 - H1	+0.010	+0.033	-0.007	-0.004	+0.045	+0.648	+0.007	-0.006	+0.001
	Al2 - K1	+0.009	+0.017	-0.004	-0.004	+0.025	+0.062	+0.004	-0.003	0.000
	Al2 - K2	+0.007	+0.012	-0.003	-0.003	+0.018	+0.058	+0.003	-0.002	0.000
	K1 - C1(Ph)	+0.008	+0.030	-0.005	0.000	+0.036	+9.128	+0.006	-0.004	+0.002
	K1 - C2(Ph)	+0.009	+0.035	-0.007	-0.002	+0.044	+2.204	+0.007	-0.006	+0.002
	K2 - C3(Ph)	+0.008	+0.029	-0.006	-0.002	+0.037	+1.352	+0.006	-0.004	+0.001
	K2 - C4(Ph)	+0.008	+0.031	-0.005	0.000	+0.037	+10.573	+0.006	-0.005	+0.001
AlD-2H₂	Al1 - H1	+0.072	+0.201	-0.107	-0.105	+0.413	+0.017	+0.070	-0.090	-0.020
	Al1 - H2	+0.072	+0.201	-0.107	-0.105	0.413	+0.017	+0.070	-0.090	-0.020
	K1 - H2	+0.012	+0.039	-0.010	-0.009	+0.059	+0.038	+0.008	-0.007	+0.001
	K2 - H1	+0.009	+0.030	-0.006	-0.003	+0.040	+0.919	+0.006	-0.005	+0.001

6 - FLP-type cooperativity in an alkali metal aluminyl complex: proposal of a hydride rebound mechanism

K2 - H2	+0.011	+0.037	-0.008	-0.007	+0.052	+0.263	+0.008	-0.006	+0.001
Al2 - H3	+0.072	+0.201	-0.107	-0.105	+0.413	+0.017	+0.070	-0.090	-0.020
Al2 - H4	+0.062	+0.174	-0.089	-0.085	+0.347	+0.046	+0.058	-0.073	-0.015
K1 - H3	+0.009	+0.030	-0.006	-0.003	+0.040	+0.928	+0.006	-0.005	+0.001
K1 - H4	+0.011	+0.037	-0.008	-0.007	+0.052	+0.262	+0.008	-0.006	+0.001
K2 - H4	+0.012	+0.039	-0.010	-0.009	+0.058	+0.038	+0.008	-0.007	+0.001
K1 - C1(Ph)	+0.008	+0.032	-0.005	0.000	+0.037	+22.151	+0.006	-0.005	+0.002
K1 - C2(Ph)	+0.009	+0.036	-0.007	-0.002	+0.045	+1.987	+0.007	-0.006	+0.002
K2 - C3(Ph)	+0.009	+0.036	-0.007	-0.002	+0.045	+1.981	+0.007	-0.006	+0.002
K2 - C4(Ph)	+0.008	+0.032	-0.005	0.000	+0.037	+21.562	+0.006	-0.005	+0.002

6.4 Conclusions

In this study it has been demonstrated that a previously postulated stepwise FLP-type mechanism is in fact feasible and energetically accessible for the activation of H₂ by **Al_D**. It was shown, through detailed computational mechanistic work and electronic structure analysis, that two equivalents of dihydrogen are activated by the cooperative action of the Lewis basic aluminyl anion and the Lewis acidic potassium cationic centres of **Al_D**. This is consistent with the observed reaction time of 5 days, at room temperature. Moreover, this result is fully consistent with the experimentally observed absence of H₂ activation in the corresponding monomeric system in which the K⁺ cation is sequestered by a 2,2,2-cryptand species. To further validate the new cooperative mechanism, the FLP-type transition state was also successfully located at the same level of theory employed by Schaefer (M062X/def2-SVP). This is in direct contrast to the result from Schaefer, that all attempts to locate such an FLP pathway were unsuccessful. These results may have implications for related alkali metal aluminyl complexes in the activation of dihydrogen^{281,297}, and possibly extend to the activation of further E—H bonds.^{88,298}

7 Mechanistic Insight into Alkali-Metal Mediation of Styrene Transfer Hydrogenation

7.1 Introduction

In Chapter 1, work by Harder was discussed, in which a series of alkaline earth metal amide complexes of the form $\text{Ae}\{\text{N}(\text{SiMe}_3)_2\}_2$ [$\text{Ae} = \text{Mg}, \text{Ca}, \text{Sr}, \text{Ba}$; $\text{N}(\text{SiMe}_3)_2 = 1,1,1,3,3,3$ -hexamethyldisilazide, HMDS (here abbreviated as N'')] were shown to catalyse the transfer hydrogenation of various alkenes.¹⁰⁶ It was found that the complex containing the smallest alkaline earth metal, magnesium, exhibited no catalytic activity at all, while the larger Ca and Ba complexes were shown to be efficient catalysts. Intrigued by the inactivity of the MgN''_2 species, Mulvey and co-workers have more recently explored the effect of an added alkali metal amide to catalyse the transfer hydrogenation of the benchmark alkenes, styrene and 1,1-diphenylethene (1,1-DPE).¹¹² Defined alkali metal magnesiate complexes, of the form AMMgN''_3 , were utilised, with 1,4-CHD as the hydrogen source (Figure 7.1).

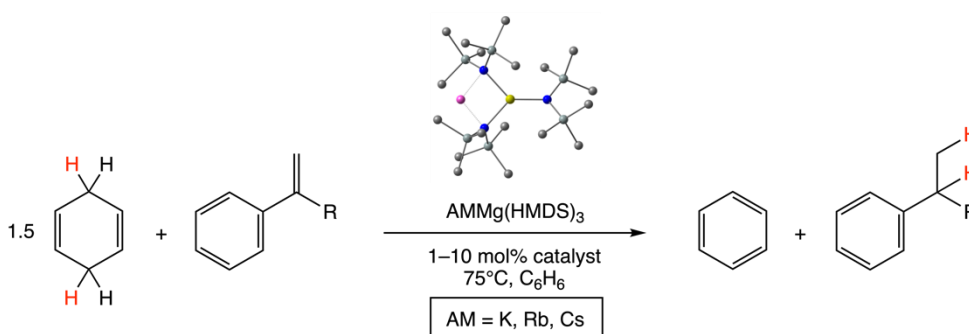


Figure 7.1: Transfer hydrogenation catalysis by AMMg(HMDS)_3 in the presence of 1.5 equivalents of 1,4-cyclohexadiene as hydrogen source and substrates styrene ($\text{R} = \text{H}$) and 1,1-diphenylethene ($\text{R} = \text{Ph}$).

As Group 1 was descended (Li-Cs), an increase in reactivity was observed. However, this came at a modest expense in selectivity for the larger alkali metals. Focussing on the results for styrene, KMgN''_3 was found to exhibit the overall most balanced performance, with the monometallic components failing to efficiently carry out the reactivity in isolation. This was either due to a lack of reactivity (MgN''_2) or a lack of selectivity (for isolated KN''). These results thus demonstrated that a level of cooperativity was present in the bimetallic systems, where even the performance of the most unreactive alkaline earth metal, magnesium, could be effectively boosted when paired with an alkali metal. Derived from Harder's experimental and computational mechanistic work, a plausible catalytic pathway was proposed (Figure 7.2).

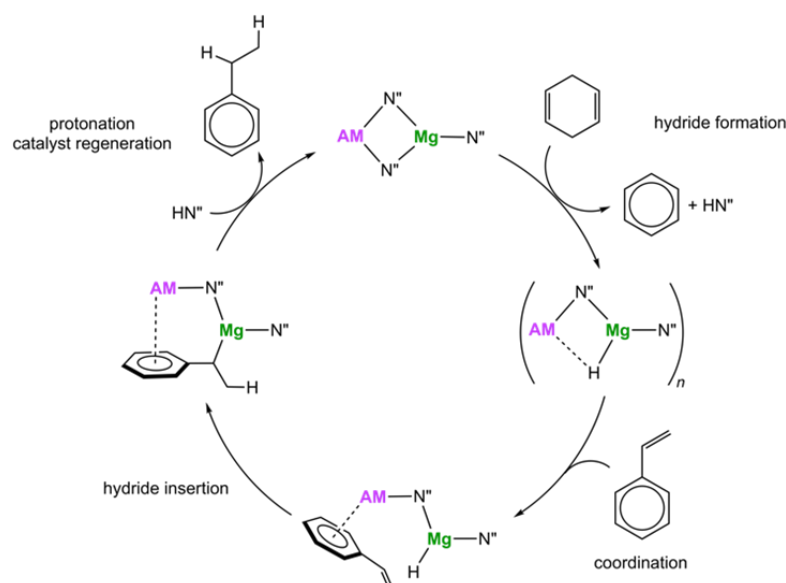


Figure 7.2: Proposed reaction mechanism for transfer hydrogenation of styrene with 1,4-CHD catalysed by AMMgN''_3 [AM = alkali metal, $\text{N}'' = \text{N}(\text{SiMe}_3)_2$].

The initial deprotonation of 1,4-CHD occurs by N'' , liberating $\text{N}''\text{H}$, and yielding an unstable Meisenheimer-type intermediate. Subsequent β -hydride elimination then

generates the mixed-metal hydride intermediate. Binding of styrene, followed by hydride transfer into the double bond generates a styryl intermediate, which can then be protonated by the previously liberated amine, $N''H$, to yield the desired product, ethylbenzene, and reform the starting alkali metal magnesiate complex.

It is known that alkali metal magnesiates have a tendency to form clusters of higher nuclearity, with the exact aggregation being undefined.²⁹⁹ However, in this present system, defined dimeric hydride magnesiates of the form $[AMMgN''_2H]_2$ were isolated and structurally characterised by X-ray crystallography. Such intermediates were proposed in the catalytic cycle above. Under catalytic conditions, the concentration of the monomeric pre-catalyst is low (1-10 mol %), relative to the amount of 1,4-CHD and substrate (styrene). Prior to a sufficient concentration buildup of the monomeric hydride intermediate, encounters between the monomeric hydride species and the substrate are more likely to occur, compared to formation of the dimeric aggregates (diffusion controlled). Therefore, it is reasonable to study the reaction mechanism using a monomeric model system. Quantum chemical calculations were carried out to elucidate the reaction mechanism of the transfer hydrogenation of styrene, catalysed by the bimetallic potassium magnesiate system, in the presence of 1,4-CHD as the hydrogen source.

7.2 Methods

All electronic structure calculations were performed with the Gaussian 16 (G16 revision B.01) suite of programs.²³² Full geometry optimizations of all (ground-state) species and subsequent analytical frequency calculations were carried out at the DFT level without imposing symmetry constraints. The TPSS meta-GGA exchange

correlation functional was used in conjunction with the BJ-damped Grimme DFT-D3 dispersion correction.^{154,164,165} A split basis set approach was utilised, to reduce computational cost during geometry optimizations. The metal centres (alkali and alkaline earth metals), atoms directly bonded to the metal centres, and atoms of small molecules relevant to key reaction steps (1,4-cyclohexadiene, styrene and benzene) were treated with Ahlrich's def2-TZVP basis set, while the remaining atoms were treated with the def2-SVPP basis set.^{210,211} An ultrafine integration grid, corresponding to a pruned grid of 99 radial shells and 590 angular points per shell, was used for all calculations. The nature of all stationary points was identified via inspection of their analytical second derivatives. Transition states correspond to first-order saddle points on the potential energy surface with exactly one imaginary vibrational frequency corresponding to the reaction coordinate, whilst minima only contain positive vibrational frequencies. Transition states were also further confirmed by visual inspection of the imaginary vibrational mode and subsequent geometry optimisations along the displacement vector in both forward and reverse direction of the reaction coordinate, giving the nearest minima connected by a transition state. The frequency calculations also provided thermal and entropic corrections to the total free energy in gas phase at $T = 348.15$ K and $p = 1$ atm within the rigid-rotor/harmonic oscillator (RRHO) approximation.²⁷⁴ Singlepoint calculations for accurate energies were performed using the PBE exchange correlation functional¹⁹⁵ in conjunction with Ahlrich's def2-QZVP basis set, corrected for dispersion effects (D3BJ). Gibbs Free Energies were corrected for benzene solvent ($\epsilon=2.2706$) effects using the polarisable continuum model with radii and non-electrostatic terms from Truhlar's solvation model based on the electron density (SMD).²³³ Final reaction free energies are determined from the electronic single-point energies plus TPSS-D3(BJ) thermal corrections and SMD solvation free energies, corrected for a reference concentration in solution of 1 mol L^{-1} . Of several methods tested, the above model chemistry gave overall best agreement with the available experimental reaction times at given temperatures.

Thermochemical data at different temperatures and concentrations were computed with the help of the GoodVibes Python program (version 3.2).³⁰⁰ Visualisations of optimized geometries were created using ChemCraft (Version 1.8).²⁴⁵

7.3 Results & Discussion

To establish a reference point for an investigation of the bimetallic species, $\text{KMg}(\text{HMDS})_3$, the reactivity of the monometallic components, $\text{Mg}(\text{HMDS})_2$ and KHMDS was initially explored. Shown in Figure 7.3 is the calculated reaction profile for $\text{Mg}(\text{HMDS})_2$ (MgN''_2 , $\text{N}'' = \text{HMDS}$), with Figure 7.4 showing the key structural features of the transition states. The binding of 1,4-cyclohexadiene (1,4-CHD) was calculated to be $16.0 \text{ kcal mol}^{-1}$ endergonic (**Mg-I1**). Subsequent direct deprotonation of 1,4-CHD occurs via the transition state **Mg-TS1**, coming with a substantial energetic span of $32.1 \text{ kcal mol}^{-1}$. Release of the disilazane ($\text{N}''\text{H}$) then yields the unstable meisenheimer type intermediate (**Mg-I3**), which sits at $20.4 \text{ kcal mol}^{-1}$. Hydride transfer to the Mg^{2+} centre can then occur via **Mg-TS2**, via a barrier of $6.7 \text{ kcal mol}^{-1}$, relative to **Mg-I3**. Upon the thermodynamically favourable release of benzene, the active hydride catalyst (**Mg-cat**) is then formed. **Mg-cat** is $1.8 \text{ kcal mol}^{-1}$ endergonic, relative to MgN''_2 .

7 - Mechanistic Insight into Alkali-Metal Mediation of Styrene Transfer Hydrogenation

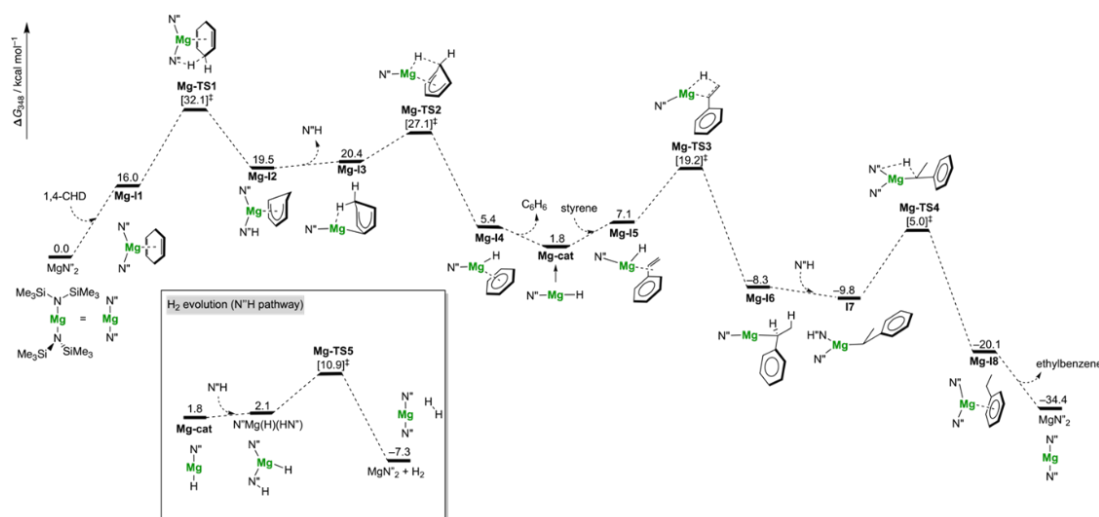


Figure 7.3: DFT-calculated Free Energy reaction profile (ΔG , $T = 348.15$ K, 1 mol L^{-1}) for transfer hydrogenation of styrene with 1,4-CHD and MgN''_2 [$\text{N}'' = \text{N}(\text{SiMe}_3)_2$].

Having formed the active catalyst, the binding of styrene can then take place, which is endergonic by $5.3 \text{ kcal mol}^{-1}$, relative to **Mg-cat** (**Mg-I5**). Hydride transfer from the magnesium to the terminal carbon of styrene occurs via transition state **Mg-TS3**, at $19.2 \text{ kcal mol}^{-1}$. The resulting intermediate, **Mg-I6** is exergonic by $8.3 \text{ kcal mol}^{-1}$, relative to MgN''_2 . **Mg-I6** is stabilised by a strong and localised $\text{Mg}-(\alpha)\text{C}$ linkage. Finally, binding of the previously liberated $\text{N}''\text{H}$ and subsequent protonation of the styryl intermediate occurs via transition state **Mg-TS4**. This protonation step has a relatively low activation barrier of $14.8 \text{ kcal mol}^{-1}$, relative to **Mg-I7**. Release of the desired product, ethylbenzene, then regenerates MgN''_2 , with the overall reaction being highly exergonic ($-34.4 \text{ kcal mol}^{-1}$). In addition to the desired conversion to the ethylbenzene, H_2 evolution was also probed as a possible side reaction competing with product formation (**Mg-TS5**). The barrier for this process was calculated to be only $10.9 \text{ kcal mol}^{-1}$, which would dominate over the hydride transfer to styrene. However, given that the rate determining step is the initial deprotonation of 1,4-CHD, this is consistent with the absence of H_2 evolution under the experimental conditions.

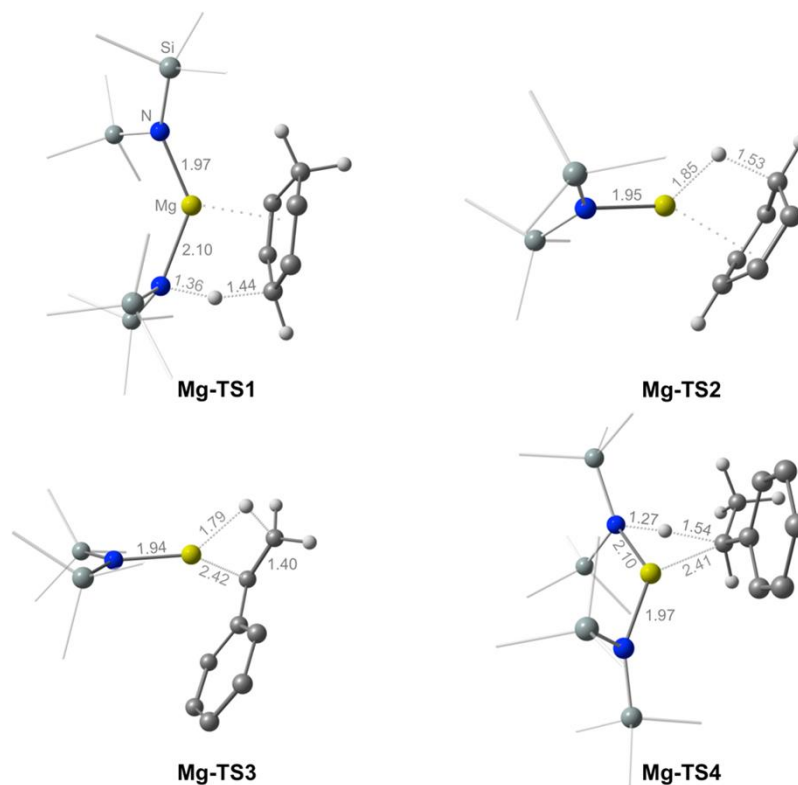


Figure 7.4: DFT-optimised geometries of all transition states along the pathway for transfer hydrogenation of styrene with 1,4-CHD and MgN_2 showing key bond distances.

The rate determining step is the initial deprotonation of 1,4-CHD, coming with a substantial activation barrier of $32.1 \text{ kcal mol}^{-1}$. This barrier is kinetically inaccessible under the conditions that the reaction was carried out. Therefore, this result is consistent with the experimentally observed inactivity of the MgN_2 catalyst. The analogous reaction pathway for CaN_2 has been previously calculated by Harder.^{106,301} Using the methodology employed throughout this project, the analogous reaction profile was recalculated for CaN_2 , shown in Figure 7.5. The located transition states and associated activation energies are in good agreement with those reported by Harder.

7 - Mechanistic Insight into Alkali-Metal Mediation of Styrene Transfer Hydrogenation

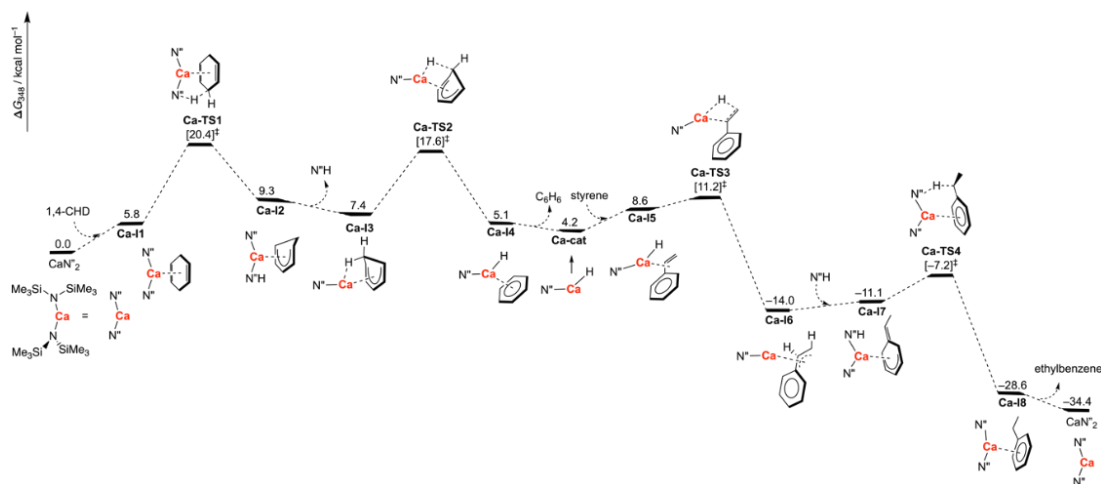


Figure 7.5: DFT-calculated Free Energy reaction profile (ΔG , $T = 348.15$ K, 1 mol L^{-1}) for transfer hydrogenation of styrene with 1,4-CHD and CaN''_2 [$\text{N}'' = \text{N}(\text{SiMe}_3)_2$].

The rate determining step is the initial deprotonation of 1,4-CHD, analogous to the reaction involving MgN''_2 , but has a barrier of only $20.4 \text{ kcal mol}^{-1}$, which is substantially lower ($11.7 \text{ kcal mol}^{-1}$). This is consistent with the experimental observations by Harder that CaN''_2 acts as an efficient catalyst in transfer hydrogenation.¹⁰⁶ The hydride transfer to styrene is achieved via a lower barrier ($11.2 \text{ kcal mol}^{-1}$), compared to MgN''_2 ($19.2 \text{ kcal mol}^{-1}$). This correlates with the decreased Ae—H ($\text{Ae} = \text{Alkaline Earth Metal}$) bond strength as Group 2 is descended, coupled with the more favourable deformation energies associated with the changes in the $\text{N}''\text{—Ae—H}$ angle as shown by Alonso and co-workers.¹⁰⁵ Due to an admixture of 3d orbital character in to the Ca—H σ bond, a decrease in this angle is observed compared to the magnesium catalyst (180° vs 134° for Mg and Ca, respectively). Furthermore, by comparing the key structures in Figure 7.4 and Figure 7.6, it is clear that the Ca^{2+} ion is oriented more towards the phenyl ring of the styryl anion (see **Ca-I7**). This results in stabilisation of the negative charge delocalised onto the ring system. This is in contrast to Mg^{2+} which preferentially and strongly binds directly to the $\alpha\text{-C}$ of the styryl anion, due to the smaller and harder nature of Mg^{2+} . These

findings are similar to previous work from both others and our own research group, where the relationship between a series of arylmethyl anions and Group 1 cations has been investigated experimentally and theoretically.^{302,303} For example, it was found that Li^+ primarily interacted with the trigonal-pyramidal $\alpha\text{-C}$ position of the diphenylmethyl anion in a σ -fashion. However, upon descending Group 1 to potassium, it was found that there was an increased interaction of the arene carbons with the alkali metal cation, with the $\alpha\text{-C}$ adopting a more planar geometry.

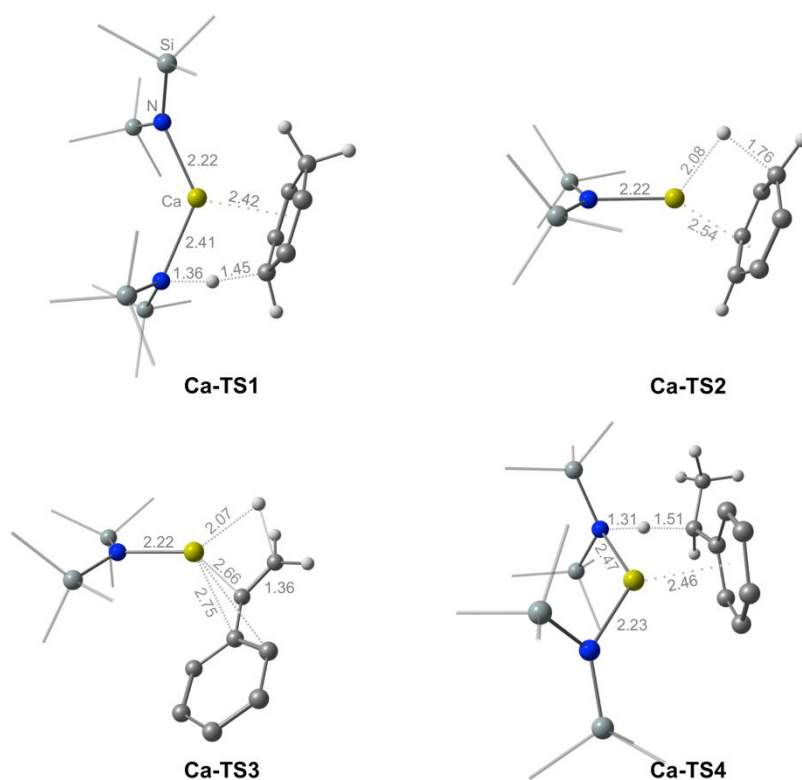


Figure 7.6: DFT-optimised geometries (TPSS/def2-TZVP/def2-SVPP) of all transition states along the pathway for transfer hydrogenation of styrene with 1,4-CHD and CaN''_2 ($\text{N}'' = \text{N}(\text{SiMe}_3)_2$).

Having calculated the reaction profile for MgN''_2 , the same process was then investigated when mediated by KN'' (Figure 7.7). Huffman has reported that unsolvated KN'' exists as a discrete dimer in the solid state, formed by the bridging

coordination of the two amide anions.³⁰⁴ Guan has more recently demonstrated similar results, by determining a dimeric structure of KN^{II} in the solid state, but this time coordinated by 2-ethylpyridine, at each potassium cation.³⁰⁵ Furthermore, Collum has investigated the solution structures of KN^{II} , and determined that weakly coordinating ligands such as toluene afforded dimers exclusively.³⁰⁶ Based on this previous work, KN^{II} was modelled as the homometallic dimer, $[\text{KN}^{\text{II}}]_2$, in this project. The structures of key intermediates and transition states are visualised in Figure 7.8. The dimer was solvated by two benzene molecules, yielding $[(\text{C}_6\text{H}_6)_2\text{KN}^{\text{II}}]_2$, where the two potassium cations are η^6 -coordinated to the benzene rings and bridged by the two amide anions. It is immediately clear that the individual steps of this reaction are more facile than in the case of MgN^{II}_2 . Ligand exchange of one benzene molecule with a molecule of 1,4-CHD was calculated to be endergonic by $1.6 \text{ kcal mol}^{-1}$, yielding **K-I1**. In **K-I1**, 1,4-CHD coordinates to the potassium cation via an η^4 coordination mode. Subsequent deprotonation of 1,4-CHD then takes place via transition state **K-TS1**, with a barrier of $20.8 \text{ kcal mol}^{-1}$. Upon release of the disilazane, the cyclohexadienyl anion moves into a stabilising bridging position between the two potassium cations, yielding **K-I3**. Rearrangement and subsequent hydride transfer from the cyclohexadienyl anion to the bridging position then gives the active hydride catalyst, **K-I4**, at $6.3 \text{ kcal mol}^{-1}$.

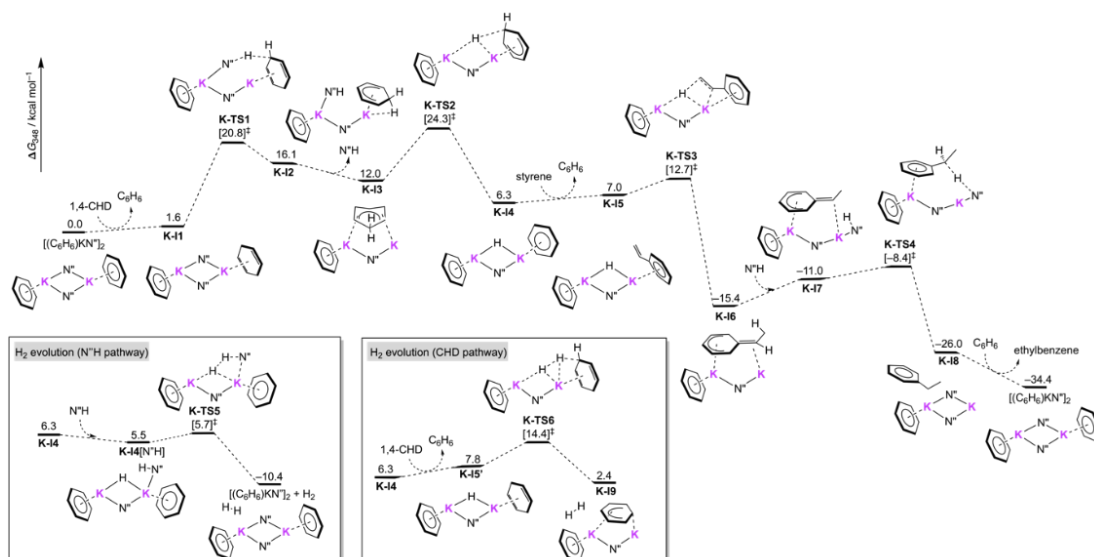


Figure 7.7: DFT-calculated Free Energy (ΔG , $T = 348.15$ K, 1 mol L^{-1}) reaction profile for transfer hydrogenation of styrene with 1,4-CHD and dimeric $[(\text{C}_6\text{H}_6)\text{KN}]_2$.

Ligand exchange of one benzene molecule with a molecule of styrene is endergonic by only $0.7 \text{ kcal mol}^{-1}$, relative to **K-14**. Facile hydride transfer to styrene can then occur via a barrier of $5.7 \text{ kcal mol}^{-1}$ (**K-TS3**), resulting in the thermodynamically favourable formation of the bridged styryl intermediate, **K-16**, at $-15.4 \text{ kcal mol}^{-1}$. Alternatively, there are two possible side reactions that may occur, starting from **K-14**. One possibility is the protonation by the liberated disilazane, which occurs via a negligible barrier of only $0.2 \text{ kcal mol}^{-1}$, following the introduction of $\text{N}^{\text{H}}\text{H}$. This results in the evolution of dihydrogen and the regeneration of the pre-catalyst (**K-TS5**). Dihydrogen evolution can also occur via the deprotonation of another molecule of 1,4-CHD, via a barrier of $14.4 \text{ kcal mol}^{-1}$ (**K-TS6**). Therefore, these dihydrogen evolution pathways are either dominant (**K-TS5**) or competitive (**K-TS6**) with the desired styrene reduction. This is consistent with the experimentally observed evolution of dihydrogen gas, resulting in only a 36% formation of the desired product despite consumption of the majority of 1,4-CHD. On the desired pathway, the final protonation by the previously liberated disilazane can occur via transition state **K-TS4**, with a barrier of

7 kcal mol⁻¹, relative to **K-I6**. Release of the product, ethylbenzene, and reintroduction of a second benzene molecule can then occur, thus regenerating [(C₆H₆)KN^{III}]₂. The overall change in Gibbs Free Energy for this process was calculated to be -34.4 kcal mol⁻¹.

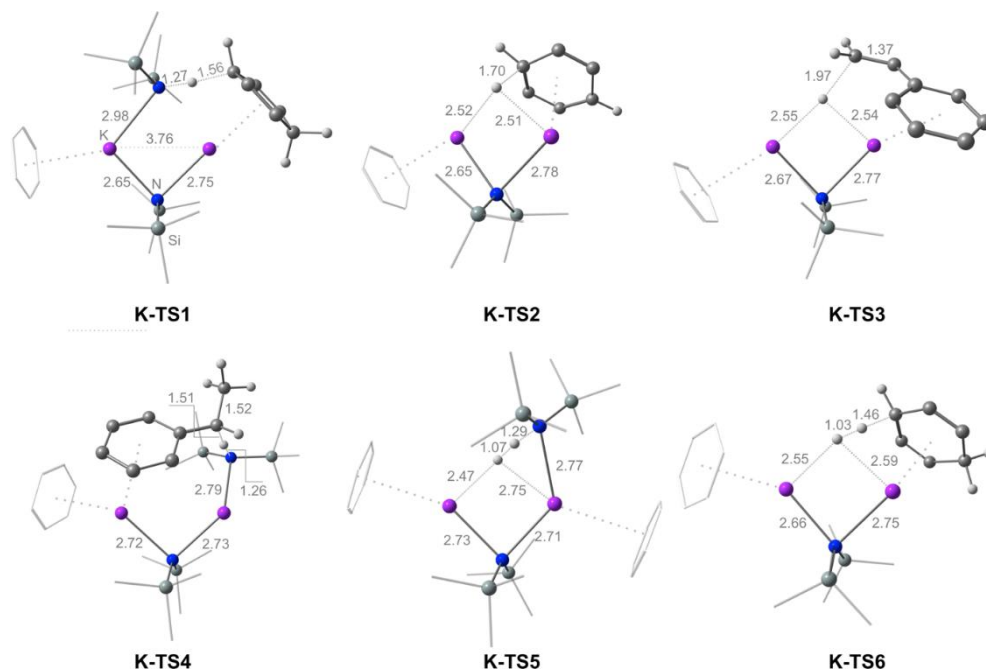


Figure 7.8: DFT-optimised geometries of all transition states along the pathway for transfer hydrogenation of styrene with 1,4-CHD and dimeric [(C₆H₆)KN^{III}]₂.

This concludes the discussion of the reactivity of the monometallic components. It has been demonstrated that neither component is an efficient catalyst in isolation. MgN^{II} was calculated to have a kinetically inaccessible barrier for the deprotonation of 1,4-CHD, while in the case of KN^{III}, dihydrogen evolution was found to be dominant over the desired styrene reduction. The mechanism of the bimetallic catalyst can now be discussed, using the above results as reference points.

The calculated reaction profile for the formation of the bimetallic hydride catalyst is shown in Figure 7.9, with the structures of key intermediates and transition states shown in Figure 7.10. Initial ligand exchange of benzene with 1,4-CHD was calculated to be 2.5 kcal mol⁻¹ exergonic (**I1**). Based on the located mechanism for the monometallic components above, a direct deprotonation of 1,4-CHD by N'' seemed intuitive. Somewhat surprisingly, this transition state, **TS2'**, was found to give a kinetically inaccessible barrier of 35.1 kcal mol⁻¹, relative to **I1**. Alternatively, dissociation of one of the bridging Mg-amide bonds via **TS1**, with a barrier of 24 kcal mol⁻¹, yields **I3** at 11.0 kcal mol⁻¹. Both potassium and magnesium engage in intramolecular agostic-type interactions in this intermediate.^{307,308} The methyl group of the decoordinated N'' nearest to the Mg²⁺ is tilted towards this centre. This is borne out in the N–Si–C_β angle (105°) which is reduced compared to the other two angles in this Si(CH₃)₃ unit (~117°). The Mg...C (2.42 Å) and corresponding Mg...H (2.11-2.16 Å) contacts of the tilted methyl group are short compared to the sum of their van der Waals radii, but long compared to the sum of their covalent radii. These structural parameters are reminiscent of the di-*tert*-butylmagnesium dimer³⁰⁹ and can be associated with agostic interactions.³¹⁰ Likewise, two hydrogens of a second methyl group on the decoordinated HMDS ligand are oriented towards the K⁺ ion. These secondary interactions, enabled by both metal centres, coupled with the increased basicity of the decoordinated N'' (stabilised by K⁺), promote the favourable deprotonation of 1,4-CHD via **TS2**, with a barrier of 27.9 kcal mol⁻¹. This is a significant reduction in the barrier, compared to the direct deprotonation (**TS2'**) and the analogous step for the monometallic MgN''₂, highlighting how the potassium ion has a central role in facilitating deprotonation of 1,4-CHD. This alternative, lower energy pathway was inspired by a previous computational study, where a similar reaction sequence involving a preorganisation step of the catalyst to an open-form was invoked in the mechanism for the ferration of aromatic substrates by a bimetallic

[(toluene)NaFe(HMDS)₃] complex.³¹¹ As a note aside, attempts to find a pathway featuring initial coordination of 1,4-CHD to the Mg centre were unsuccessful.

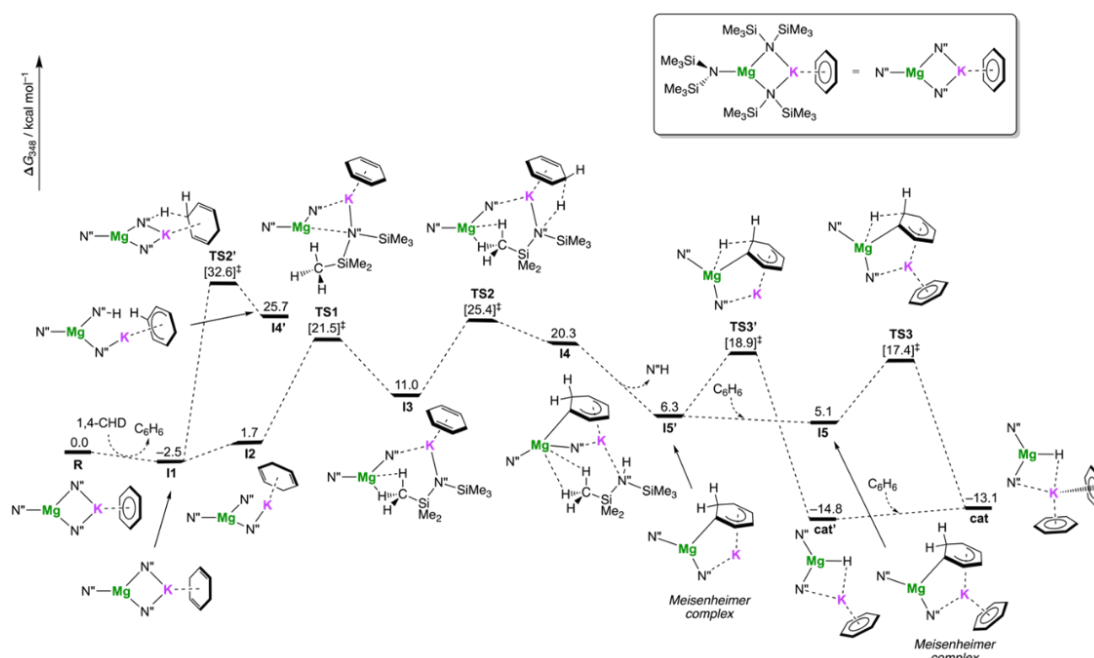


Figure 7.9: DFT-calculated Free Energy reaction profile (ΔG , $T = 348.15$ K, 1 mol L^{-1}) for the formation of the magnesium hydride catalyst from 1,4-CHD and $(\text{C}_6\text{H}_6)\text{KMgN}^3$.

Upon release of the disilazane, the Meisenheimer complex is formed (**I5'**), where the magnesium and potassium ions work together to stabilize the cyclohexadienyl anion. For the magnesium ion, a more directed or localized interaction with a single carbon center is preferred, while for the potassium ion, an η^4 coordination mode is preferred, consistent with previous reports.^{302,303} The cyclohexadienyl anion is ideally positioned to transfer the hydride to magnesium via **TS3**, following coordination of benzene solvent, or alternatively via **TS3'**, in the absence of coordinated benzene. Both possibilities are energetically competitive, with barriers of 11.1 and 12.6 kcal mol⁻¹ for **TS3** and **TS3'**, respectively. In the absence of an added benzene molecule, **cat'** is

formed, which can be considered in equilibrium with **cat**, with two benzene molecules coordinated. The energy difference is only 1.7 kcal mol⁻¹ between these species.

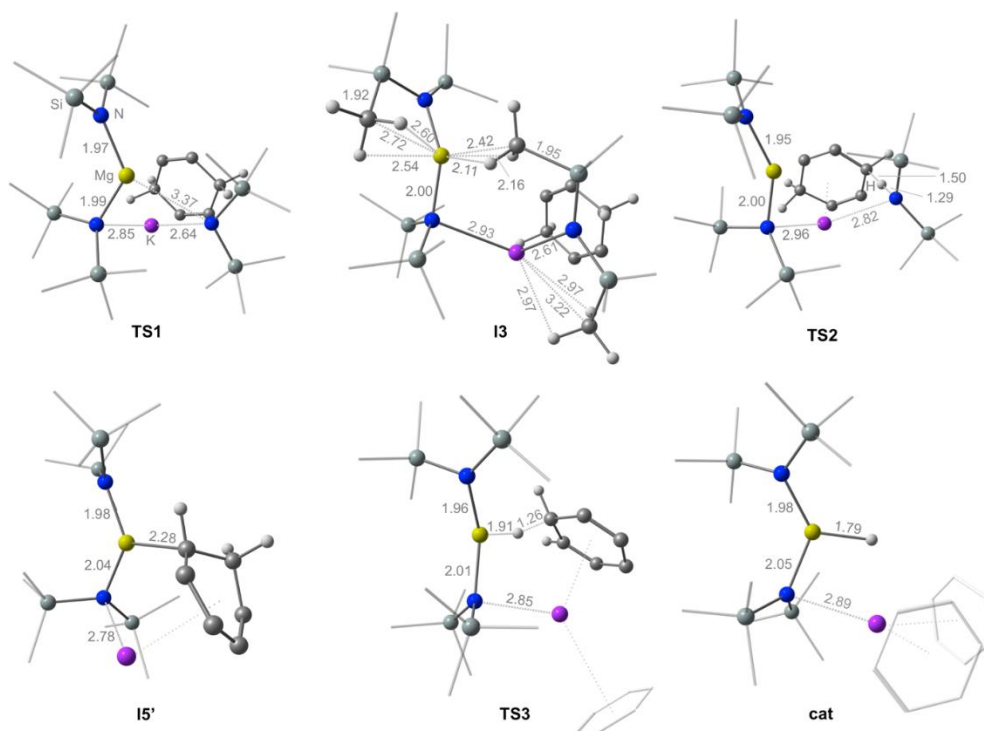


Figure 7.10: DFT-optimised geometries of key stationary points along the pathway for formation of magnesium hydride catalyst (C₆H₆)₂KMg(H)N''₂ showing key bond distances.

Having formed the bimetallic hydride catalyst species (**cat**), the subsequent hydrogenation of styrene can now be discussed. The reaction profile for this process is shown in Figure 7.11, with the structures of key intermediates and transition states shown in Figure 7.12, Figure 7.13 and Figure 7.14. The ligand exchange of one benzene molecule with one molecule of styrene is 1.5 kcal mol⁻¹ endergonic. Subsequent hydride transfer to the terminal carbon of styrene occurs via transition state **TS4**, with a facile barrier of 10 kcal mol⁻¹, relative to **cat**. In this transition state, the potassium cation acts as an anchor point for styrene, while polarising the double bond, thus priming styrene for the hydride transfer. For MgN''₂, the analogous step

has an activation barrier of 17.4 kcal mol⁻¹, highlighting the synergistic effect of the bimetallic catalyst, which has a significantly reduced barrier. In the forward direction, this yields the α -styryl intermediate (α -**17**) in a strongly exergonic reaction having a relative Gibbs Free Energy of -24.9 kcal mol⁻¹.

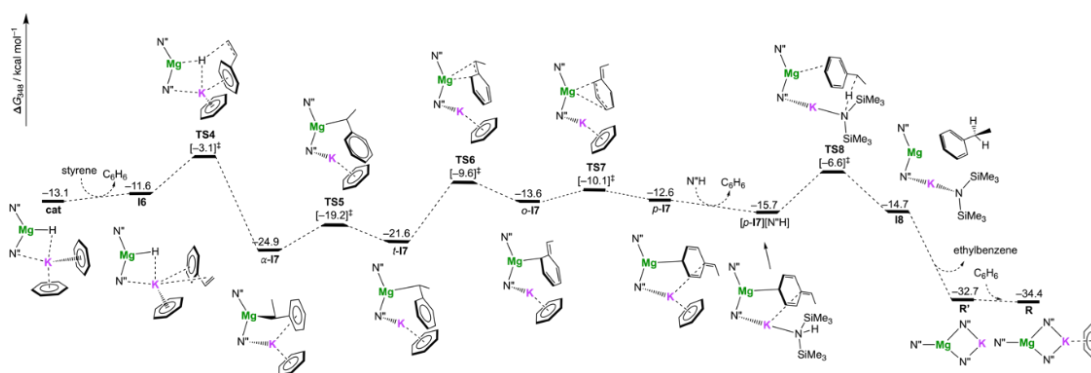


Figure 7.11: DFT-calculated Free Energy reaction profile (ΔG , $T = 348.15$ K, 1 mol L^{-1}) for styrene transfer hydrogenation by $(\text{C}_6\text{H}_5)_2\text{K}(\text{H})\text{MgN}^{\text{n}2}$.

Examination of the structure of α -**17** reveals significant stabilisation, stemming from the short and strong Mg—C bond (2.22 Å), coupled with an η^6 -interaction between the potassium cation and the phenyl ring ($\text{K} \cdots \text{C}_{\text{centroid}} = 3.08 \text{ Å}$). Although this intermediate was not experimentally isolated, this bonding motif bears a close resemblance to the previously isolated bimetallic complex $^t\text{Bu}_2\text{Zn}(\text{PhCH}_2)\text{K} \cdot \text{Me}_6\text{TREN}$ ($\text{Me}_6\text{TREN} = \text{tris}(N,N\text{-dimethyl-2-aminoethyl})\text{amine}$), in which the benzyl anion acts as a dual σ - and π -coordinating ligand (to Zn^{2+} and K^+ , respectively).³¹²

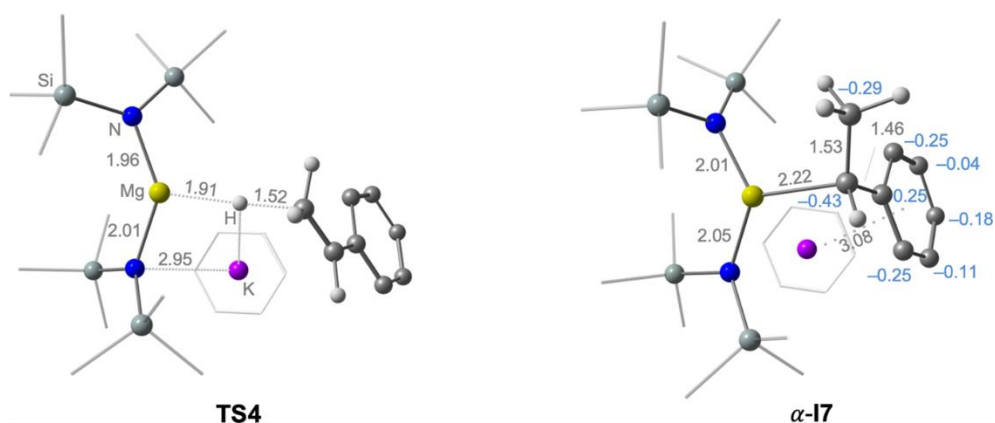


Figure 7.12: DFT-optimised geometries of the transition state **TS4** for hydride transfer forming the alkyl intermediate **α -17** showing key bond distances and Mulliken charges (blue).

The final step that will yield the desired product and regenerate the starting complex involves protonation of the strong Mg—C bond of **α -17**. After considering several different possibilities, it emerged from the calculations that protonation necessitates decoordination of the α -C from the magnesium centre. The most favourable pathway that achieves this involves a delocalisation of the negative charge from the α -C to the *para*-position of the phenyl ring. Initial rotation of the styryl about the C_{α} —Mg²⁺ vector occurs via **TS5**, with a facile barrier of 5.7 kcal mol⁻¹, yielding ***t*-17** at -21.6 kcal mol⁻¹. Subsequent breakage of the C_{α} —Mg²⁺ bond can then occur via a barrier of 12.0 kcal mol⁻¹. The resulting structure (***o*-17**) has the magnesium centre interacting with the styryl fragment via the *ortho*-position of the phenyl ring, while the potassium centre interacts with the exocyclic C=C bond. Delocalisation of the negative charge to the *para*-position of the phenyl ring can then take place via a facile local barrier of 3.5 kcal mol⁻¹ (**TS7**), yielding ***p*-17** at -12.6 kcal mol⁻¹.

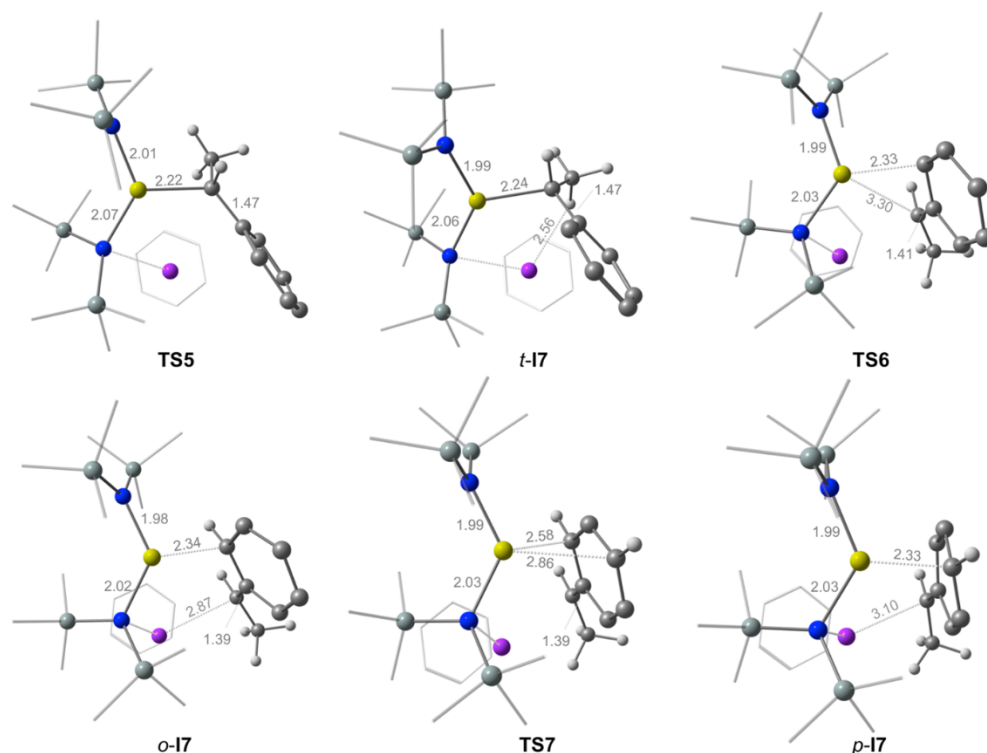


Figure 7.13: DFT-optimised geometries of the stationary points along the pathway for protonation of the alkyl intermediate α -I7 showing key bond distances.

Finally, exchange of benzene with the previously liberated disilazane, $N''H$, was calculated to be $3.1 \text{ kcal mol}^{-1}$ exergonic, yielding $[p\text{-I7}][N''H]$ at $-15.7 \text{ kcal mol}^{-1}$. Protonation can then take place efficiently, via an activation barrier of $18.3 \text{ kcal mol}^{-1}$ (**TS8**). Following removal of the product, ethylbenzene, and addition of a molecule of benzene, the geometry optimization reforms the starting bimetallic complex (**R**) in a barrierless process.

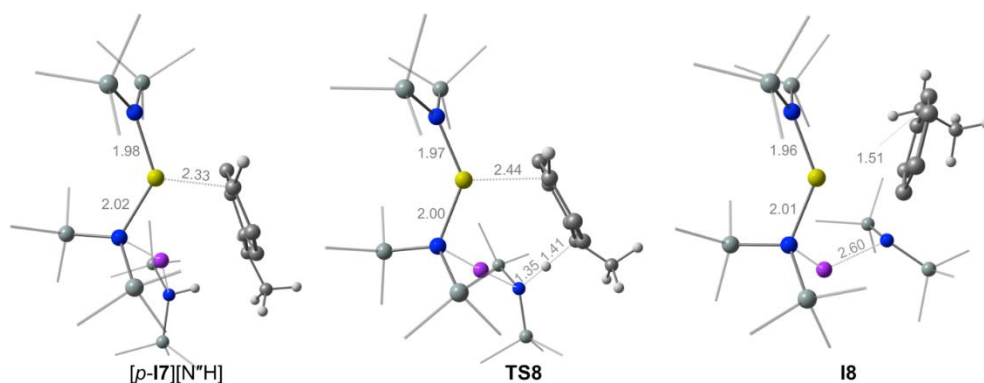


Figure 7.14: DFT-optimised geometries of the stationary points along the pathway for protonation of the alkyl intermediate α -17 showing key bond distances.

Several alternative pathways encompassing direct protonation at C_α , a proton shuttle mechanism, and initial coordination of $N''H$ to Mg prior to proton transfer were found to be significantly higher in energy (Figure 7.15). First, the direct protonation of α -17 was calculated to occur via an activation barrier of 40.0 kcal mol⁻¹, which is kinetically inaccessible at the experimental conditions, and highlights the strength of the Mg— C_α bond. In addition, a proton shuttle pathway was calculated, following initial protonation of one of the N'' ligands ligated to the Mg²⁺ centres in α -17. Whilst the intramolecular proton transfer to the α -C of styrene was found to have a moderate local barrier of 17.5 kcal mol⁻¹, the protonation of the N'' ligand furnishing α -17H⁺ [(C₆H₆)₂KMg(N'')($N''H$)(styryl)₂]⁺ is highly unfavourable ($\Delta G > 50$ kcal mol⁻¹). This effect can be understood when one considers that protonation of the negatively charged N'' will weaken the bonding interaction with Mg²⁺. Coordination of $N''H$ to Mg²⁺ prior to H⁺ transfer with concomitant displacement of the Mg— C_α bond and η^6 -coordination of the phenyl ring to the K⁺ centre was also considered. Although the anionic C_α centre is stabilised by a hydrogen bond from the N—H group, the loss of the favourable electrostatic interaction between Mg²⁺ and C_α pushes this intermediate energetically to an unfavourable 8.0 kcal mol⁻¹, following the corresponding transition state for displacement/insertion (**TS7'''** at 11.3 kcal mol⁻¹). Proton transfer can then

occur relatively easily through **TS8'''**, however the overall energetic span for this step is a considerable 36.2 kcal mol⁻¹. These high activation energies are incompatible with the experimental conditions, thus rendering these pathways in which the styryl fragment remains “locked” in place unviable.

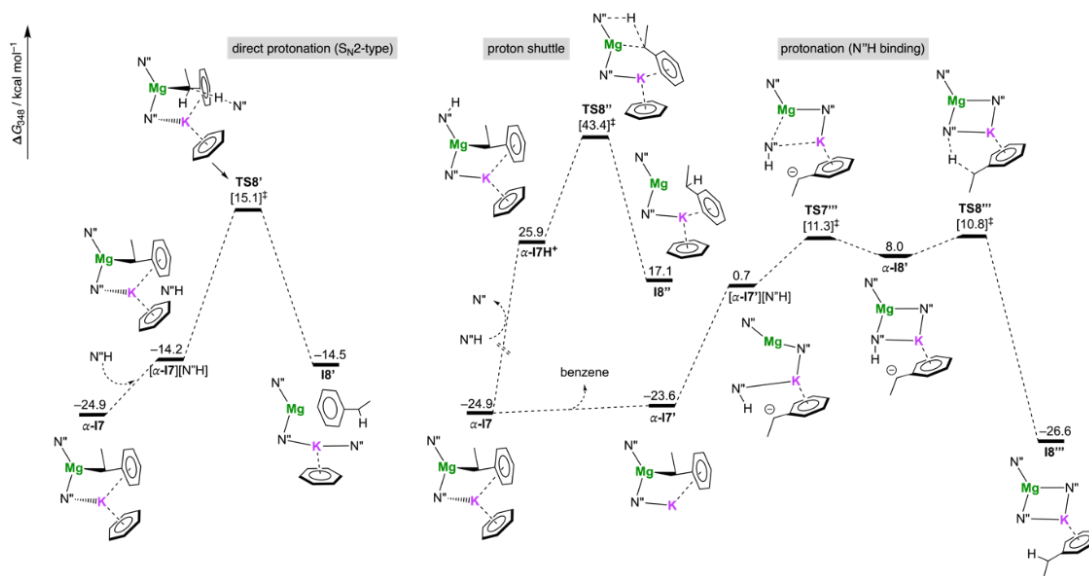


Figure 7.15: DFT-calculated Free Energy reaction profile (ΔG , $T = 348.15$ K, 1 mol L⁻¹) for the unfavourable protonation mechanisms of the styryl intermediate α -17.

In addition to the above alternative pathways to protonation, two previously reported alternatives to product formation were also considered (Figure 7.16). In the “CHD Pathway”, ligand exchange of the benzene molecule coordinated to α -17 with a molecule of 1,4-CHD was considered. This was calculated to be 0.9 kcal mol⁻¹ exergonic. Subsequent proton transfer from 1,4-CHD to the α -C of α -17 to yield ethylbenzene (**TS9**) comes with a barrier of 32.8 kcal mol⁻¹. In the “Meisenheimer Pathway”, the formation of a hydride catalyst is forgone altogether, with a hydride instead being transferred from the Meisenheimer intermediate **I5'** (**TS10**). This process comes with an activation barrier of 31.7 kcal mol⁻¹. Both of these alternatives,

while worth considering, come with substantial activation barriers, and are hence unfeasible at the experimental conditions.

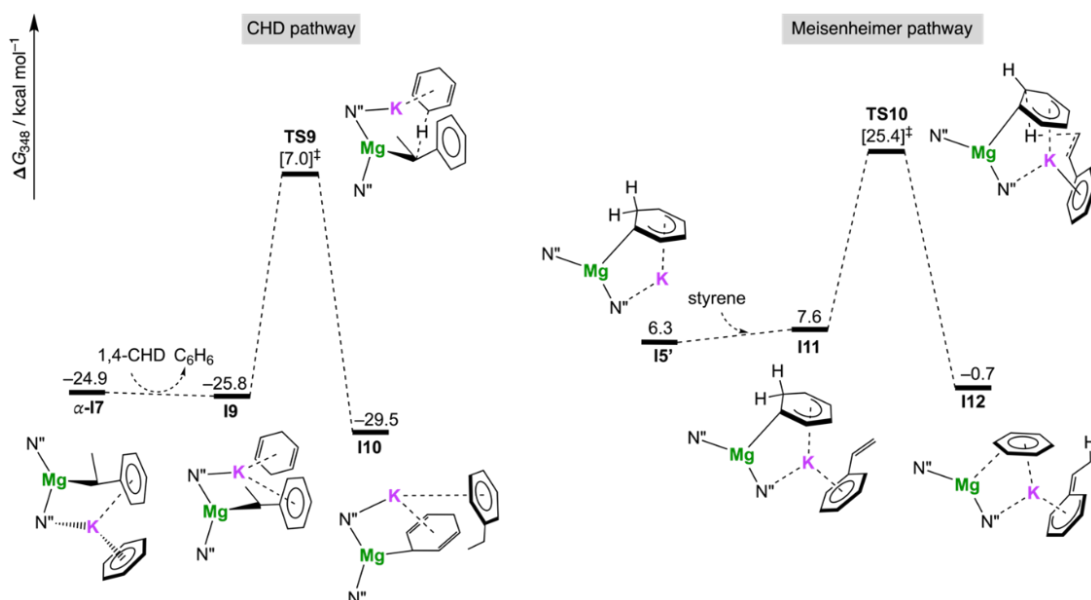


Figure 7.16: DFT-calculated Free Energy reaction profile (ΔG , $T = 348.15 \text{ K}$, 1 mol L^{-1}) for two alternative pathways (CHD and Meisenheimer) in the transfer hydrogenation mediated by $(\text{C}_6\text{H}_6)\text{K}(\text{H})\text{MgN}''_2$.

Experimentally, it was observed that small amounts of H_2 were formed during the catalysis. To probe this, the barrier to dihydrogen evolution was calculated (Figure 7.17) and found to be $21.2 \text{ kcal mol}^{-1}$ (**TS11**). This barrier is comparable, but higher than the overall energetic span of $18.3 \text{ kcal mol}^{-1}$, calculated for the protonation of $\alpha\text{-17}$, therefore making these results consistent with the experimental observations. In addition, the activation barrier for styrene polymerisation was calculated to be $32.1 \text{ kcal mol}^{-1}$ (**TS12**), which is substantially higher than the hydrogenation pathway, and thus disfavoured.

7 - Mechanistic Insight into Alkali-Metal Mediation of Styrene Transfer Hydrogenation

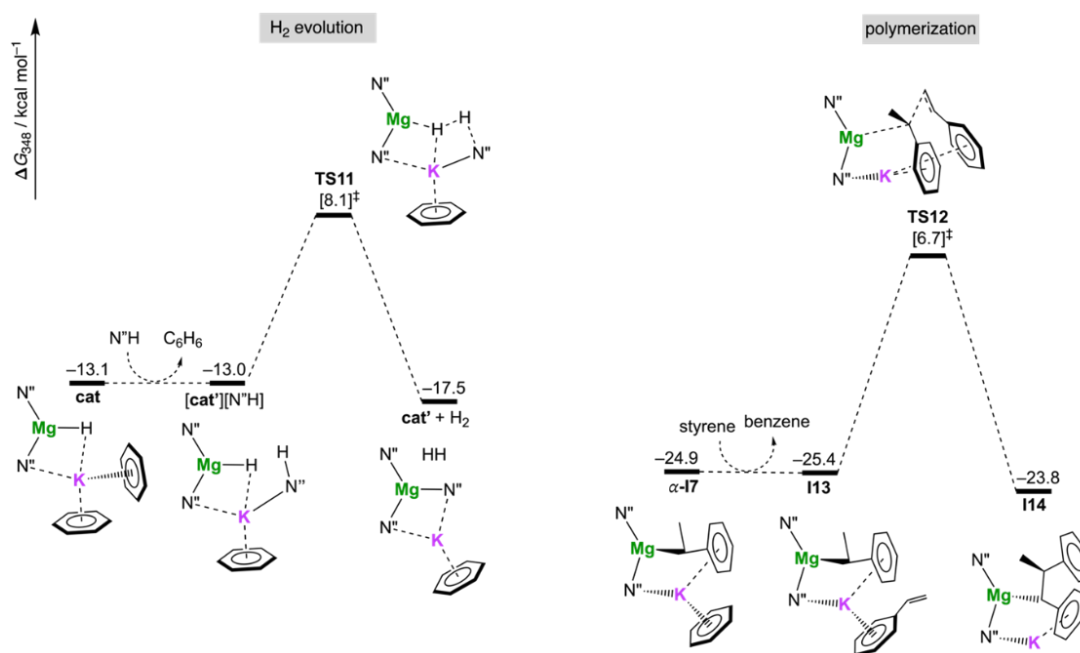


Figure 7.17: DFT-calculated Free Energy reaction profile (ΔG , $T = 348.15 \text{ K}$, 1 mol L^{-1}) for two possible side reactions occurring during transfer hydrogenation mediated by $(\text{C}_6\text{H}_6)\text{K}(\text{H})\text{MgN}^{\text{R}}_2$.

As a final point of discussion, it was observed experimentally, that during the reduction of styrene with $\text{NaMgN}^{\text{R}}_3$, precipitation of a crystalline polymer of formula $[(\text{NaMgN}^{\text{R}}_2)_2]_{\infty}$ occurred. However, under the same conditions, formation of crystalline $[\text{AMMg}(\text{HMDS})_2\text{H}]_2$ ($\text{AM} = \text{K, Rb, Cs}$) was not observed. The sodium species was separately synthesised, along with its potassium and rubidium analogues. All complexes were structurally characterised by X-ray crystallography, and found to possess a common inverse crown motif (Figure 7.19).^{112,313} These hydride complexes were postulated to be an intermediate in the catalytic cycle (Figure 7.2), and these structures provided support to this hypothesis. To highlight the important role of $\text{N}^{\text{R}}\text{H}$ in the protonation step of the hydrogenation, the reduction of styrene under catalytic conditions with the isolated inverse crown hydride complex $[(\text{C}_6\text{H}_6)\text{KMg}(\text{HMDS})_2\text{H}]_2$ was carried out. This resulted in polymerisation of the substrate, due to the insufficient concentrations of $\text{N}^{\text{R}}\text{H}$ present to enable protonation of the styryl intermediate. Given these results, a mechanism involving the dimeric hydride species is conceivable, and

was thus explored. A comparison of the key bond parameters between the calculated and experimental values of $[\text{KMg}(\text{HMDS})_2(\text{H})]_2$ is shown in Table 7.1, with overall good agreement achieved. In Figure 7.18, the calculated reaction profile for the transfer hydrogenation of styrene by $[(\text{C}_6\text{H}_6)\text{KMg}(\text{HMDS})_2\text{H}]_2$ is shown, with the structures of key intermediates and transition states shown in Figure 7.19.

Table 7.1: Comparison of key bond parameters (bond distances in Å, bond angles in °) for the dimeric inverse crown complex $[\text{KMg}(\text{HMDS})_2(\text{H})]_2$. Two units were identified in the crystallographic structure, for which bond metrics are reported.

Parameter	X-ray (unit 1 / unit 2)	DFT
Mg1...Mg2	2.934 / 2.923	2.912
Mg1-H1	1.88(3) / 1.91(3)	1.914
Mg1-H2	1.88(3) / 1.91(3)	1.914
Mg1-N1	2.070(2) / 2.066(2)	2.065
Mg1-N2	2.070(2) / 2.066(2)	2.065
Mg2-H1	1.88(3) / 1.91(3)	1.913
Mg2-H2	1.88(3) / 1.91(3)	1.914
Mg2-N3	2.070(2) / 2.066(2)	2.065
Mg2-N4	2.070(2) / 2.066(2)	2.065
K1...N1	2.922(2) / 2.871(2)	2.785
K1...N3	2.922(2) / 2.871(2)	2.785
K2...N2	2.922(2) / 2.871(2)	2.785
K2...N4	2.922(2) / 2.871(2)	2.785

7 - Mechanistic Insight into Alkali-Metal Mediation of Styrene Transfer Hydrogenation

K1...Mg1	3.614(9) / 3.600(9)	3.488
K1...Mg2	3.614(9) / 3.600(9)	3.488
N1-Si1	1.713(2) / 1.716(2)	1.746
N1-Si2	1.719(2) / 1.715(2)	1.746
Mg1-Mg2-H1	38.9(13) / 39.9(12)	40.46
Mg1-Mg2-H2	38.9(13) / 39.9(12)	40.46
H1-Mg-H2	78.0(3)	80.91
H1-Mg-H2	78.0(3)	80.91
N1-Mg1-N2	125.07(14) / 126.12(15)	126.54
N3-Mg2-N4	125.07(14) / 126.12(15)	126.54
N1-K1-N3	111.97(8) / 113.26(9)	117.80

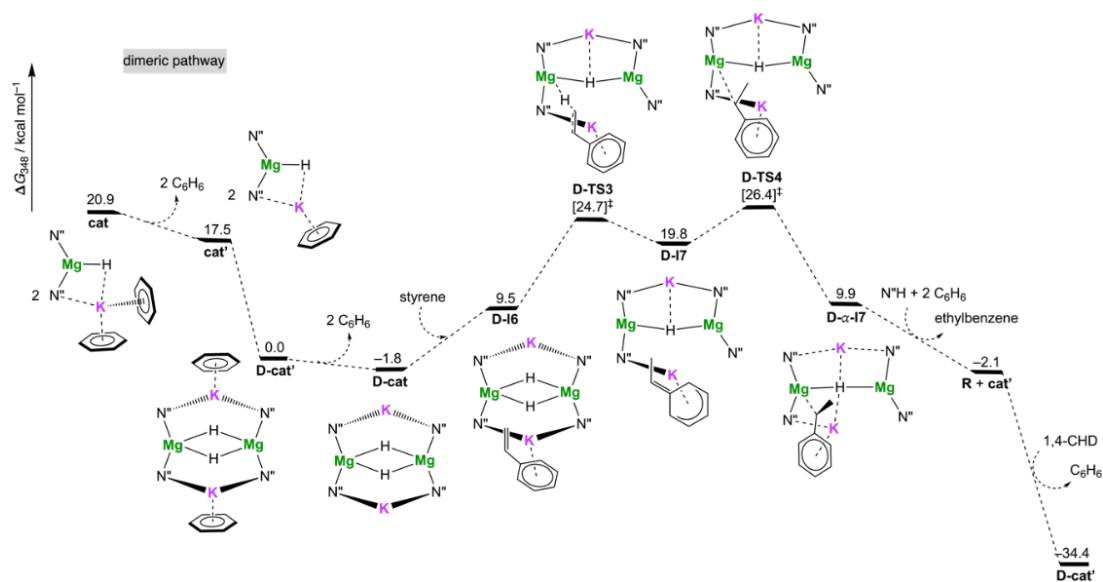


Figure 7.18: DFT-calculated Free Energy reaction energy profile (ΔG , $T = 348.15 \text{ K}$, 1 mol L^{-1}) for transfer hydrogenation of styrene via dimeric $[\text{KMg}(\text{H})\text{N}''_2]_2$.

Dimerisation of **cat**, with the concomitant loss of two molecules of benzene gives **D-cat'**, which is 20.9 kcal mol⁻¹ exergonic. **D-cat'** is in equilibrium with its solvent free counterpart, with 1.8 kcal mol⁻¹ in the difference. The overall dimerisation energy is therefore 22.7 kcal mol⁻¹, which is consistent with the observation that this compound crystallises from solution. Subsequent binding of styrene is 11.3 kcal mol⁻¹ endergonic, where the potassium ion interacts with styrene in an η^6 -fashion. The exocyclic C=C bond of styrene is favourably positioned to receive one of the bridging hydrides. This occurs via **D-TS3**, with an activation barrier of 28.2 kcal mol⁻¹. The resulting intermediate, **D-I7** is relatively unstable at 19.8 kcal mol⁻¹, but through rearrangement via **D-TS4**, with a facile local activation barrier of 6.6 kcal mol⁻¹, the more stable **D- α -I7** can be generated at 9.9 kcal mol⁻¹.

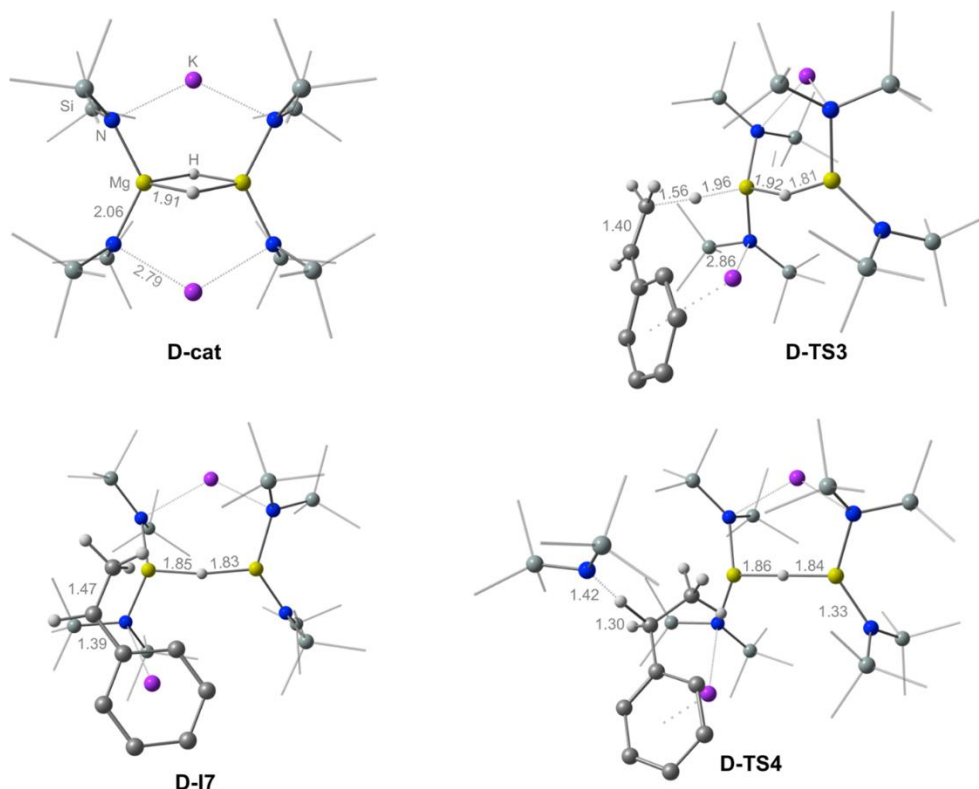


Figure 7.19: DFT-optimised geometries of key stationary points along the pathway for transfer hydrogenation of styrene catalysed by [KMg(H)N''₂]₂ showing key bond distances.

From here, although not explicitly calculated, protonation via the previously liberated N^{H} and release of ethylbenzene could occur. This process is $12.0 \text{ kcal mol}^{-1}$ exergonic and the proton transfer would occur through a transition state similar to the one calculated for the monomer discussed above. This mechanism provides an explanation for the experimental isolation of $[(\text{C}_6\text{H}_6)\text{KMg}(\text{HMDS})_2\text{H}]_2$, and its subsequent reactivity with styrene. Although the aggregation of the monomeric metal hydride species is thermodynamically favourable, there are factors that point towards the primary mechanism being monomeric. The concentrations of styrene and 1,4-CHD are high, relative to the amount of forming monomeric hydride catalyst, which would be present in relatively low concentrations at the beginning stages of catalysis. Hence, encounters between the monomeric hydride catalyst (**cat**) and the substrate will be far more likely, statistically speaking, than self-aggregation. Furthermore, the independent synthesis of the crystalline $[(\text{C}_6\text{H}_6)\text{NaMg}(\text{HMDS})_2\text{H}]_2$ and $[(\text{C}_6\text{H}_6)\text{KMg}(\text{HMDS})_2\text{H}]_2$ required 2-3 days at elevated temperatures¹¹², with subsequent catalytic activity hampered by insolubility in benzene. Thus, it is a reasonable assumption that the monomer is the primary catalyst in the early stages of catalysis, with the dimer becoming operative in the later stages, once a sufficient concentration in solution has built up.

7.4 Conclusions

In this chapter, the mechanism of styrene transfer hydrogenation, mediated by KMgN^{H}_3 , with 1,4-CHD acting as the hydrogen source, was investigated. The calculations have demonstrated that the isolated monometallic components, MgN^{H}_2 and KN^{H} , are inefficient catalysts. In the case of MgN^{H}_2 , the inefficiency stems from the inability to deprotonate 1,4-CHD at the experimental reaction conditions. This is the rate determining step of this pathway, with an overall energetic span of 32.1 kcal

mol⁻¹ being calculated. For KN⁺, the inefficiency stems from a complete lack of selectivity, with dihydrogen evolution being dominant over the desired styrene reduction. The overall energetic span of the KN⁺ pathway was calculated to be 24.3 kcal mol⁻¹. When combined into the bimetallic KMgN⁺₃, the synergistic action of potassium and magnesium work to alleviate these drawbacks. The deprotonation of 1,4-CHD is facilitated through an open form intermediate, that increases the basicity of the amide (N⁺) and provides a stabilising coordination site for 1,4-CHD via the potassium ion. This lowers the barrier, relative to that of MgN⁺₂ or the alternative direct deprotonation step. However, this step is still rate determining and dictates the overall energetic span 27.9 of kcal mol⁻¹. In the hydride transfer to styrene, potassium plays a critical role in acting as an anchor point, while activating the double bond, thus priming styrene for receiving the hydride from the magnesium centre. The protonation of the thermodynamically stable styryl intermediate was facilitated by an initial delocalisation of the negative charge from the α to the *para* position of the phenyl ring. This delocalisation is dependent on the stabilising influence of the potassium ion, which then allows subsequent quenching and protonation of the styryl intermediate to generate ethylbenzene, the desired product. The possibility of a dimeric mechanism for the hydrogenation was also explored. It was determined that although this pathway is feasible energetically speaking, the relative concentrations of the styrene, 1,4-CHD and the active hydride catalyst promote a monomeric mechanism early on in the catalysis. This study has shown that the cooperative action between Mg²⁺ and K⁺ enhances the catalytic ability of the isolated monometallic species. The K⁺ helps to direct various steps of the reactivity away from Mg²⁺, shown to be inactive in isolation. In return, Mg²⁺ acts as an anchor point and stabilises key intermediates such as α -I7. By working in unison, the transfer hydrogenation could be efficiently catalysed, with the individual strengths of each metal cation being exploited.

8 Conclusion

The overarching aim of the work described in this thesis was to make a sizeable contribution to the field of main group chemistry, primarily concerning Group 1, Group 2 and Group 13, through the use of quantum chemical calculations. The approach taken was to carry out a mixture of collaborative work with experimental chemists, as well as independent theoretical work. The purpose of this mixture was to ensure that the computational work was consistently informed by experimental design and insight. Furthermore, higher-level methodologies were employed to gain deeper insight and to attempt to address fundamental questions regarding the molecular electronic structure and reactivity of the studied complexes. Truncation to model systems was occasionally required in order to reduce cost. However, attempts to draw parallels to synthetically realised systems were made whenever possible. Several broad conclusions can be derived from the work described in this thesis. In Chapter 3, it was highlighted how a multi-faceted approach is necessary, if one wishes to reliably and accurately model the exotic electronic structure of complexes such as the dialumenes. A density based approach, in addition to an energy based approach to the analysis was revealing of the shortcomings of various single-reference, multi-reference and density functional based methods. It was revealed that despite the moderate amount of singlet biradicaloid character present in Al_2H_2 , single-reference coupled cluster methods performed excellently in describing both the bond dissociation energy and the density, when benchmarked against a near-FCI method. A primary takeaway from the work described in Chapters 4 and 5 is that a consideration of the full spectrum of reactivity is necessary when investigating the activation of small molecules by low-oxidation state main group complexes. Parallels are regularly drawn between the frontier orbitals of monomeric low-oxidation state main group complexes and traditional transition metal complexes. However, as shown in Chapter 5, association

to a dimer in solution, and subsequent activation of dihydrogen provides access to a lower energy pathway, compared to the alternative direct activation at the monomer. Thus, by considering all mechanistic possibilities, based on the available evidence, the calculations revealed a more complete picture of the reactivity. This full spectrum of reactivity not only refers to a consideration of both monomeric and dimeric pathways, but in the context of dialumenes, also refers to the possibility of singlet biradicaloid reactivity, where relevant. This necessitates a careful choice of computational methodology, as outlined in Chapter 3. Moving away from neutral species, in Chapter 6, it was described how a previously postulated FLP-like mechanism for the activation of dihydrogen by an alkali metal alumanyl complex, does in fact exist, and is kinetically accessible under the experimental conditions. This is in direct contrast to previous computational work carried out by Schaefer, where no such pathway could be located. This well-defined FLP-like transition state demonstrates clear cooperativity between the metal centres, as evidenced by extensive electronic structure analysis. Broadly speaking, this FLP-like mechanism could possibly be extended to, and have implications for related alkali metal alumanyl systems, not just for the activation of H_2 , but also other strong $\text{E}-\text{H}$ bonds. Finally, in Chapter 7, alkali metal mediation was explored, in the context of the transfer hydrogenation of styrene by a potassium magnesiate complex. Consistent with experiment, the calculations demonstrate how the monometallic components in isolation are incompetent catalysts. However, in the bimetallic complex, the synergistic effects between the potassium and magnesium cations, could be exploited. The calculations have demonstrated that the potassium cation helps to direct various difficult steps of the reactivity away from the magnesium cation, while the magnesium cation acts as a stabilising anchor point for key intermediates throughout the reactivity. An investigation of how the identity of the alkali or alkaline earth metal alters the mechanistic steps is a possible direction for future work. In addition, careful inspection of the suitability of the computational model employed, as the identity of the metal

8 - Conclusion

centres are varied, will likely be essential for the reliable description of the electronic structures and mechanistic steps in any future work.

9 Bibliography

- (1) Power, P. P. *Nature* **2010**, *463*, 171–177.
- (2) Weetman, C.; Inoue, S. *Chem. Cat. Comm.* **2018**, *10*, 4213–4228.
- (3) Chu, T.; Nikonov, G. I. *Chem. Rev.* **2018**, *118*, 3608–3680.
- (4) Weetman, C. *Chem. Eur. J.* **2021**, *27*, 1941.
- (5) Kutzelnigg, W. *Angew. Chem. Int. Ed.* **1984**, *23*, 272–295.
- (6) Jacobsen, H.; Ziegler, T. *J. Am. Chem. Soc.* **1994**, *116*, 3667–3679.
- (7) Hoppe, R. *Bunsenges. Phys. Chem.* **1966**, *70*, 1182–1182.
- (8) Davidson, P. J.; Lappert, M. F. *J. Chem. Soc., Chem. Commun.* **1973**, 317.
- (9) Goldberg, D. E.; Harris, D. H.; Lappert, M. F.; Thomas, M. K. *J. Chem. Soc., Chem. Commun.* **1976**, *120*, 261–262.
- (10) West, R.; Fink, M. J. *Science* **1981**, *214*, 1343–1344.
- (11) Yoshifuji, M.; Shima, I.; Inamoto, N.; Hirotsu, K.; Higuchi, T. *J. Am. Chem. Soc.* **1981**, *103*, 4587–4589.
- (12) Brook, A. G.; Abdesaken, F.; Gutekunst, B.; Gutekunst, G.; Kallury, R. K. *J. Chem. Soc., Chem. Commun.* **1981**, 191–192.
- (13) Sekiguchi, A.; Kinjo, R.; Ichinohe, M. *Science* **2004**, *305*, 1755–1757.
- (14) Stender, M.; Phillips, A. D.; Wright, R. J.; Power, P. P. *Angew. Chem. Int. Ed.* **2002**, *41*, 1785–1787.
- (15) Phillips, A. D.; Wright, R. J.; Olmstead, M. M.; Power, P. P. *J. Am. Chem. Soc.* **2002**, *124*, 5930–5931.
- (16) Pu, L.; Twamley, B.; Power, P. P. *J. Am. Chem. Soc.* **2000**, *122*, 3524–3525.

- (17) Fjeldberg, T.; Haaland, A.; Schilling, B. E. R.; Lappert, M. F.; Thorne, A. J. *J. Chem. Soc., Dalton Trans.* **1986**, 1551–1556.
- (18) Trinquier, Georges.; Malrieu, J. Paul. *J. Phys. Chem.* **1990**, 94, 6184–6196.
- (19) Wedler, H. B.; Wendelboe, P.; Power, P. P. *Organometallics* **2018**, 37, 2929–2936.
- (20) Su, J.; Li, X.-W.; Crittendon, R. C.; Robinson, G. H. *J. Am. Chem. Soc.* **1997**, 119, 5471–5472.
- (21) Braunschweig, H.; Dewhurst, R. D.; Hammond, K.; Mies, J.; Radacki, K.; Vargas, A. *Science* **2012**, 336, 1420–1422.
- (22) Wang, Y.; Quillian, B.; Wei, P.; Wannere, C. S.; Xie, Y.; King, R. B.; Schaefer, H. F.; Schleyer, P. v. R.; Robinson, G. H. *J. Am. Chem. Soc.* **2007**, 129, 12412–12413.
- (23) Bag, P.; Porzelt, A.; Altmann, P. J.; Inoue, S. *J. Am. Chem. Soc.* **2017**, 139, 14384–14387.
- (24) Hardman, N. J.; Wright, R. J.; Phillips, A. D.; Power, P. P. *Angew. Chem. Int. Ed.* **2002**, 41, 2842–2844.
- (25) Wright, R. J.; Phillips, A. D.; Hardman, N. J.; Power, P. P. *J. Am. Chem. Soc.* **2002**, 124, 8538–8539.
- (26) Wright, R. J.; Phillips, A. D.; Hino, S.; Power, P. P. *J. Am. Chem. Soc.* **2005**, 127, 4794–4799.
- (27) Spikes, G. H.; Fettingner, J. C.; Power, P. P. *J. Am. Chem. Soc.* **2005**, 127, 12232–12233.
- (28) Peng, Y.; Brynda, M.; Ellis, B. D.; Fettingner, J. C.; Rivard, E.; Power, P. P. *Chem. Commun.* **2008**, 6042–6044.

- (29) Zhao, L.; Huang, F.; Lu, G.; Wang, Z.-X.; Schleyer, P. von R. *J. Am. Chem. Soc.* **2012**, *134*, 8856–8868.
- (30) Peng, Y.; Guo, J.-D.; Ellis, B. D.; Zhu, Z.; Fettinger, J. C.; Nagase, S.; Power, P. P. *J. Am. Chem. Soc.* **2009**, *131*, 16272–16282.
- (31) Peng, Y.; Ellis, B. D.; Wang, X.; Power, P. P. *J. Am. Chem. Soc.* **2008**, *130*, 12268–12269.
- (32) Welch, G. C.; San Juan, R. R.; Masuda, J. D.; Stephan, D. W. *Science* **2006**, *314*, 1124–1128.
- (33) Stephan, D. W. *Chem. Commun.* **2010**, *46*, 8526–8533.
- (34) Stephan, D. W. *Science* **2016**, *354*, aaf7229.
- (35) Scott, D. J.; Fuchter, M. J.; Ashley, A. E. *Chem. Soc. Rev.* **2017**, *46*, 5689–5700.
- (36) Stender, M.; Phillips, A. D.; Power, P. P. *Chem. Commun.* **2002**, 1312–1313.
- (37) McCahill, J. S. J.; Welch, G. C.; Stephan, D. W. *Angew. Chem. Int. Ed.* **2007**, *46*, 4968–4971.
- (38) Otten, E.; Neu, R. C.; Stephan, D. W. *J. Am. Chem. Soc.* **2009**, *131*, 9918–9919.
- (39) Mömming, C. M.; Otten, E.; Kehr, G.; Fröhlich, R.; Grimme, S.; Stephan, D. W.; Erker, G. *Angew. Chem. Int. Ed.* **2009**, *48*, 6643–6646.
- (40) Peng, Y.; Ellis, B. D.; Wang, X.; Fettinger, J. C.; Power, P. P. *Science* **2009**, *325*, 1668–1670.
- (41) Uhl, W. *Z. Naturforsch. B* **1988**, *43*, 1113–1118.

- (42) Klinkhammer, K.-W.; Uhl, W.; Wagner, J.; Hiller, W. *Angew. Chem. Int. Ed.* **1991**, *30*, 179–180.
- (43) Dohmeier, C.; Robl, C.; Tacke, M.; Schnöckel, H. *Angew. Chem. Int. Ed.* **1991**, *30*, 564–565.
- (44) Schulz, S.; Roesky, H. W.; Koch, H. J.; Sheldrick, G. M.; Stalke, D.; Kuhn, A. *Angew. Chem. Int. Ed.* **1993**, *32*, 1729–1731.
- (45) Ganesamoorthy, C.; Loerke, S.; Gemel, C.; Jerabek, P.; Winter, M.; Frenking, G.; Fischer, R. A. *Chem. Commun.* **2013**, *49*, 2858–2860.
- (46) Liu, Y.; Li, J.; Ma, X.; Yang, Z.; Roesky, H. W. *Coord. Chem. Rev.* **2018**, *374*, 387–415.
- (47) Dohmeier, C.; Baum, E.; Ecker, A.; Köppe, R.; Schnöckel, H. *Organometallics* **1996**, *15*, 4702–4706.
- (48) Sitzmann, H.; Lappert, M. F.; Dohmeier, C.; Üffing, C.; Schnöckel, H. *J. Organomet. Chem.* **1998**, *561*, 203–208.
- (49) Hofmann, A.; Troster, T.; Kupfer, T.; Braunschweig, H. *Chem. Sci.* **2019**, *10*, 3421–3428.
- (50) Cui, C.; Roesky, H. W.; Schmidt, H.-G.; Noltemeyer, M.; Hao, H.; Cimpoesu, F. *Angew. Chem. Int. Ed.* **2000**, *39*, 4274–4276.
- (51) Chu, T.; Korobkov, I.; Nikonov, G. I. *J. Am. Chem. Soc.* **2014**, *136*, 9195–9202.
- (52) Bakewell, C.; White, A. J. P.; Crimmin, M. R. *Angew. Chem. Int. Ed.* **2018**, *57*, 6638–6642.
- (53) Bakewell, C.; White, A. J. P.; Crimmin, M. R. *Chem. Sci.* **2019**, *10*, 2452–2458.

- (54) Bag, P.; Weetman, C.; Inoue, S. *Angew. Chem. Int. Ed.* **2018**, *57*, 14394–14413.
- (55) Nesterov, V.; Reiter, D.; Bag, P.; Frisch, P.; Holzner, R.; Porzelt, A.; Inoue, S. *Chem. Rev.* **2018**, *118*, 9678–9842.
- (56) Lundell, K. A.; Zhang, X.; Boldyrev, A. I.; Bowen, K. H. *Angew. Chem. Int. Ed.* **2017**, *56*, 16593–16596.
- (57) Zhang, X.; Popov, I. A.; Lundell, K. A.; Wang, H.; Mu, C.; Wang, W.; Schnöckel, H.; Boldyrev, A. I.; Bowen, K. H. *Angew. Chem. Int. Ed.* **2018**, *130*, 14256–14260.
- (58) Barthélemy, A.; Scherer, H.; Daub, M.; Bugnet, A.; Krossing, I. *Angew. Chem. Int. Ed.* **2023**, *62*, e202311648.
- (59) Weetman, C.; Porzelt, A.; Bag, P.; Hanusch, F.; Inoue, S. *Chem. Sci.* **2020**, *11*, 4817–4827.
- (60) Holzner, R.; Porzelt, A.; Karaca, U. S.; Kiefer, F.; Frisch, P.; Wendel, D.; Holthausen, M. C.; Inoue, S. *Dalton Trans.* **2021**, *50*, 8785–8793.
- (61) Falconer, R. L.; Byrne, K. M.; Nichol, G. S.; Krämer, T.; Cowley, M. J. *Angew. Chem. Int. Ed.* **2021**, *60*, 24702–24708.
- (62) Falconer, R. L.; Nichol, G. S.; Smolyar, I. V.; Cockroft, S. L.; Cowley, M. J. *Angew. Chem. Int. Ed.* **2020**, *60*, 2047–2052.
- (63) Wright, R. J.; Phillips, A. D.; Power, P. P. *J. Am. Chem. Soc.* **2003**, *125*, 10784–10785.
- (64) Agou, T.; Nagata, K.; Tokitoh, N. *Angew. Chem. Int. Ed.* **2013**, *52*, 10818–10821.

- (65) Bakewell, C.; Hobson, K.; Carmalt, C. *Angew. Chem. Int. Ed.* **2022**, *61*, e202205901.
- (66) Lehmann, A.; Queen, J. D.; Roberts, C. J.; Rissanen, K.; Tuononen, H. M.; Power, P. P. *Angew. Chem. Int. Ed.* **2024**, *63*, e202412599.
- (67) Mears, K. L.; Power, P. P. *Acc. Chem. Res.* **2022**, *55*, 1337–1348.
- (68) Caputo, C. A.; Koivistoinen, J.; Moilanen, J.; Boynton, J. N.; Tuononen, H. M.; Power, P. P. *J. Am. Chem. Soc.* **2013**, *135*, 1952–1960.
- (69) Moilanen, J.; Power, P. P.; Tuononen, H. M. *Inorg. Chem.* **2010**, *49*, 10992–11000.
- (70) Schmidt, E. S.; Jockisch, A.; Schmidbaur, H. *J. Am. Chem. Soc.* **1999**, *121*, 9758–9759.
- (71) Baker, R. J.; Farley, R. D.; Jones, C.; Kloth, M.; Murphy, D. M. *J. Chem. Soc., Dalton Trans.* **2002**, 3844–3850.
- (72) Fedushkin, I. L.; Lukoyanov, A. N.; Fukin, G. K.; Ketkov, S. Yu.; Hummert, M.; Schumann, H. *Chem. Eur. J.* **2008**, *14*, 8465–8468.
- (73) Segawa, Y.; Yamashita, M.; Nozaki, K. *Science* **2006**, *314*, 113–115.
- (74) Segawa, Y.; Suzuki, Y.; Yamashita, M.; Nozaki, K. *J. Am. Chem. Soc.* **2008**, *130*, 16069–16079.
- (75) Weber, L. *Eur. J. Inorg. Chem.* **2017**, 2017, 3461–3488.
- (76) Schwamm, R. J.; Anker, M. D.; Lein, M.; Coles, M. P.; Fitchett, C. M. *Angew. Chem. Int. Ed.* **2018**, *130*, 5987–5989.
- (77) Anker, M. D.; Altaf, Y.; Lein, M.; Coles, M. P. *Dalton Trans.* **2019**, 48, 16588–16594.

- (78) Hicks, J.; Vasko, P.; Goicoechea, J. M.; Aldridge, S. *Nature* **2018**, 557, 92–95.
- (79) Heilmann, A.; Hicks, J.; Vasko, P.; Goicoechea, J. M.; Aldridge, S. *Angew. Chem. Int. Ed.* **2020**, 59, 4897–4901.
- (80) Hicks, J.; Vasko, P.; Goicoechea, J. M.; Aldridge, S. *J. Am. Chem. Soc.* **2019**, 141, 11000–11003.
- (81) Schwamm, R. J.; Anker, M. D.; Lein, M.; Coles, M. P. *Angew. Chem. Int. Ed.* **2019**, 58, 1489–1493.
- (82) Schwamm, R. J.; Coles, M. P.; Hill, M. S.; Mahon, M. F.; McMullin, C. L.; Rajabi, N. A.; Wilson, A. S. S. *Angew. Chem. Int. Ed.* **2020**, 59, 3928–3932.
- (83) Grams, S.; Eyselein, J.; Langer, J.; Farber, C.; Harder, S. *Angew. Chem. Int. Ed.* **2020**, 59, 15982–15986.
- (84) Schwamm, R. J.; Hill, M. S.; Liu, H. Y.; Mahon, M. F.; McMullin, C. L.; Rajabi, N. A. *Chem. Eur. J.* **2021**, 27, 14971–14980.
- (85) Feng, G.; Chan, K. L.; Lin, Z.; Yamashita, M. *J. Am. Chem. Soc.* **2022**, 144, 22662–22668.
- (86) Grams, S.; Mai, J.; Langer, J.; Harder, S. *Organometallics* **2022**, 41, 2862–2867.
- (87) Grams, S.; Mai, J.; Langer, J.; Harder, S. *Dalton Trans.* **2022**, 51, 12476–12483.
- (88) Gentner, T. X.; Evans, M. J.; Kennedy, A. R.; Neale, S. E.; McMullin, C. L.; Coles, M. P.; Mulvey, R. E. *Chem. Commun.* **2022**, 58, 1390–1393.
- (89) Koshino, K.; Kinjo, R. *J. Am. Chem. Soc.* **2020**, 142, 9057–9062.
- (90) Kurumada, S.; Takamori, S.; Yamashita, M. *Nat. Chem.* **2020**, 12, 36–39.

- (91) Yan, C.; Kinjo, R. *Angew. Chem. Int. Ed.* **2022**, *61*, e202211800.
- (92) Jackson, R. A.; Matthews, A.; Vasko, P.; Mahon, M. F.; Hicks, J.; Liptrot, D. J. *Chem. Commun.* **2023**, *59*, 5277–5280.
- (93) Sarkar, D.; Vasko, P.; Roper, A. F.; Crumpton, A. E.; Roy, M. M. D.; Griffin, L. P.; Bogle, C.; Aldridge, S. *J. Am. Chem. Soc.* **2024**, *146*, 11792–11800.
- (94) de Vries, J. G.; Elsevier, C. J. *The Handbook of Homogeneous Hydrogenation*; Wiley VCH: Weinheim, **2006**.
- (95) Young, J. F.; Osborn, J. A.; Jardine, F. H.; Wilkinson, G. *Chem. Commun.* **1965**, 131–132.
- (96) Crabtree, R. H.; Morris, G. E. *J. Organomet. Chem.* **1977**, *135*, 395–403.
- (97) *The Periodic Table of Endangered Elements*. American Chemical Society. <https://www.acs.org/greenchemistry/research-innovation/endangered-elements.html>.
- (98) Spielmann, J.; Harder, S. *Chem. Eur. J.* **2007**, *13*, 8928–8938.
- (99) Spielmann, J.; Buch, F.; Harder, S. *Angew. Chem. Int. Ed.* **2008**, *47*, 9434–9438.
- (100) Hill, M. S.; Liptrot, D. J.; Weetman, C. *Chem. Soc. Rev.* **2016**, *45*, 972–988.
- (101) Wilson, A. S. S.; Dinoi, C.; Hill, M. S.; Mahon, M. F.; Maron, L. *Angew. Chem. Int. Ed.* **2018**, *57*, 15500–15504.
- (102) Shi, X.; Cheng, J. *Dalton Trans.* **2019**, *48*, 8565–8568.
- (103) Bauer, H.; Alonso, M.; Färber, C.; Elsen, H.; Pahl, J.; Causero, A.; Ballmann, G.; De Proft, F.; Harder, S. *Nature Cat.* **2018**, *1*, 40–47.
- (104) Bauer, H.; Alonso, M.; Fischer, C.; Rosch, B.; Elsen, H.; Harder, S. *Angew. Chem. Int. Ed.* **2018**, *57*, 15177–15182.

- (105) De Tobel, B.; Hamlin, T. A.; Fonseca Guerra, C.; Harder, S.; De Proft, F.; Alonso, M. *Polyhedron* **2024**, *248*, 116751.
- (106) Bauer, H.; Thum, K.; Alonso, M.; Fischer, C.; Harder, S. *Angew. Chem. Int. Ed.* **2019**, *58*, 4248–4253.
- (107) Pollard, V. A.; Fuentes, M. A.; Kennedy, A. R.; McLellan, R.; Mulvey, R. E. *Angew. Chem. Int. Ed.* **2018**, *57*, 10651–10655.
- (108) Davin, L.; Hernan-Gomez, A.; McLaughlin, C.; Kennedy, A. R.; McLellan, R.; Hevia, E. *Dalton Trans.* **2019**, *48*, 8122–8130.
- (109) Zhang, X.-Y.; Du, H.-Z.; Zhai, D.-D.; Guan, B.-T. *Org. Chem. Front.* **2020**, *7*, 1991–1996.
- (110) Byrne, K. M.; Bjornsson, R.; Krämer, T. *Phys. Chem. Chem. Phys.* **2024**, *26*, 30018–30034.
- (111) Kraemer, T.; Byrne, K. M.; Hicks, J.; Griffin, L. P.; Aldridge, S. *Chem. Eur. J.* **2025**, e202500095.
- (112) Mulvey, R. E.; Gentner, T. X.; Kennedy, A. R.; Hevia, E. *Chem. Cat. Comm.* **2021**, *13*, 1–9.
- (113) Byrne, K. M.; Robertson, S. D.; Mulvey, R. E.; Kraemer, T. *ChemCatChem* **2024**, e202400655.
- (114) Hartree, D. R. *Proc. Cambridge Phil. Soc.* **1928**, *24*, 426–437.
- (115) Slater, J. C. *Phys. Rev.* **1930**, *35*, 210–211.
- (116) Roothaan, C. C. J. *Rev. Mod. Phys.* **1951**, *23*, 69–89.
- (117) Brillouin, L. *Actualities Sci. Ind.* **1934**, 71.
- (118) Møller, C.; Plesset, M. *Phys. Rev.* **1934**, 46.

- (119) Čížek, J. *J. Chem. Phys.* **1966**, *45*, 4256–4266.
- (120) Cioslowski, J. *Quantum-Mechanical Prediction of Thermochemical Data*; Springer Science & Business Media, **2002**.
- (121) Löwdin, P.-O. *Phys. Rev.* **1955**, *97*, 1474–1489.
- (122) Edmiston, C.; Krauss, M. *J. Chem. Phys.* **1965**, *42*, 1119–1120.
- (123) Edmiston, C.; Krauss, M. *J. Chem. Phys.* **1966**, *45*, 1833–1839.
- (124) Ahlrichs, R.; Kutzelnigg, W. *J. Chem. Phys.* **1968**, *48*, 1819–1832.
- (125) Gelus, M.; Ahlrichs, R.; Staemmler, V.; Kutzelnigg, W. *Theoret. Chim. Acta* **1971**, *21*.
- (126) Staemmler, V.; Jungen, M. *Chemical Physics Letters* **1972**, *16*, 187–191.
- (127) Kutzelnigg, W.; Staemmler, V.; Hoheisel, C. *Chem. Phys.* **1973**, *1*, 27–44.
- (128) Driessler, F.; Ahlrichs, R.; Staemmler, V.; Kutzelnigg, W. *Theoret. Chim. Acta* **1973**, *30*, 315–326.
- (129) Meyer, W. *J. Chem. Phys.* **1973**, *58*, 1017–1035.
- (130) Meyer, W. *Theoret. Chim. Acta* **1974**, *35*, 277–292.
- (131) Meyer, W.; Rosmus, P. *J. Chem. Phys.* **1975**, *63*, 2356–2375.
- (132) Werner, H.-J.; Meyer, W. *Mol. Phys.* **1976**, *31*, 855–872.
- (133) Dykstra, C. E.; Schaefer, H. F., III; Meyer, W. *J. Chem. Phys.* **1976**, *65*, 5141–5146.
- (134) Neese, F.; Wennmohs, F.; Hansen, A. *J. Chem. Phys.* **2009**, *130*, 114108.
- (135) Neese, F.; Hansen, A.; Liakos, D. G. *J. Chem. Phys.* **2009**, *131*, 064103.
- (136) Riplinger, C.; Neese, F. *J. Chem. Phys.* **2013**, *138*, 034106.

- (137) Riplinger, C.; Sandhoefer, B.; Hansen, A.; Neese, F. *J. Chem. Phys.* **2013**, *139*, 134101.
- (138) Sparta, M.; Neese, F. *Chem. Soc. Rev.* **2014**, *43*, 5032–5041.
- (139) Chilkuri, V. G.; Neese, F. *J. Comput. Chem.* **2021**, *42*, 982–1005.
- (140) Chilkuri, V. G.; Neese, F. *J. Chem. Theory. Comput.* **2021**, *17*, 2868–2885.
- (141) Thomas, L. H. *Proc. Camb. Phil. Soc.* **1927**, *23*, 542–548.
- (142) Slater, J. C. *Phys. Rev.* **1951**, *81*, 385–390.
- (143) Hohenberg, P.; Kohn, W. *Phys. Rev.* **1964**, *136*, B864–B871.
- (144) Kohn, W.; Sham, L. J. *Phys. Rev.* **1965**, *140*, A1133–A1138.
- (145) Ceperley, D. M.; Alder, B. J. *Phys. Rev. Lett.* **1980**, *45*, 566–569.
- (146) Vosko, S. H.; Wilk, L.; Nusair, M. *Can. J. Phys.* **1980**, *58*, 1200–1211.
- (147) Becke, A. D. *Phys. Rev. A* **1988**, *38*, 3098–3100.
- (148) Becke, A. D. *J. Chem. Phys.* **1986**, *84*, 4524–4529.
- (149) Perdew, J. P.; Burke, K.; Ernzerhof, M. *Phys. Rev. Lett.* **1996**, *77*, 3865–3868.
- (150) Perdew, J. P. *Phys. Rev. B* **1986**, *33*, 8822–8824.
- (151) Lee, C.; Yang, W.; Parr, R. G. *Phys. Rev. B* **1988**, *37*, 785–789.
- (152) Becke, A. D.; Roussel, M. R. *Phys. Rev. A* **1989**, *39*, 3761–3767.
- (153) Proynov, E. I.; Sirois, S.; Salahub, D. R. *Int. J. Quantum Chem.* **1997**, *64*, 427–446.
- (154) Tao, J.; Perdew, J. P.; Staroverov, V. N.; Scuseria, G. E. *Phys. Rev. Lett.* **2003**, *91*, 146401.
- (155) Becke, A. D. *J. Chem. Phys.* **1993**, *98*, 1372–1377.

- (156) Becke, A. D. *J. Chem. Phys.* **1993**, *98*, 5648–5652.
- (157) Stephens, P. J.; Devlin, F. J.; Chabalowski, C. F.; Frisch, M. J. *J. Phys. Chem.* **1994**, *98*, 11623–11627.
- (158) Adamo, C.; Barone, V. *Chem. Phys. Lett.* **1997**, *274*, 242–250.
- (159) Adamo, C.; Cossi, M.; Barone, V. *J. Mol. Struct. (Theochem)* **1999**, *493*, 145–157.
- (160) Zhao, Y.; Truhlar, D. G. *Theor. Chem. Acc.* **2008**, *120*, 215–241.
- (161) Grimme, S. *J. Chem. Phys.* **2006**, *124*, 034108.
- (162) Bousquet, D.; Brémond, E.; Sancho-García, J. C.; Ciofini, I.; Adamo, C. *J. Chem. Theory Comput.* **2013**, *9*, 3444–3452.
- (163) Goerigk, L.; Grimme, S. *J. Chem. Theory Comput.* **2011**, *7*, 291–309.
- (164) Grimme, S.; Antony, J.; Ehrlich, S.; Krieg, H. *J. Chem. Phys.* **2010**, *132*, 154104.
- (165) Grimme, S.; Ehrlich, S.; Goerigk, L. *J. Comput. Chem.* **2011**, *32*, 1456–1465.
- (166) Caldeweyher, E.; Bannwarth, C.; Grimme, S. *J. Chem. Phys.* **2017**, *147*, 034112.
- (167) Goerigk, L.; Hansen, A.; Bauer, C.; Ehrlich, S.; Najibi, A.; Grimme, S. *Phys. Chem. Chem. Phys.* **2017**, *19*, 32184–32215.
- (168) Boys, S. F. *Proc. R. Soc. A: Math. Phys. Eng. Sci.* **1950**.
- (169) Hehre, W. J.; Stewart, R. F.; Pople, J. A. *J. Chem. Phys.* **1969**, *51*, 2657–2664.
- (170) Woon, D. E.; Dunning, T. H., Jr. *J. Chem. Phys.* **1995**, *103*, 4572–4585.
- (171) Ditchfield, R.; Hehre, W. J.; Pople, J. A. *J. Chem. Phys.* **1971**, *54*, 724–728.

- (172) Dunning, T. H., Jr. *J. Chem. Phys.* **1989**, *90*, 1007–1023.
- (173) Woon, D. E.; Dunning, T. H., Jr. *J. Chem. Phys.* **1993**, *98*, 1358–1371.
- (174) Krishnan, R.; Frisch, M. J.; Pople, J. A. *J. Chem. Phys.* **1980**, *72*, 4244–4245.
- (175) Wilson, A. K.; van Mourik, T.; Dunning, T. H. *J. Mol. Struct. (Theochem)* **1996**, *388*, 339–349.
- (176) Metz, B.; Stoll, H.; Dolg, M. *J. Chem. Phys.* **2000**, *113*, 2563–2569.
- (177) Peterson, K. A. *J. Chem. Phys.* **2003**, *119*, 11099–11112.
- (178) Peterson, K. A.; Figgen, D.; Goll, E.; Stoll, H.; Dolg, M. *J. Chem. Phys.* **2003**, *119*, 11113–11123.
- (179) Matthews, D. A.; Cheng, L.; Harding, M. E.; Lipparini, F.; Stopkiewicz, S.; Jagau, T.-C.; Szalay, P. G.; Gauss, J.; Stanton, J. F. *J. Chem. Phys.* **2020**, *152*, 214108.
- (180) Feyereisen, M.; Fitzgerald, G.; Komornicki, A. *Chem. Phys. Lett.* **1993**, *208*, 359–363.
- (181) Pinski, P.; Riplinger, C.; Valeev, E. F.; Neese, F. *J. Chem. Phys.* **2015**, *143*, 034108.
- (182) Neese, F. *WIREs Comput. Mol. Sci.* **2022**, *12*, e1606.
- (183) Lee, C.; Yang, W.; Parr, R. G. *Phys. Rev. B* **1988**, *37*, 785–789.
- (184) Sharma, S.; Holmes, A. A.; Jeanmairet, G.; Alavi, A.; Umrigar, C. J. *J. Chem. Theory Comput.* **2017**, *13*, 1595–1604.
- (185) Holmes, A. A.; Tubman, N. M.; Umrigar, C. J. *J. Chem. Theor. Comput.* **2016**, *12*, 3674–3680.
- (186) White, S. R. *Phys. Rev. Lett.* **1992**, *69*, 2863–2866.

- (187) White, S. R. *Phys. Rev. B* **1993**, *48*, 10345–10356.
- (188) Smith, J. E. T.; Mussard, B.; Holmes, A. A.; Sharma, S. *J. Chem. Theor. Comput.* **2017**, *13*, 5468–5478.
- (189) Zhai, H.; Larsson, H. R.; Lee, S.; Cui, Z.-H.; Zhu, T.; Sun, C.; Peng, L.; Peng, R.; Liao, K.; Tölle, J.; Yang, J.; Li, S.; Chan, G. K.-L. *J. Chem. Phys.* **2023**, *159*, 234801.
- (190) Zhai, H.; Chan, G. K.-L. *J. Chem. Phys.* **2021**, *154*, 224116.
- (191) Sun, Q. *J. Comput. Chem.* **2015**, *36*, 1664–1671.
- (192) Sun, Q.; Berkelbach, T. C.; Blunt, N. S.; Booth, G. H.; Guo, S.; Li, Z.; Liu, J.; McClain, J. D.; Sayfutyarova, E. R.; Sharma, S.; Wouters, S.; Chan, G. K.-L. *WIREs Comput. Mol. Sci.* **2018**, *8*, e1340.
- (193) Sun, Q.; Zhang, X.; Banerjee, S.; Bao, P.; Barbry, M.; Blunt, N. S.; Bogdanov, N. A.; Booth, G. H.; Chen, J.; Cui, Z.-H.; Eriksen, J. J.; Gao, Y.; Guo, S.; Hermann, J.; Hermes, M. R.; Koh, K.; Koval, P.; Lehtola, S.; Li, Z.; Liu, J.; Mardirossian, N.; McClain, J. D.; Motta, M.; Mussard, B.; Pham, H. Q.; Pulkin, A.; Purwanto, W.; Robinson, P. J.; Ronca, E.; Sayfutyarova, E. R.; Scheurer, M.; Schurkus, H. F.; Smith, J. E. T.; Sun, C.; Sun, S.-N.; Upadhyay, S.; Wagner, L. K.; Wang, X.; White, A.; Whitfield, J. D.; Williamson, M. J.; Wouters, S.; Yang, J.; Yu, J. M.; Zhu, T.; Berkelbach, T. C.; Sharma, S.; Sokolov, A. Yu.; Chan, G. K.-L. *J. Chem. Phys.* **2020**, *153*, 024109.
- (194) Bjornsson, R., *ASH – a Multiscale Modelling Program*, **2024**.
- (195) Perdew, J. P.; Burke, K.; Ernzerhof, M. *Phys. Rev. Lett.* **1996**, *77*, 3865–3868.
- (196) Bartók, A. P.; Yates, J. R. *J. Chem. Phys.* **2019**, *150*, 161101.

- (197) Staroverov, V. N.; Scuseria, G. E.; Tao, J.; Perdew, J. P. *J. Chem. Phys.* **2003**, *119*, 12129–12137.
- (198) Mardirossian, N.; Head-Gordon, M. *Phys. Chem. Chem. Phys.* **2014**, *16*, 9904–9924.
- (199) Kozuch, S.; Martin, J. M. L. *Phys. Chem. Chem. Phys.* **2011**, *13*, 20104–20107.
- (200) Kállay, M.; Nagy, P. R.; Mester, D.; Rolik, Z.; Samu, G.; Csontos, J.; Csóka, J.; Szabó, P. B.; Gyevi-Nagy, L.; Hégyely, B.; Ladjánszki, I.; Szegedy, L.; Ladóczki, B.; Petrov, K.; Farkas, M.; Mezei, P. D.; Ganyecz, Á. *J. Chem. Phys.* **2020**, *152*, 074107.
- (201) Karton, A.; Martin, J. M. L. *Theor. Chem. Acc.* **2006**, *115*, 330–333.
- (202) Zhong, S.; Barnes, E. C.; Petersson, G. A. *J. Chem. Phys.* **2008**, *129*, 184116.
- (203) Helgaker, T.; Klopper, W.; Koch, H.; Noga, J. *J. Chem. Phys.* **1997**, *106*, 9639–9646.
- (204) Halkier, A.; Helgaker, T.; Jørgensen, P.; Klopper, W.; Koch, H.; Olsen, J.; Wilson, A. K. *Chem. Phys. Lett.* **1998**, *286*, 243–252.
- (205) Becke, A. D.; Edgecombe, K. E. *J. Chem. Phys.* **1990**, *92*, 5397–5403.
- (206) Savin, A.; Becke, A. D.; Flad, J.; Nesper, R.; Preuss, H.; von Schnering, H. G. *Angew. Chem. Int. Ed.* **1991**, *30*, 409–412.
- (207) Savin, A.; Silvi, B.; Colonna, F. *Can. J. Chem.* **1996**, *74*, 1088–1096.
- (208) Lu, T.; Chen, F. *J. Comput. Chem.* **2012**, *33*, 580–592.
- (209) Bauer, C. A.; Hansen, A.; Grimme, S. *Chem. Eur. J.* **2017**, *23*, 6150–6164.
- (210) Weigend, F.; Ahlrichs, R. *Phys. Chem. Chem. Phys.* **2005**, *7*, 3297–3305.
- (211) Weigend, F. *Phys. Chem. Chem. Phys.* **2006**, *8*, 1057–1065.

- (212) Chan, G. K.-L.; Sharma, S. *Annu. Rev. Phys. Chem.* **2011**, *62*, 465–481.
- (213) Grützmacher, H.; Fässler, T. F. *Chem. Eur. J.* **2000**, *6*, 2317–2325.
- (214) Laplaza, R.; Polo, V.; Contreras-García, J. *Phys. Chem. Chem. Phys.* **2019**, *21*, 20927–20938.
- (215) Savin, A.; Nesper, R.; Wengert, S.; Fässler, T. F. *Angew. Chem. Int. Ed.* **1997**, *36*, 1808–1832.
- (216) Vuckovic, S.; Song, S.; Kozłowski, J.; Sim, E.; Burke, K. *J. Chem. Theory Comput.* **2019**, *15*, 6636–6646.
- (217) Wu, Q.; Yang, W. *J. Chem. Phys.* **2003**, *118*, 2498–2509.
- (218) Nam, S.; McCarty, R. J.; Park, H.; Sim, E. *J. Chem. Phys.* **2021**, *154*, 124122.
- (219) Head-Gordon, M. *Chem. Phys. Lett.* **2003**, *372*, 508–511.
- (220) Grimme, S.; Hansen, A. *Angew. Chem. Int. Ed.* **2015**, *54*, 12308–12313.
- (221) Brorsen, K. R.; Yang, Y.; Pak, M. V.; Hammes-Schiffer, S. *J. Phys. Chem. Lett.* **2017**, *8*, 2076–2081.
- (222) Medvedev, M. G.; Bushmarinov, I. S.; Sun, J.; Perdew, J. P.; Lyssenko, K. A. *Science* **2017**, *355*, 49–52.
- (223) Gould, T. *J. Chem. Phys.* **2023**, *159*, 204111.
- (224) Landeros-Rivera, B.; Gallegos, M.; Munárriz, J.; Laplaza, R.; Contreras-García, J. *Phys. Chem. Chem. Phys.* **2022**, *24*, 21538–21548.
- (225) Mezei, P. D.; Csonka, G. I.; Kállay, M. *J. Chem. Theory Comput.* **2017**, *13*, 4753–4764.
- (226) Brémond, É.; Tognetti, V.; Chermette, H.; Sancho-García, J. C.; Joubert, L.; Adamo, C. *J. Chem. Theory Comput.* **2022**, *18*, 293–308.

- (227) Verma, P.; Truhlar, D. G. *Phys. Chem. Chem. Phys.* **2017**, *19*, 12898–12912.
- (228) Ranasinghe, D. S.; Perera, A.; Bartlett, R. J. *J. Chem. Phys.* **2017**, *147*, 204103.
- (229) Gould, T. *J. Chem. Theory Comput.* **2017**, *13*, 2373–2377.
- (230) Hicks, J.; Vasko, P.; Goicoechea, J. M.; Aldridge, S. *Angew. Chem. Int. Ed.* **2021**, *60*, 1702–1713.
- (231) Coles, M. P.; Evans, M. J. *Chem. Commun.* **2023**, *59*, 503–519.
- (232) Gaussian 16, Revision B.01, Frisch, M. J.; Trucks, G. W.; Schlegel, H. B.; Scuseria, G. E.; Robb, M. A.; Cheeseman, J. R.; Scalmani, G.; Barone, V.; Petersson, G. A.; Nakatsuji, H.; Li, X.; Caricato, M.; Marenich, A. V.; Bloino, J.; Janesko, B. G.; Gomperts, R.; Mennucci, B.; Hratchian, H. P.; Ortiz, J. V.; Izmaylov, A. F.; Sonnenberg, J. L.; Williams-Young, D.; Ding, F.; Lipparini, F.; Egidi, F.; Goings, J.; Peng, B.; Petrone, A.; Henderson, T.; Ranasinghe, D.; Zakrzewski, V. G.; Gao, J.; Rega, N.; Zheng, G.; Liang, W.; Hada, M.; Ehara, M.; Toyota, K.; Fukuda, R.; Hasegawa, J.; Ishida, M.; Nakajima, T.; Honda, Y.; Kitao, O.; Nakai, H.; Vreven, T.; Throssell, K.; Montgomery, J. A., Jr.; Peralta, J. E.; Ogliaro, F.; Bearpark, M. J.; Heyd, J. J.; Brothers, E. N.; Kudin, K. N.; Staroverov, V. N.; Keith, T. A.; Kobayashi, R.; Normand, J.; Raghavachari, K.; Rendell, A. P.; Burant, J. C.; Iyengar, S. S.; Tomasi, J.; Cossi, M.; Millam, J. M.; Klene, M.; Adamo, C.; Cammi, R.; Ochterski, J. W.; Martin, R. L.; Morokuma, K.; Farkas, O.; Foresman, J. B.; Fox, D. J. Gaussian, Inc., Wallingford CT, **2016**.
- (233) Marenich, A. V.; Cramer, C. J.; Truhlar, D. G. *J. Phys. Chem. B* **2009**, *113*, 6378–6396.
- (234) McLean, A. D.; Chandler, G. S. *J. Chem. Phys.* **1980**, *72*, 5639–5648.

- (235) Krishnan, R.; Binkley, J. S.; Seeger, R.; Pople, J. A. *J. Chem. Phys.* **1980**, *72*, 650–654.
- (236) Boys, S. F.; Bernardi, F. *Mol. Phys.* **1970**, *19*, 553–566.
- (237) Simon, S.; Duran, M.; Dannenberg, J. J. *The Journal of Chemical Physics* **1996**, *105*, 11024–11031.
- (238) Glendening, E. D.; Landis, C. R.; Weinhold, F. *J. Comput. Chem.* **2013**, *34*, 1429–1437.
- (239) AIMAll (Version 19.10.12), Keith, T. A., TK Gristmill Software, Overland Park KS, USA, **2019** (aim.tkgristmill.com).
- (240) London, F. *J. Phys. Radium* **1937**, *8*, 397–409.
- (241) McWeeny, R. *Phys. Rev.* **1962**, *126*, 1028–1034.
- (242) Ditchfield, R. *Mol. Phys.* **1974**, *27*, 789–807.
- (243) Wolinski, K.; Hinton, J. F.; Pulay, P. *J. Am. Chem. Soc.* **1990**, *112*, 8251–8260.
- (244) Cheeseman, J. R.; Trucks, G. W.; Keith, T. A.; Frisch, M. J. *J. Chem. Phys.* **1996**, *104*, 5497–5509.
- (245) Zhurko, A., *Chemcraft – graphical software for visualization of quantum chemistry computations*, version 1.8 (build 654), <https://www.chemcraftprog.com>, Ivanovo, **2005**.
- (246) Pettersen, E. F.; Goddard, T. D.; Huang, C. C.; Couch, G. S.; Greenblatt, D. M.; Meng, E. C.; Ferrin, T. E. *J. Comput. Chem.* **2004**, *25*, 1605–1612.
- (247) Matta, C. F.; Boyd, R. J. In *The Quantum Theory of Atoms in Molecules*; John Wiley & Sons, Ltd, **2007**; pp 1–34.
- (248) Dominikowska, J.; Palusiak, M. *Struct. Chem.* **2012**, *23*, 1173–1183.

- (249) Kira, M.; Iwamoto, T. In *Advances in Organometallic Chemistry*; West, R., Hill, A. F., Eds.; Academic Press, **2006**; Vol. 54, pp 73–148.
- (250) Carter, E. A.; Goddard, W. A. I. *J. Phys. Chem.* **1986**, 90, 998–1001.
- (251) Trinquier, G.; Malrieu, J.-P. *J. Am. Chem. Soc.* **1987**, 109, 5303–5315.
- (252) Malrieu, J. P.; Trinquier, G. *J. Am. Chem. Soc.* **1989**, 11, 5916–5921.
- (253) Karni, M.; Apeloig, Y. *J. Am. Chem. Soc.* **1990**, 112, 8589–8590.
- (254) Kubas, G. J. *Metal Dihydrogen and σ -Bond Complexes: Structure Theory and Reactivity*; Springer US: Boston, MA, **2001**.
- (255) Mas-Ballesté, R.; Lledós, A. In *Comprehensive Inorganic Chemistry II (Second Edition)*; Reedijk, J., Poeppelmeier, K., Eds.; Elsevier: Amsterdam, **2013**; pp 727–766.
- (256) Nagata, K.; Murosaki, T.; Agou, T.; Sasamori, T.; Matsuo, T.; Tokitoh, N. *Angew. Chem. Int. Ed.* **2016**, 55, 12877.
- (257) Queen, J. D.; Lehmann, A.; Fettingner, J. C.; Tuononen, H. M.; Power, P. P. *J. Am. Chem. Soc.* **2020**, 142, 20554–20559.
- (258) Neese, F. *WIREs Comput. Mol. Sci.* **2012**, 2, 73–78.
- (259) Neese, F. *WIREs Comput. Mol. Sci.* **2018**, 8, e1327.
- (260) te Velde, G.; Bickelhaupt, F. M.; Baerends, E. J.; Fonseca Guerra, C.; van Gisbergen, S. J. A.; Snijders, J. G.; Ziegler, T. *J. Comput. Chem.* **2001**, 22, 931–967.
- (261) Riplinger, C.; Neese, F. *J. Chem. Phys.* **2013**, 138, 034106.
- (262) Riplinger, C.; Sandhoefer, B.; Hansen, A.; Neese, F. *J. Chem. Phys.* **2013**, 139, 134101.

- (263) Guo, Y.; Riplinger, C.; Becker, U.; Liakos, D. G.; Minenkov, Y.; Cavallo, L.; Neese, F. *J. Chem. Phys.* **2018**, *148*, 011101.
- (264) Guo, Y.; Riplinger, C.; Liakos, D. G.; Becker, U.; Saitow, M.; Neese, F. *J. Chem. Phys.* **2020**, *152*, 024116.
- (265) Van Lenthe, E.; Baerends, E. J. *J. Comput. Chem.* **2003**, *24*, 1142–1156.
- (266) Zeist, W.-J. van; Bickelhaupt, F. M. *Org. Biomol. Chem.* **2010**, *8*, 3118–3127.
- (267) Wendel, D.; Szilvási, T.; Jandl, C.; Inoue, S.; Rieger, B. *J. Am. Chem. Soc.* **2017**, *139*, 9156–9159.
- (268) Zhang, X.; Cao, Z. *Dalton Trans.* **2016**, *45*, 10355–10365.
- (269) McOnie, S. L.; Özpınar, G. A.; Bourque, J. L.; Müller, T.; Baines, K. M. *Dalton Trans.* **2021**, *50*, 17734–17750.
- (270) Sharif, Z. M.; Özpınar, G. A.; McOnie, S. L.; Boyle, P. D.; Müller, T.; Baines, K. M. *Chem. Eur. J.* **2023**, *29*, e202301003.
- (271) Villegas-Escobar, N.; Toro-Labbé, A.; Schaefer III., H. F. *Chem. Eur. J.* **2021**, *27*, 17369–17378.
- (272) Villegas-Escobar, N.; Gutiérrez-Oliva, S.; Toro-Labbé, A. *J. Phys. Chem. C* **2015**, *119*, 26598–26604.
- (273) Ribeiro, R. F.; Marenich, A. V.; Cramer, C. J.; Truhlar, D. G. *J. Phys. Chem. B* **2011**, *115*, 14556–14562.
- (274) Grimme, S. *Chem. Eur. J.* **2012**, *18*, 9955–9964.
- (275) Illas, F.; Moreira, I. P. R.; de Graaf, C.; Barone, V. *Theor. Chem. Acc.* **2000**, *104*, 265–272.

- (276) Szabo, A.; Ostlund, N. S. *Modern Quantum Chemistry*; Dover: New York, NY, **1996**.
- (277) Yamaguchi, K.; Takahara, Y.; Fueno, T.; Houk, K. N. *Theoret. Chim. Acta* **1988**, 73, 337–364.
- (278) Yamaguchi, K.; Okumura, M.; Mori, W.; Maki, J.; Takada, K.; Noro, T.; Tanaka, K. *Chem. Phys. Lett.* **1993**, 210, 201–210.
- (279) Yamanaka, S.; Okumura, M.; Nakano, M.; Yamaguchi, K. *J. Mol. Struct.* **1994**, 310, 205–218.
- (280) Kitagawa, Y.; Saito, T.; Nakanishi, Y.; Kataoka, Y.; Matsui, T.; Kawakami, T.; Okumura, M.; Yamaguchi, K. *J. Phys. Chem. A* **2009**, 113, 15041–15046.
- (281) Banerjee, S.; Ballmann, G. M.; Evans, M. J.; O'Reilly, A.; Kennedy, A. R.; Fulton, J. R.; Coles, M. P.; Mulvey, R. E. *Chem. Eur. J.* **2023**, 29, e202301849.
- (282) Hinz, A.; Breher, F. *Angew. Chem. Int. Ed.* **2018**, 57, 8818–8820.
- (283) Ishida, K.; Morokuma, K.; Komornicki, A. *J. Chem. Phys.* **1977**, 66, 2153–2156.
- (284) P. Mitoraj, M.; Michalak, A.; Ziegler, T. *J. Chem. Theory Comput.* **2009**, 5, 962–975.
- (285) Fonseca Guerra, C.; Handgraaf, J.-W.; Baerends, E. J.; Bickelhaupt, F. M. *J. Comput. Chem.* **2004**, 25, 189–210.
- (286) Franchini, M.; Philipsen, P. H. T.; van Lenthe, E.; Visscher, L. *J. Chem. Theory Comput.* **2014**, 10, 1994–2004.
- (287) Becke, A. D. *J. Chem. Phys.* **1988**, 88, 2547–2553.
- (288) Franchini, M.; Philipsen, P. H. T.; Visscher, L. *J. Comput. Chem.* **2013**, 34, 1819–1827.

- (289) Bader, R. F. W. *Acc. Chem. Res.* **1985**, *18*, 9–15.
- (290) Özgün, T.; Bergander, K.; Liu, L.; Daniliuc, C. G.; Grimme, S.; Kehr, G.; Erker, G. *Chem. Eur. J.* **2016**, *22*, 11958–11961.
- (291) Bursch, M.; Mewes, J. M.; Hansen, A.; Grimme, S. *Angew. Chem. Int. Ed.* **2022**, *61*, e202205735.
- (292) Frey, G. D.; Masuda, J. D.; Donnadieu, B.; Bertrand, G. *Angew. Chem. Int. Ed.* **2010**, *49*, 9444–9447.
- (293) Xu, M.; Jupp, A. R.; Qu, Z.-W.; Stephan, D. W. *Angew. Chem. Int. Ed.* **2018**, *130*, 11216–11220.
- (294) Fernández, I.; Bickelhaupt, F. M. *Chem. Soc. Rev.* **2014**, *43*, 4953–4967.
- (295) Vermeeren, P.; van der Lubbe, S. C. C.; Fonseca Guerra, C.; Bickelhaupt, F. M.; Hamlin, T. A. *Nat. Protoc.* **2020**, *15*, 649–667.
- (296) Cremer, D.; Kraka, E. *Angew. Chem. Int. Ed.* **1984**, *23*, 627–628.
- (297) Evans, M. J.; Anker, M. D.; McMullin, C. L.; Neale, S. E.; Coles, M. P. *Angew. Chem. Int. Ed.* **2021**, *60*, 22289–22292.
- (298) Liu, H.-Y.; Hill, M. S.; Mahon, M. F.; McMullin, C. L.; Schwamm, R. J. *Organometallics* **2023**.
- (299) Martínez-Martínez, A. J.; Armstrong, D. R.; Conway, B.; Fleming, B. J.; Klett, J.; Kennedy, A. R.; Mulvey, R. E.; Robertson, S. D.; O'Hara, C. T. *Chem. Sci.* **2013**, *5*, 771–781.
- (300) Luchini, G.; Alegre-Requena, J. V.; Funes-Ardoiz, I.; Paton, R. S. *F1000Research* **2020**, *9*, 291.
- (301) Westerhausen, M. *Inorg. Chem.* **1991**, *30*, 96–101.

- (302) Davidson, M. G.; Garcia-Vivo, D.; Kennedy, A. R.; Mulvey, R. E.; Robertson, S. D. *Chem. Eur. J.* **2011**, *17*, 3364–3369.
- (303) Robertson, S. D.; Rae, A.; Byrne, K. M.; Brown, S. A.; Kennedy, A. R.; Krämer, T.; Mulvey, R. E. *Chem. Eur. J.* **2022**, *28*.
- (304) Tesh, K. F.; Hanusa, T. P.; Huffman, J. C. *Inorg. Chem.* **1990**, *29*, 1584–1586.
- (305) Li, S.-Y.; Li, Y.; Du, H.-Z.; Wu, J.; Luo, G.; Guan, B.-T. *Organometallics* **2024**, *43*, 526–531.
- (306) Spivey, J. A.; Collum, D. B. *J. Am. Chem. Soc.* **2024**, *146*, 17827–17837.
- (307) Kennedy, A. R.; Mulvey, R. E.; Rowlings, R. B. *J. Organomet. Chem.* **2002**, *648*, 288–292.
- (308) C. Forbes, G.; R. Kennedy, A.; Mulvey, R. E.; Roberts, B. A.; Rowlings, R. B. *Organometallics* **2002**, *21*, 5115–5121.
- (309) Starowieyski, K. B.; Lewinski, J.; Wozniak, R.; Lipkowski, J.; Chrost, A. *Organometallics* **2003**, *22*, 2458–2463.
- (310) Brookhart, M.; Green, M. L. H.; Parkin, G. *Proc. Natl. Acad. Sci. USA* **2007**, *104*, 6908–6914.
- (311) Maddock, L. C. H.; Mu, M.; Kennedy, A. R.; Garcia-Melchor, M.; Hevia, E. *Angew. Chem. Int. Ed.* **2021**, *60*, 15296–15301.
- (312) Armstrong, D. R.; Davidson, M. G.; Garcia-Vivo, D.; Kennedy, A. R.; Mulvey, R. E.; Robertson, S. D. *Inorg. Chem.* **2013**, *52*, 12023–12032.
- (313) Gallagher, D. J.; Henderson, K. W.; Kennedy, A. R.; O'Hara, C. T.; Mulvey, R. E.; Rowlings, R. B. *Chem. Commun.* **2002**, 376–377.